Taper Junctions in modular total hip arthroplasty

Reynol Alejandro Diaz-Lopez

Submitted in accordance with the requirements for the degree of Doctor of Philosophy

School of Engineering and Materials Sciences

Queen Mary University of London

April 2023

Statement of originality

I, Reynol Alejandro Diaz-Lopez, confirm that the research included within this thesis is my own work or that where it has been carried out in collaboration with, or supported by others, that this is duly acknowledged below, and my contribution indicated. Previously published material is also acknowledged below.

I attest that I have exercised reasonable care to ensure that the work is original and does not to the best of my knowledge break any UK law, infringe any third party's copyright or other Intellectual Property Right, or contain any confidential material.

I accept that the College has the right to use plagiarism detection software to check the electronic version of the thesis.

I confirm that this thesis has not been previously submitted for the award of a degree by this or any other university.

The copyright of this thesis rests with the author and no quotation from it or information derived from it may be published without the prior written consent of the author.

Signature: Diaz-Lopez, R.A.

Date: 15/02/2023

Details of collaboration and publications:

R.A. Diaz-Lopez, P.H. Wen, J.C. Shelton, Influence of taper design and loading on taper micromotion, Journal of the Mechanical Behavior of Biomedical Materials, Volume 128, 2022, ISSN 1751-6161,
DOI: https://doi.org/10.1016/j.jmbbm.2022.105106.

Abstract

Morse tapers are widely used in modular total hip joint replacements (THRs) to attach the femoral head onto the femoral stem. Despite the success of THR procedures, the taper junction has been associated with failures due to damage at the interface generated by fretting and corrosion. Taper design parameters including taper clearance, length, diameter, and assembly conditions have been previously shown to influence the generation of micromotions associated with taper damage. However, the role of taper geometry and surface topography on the mechanisms that influence damage is not well understood.

3D FE models of CoCr alloy femoral heads assembled onto Ti alloy trunnions were developed to investigate the contact environment and the relative motions generated in the taper interface during loading. The maximum accumulated micromotions (49 μm) over a walking cycle were found in tapers with an oval trunion and high clearance. The components of the micromotions (pistoning, normal and tangential) varied with the taper geometry and loading activity. The largest contribution of micromotion in the oval taper arise from tangential motion whilst for a round taper the relative motions were dominated by normal and pistoning.

The effect of surface topography (form, waviness and roughness) on the micromotions generated were studied using 2D and 3D models. Contact conditions in the taper interface as a result of the interaction of different surface topographies at different assembly forces were studied. Idealised taper surfaces were found to be different from real, measured surfaces when assembled and generated different contact conditions. Power Spectrum Density (PSD) analysis showed that idealised surfaces comprised of only one spatial wave frequency while measured data contained 3 - 7 spatial wave frequencies. When surfaces where assembled, the measured surfaces showed flattening of the roughness peaks and large plastic strains which reached values that indicated material failure (>0.6). In measured bore surfaces, intermittent contact of deformed trunnion peaks was identified as the assembly force increased. The interaction of the surfaces in the 2D models led to the estimation of a global coefficient of friction (COF); surface roughness and adhesion had a significant effect on this estimation, for example when using a local COF of 0.21 to simulated adhesion, the estimated global COF ranged from 0.21 to 0.46. Using a value of friction from this estimated global COF in the 3D taper model under walking conditions influenced the results obtained; a high COF (0.46) decreased the magnitude of resultant micromotions but increased the magnitude of normal and tangential relative motions magnitudes by 15% and 115% respectively and decreased pistoning by 145% compared to motions generated with a global COF of 0.21.

Findings from these studies suggest that the surface topography variations comprising roughness, waviness and form determine the taper performance. These findings help to understand the role of surface design in tapers and highlight the importance of manufacturing processes which will significantly affect a taper's performance.

Acknowledgements

I would like to express the deepest appreciation to my supervisor, Prof Julia Shelton, for her unvaluable support and patience during throughout my PhD research journey. Words are not enough to express the gratitude for providing me the opportunity to work under her supervision.

Adam, Soraya, Chris, and Gary thank you so much for being there and listening to me when I needed the most, thanks for your endless laughs and fond memories. You were one of the best findings of this journey.

Lastly, I would like to thank my family for their support and belief in me. Your words of wisdom, kindness, and patience kept me going on this journey.

Thank you all.

List of tables

List of Figures

1 Introduction

Corrosion at the interface of the head-neck taper junction in modular total hip joint replacements (THR), also known as trunnionosis has been identified as a source of metal debris that can cause the failure of the implant (Mistry et al., 2016; Pastides, 2013; Weiser & Lavernia, 2017). It is estimated that up to 3% of THR revisions procedures are due to corrosion at the taper interface, which accounted for approximately 2000 revision procedures due to trunniononsis between 2013 and 2021 in the UK alone (Drummond et al., 2015; NJR, 2022; Porter et al., 2014a).

Initially trunniononsis was associated exclusively with Metal-on-Metal (MoM) bearings due to higher friction at the femoral head–acetabular cup interface that may increase bending moments and relative motions at the head-neck taper interface (Drummond et al., 2015; Liao et al., 2013). It was suggested that non-MoM bearings including Metal-on-Polyethylene (MoP), Ceramic-on-Polyethylene (CoP) and Ceramic-on-Ceramic (CoC), would display significantly lower rates of corrosion in the taper interface. However recent reports have shown that there is a risk of adverse reactions to metal debris (ARMD) in non-MoM bearings, which accounts for up to 7.5% of ARMD related revision produces, with CoC bearings appearing to present a higher risk compared to other non-MoM bearings (Bhalekar et al., 2019; del Balso et al., 2021; Matharu et al., 2016).

Investigations associated with taper junctions at the head-neck interface have studied factors that can trigger corrosion and wear damage, where the relative motions, referred to as micromotions, occurring at the taper interface have been identified as a predictor for taper damage. These micromotions can assist corrosion damage via fretting in a process called mechanical assisted crevice corrosion (MACC) (Baxmann et al., 2013; Falkenberg et al., 2019; Mali & Gilbert, 2015). Furthermore, micromotions at the taper interface can allow fluid ingress and egress into the taper increasing the risk for corrosion (Mali, 2016; Raji & Shelton, 2019). Relative motion magnitudes at the taper interface are affected by several factors including assembly conditions, trunnion flexural rigidity, taper length, clearance angle, head size, offset

and surface finish (Berstock et al., 2018; Falkenberg et al., 2019; Feyzi et al., 2021a). The nature of these micromotions and how they are affected by the geometrical design of tapers has not been previously described. Furthermore, in most previous studies the shape of tapers has been assumed to be a perfect cone, even though recent studies have shown that both taper components are neither perfectly circular nor straight (Bitter et al., 2018; Wade et al., 2020).

The role in damage generation at the taper interface of modular THR on surface finish variations is inconclusive (Arnholt et al., 2017; Brock et al., 2015). Smooth and rough surfaces have been widely used in trunnion surfaces (Munir et al., 2015; Whittaker et al., 2017). Trunnion threaded rough surfaces in tapers were developed to reduce contact stresses in ceramic heads following the assembly of the femoral head into the trunnion. The risk of fracturing the ceramic femoral head is reduced due to the threaded peaks flattening during assembly (El-Zein et al., 2021; Weiser & Lavernia, 2017). More recently rough trunnions are also coupled with metallic femoral heads (del Balso et al., 2021; NJR, 2022). However, regardless of the taper surface finish and material combination, the taper junction continues to be associated with the failure of the THR. Recent studies have showed that the contact environment in the taper interface of smooth and rough surfaces of the taper components are different (Bechstedt et al., 2020; Gustafson et al., 2020a, 2022; Lundberg et al., 2015; Witt et al., 2015), however how these changes affect the taper stability and its role on fretting corrosion generation is unclear.

2 Literature review

2.1 Total hip replacements

A total hip replacement (THR) is a medical procedure that attempts to restore the mobility and functionality of a diseased hip joint suffering from a range of conditions including, osteoarthritis, rheumatoid arthritis, hip dysplasia and trauma. In England and Wales alone, approximately 90,000 primary THR procedures were performed in 2021, and currently in the US approximately 2.5 million people are living with a hip replacement (Fawsitt et al., 2019; NJR, 2022). THR procedures were initially indicated only for the elderly and individuals with severe locomotor limitations associated with comorbidities. However, due to the development of new materials, designs and procedures, currently many conditions in the hip joint that compromises an individual's quality of life, including younger people and athletes, has become a valid justification to indicate a hip replacement. The improvements in hip replacement devices have been directed to increase the longevity of the device while a relatively high-activity profile of the individual is maintained. During a hip replacement procedure, the hip joint components, namely the femoral head and acetabulum are replaced. In total hip replacements, both of hip joint components are removed and replaced with a femoral head that articulates with an acetabular cup. The head is typically attached to the femur using a femoral stem (Figure 2.1). THR devices can differ in the materials used, the size of the implant and the insertion technique. The patient's conditions such as bone quality, anatomy, age, and mechanical demand are considered (Anakwe et al., 2011; Callaghan, 2016; Mistry et al., 2016; Pennock et al., 2002).

The first modern hip joint replacement was developed by Wiles which was improved and popularised by John Charnley in 1950. Charnley revolutionised the THR field by introducing low-friction arthroplasty, the fixation of THR components to the femoral bone with acrylic cement and the use of high-density polyethylene as an acetabular bearing material (Learmonth et al., 2007; Rogers et al., 2012).
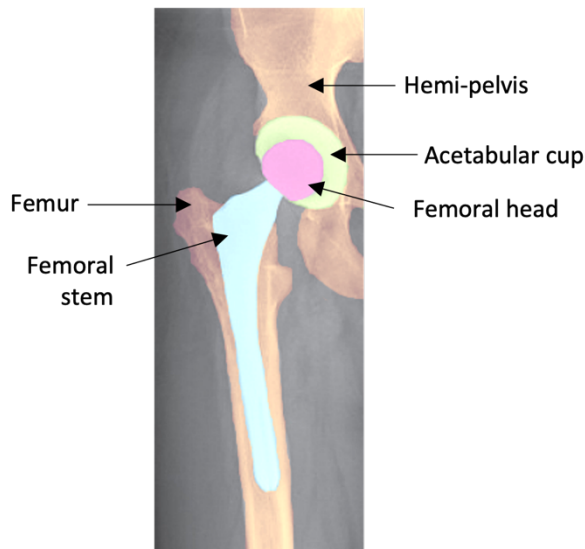
Figure 2.1. Uncemented modular total hip replacement device and its components, modified from (Callaghan, 2016).

Modularity in femoral and acetabular components was introduced to reduce the need to stock many sizes of femoral heads and stems, to adjust the THR device dimensions to cover the patient's anatomical requirements during surgery, as well as facilitating the changing of damaged components during revision operations. Modularity in the femoral components can be introduced through extra junctions between the neck and stem and/or the metaphysis and diaphysis which allows further independent adjustments. These adjustments include the vertical and horizontal distances between the centre of rotation of the femoral head and the longest axis of the femur, leg length and neck angle (Krishnan et al., 2013; Lecerf et al., 2009). There are three main regions of modularity which have been introduced namely proximal, mid-stem and distal. Proximal modularity was introduced as head-neck junctions, neck-stem junctions, anterior-posterior pads, which are not widely used now, modular collars, proximal shoulders and stem sleeves as shown in Figure 2.2. Modular junctions, which include head-neck and neck-stem of modular femoral components are coupled using taper mechanisms. Taper junctions in head-neck junctions referred as 'Morse tapers', are a type of self-holding taper where the male part (trunnion) and female part (bore) are held together by friction and compression forces with the intention of preventing relative movement between them (Krishnan et al., 2013; Oberg et al., 2012).

Figure 2.2. Modular femoral components of a THR with a head-neck junction (a), and neck-stem junctions (b), femoral pads (c), proximal shoulders (d), and stem sleeves (e) adapted from (Krishnan et al., 2013; McTighe et al., 2015a).

2.1.1 Taper design

The Morse taper was developed by Stephen A. Morse in 1964 to join two rotating machine components. A Morse taper consists of two cone elements, the trunnion and bore which are uniformly tapered. When the trunnion is introduced into the bore, trunnion and bore surfaces come into intimate contact; the conical femoral bore component compresses the trunnion generating stresses inside the bulk region of the components keeping both components fixed together. The design of Morse tapers is not entirely standarised in the orthopaedic industry, varying between manufacturers. The strength and stability of the taper junction is determined by a number of factors, including component geometry namely taper clearance, proximal and distal diameter of the taper components, trunnion length, surface finish, contact conditions between the bore and trunnion as well as material properties, coefficient of friction, size and density of the femoral head.
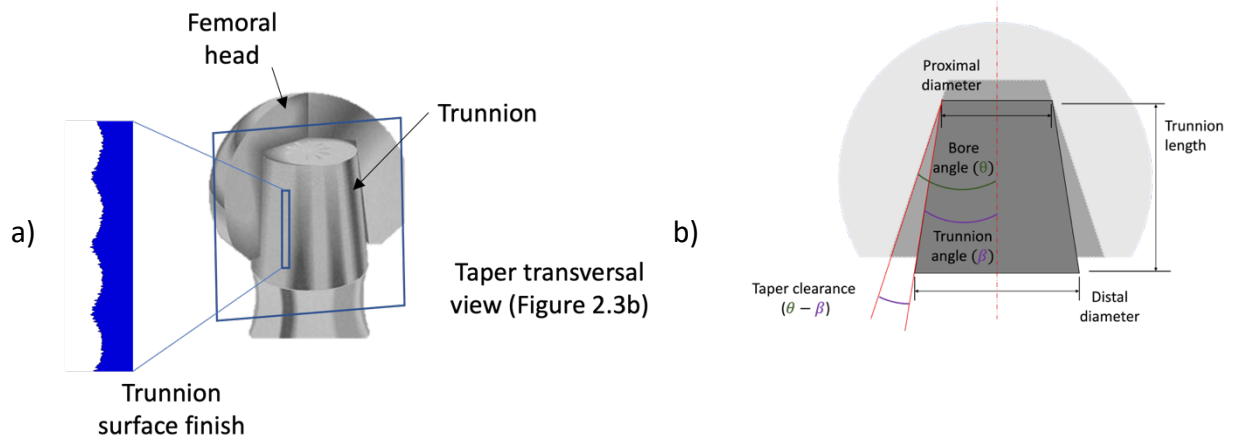
Figure 2.3. (a) Femoral head bore and trunnion components and (b) transverse view of design features of a taper junction.

Tapers are available in a range of sizes which are usually specified by their proximal and distal diameters measured in millimetres. Commercially available taper sizes include 9 mm/11 mm, 10/12, 11/13, 12/14 and 14/16, however tapers of the same size may not have the same taper angle as the cone angle is also in function of the taper length. Tapers can also be specified by their name such as Type-I, PCA, C-taper and are found with different proximal and distal diameter sizes, 11.7 ± 0.9/12.7 ± 0.9, 12.3 ± 0.7 /13.3 ± 0.5, 12.4 ± 0.4 /13.8 ±0.7 respectively. Modern tapers have been designed to be smaller (10/12 referred to as V40), in comparison to previous designs in order to improve the range of motion of a THR device by avoiding the impingement of femoral neck with the acetabular cup (Haschke et al., 2019; Morlock et al., 2014; Triantafyllopoulos et al., 2016; Werner et al., 2015) . The original Morse taper had an angle of 2.833°, which is relatively small compared to contemporary designs which have an angle of approximately 5.725° (Morlock et al., 2020). The clearance angle of a Morse taper is defined by the mismatch between the trunnion and bore angle. The locking of the bore and trunnion components can generate material transfer across the zone of contact; the strength of the locking is determined by the relative dimensions of the bore and trunnion as well as the assembly force (Hernigou et al., 2013; Hussenbocus et al., 2015).

Topography of the bore and trunnion components is varied as it is dependent on the manufacturer. Taper components are typically fabricated on a lathe, where

manufacturers can adapt the surface finish of the taper components to their needs by adjusting the tool's speed, feeding rate, and cutting tool (Hernigou et al., 2013; Munir et al., 2015). The surfaces are characterised by a series of peak and valleys of different heights and lengths, which can be described with roughness parameters namely arithmetic average profile roughness (Ra), average maximum height of the profile (Rz) and mean line peak spacing (RSm) (Mueller et al., 2017). Taper surfaces can be fabricated with smooth or rough surface and are classified in function of their Ra and Rz roughness parameters (Figure 2.4). A taper surface is considered smooth if the Ra and Rz values are less than 2 μm and 5 μm respectively, and rough if these values are exceeded (Mueller et al., 2017). Trunnion surfaces as well as femoral head bore surfaces present a large variability in the surface roughness as a result of different manufacturing processes (Table 2.1). Threaded surfaces were developed in order to increase the contact ratio and decrease stress concentrations in ceramic femoral heads by plastically deforming the trunnion threaded surface (peak flattening) during assembly (Hernigou et al., 2013; Hothi et al., 2015; Munir et al., 2015; Whittaker et al., 2017). The threaded trunnions are now commonly used for metal heads as well. RSm provides information on the spacing between the machined grooves generated by the lathe process, however this parameter is seldom used to describe taper surfaces (Mueller et al., 2017).

a) Smooth surface   b) Rough surface
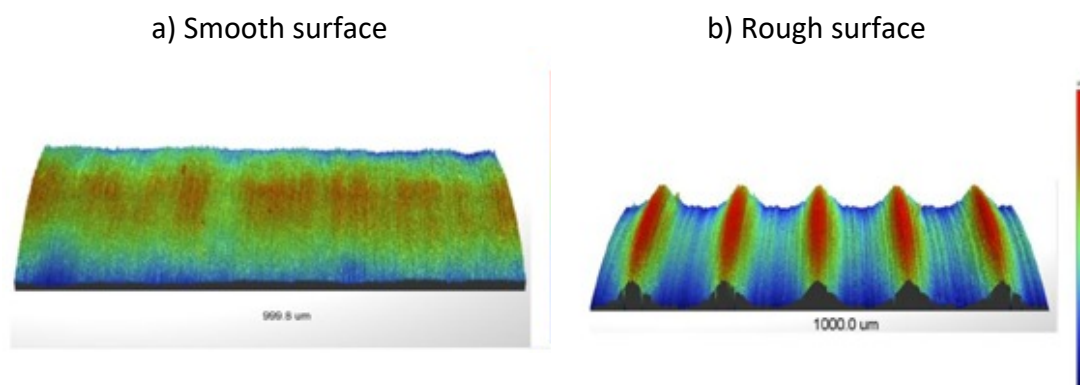
Figure 2.4 Taper surface with (a) smooth and (b) rough topography adapted from (Munir et al., 2015).

Table 2.1. Type of surface and roughness parameters of trunnion and bore components from different manufacturers (Mueller et al., 2017).

Component	Manufacturer	Surface finish	Ra (µm)	Rz (µm)	RSm (µm)
Trunnion	Stryker	Smooth	0.49 ± 0.08	2.63 ± 0.49	114.55 ± 2.91
Trunnion	Biomet	Rough	2.47 ± 0.01	9.36 ± 0.14	256.44 ± 0.04
Trunnion	Falcon	Rough	2.48 ± 0.11	9.92 ± 0.27	190.13 ± 0.12
Trunnion	DePuy	Rough	3.54 ± 0.02	14.25 ± 0.41	205.45 ± 0.24
Trunnion	Zimmer	Rough	13.65 ± 1.5	49.48 ± 4.44	143.58 ± 0.43
Bore	Stryker	Smooth	1.48 ± 0.85	1.32 ± 0.83	24.34 ± 5.68
Bore	Biomet	Smooth	0.32 ± 0.04	1.60 ± 0.15	34.12 ± 4.54
Bore	Falcon	Smooth	0.51 ± 0.01	2.89 ± 0.08	55.31 ± 1.34
Bore	DePuy	Smooth	0.62 ± 0.02	3.78 ± 0.18	43.52 ± 2.14
Bore	Zimmer	Smooth	13.65 ± 1.5	6.57 ± 3.11	65.65 ± 18.18
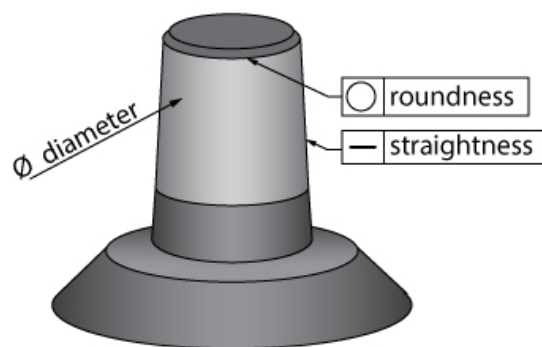
Figure 2.5. Roundness and straightness parameters of a trunnion adapted from (McTighe et al., 2015b).

Other taper specifications that are included in the design of taper junctions are the straightness and roundness of the components (Figure 2.5). These parameters are obtained by analysing the relationship between x, y and z coordinates of coordinate measurement machine (CMM) data. Recent investigations have shown that both trunnion and bore surfaces are far from ideal cones and present a variation on roundness and straightness generating oval trunnion with up to 6 µm out of ovality

(Figure 2.6a) and femoral head bores with concave surfaces with up to 3 μm of deviation from a straight line as shown in Figure 2.6b (Wade et al., 2020).
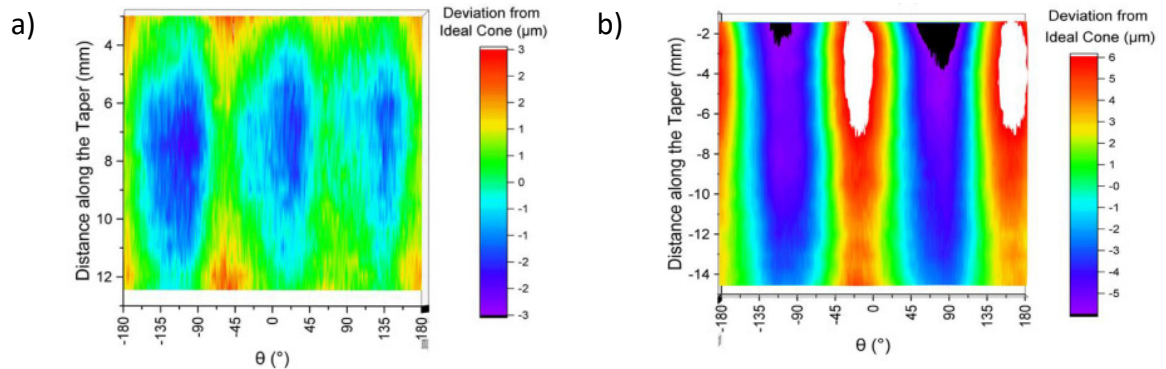
Figure 2.6. Deviation distance from an ideal cone for (a) femoral head bores and (b) trunnions; adapted from (Wade et al., 2020).

The head-neck junction components namely the trunnion and femoral head bore comprise of different material combinations that have been optimised for its specific function and durability. Cobalt-Chromium-Molybdenum (CoCrMo) alloy and alumina/zirconia toughened ceramics are commonly used for femoral heads due to their scratch and wear resistance properties. Trunnion components typically use steel alloys, TMZF (Ti-12Mo-6Zr-2Fe), and Ti6Al4V. (Raju et al., 2017; Swaminathan & Gilbert, 2012). The surface of these metallic components typically have a thin chemical inert oxide layer, 1-4 nm for Ti alloys and 2.6 nm for CoCrMo, that protects the bulk material from corrosion damage; this layer is generated by a process applied to the alloys when exposed to oxygen called passivation (Gilbert, 2012; Gilbert, Mali, et al., 2015; Hanawa et al., 2001; Mali, 2016). Metals used for orthopaedic devices are over passivated prior to implantation in order to protect the device components from the hostile physiological environment (Oladokun et al., 2019).

2.1.2   Environment of taper interface

During hip joint loading, the taper interface experiences a complex combination of forces and moments. The femoral head-neck junction enables load transfer through the taper axis between the femoral head and femoral stem (Farhoudi et al., 2015;

Gilbert, Mali, et al., 2015; Hall et al., 2018). The taper interface therefore experiences contact forces, frictional moments and bending moments (Figure 2.7).
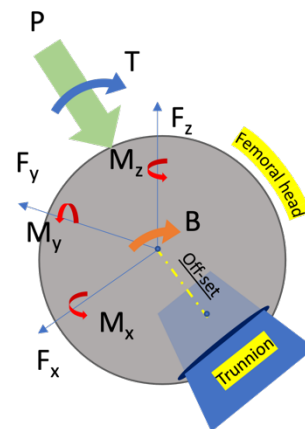
Figure 2.7. Forces (F) and moments (M) acting on the taper interface resulting from the joint force (P), frictional bearing (T) and bending moments (B).

Forces acting on the taper junction arise from the reaction forces due to the loading of the device whilst moments are the product of frictional moments at the bearing surface and bending moments caused by the offset between the centre of rotation and centre of the trunnion (Bergmann et al., 2016; Mali, 2016; Porter et al., 2014b). Different reaction forces and moments have been associated with daily activities including walking, sit-to-stand, stair climbing, jogging, and cycling, Figure 2.8 (Bergmann et al., 2016); forces and moments activity data is based on the obtained average forces and moments from 10 individuals with instrumented THR devices and an implantation time ranging between 10 and 13 months (Bergmann et al., 2016).
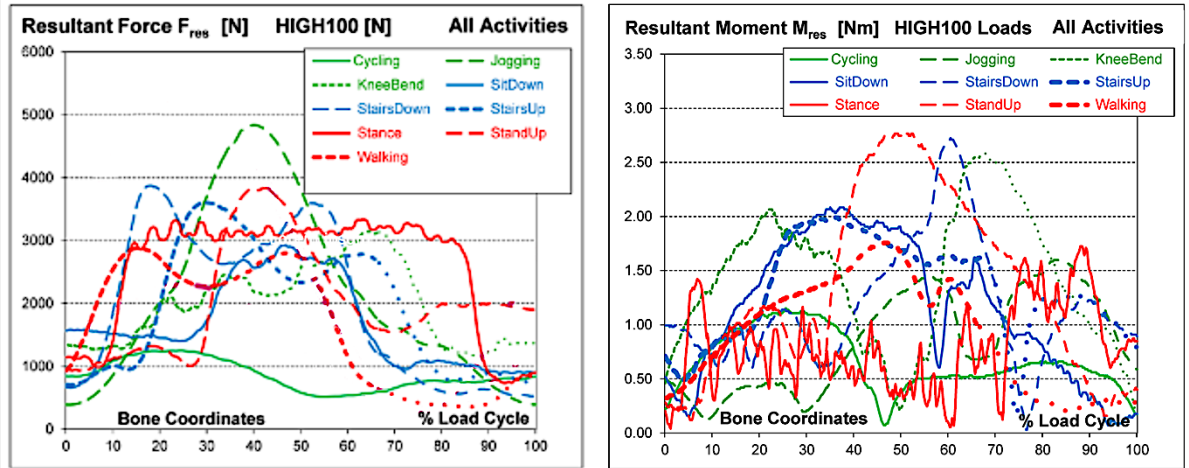
Figure 2.8. Resultant forces acting in an instrument hip joint implant during different activity cycles adapted from (Bergmann et al., 2016).

During the assembly of the trunnion with the femoral bore and during loading of the hip joint, normal and shear stresses are generated at the contact regions between the trunnion and bore surfaces. Shear stresses generated in the taper interface surface are the product of the interaction between normal forces and the coefficient of friction during sliding (Fessler & Fricker, 1989; MacLeod et al., 2016). The coefficient of friction (COF) is the relationship between the reaction tangential and normal forces (Equation 2.1) acting in a surface and indicates the amount of energy that it is required for a surface pair to slide (Figure 2.9) (Bitter et al., 2016; Green, 1955; Mulvihill et al., 2011). The COF is affected by the nature and the roughness of the interacting surfaces. In taper junctions the COF has been characterised as being from 0.14 to 0.5 (Bitter et al., 2016; Feyzi et al., 2021a).

$$\mu = \frac{Tangential\ reaction\ force}{Normal\ force}$$ Equation 2.1
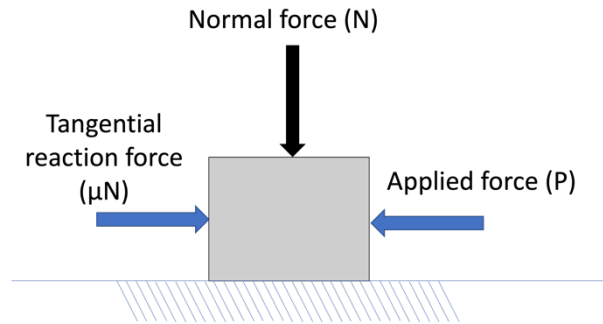
Figure 2.9. Schematics of tangential reaction forces result of the coefficient of friction.

2.2 Complications with head-neck taper junctions

In THR devices each modular junction, including the head-neck junction, introduces the potential for fretting, corrosion, wear, fatigue, and failure. Furthermore, after assembly of the femoral head bore onto the trunnion crevices may be generated due to geometrical restrictions of the components (Mali, 2016; Morlock et al., 2020). Cyclic loading of the modular hip joint implant with a changing magnitude and direction of the load vector, introduces oscillatory movement between the femoral head and femoral stem (Bergmann et al., 2010; Morlock et al., 2020). This relative motion can disrupt the passive oxide layer through fretting, thereby altering the potential and acidity of the local fluid environment, which eventually will result in the depletion of the protective surface oxide layer (Gilbert, 2012). This process has been called mechanically assisted crevice corrosion (MACC) and can generate metal ions that will migrate into the body and harmfully interact with soft tissue locally and systemically leading to necrosis, local synovitis, osteolysis, component loosening and early failure (Gilbert, 2012; Mali, 2016; Swaminathan & Gilbert, 2012). Implant failure and adverse soft tissue reactions due to the presence of metal ions that originate at the taper interface has been named as 'trunnionosis' (Pastides, 2013).

2.2.1 Taper corrosion

Corrosion in the head-neck junction of modular THR devices is generated through different modes (electrochemical and mechanical) and includes galvanic, fretting, crevice, pitting, and intergranular corrosion mechanisms (Pivec et al., 2014; Pourzal et al., 2018). In modular taper junctions, fretting and crevice corrosion are prevalent

due to crevices existing in the taper interface as well as the cyclic mechanical environment (Figure 2.10) (Berstock et al., 2018; Morlock et al., 2020; Pourzal et al., 2018).

Corrosion can occur on both of the taper components, however, on the trunnion it is less frequently observed and also appears to be less severe. Usually, higher corrosion damage is found at the bore opening opposite to the region of wear damage. The damage patterns on the taper interface are associated with a mechanical process, referred to as toggling, where the generation of corrosion damage occurs in the taper interface (English et al., 2015; Langton et al., 2012; Tan et al., 2015).
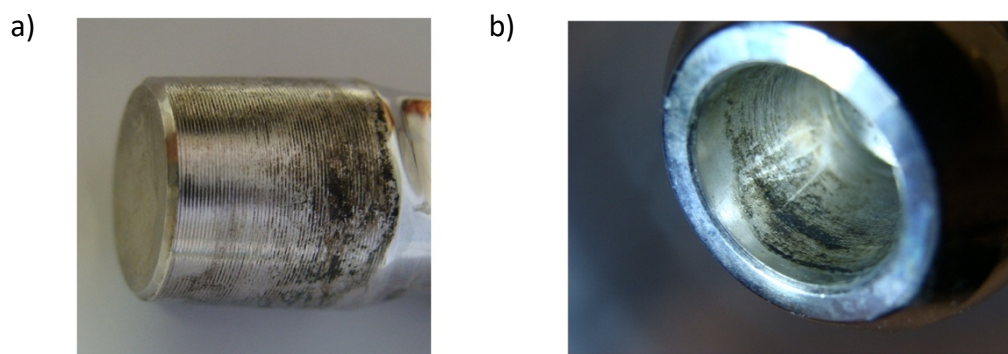
Figure 2.10. Fretting and corrosion damage on a (a) Ti-alloy trunnion and (b) CoCr femoral head bore. Components were retrieved from a failed metal-on-polyethylene THR. Adapted from (Hussenbocus et al., 2015).

2.2.2 Taper fretting

Taper damage is not purely driven by electrochemical damage processes, such as corrosion, but it can also be initiated by micromotions (Feyzi et al., 2021a; Lundberg et al., 2015; Pourzal et al., 2018). Fretting in the taper interface is caused through the cyclic relative motions over the contacting regions of the bore and trunnion surfaces, which results in the passive film disruption and wear of the contacting surfaces, subsequently initiating corrosion (Royhman et al., 2021). Micromotions can also lead

to changes in the geometry of the contacting surfaces widening already existing crevices and facilitating the fluid ingress into the taper interface (Feyzi et al., 2021a; Kaur et al., 2019).

2.3 Clinical detection of taper wear damage

Adverse local tissue reactions (ALTR) associated with corrosion at the head-neck junction can clinically manifest itself in different ways (Fitz et al., 2020; Whitehouse et al., 2015). Pain in the hip joint or groin is the principal symptom reported in trunnionsis cases, however pain can also be associated with other conditions not related to taper corrosion such as bursitis, aseptic loosening and referred pain (Plummer et al., 2016). A systematic evaluation is required to identify the cause of pain, instability and/or metal ions; which includes a clinical evaluation, inflammatory markers, metal ion levels in blood, radiography and cross-sectional imaging, corrosion scoring systems as described in Table 2.2.

Table 2.2. Clinical evaluation to help identify failure of the THR implant due to metal debris.

Evaluation	Parameters considered	Reference
Clinical evaluation	Onset duration of pain, severity, location, pain characteristics, palpable swelling	(Plummer et al., 2016)
Inflammatory markers	Synovial fluid cell count, erythrocyte sedimentation, proteins.	(Fitz et al., 2020)
Metal ion levels in blood	Co, Cr, and Ti levels	(Fillingham et al., 2017)
Radiography	Implant type and alignment	(McGrory & McKenney, 2016)
MRI	Severity of tissue damage	(McGrory & McKenney, 2016)
Implant damage	Goldberg scoring system	(Goldberg et al., 2002)

In THR devices utilising a metal head, once corrosion in the taper junction has been identified revision surgery is required (Fitz et al., 2020; Pivec et al., 2014). The most common surgical approach is replacing the damaged metal femoral head with a ceramic one. The goal of revision surgical treatments is to remove the source of metal

ions and to restore the hip stability (Fitz et al., 2020). A Ti alloy sleeve is commonly used on the newly implanted ceramic head to provide an optimal taper fit and reduce further taper corrosion (Pivec et al., 2014).

2.4   Factors affecting taper wear and corrosion damage

Modular junctions exposed to body fluids and micromotions will develop some degree of corrosion. In the head-neck junction the micromotions generated at the interface are influenced by several factors related to implant design factors, surgical and patient factors (Fitz et al., 2020; Hothi et al., 2017; Pourzal et al., 2018). The amount of fretting damage is determined by the magnitude of micromotions, taper contact pressure, and number cycles (Mali & Gilbert, 2015; Royhman et al., 2021; Swaminathan & Gilbert, 2012). However, evidence for the severity of corrosion damage at the taper interface *in vivo* as a function of time is contradictory (Morlock et al., 2020; Nassif et al., 2014; Pourzal et al., 2018; Triantafyllopoulos et al., 2016). The degradation processes in tapers due to fretting, wear and corrosion can be investigated by studying the mechanical factors which these processes are in function of, such as micromotions, contact pressures, strains, or a combination of these (Feyzi et al., 2021a). Throughout this study, the magnitude of micromotions predicted in FE models of tapers are used to estimate the severity of fretting and wear damage in the taper interface.

2.4.1   Implant design factors

2.4.1.1   Femoral head size

Larger femoral heads (>36mm) were introduced in THR devices to reduce impingement and the risk of dislocation whilst increasing the joint's range of motion; however larger heads can also result in elevated stresses, fretting and corrosion damage at the taper junction due to higher torsional and frictional moments (del Balso et al., 2015; El-Zein et al., 2021; Norman et al., 2019; Panagiotidou et al., 2017; Raji & Shelton, 2019; Triantafyllopoulos et al., 2016; Tsikandylakis et al., 2018). Indeed, a large femoral head has been identified as a predictor for corrosion damage in the head-neck junctions (Hothi et al., 2015, 2017; Lavernia et al., 2015).

2.4.1.2 Bearing material combination

The material combination at the bearing surfaces of the THR implant has been shown to influence the fretting and corrosion damage at the taper interface (El-Zein et al., 2021; Ouellette et al., 2019). Materials of the femoral head and acetabular cup will determine the frictional forces of the bearing which will directly affect the frictional moments that are generated during activities (Farhoudi et al., 2015, 2016). Indeed, non-Metal-on-Metal (non-MoM) bearings generate lower fretting and corrosion damage compared to MoM bearings (Gilbert, Sivan, et al., 2015; Jaekel et al., 2014; Kocagöz et al., 2013; Matharu et al., 2016). Ceramic heads may mitigate fretting and corrosion damage but do not completely eliminate it (Kocagöz et al., 2013).

2.4.1.3 Head off-set

The offset distance in a modular THR implant allows the surgeon to intraoperatively restore the physiological centre of the hip joint (Cartner et al., 2017; del Balso et al., 2021). An offset of 0 mm indicates that the centre of the femoral head is coincident with the trunnion and bore engagement point; offset distances range from -3 to +12 mm (Cartner et al., 2017). Nevertheless, THR implants with offsets deviating from a neutral distance (0 mm) have been associated with higher fretting corrosion scores. It has been suggested that the femoral head offset, in addition to the femoral head size, contributes to the resultant moment arm at THR head-neck junction resulting in larger micromotions at the taper interface (Cartner et al., 2017; del Balso et al., 2021). This concept has been supported by studies on THR using both numerical simulations and experimental work (Dyrkacz et al., 2015; Krull et al., 2018).

2.4.1.4 Taper material combination

Material combination in the taper junctions has been reported to determine the extent of damage at the junction interface and the manner the implant may fail (del Balso et al., 2021; Morlock et al., 2020; Pastides, 2013). Corrosion in junctions involving a Ti-alloy bore and trunnion components is not generally recognised until mechanical failure occurs due to the absence of biological response to Ti debris (Gibon et al., 2017; Lützner et al., 2020). In CoCr femoral heads assembled with Ti-

alloy trunnions, failure occurs due to the biological response to the CoCr debris created by corrosion in the taper interface with no mechanical failure of the implant typically involved. For CoCr trunnions assembled with CoCr and ceramic femoral heads less metal debris is generated than for Ti-alloy trunnions (Kocagöz et al., 2013; Morlock et al., 2020). The different alloy combinations determine the electrochemistry environment of the taper junction which thereby regulates the corrosion process in the taper interface. CoCr/CoCr taper combinations generate lower corrosion damage scores although CoCr stems are not widely used (del Balso et al., 2021; Gilbert, Mali, et al., 2015; Goldberg & Gilbert, 2003). The material combination also affects the mechanical response of the taper junction; metal components require greater pull-out forces than ceramics due to higher COF values (Fessler & Fricker, 1989; Mueller et al., 2021; Rehmer et al., 2012).

2.4.1.5 Taper clearance

The clearance angle in taper junctions at the femoral head-neck junction has been thoroughly studied as it has shown to affect the contact environment in the taper interface as well as the junction's performance. The taper clearance determines the extent of contact and the engagement point between the bore and trunnion (Fallahnezhad et al., 2017; Kao et al., 2016; Kocagöz et al., 2013). The taper clearance angle can range from positive to negative (Figure 2.11); a positive angle indicates that the femoral head bore angle is greater than the trunnion resulting in a proximal engagement, whilst a negative angle specifies a greater angle in the trunnion component resulting in a distal engagement (Hernigou et al., 2013; Pennock et al., 2002; Raji & Shelton, 2019). Naturally, an angle of zero indicates that the taper component angles are the same, making the trunnion theoretically fully in contact with the bore (English et al., 2015; Kocagöz et al., 2013). Tapers with proximal contact can allow fluid ingress into the interface through the opening generated due to the bore and trunnion mismatch (Gilbert, 2012; Raji & Shelton, 2019). Indeed, the location where the trunnion and bore engage along with the extent of contact have been reported to affect wear and corrosion damage due to fretting; findings are summarised in Table 2.2. Interestingly, when surface finish of taper components is considered in retrieval and experimental studies the effect of taper clearance on

damage generation is not conclusive, suggesting that the surface finish may have a larger role in the taper damage generation.

| a) Positive clearance | b) No clearance | c) Negative clearance |
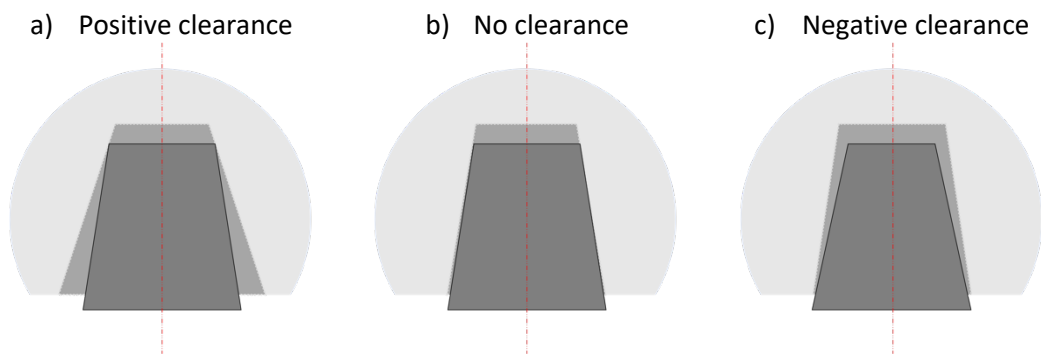
Figure 2.11. Schematics of locations engagements determined by taper clearance namely (a) positive, (b) no clearance, (c) negative.

Table 2.3. Summary of investigations studying the effect of taper clearance angle on damage generation at the taper interface.

Type of study	Parameter	Affects	Type of surface considered	Reference
FEA	Negative clearance angle	Decreases wear	Ideal cones	(Fallahnezhad et al., 2017)
FEA	Positive clearance angle	Increases micromotions	Ideal cones	(Fallahnezhad et al., 2017)
FEA	Positive clearance angle	Increases micromotions	Ideal cones	(Ashkanfar et al., 2017a)
FEA	Positive clearance angle	Increases taper gaps	Ideal cones	(Raji & Shelton, 2019)
FEA	Positive clearance angle	Increases wear damage	Ideal cones	(Donaldson et al., 2014)
Retrieval	Clearance angle	No correlation with taper damage	Smooth and rough	(Kocagöz et al., 2013)
Retrieval	Positive clearance angle	Increases damage	N/A	(Kao et al., 2016)
Retrieval	Clearance angle	No correlation with taper damage	Smooth and rough	(Pourzal et al., 2016)
Retrieval	Proximal clearance angle	Increases taper damage	N/A	(Brock et al., 2015)
Retrieval	Larger taper contact	Increases taper damage	N/A	(Nassif et al., 2014)
Experimental	No clearance angle	Increases pull-off forces	Smooth and rough	(Mueller et al., 2021)
Experimental	Positive clearance angle	Decreases pull-off forces	Smooth and rough	(Yavari & Hasbullah, 2017)

2.4.1.6 Taper diameter

The size of tapers defined by proximal and distal diameters affects the damage scores in taper interfaces as they influence the taper contact mechanics (del Balso et al., 2021; Pastides, 2013; Porter et al., 2014a). Original Morse tapers were manufactured as 14/16, and in the 1990's taper size was reduced to 12/14, 11/13 and 9/10. Thicker trunnions have been associated with larger fretting scores due to a larger taper diameter increasing the total contact in the taper interface as well as reducing the joint's range of motion (ROM) (Morlock et al., 2014; Nassif et al., 2014). Thinner tapers were introduced in order to decrease the risk of impingement with the acetabular cup and increase the joint's ROM (Berstock et al., 2018; Morlock et al.,

2020). However, the downsides of utilising smaller taper diameters are the increase of contact stresses in the taper interface by reducing the contact area between the bore and trunnion and a reduction the taper's bending stiffness increasing the risk of generating larger micromotions (Morlock et al., 2020; Werner et al., 2015). Currently, 12/14 tapers are the most frequent taper size, but other sizes are also commercially available and used (Baleani et al., 2017; Mueller et al., 2017; NJR, 2022).

2.4.1.7   Trunnion length

Shorter trunnions were developed to improve the range of motion of THR devices by increasing the head-neck ratio (Figure 2.12). The length reduction of trunnions from 20 to approximately 10 mm resulted in trunnions sitting entirely within the femoral head bore (Brock et al., 2015; Morlock et al., 2020). Nevertheless, shorter trunnions have been associated with higher fretting and corrosion damage scores due to their susceptibility to edge loading and higher contact stresses (Brock et al., 2015; Hothi et al., 2015). Shorter trunnions generate relatively larger taper gaps that may allow fluid ingress into the junction's interface (Raji & Shelton, 2019).

Head-neck ratio = $\frac{Dh}{Dn}$
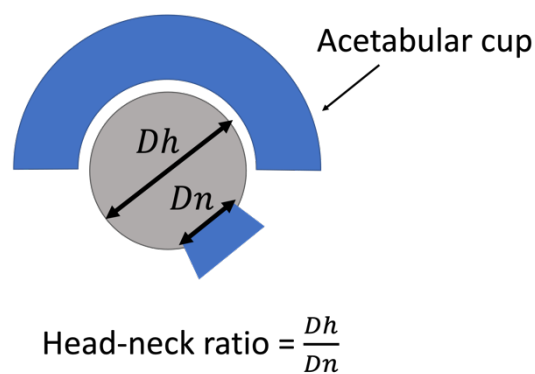
Figure 2.12. Schematic of head-neck ratio.

2.4.1.8   Flexural rigidity

Flexural rigidity in trunnions describes the stiffness of a trunnion when subjected to bending moments and is determined using Equation 2.2.

$$Flexural\ Rigidity = E * I = E * \left(\frac{\pi * ND_z^4}{64}\right)$$
<div align="right">Equation 2.2</div>

Where E is the modulus of elasticity of the trunnion and I is the moment of inertia at the trunnion's geometric centroid ND_z (Porter et al., 2014a).

Head tapers coupled with trunnions with higher flexural rigidity exhibit less fretting and corrosion damage (Higgs et al., 2016; Morlock et al., 2020; Porter et al., 2014a). Flexural rigidity is a function of a trunnion's material properties and geometry; thinner trunnions manufactured from lower elastic modulus materials are more likely to bend under loading conditions generating greater fretting corrosion damage and increasing the risk of fluid ingress into the taper interface (Brock et al., 2015; Raji & Shelton, 2019).

2.4.1.9 Taper surface topography

Taper surface finish can affect the mechanical response of the taper junction as well as the fretting corrosion damage scores; however, the extent of the surface effect on taper damage generation remains unknown and findings are inconclusive as summarised in Table 2.4.

Table 2.4. Summary of investigations studying the effect of taper surface topography angle on damage generation at the taper interface.

Type of study	Type of surface	Related finding	Compared to:	Reference
FEA	Rough surface	Higher damage scores	Smooth surface	(Ashkanfar et al., 2017b)
FEA	Rough surface	Contact conditions different	Smooth surface	(Gustafson et al., 2022)
FEA	Rough surface	Contact conditions different	Smooth surface	(Lundberg et al., 2015)
Retrieval	Rough surface	Lower damage scores	Smooth surface	(Pourzal et al., 2016)
Retrieval	Rough surface	Higher damage scores	Smooth surface	(Brock et al., 2015)
Retrieval	Rough surface	Higher damage scores	Smooth surface	(Hothi et al., 2015)
Retrieval	Rough surface	Damage is determined by surface topography	Different rough surface topographies	(Stockhausen et al., 2021)
Retrieval	Smooth and rough surfaces	Damage is not determined by surface topography	N/A	(Arnholt et al., 2017)
Retrieval	Rough surfaces	Higher corrosion scores	Smooth surface	(Whittaker et al., 2017)
Experimental	Smooth surface	Higher pull-out forces	Rough surface	(Yavari & Hasbullah, 2017)
Experimental	Rough surface	Lower corrosion scores	Smooth surface	(Panagiotidou et al., 2013)
Experimental	Smooth surface	Higher pull-out forces	Rough surface	(Jauch-Matt et al., 2017)
Experimental	Surface topography	Minor role in taper strength	Rough and smooth surfaces	(Mueller et al., 2021)

The lack of conclusive evidence on the relationship between taper surface topography and corrosion damage may be related to a number of factors. Taper surface design is not standardised; there is a great variation in bore and trunnion surfaces even within same taper designs of the same manufacturer making the study of the taper surface effect alone more difficult (Hothi et al., 2015; Whittaker et al., 2017). Another possible reason can be that surface roughness is determined by roughness parameters that average the magnitude of amplitude and wavelength surface features creating an overgeneralisation of the taper surface (Munir et al.,

2015; Walton et al., 2019; Whittaker et al., 2017). Taper surface can share similar roughness parameters namely Ra, Rz but their profiles will be significantly different, as can be seen in surface roughness of Figure 2.13 (Denkena et al., 2011). Furthermore, peaks that conform rough surfaces are shown to have different shapes as shown in Figure 2.14 (Stockhausen et al., 2021). These surface generalisations disregard surface features that can be found at different scales which will affect the taper contact mechanics and the processes that drive fretting corrosion damage. Ploughing and cutting are mechanisms that have been reported to occur in the micro region of the taper surfaces and affect the tribology properties and generation of wear particles in taper interface (Fischer et al., 2023). These mechanisms are affected by the micro topology of the taper surfaces where rough surfaces showed lower wear loss under fretting corrosion (Fischer et al., 2023).
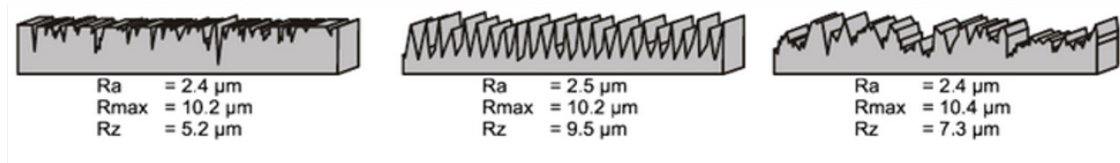
Figure 2.13. Arithmetic mean roughness for different roughness profiles adapted from (Denkena et al., 2011).
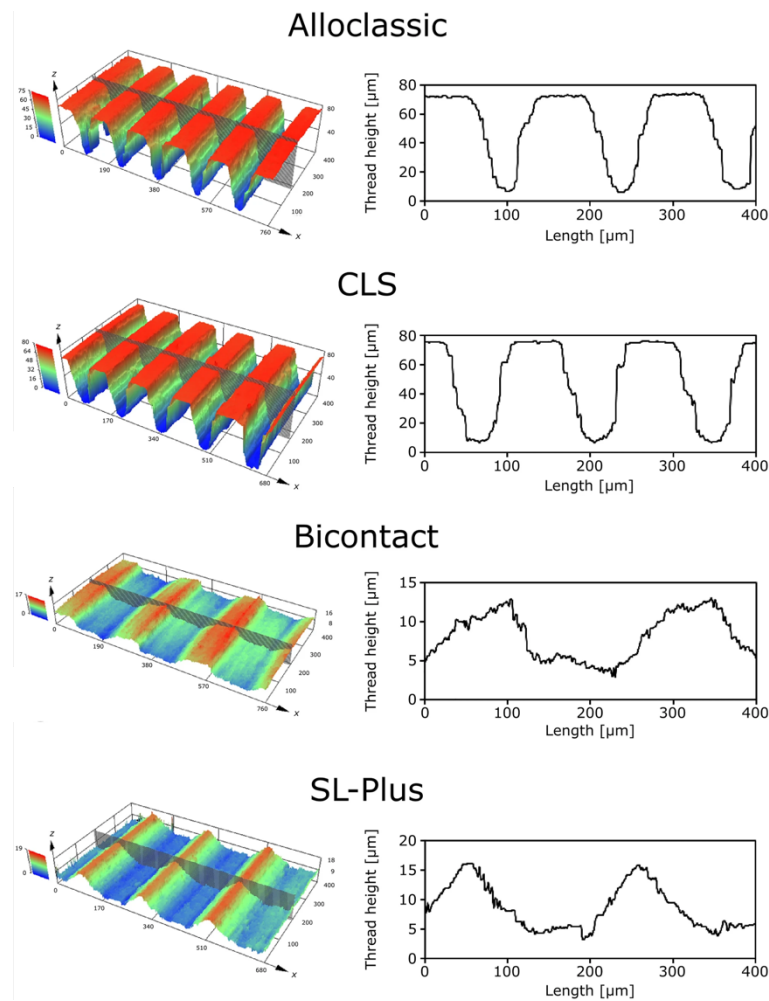
Figure 2.14. Surface roughness profiles for different taper designs. Profiles are characterised by the shape of their peaks; adapted from (Stockhausen et al., 2021).

2.4.2 Surgical

Intraoperative conditions during the assembly of the femoral head bore into the trunnions, namely, assembly force and taper cleanliness, are related to the junction's performance and integrity (Dransfield et al., 2019; Krull et al., 2018). Taper junctions are designed for clean and dry assembly conditions; contamination of the interface with bone, water, blood, and fat during assembly can cause an increase in the micromotions, resulting from a change in the friction environment between the bore and trunnion surfaces (Dransfield et al., 2019; Falkenberg et al., 2019; Pennock et al., 2002). Fixation strength and contact area between the taper components directly increase with impaction force but consecutive impactions may weaken the initial taper fixation (English et al., 2016; Gustafson et al., 2020a; Morlock et al., 2020).

Furthermore, a poor assembly force can cause a loose fixation increasing the risk of relative motions *in vivo* (Dransfield et al., 2019; English et al., 2016; Gustafson et al., 2020b; Lundberg et al., 2015; Rehmer et al., 2012). A single impact of 4 kN is sufficient to achieve fixation of the femoral head into the trunnion. However, despite the understanding that impact forces larger than 6 kN would create a stronger fixation these are discouraged as it may damage the THR components and femoral bone during assembly (Dransfield et al., 2019; Fallahnezhad et al., 2019; Rehmer et al., 2012).

2.4.3   Patient

The loading environment at the hip joint arising from the patient's daily activities directly influences the micromotions occurring at the taper interface (Bergmann et al., 2016). It has been suggested that activities in which the implanted leg is highly flexed while loaded, e.g., standing in one leg while climbing stairs, can be detrimental to the taper junction as the combination of bending moments and relatively high forces can result in edge loading and toggling (Bergmann et al., 2016; Raji & Shelton, 2019). The magnitude and direction of loads are influenced by body weight, increasing forces and moments experienced at the taper junction (Bergmann et al., 2010, 2016). Furthermore, inflammatory conditions in the local body fluid increase the risk of corrosion in the implant (Morlock et al., 2020).

2.5   Studying the taper junction

Investigations on the relationship between taper design parameters with corrosion and wear damage on the taper interface can be classified by the methodologies used, namely classified in clinical evidence, retrieval analyses, experimental studies, and *in silico* studies. Experimental and *in silico* studies attempt to simulate mechanical, chemical conditions or both, that junctions may undergo during assembly and *in vivo*.

2.5.1   Clinical evidence and retrieval

Retrieval analysis makes use of clinical and experimental evidence to identify and associate design parameters with factors that directly affect wear and corrosion

processes in the taper interface. Evidence can include recorded symptoms associated with implant failure, retrieved damage components and experimental data.

Characterisation of corrosion damage in retrieved taper components can be estimated using microscopic and macroscopic imaging techniques. The most common visual assessment, developed by Goldberg, categorises corrosion and fretting damage in four degrees of severity where a value of 1 indicates no visible damage and 4 indicates severe corrosion and/or fretting scars as shown in Figure 2.15 (Goldberg et al., 2002; Goldberg & Gilbert, 2003). These scores have shown correlation with volume material loss in the taper junction (Berstock et al., 2018; Eliaz, 2019; Morlock et al., 2020).
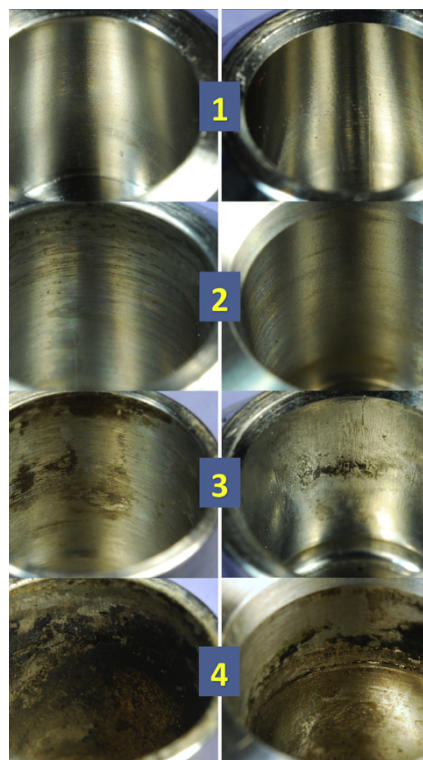
Figure 2.15. Goldberg corrosion scores, a value of 1 indicates no visible damage and 4 indicates severe corrosion and/or fretting scars adapted from (Higgs et al., 2016)

2.5.1.1 Surface finish analysis

Material loss due to corrosion and wear damage in a taper component surface can be estimated using out-of-roundness, coordinate measuring machines (CMM), and contact/optical profilometers (Bone et al., 2015; Racasan et al., 2015a). In addition to material loss, these techniques can also be used to characterise taper surfaces before implantation and use the measured data for further analysis (Wade et al., 2020; Witt et al., 2015).

Out-of-roundness machines are used to characterise the form variations of spherical and cylindrical parts with a gauge resolution of 1.2 nm (Racasan et al., 2015b). Similarly, CMM machines generate three-dimensional (3D) coordinates of the region of interest, but do not have inbuilt algorithms to provide form analysis (Bone et al., 2015). Contact profilometers measure the surface variations of defined line and usually include software tools to remove straightness and form deviations (Bone et al., 2015; Dransfield et al., 2021; Walton et al., 2019). The resolution of the measurement data of these contact methods is limited by the stylus diameter used. Optical profilometers utilise light instead of solid state probes to detect surface variations, however the accuracy of detected surface irregularities is a function of the orientation of the light reflected from the material surface (Cartner et al., 2017; Podulka, 2022; Racasan et al., 2015b).

2.5.2 Experimental

Experimental studies in tapers have investigated the mechanical response, contact environment and damage in the taper interface and how they are affected by taper design differences and environment conditions. Experimental studies have investigated corrosion tests under different liquid conditions, as well as hip simulators to simulate the complex loading that the junction may experience *in vivo* (Elkins et al., 2014; Liu et al., 2019; Pourzal et al., 2018; Swaminathan & Gilbert, 2012). The disadvantage of these studies is that they can be very expensive and time consuming, and not all parameters of interest can be directly measured, such as the contact conditions and micromotions generated in the taper interface.

2.5.3   In silico

Numerical models of taper junctions present a strong alternative to experimental studies as they are relatively cheap and fast and allow the study of variables which are not easy to obtain experimentally. FE studies have focused on parameters that affect fretting damage namely micromotions and contact pressures. Some other studies have estimated the evolution of wear damage and volume of material loss. Table 2.5 summarises the features of FE models considered in FE studies of taper junctions. However, these studies have all considered the tapers to be perfect cones with no surface features. Indeed, this oversimplification of the taper surface has resulted in most of the studies the taper junction does not reaching plastic deformation during assembly, despite considering plasticity behaviour in the material properties, even though such plastic deformation has been reported (Mueller et al., 2021; Witt et al., 2015). Nevertheless, recent studies that have considered smooth and rough taper surfaces utilising a sinusoidal function, have highlighted the importance of including surface features in numerical models when studying the contact environment in the taper interface (Bechstedt et al., 2020; Godoy et al., 2022; Gustafson et al., 2020a, 2022).

Table 2.5. Summary of features of FE models used to study the influence of taper design on the taper junction mechanical response and wear estimation.

FE model	Loading conditions	Element size (mm)	Type of analysis	COF	Plasticity		Surface geometry	Reference
					Considered	Reached		
3D	Assembly + walking activity	0.2	Implicit	0.21	No	N/A	Ideal cones	(English et al., 2016)
3D	Assembly + Twist-off disassembly	0.15	Explicit	0.3	Yes	No	Ideal cones	(Fallahnezhad et al., 2016)
3D	Assembly + Activity forces	0.15	Explicit	0.3	Yes	No	Ideal cones	(Farhoudi et al., 2017)
3D	Assembly + walking activity	Smooth:0.15 Rough: 0.012	Implicit	0.21	Yes	No	Ideal cones, and sinusoidal surface	(Ashkanfar et al., 2017b)
3D	Assembly + walking activity	0.18	Implicit	0.21	No	N/A	Ideal cones	(Ashkanfar et al., 2017a)
3D	Assembly + Activity forces	0.15	Explicit	0.3	Yes	No	Ideal cones	(Fallahnezhad, Farhoudi, et al., 2018)
3D	Assembly + Activity/Hip Sim	0.9	Static	0.21	No	N/A	Ideal cones	(Raji & Shelton, 2019)
3D	Assembly + Axial loads	0.2	n/a	0.29	Yes	Yes after cyclic loading	Ideal circular & oval cones	(Bitter et al., 2019)
3D	Assembly + sinusoidal loading	0.25	Static	0.29	No	No	Ideal cones	(Messellek et al., 2020)
3D + 2D	Assembly + walking activity	0.18	Implicit	0.21	Yes	No	Ideal cones	(Fallahnezhad et al., 2017)
2D Multi scale	Assembly + sinusoidal loading	n/a	Static	0.52 (µscale)	Yes	Yes, after cyclic loading.	Microgrooved, ideal wedge.	(Zhang et al., 2013)
2D Asymmetric	Assembly	n/a	Static	0.28	Yes	Yes	Ideal smooth, ideal rough and measured	(Gustafson et al., 2020a)
2D	Assembly	n/a	Static	0.28	Yes	Yes	Sinusoidal waves	(Gustafson et al., 2022)

2.5.4 Friction in tapers

Coefficient of friction (COF) between the trunnion and bore surfaces determines the mechanical response of the modular junction. The COF in the taper junction influences the micromotions generated in the taper interface, therefore affecting the fretting wear damage that the junction can experience (Bitter et al., 2016; Donaldson et al., 2014; Fessler & Fricker, 1989). Higher COF are associated with lower material loss due to less fretting. It is believed that rougher taper surfaces will generate a higher COF (Smith & Scott, 1996), however it has been reported that disassembly of smooth surfaces requires of greater pull-off forces implying a higher COF than rough surfaces (Brock et al., 2015; Jauch-Matt et al., 2017; Yavari & Hasbullah, 2017). This may be due to different mechanisms, namely mechanical interlock and surface adhesion, generating friction forces which are affected by material properties and surface topography.

2.5.5 Experimental estimation of COF in tapers

The COF in tapers has been estimated experimentally by studying pull-off forces and tangential/normal forces (Bitter et al., 2017; Fessler & Fricker, 1989). Fessler and Fricker obtained the COF through static analysis of pull-off forces (Equation 2.3).

$$P = \mu A\bar{p}\cos\alpha - A\bar{p}\sin\alpha \qquad\qquad \text{Equation 2.3}$$

Where P is the pull-off force, A the contact area, $\bar{p}$ the mean taper pressure, α head taper half angle and μ the coefficient of friction (Figure 2.16). In this study, the COF was obtained for different conditions including dry, blood, and water resulting in values of 0.13 and 0.09 and 0.23 respectively (Fessler & Fricker, 1989).
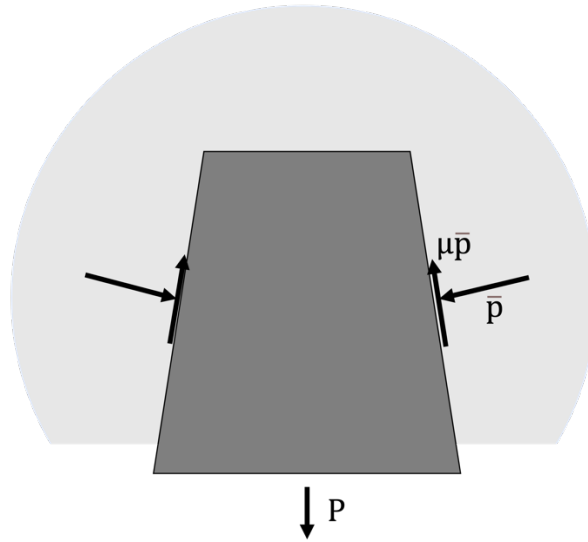
Figure 2.16. Diagram showing the static forces generated in the taper junction in a pull-off test modified from (Fessler & Fricker, 1989).

More recently, Bitter et al. investigated trunnion and bore surfaces with different resultant normal forces and obtained an estimated COF by calculating the relationship between resultant normal and tangential forces of the surfaces and obtaining a static COF of 0.29 in a smooth taper and 0.19 in a rough taper was obtained. This study highlighted the sensitivity of surface finish on the COF in tapers (Bitter et al., 2017).

2.5.6   Numerical estimation of COF in tapers

The COF in unlubricated surfaces can be estimated following Green's observations (Green, 1955) on friction of sliding surfaces. Numerical models of Ti-alloy surfaces have shown a good approximation to COF values reported in the literature (Li et al., 2022; Mulvihill et al., 2011). However, such technique has not been implemented in taper surface couplings.

2.6 Thesis Aims and Objectives

The current thesis aims to:

- Understand factors that influence the mechanical performance of tapers.
- Establish the relative motions generated in the taper interface.
- Understand the role of surface finish in the taper mechanics.

Objectives

- Identify taper design parameters associated with high wear and corrosion damage in the taper interface from the literature.
- Develop a 3D FE model to study the generation of relative motions under different taper designs and loading conditions.
- Characterise the surfaces of commercially available bore and trunnion components.
- Develop a 2D FE model using measured surface data to study the taper contact mechanics.
- Develop a methodology associating a coefficient of friction with a surface pair.
- Apply the derived coefficient of frictions onto the 3D FE model of a taper.

The overall structure and hierarchy of studies performed in this thesis are shown in Figure 2.17. The high-level factors are shown in black which influence the implant failure caused by metal debris which originate in the head-neck junction. This diagram shows factors and their relationships with fretting that causes debris. Boxes in white contain parameters/data reported in the literature and were used to develop the FE models for this thesis and build conclusions. Boxes in green contain the topics studied/tested in the present thesis.
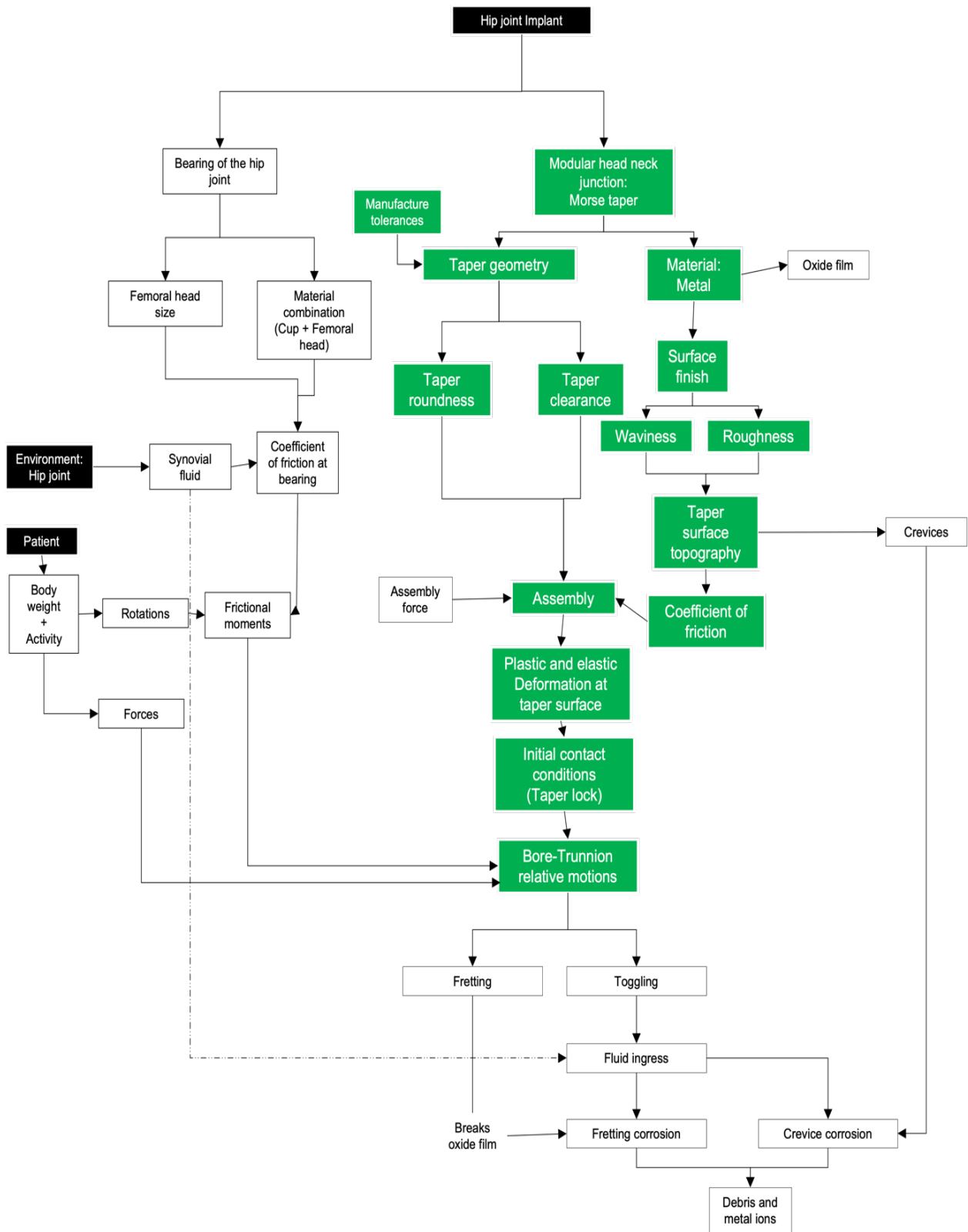
Figure 2.17. Diagram showing the topics explored (in green) in the present study

3 Finite element model development, analysis, and validation

3.1 Introduction

The influence of taper design on the junction's strength and wear generation has previously been studied utilising the finite element (FE) method. These FE models include idealised conical geometries to simulate the Morse taper (English et al., 2016; Feyzi et al., 2021b). Taper FE models have predicted wear damage and taper mechanical response with relatively good accuracy resulting in a cost-effective alternative analysis compared to experimental studies. This chapter describes in detail the development process of the FE models and analysis used to undertake an investigation on the different taper design parameters that can affect the contact mechanics and micromotions between the bore and the trunnion result from external loading. This study has been divided into two sections, round tapers and oval tapers. Ideal tapers are those that have no deviation on their lateral surface resulting in a circular taper, whilst oval tapers consider lateral deviations generating the ovality. FE model of these tapers simulate the taper assembly, pre-loading, and a single cycle of walking. In order to obtained more accurate FE model predictions, a converge analysis was undertaken for these models using contact parameters generated in the taper interface, namely von Mises stress and micromotions, that are related to wear damage in tapers. For ideal tapers, in addition to the walking activity, tapers were subjected to other activities namely, stair climbing, sit-to-stand, jogging and cycling. All these studies generated the prediction of contact parameters and surface contours of contacting areas, maximum taper separation and relative motions and their components throughout the taper interface during an activity cycle. The development process of the geometrical models and boundary conditions used in the FE models is described in this chapter utilising the reported methodologies, and where appropriate refined approaches.

3.2   3D geometries, material properties and contact conditions

A three-dimensional model of a commercially available femoral head and a 12/14 trunnion was developed. Dimensions of the femoral head bore and trunnion were taken from the most common modular THR devices reported in the literature (Brock et al., 2015; Hernigou et al., 2013; Kocagöz et al., 2013). For this investigation, the length and proximal diameters of the bore and trunnion taper, and size of the femoral head remained unchanged throughout the changes in taper designs. The distal diameter of the bore taper also remained constant thereby retaining a constant bore angle. The distal diameter of the trunnion alone was adjusted according to the angle mismatch required; with the other parameters kept constant, its magnitude is a function of the trunnion's angle (Figure 3.1).
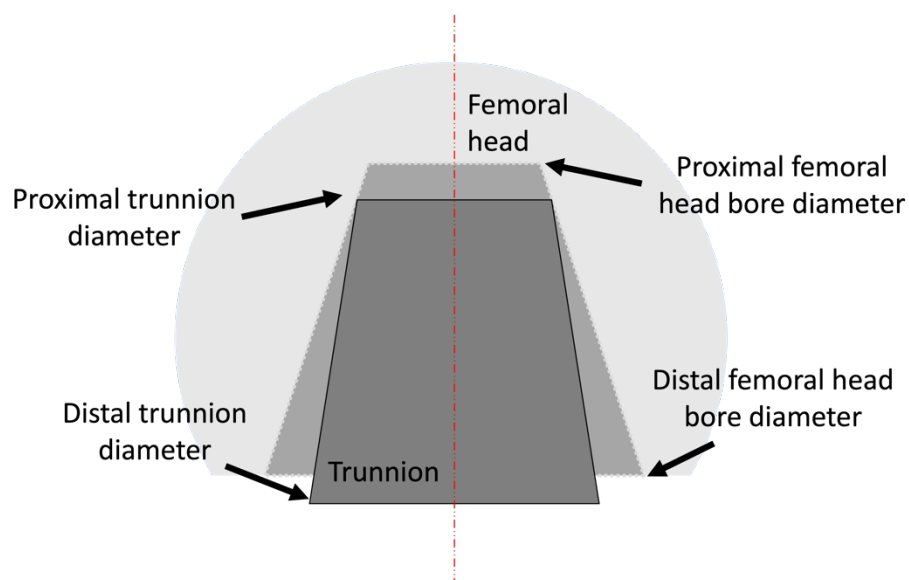
Figure 3.1. Schematics of a trunnion and femoral head's bore proximal and distal diameters.

The taper surface was modelled as perfectly smooth, as the current state of art of taper FE modelling has established that simulating smooth tapers with a truncated cone geometry predicts the mechanical response of modular THR tapers (Ashkanfar et al., 2017a; English et al., 2015, 2016; Farhoudi et al., 2015, 2017). Recent studies have reported that the shape of the taper's circumference is not precisely circular, with out of roundness deviations up to 6 μm in trunnions, with the major axis parallel to the Superolateral - Inferolateral (SI) axis (Figure 3.2). Considering these

manufacturing issues, the present study also includes the effect of these taper geometric variations on the taper contact mechanics during different activities; out of roundness is introduced to the 3D geometry model of a trunnion as a reduction in the diameter in the minor axis as shown in Figure 3.2. For oval tapers the diametrical difference remains constant over the taper length.
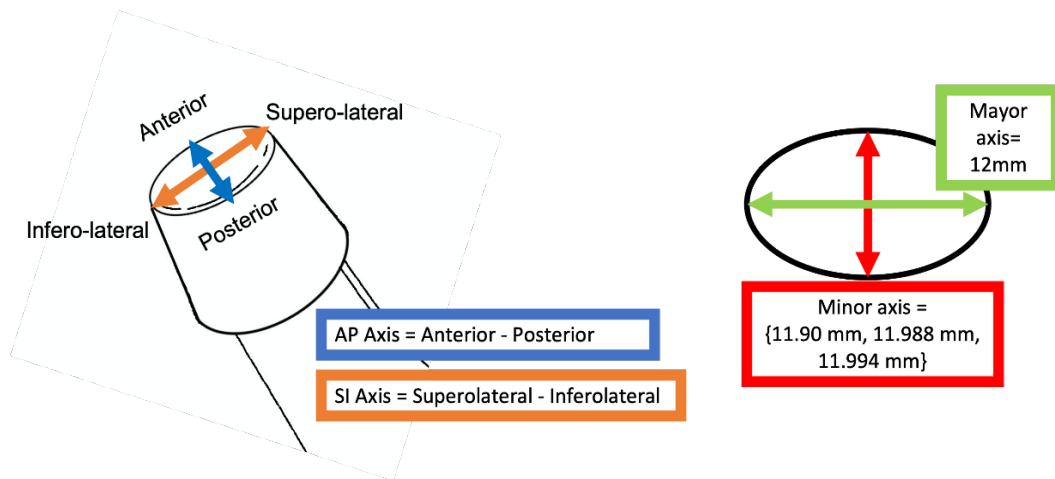
Figure 3.2. Schematic defining the orientation of the out roundness and the taper diameters at the proximal end of the tapers.

Individual material properties assigned to the femoral head and trunnion are shown in Table 3.1. Material properties corresponding to CoCrMo and Ti6Al4V, were selected for the femoral bore and trunnion, respectively; this material combination was selected as it has been reported to display high rates of corrosion, even in conditions where the taper interface has been isolated from fluid ingress. Material models for CoCrMo and Ti6Al4V (

) are elastic with strain hardening and perfect plastic after reaching the material's ultimate strength. Contact interaction between the taper surfaces is modelled as a finite sliding surface-to-surface contact, where the bore surface is defined as the master, and the trunnion as the slave surface. The contact interaction coefficient of friction is modelled with a penalty contact formulation.

Table 3.1. Material properties assigned to the femoral head and trunnion (Ashkanfar et al., 2017a; English et al., 2015).

Part	Material	Elastic modulus (GPa)	Poisson's ratio (v)	Density (g/cm^3)	Yield stress (MPa)	Ultimate strength (MPa)
Femoral head	CoCrMo	230	0.3	8.4	910	1350
Trunnion	Ti6Al4V	116	0.31	4.4	865	945
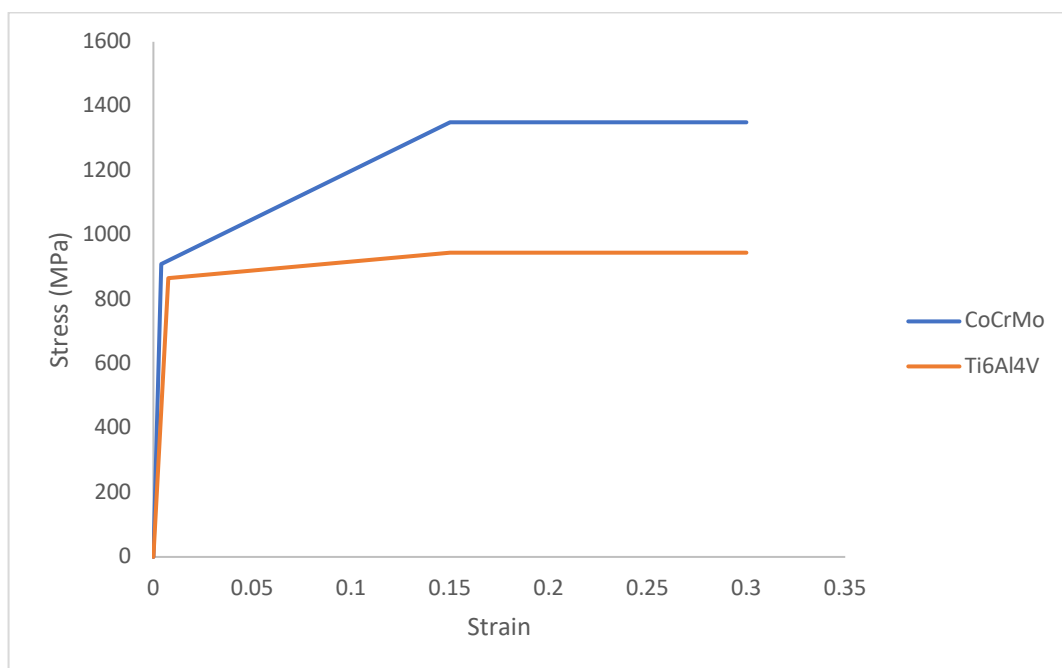
Figure 3.3. Material models assigned to the femoral head and trunnion.

3.3   Boundary and loading conditions

To study the contact environment occurring at the taper interface, the FE model must be able to simulate both the making of the taper lock and the subsequent response to the loading of external forces. The distal taper gap opening and the distribution of the contacting surfaces between the trunnion and the bore were investigated after making the taper and during subsequent loading. Considering this, 3D geometries of a trunnion and femoral head were created. As the mechanical behaviour of the rest of the modular THR device and anatomical elements of the hip joint are not in the scope of this study, these parts were not included in the 3D model. Nonetheless, the defined boundary conditions and loading conditions of the FE model do include these

elements as they can affect frictional moments and loading conditions during activities. The FE model of this investigation comprises of three steps, namely the assembly, pre-load and activity step.

3.3.1   Assembly

The assembly phase involves the simulation of the assembly process of the taper junction by impacting the femoral head onto the trunnion. In this step, the base of the trunnion is constrained in all degrees of freedom, the femoral head is allowed to move only on the same direction of the trunnion length. A load is applied to a reference point in the centre of the femoral head (RP-2) coupled to the outer surface of the head (Figure 3.4).
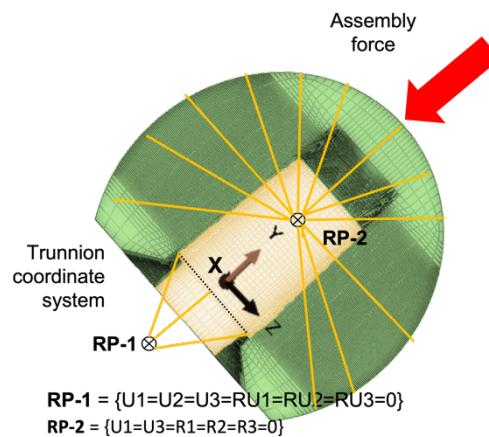
Figure 3.4. Taper coordinate system, location of boundary and loading conditions for the first phase, defined as the assembly phase.

This load simulates the load-time history event of the head-stem assembly impact. The total time of the assembly step is of 1 ms, where the impact event length is 0.7 ms as shown in Figure 3.5 (English et al., 2016).
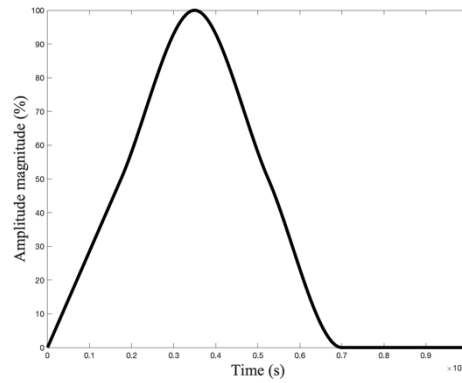
Figure 3.5. Assembly step load-time history simulating the assembly impact event.

3.3.2 Pre-loading

For the second and third steps, the outer surface of the femoral head was constrained in all degrees of freedom (not allow to rotate or translate) during the entire step. Frictional moments and external loads of different activities, including walking, jogging, stair climbing, cycling, sit-to-stand, are applied at the bottom face of the trunnion through a reference point (RP-1) coupled to this surface.
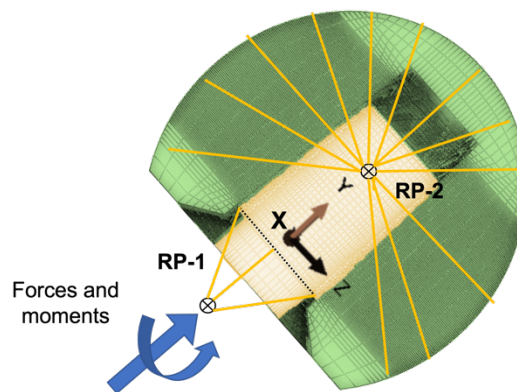
Figure 3.6. Taper coordinate system, location of boundary and loading conditions for the preload and activity phase.

On the preload step, constant forces of the initial activity forces were applied to the base of the trunnion (Figure 3.6). This second step in the current model is included in order that the predicted micromotions and taper gap openings resulting from activity

39

forces and moments alone are considered, as in physiological use THR devices are not loaded directly after their assembly.

3.3.3 Activity

Finally, on the third step, or activity phase, activity forces presented in Figure 3.7 were applied on the base of the trunnion. Forces and moments described in Bergmann et al. (2016)'s study were reported using the implant coordinate system. In order to apply these forces into the base of the trunnion through the trunnion's coordinate system (Figure 3.6) forces vectors were multiplied by rotation matrixes on the X, Y and Z axis using average implant orientations ($[X_R, Y_R, Z_R]$ = [4.5°, −1.4°, −12.5°]) and neck angle orientation (Y_R = −35°). These angles were obtained from the average (n=10) implantation orientation of individuals with instrumented THR devices (Bergmann et al., 2016) and the average (n=190) neck angle orientation relative to the femur (Boese et al., 2016; Clark et al., 1987).

(a) Walking

Forces

Frictional moments

(b) Stair climbing

(c) Jogging

(d) Sit-to-stand

(e) Cycling

Figure 3.7. Forces and frictional moments representative of daily activities, for (a) walking, (b) stairs up, (c) jogging, (d) sit-to-stand and (e) cycling applied to the base of the trunnion; adapted from (Bergmann et al., 2016).

3.4   Model optimisation: Static or Dynamic

Due to the nature of the assembly and activity steps, inertia forces of the involved geometries can affect the predicted mechanics of the taper. The following analysis

was undertaken to investigate the potential effect inertia may have on the proposed FE model. Assembly and activity steps were solved using a Static and Dynamic-implicit solver in Abaqus 2019 CAE using Apocrita High Performance Computer facility at Queen Mary University of London. Geometries of a femoral head and trunnion with a taper mismatch of 0.07°, and material properties, boundary and loading conditions described in sections 3.2 and 3.3 were used for this analysis. For the impact phase, an impact force of 4 kN was used and for the activity phase, forces and frictional moments specific to the walking activity of a 75 kg subject were used.

Tables 3.2 and 3.3 show the percentage differences between Static and Dynamic-Implicit for contact pressure and contact area at the taper interface of the assembly and activity (walking) steps. As shown in these tables, inertia has a considerable effect on the assembly step where contact pressure and contact area differences were of 15.6% and 24.26% respectively. In contrast, the activity phase was not sensitive to inertia forces where differences between Static and Dynamic-implicit are negligible and could therefore be ignored. Thus, considering these results, for this investigation, the assembly step will be solved using a Dynamic-Implicit approach and the activity phase using a Static approach.

Table 3.2. Predicted maximum contact pressure and area at the taper interface at 0.35 ms in the assembly step.

Type of analysis	Contact pressure (MPa)	Contact area (mm^2)
Static	155.0	273.22
Dynamic-Implicit	181.0	348.65
Difference (%)	15.6	24.26

Table 3.3. Predicted maximum contact pressure and area at the taper interface at the largest resultant force magnitude in the walking step.

Type of analysis	Contact pressure (MPa)	Contact area (mm^2)
Static	194.1	367.72
Dynamic-Implicit	194.0	367.72
Difference (%)	0.05	0.0

Dynamic-Implicit analysis for problems involving material response in Abaqus CAE require a certain level of discretisation to converge to an acceptable result. Thereby, a convergence analysis was undertaken for the assembly step to determine the number increments needed to solve the bespoke step. The analysis used the same geometries, materials, boundary and loading conditions used in the static vs dynamic implicit study. This convergence analysis considered the following number of increments 10, 24, 52, 100, 336 and 1000 to study the effect of number of increments on the von Mises stress at the taper interface at the end of the assembly step. Percentage difference is calculated using Equation 3.1.

$$Percentage\ difference\ (\%) = \left(\frac{Stress_n - Stress_{n-1}}{Stress\ n}\right) * 100. \qquad \text{Equation 3.1}$$

Where *Stress* is the predicted von Mises stress and *n* is the number of increments set used in the model. As Figure 3.8 shows, the assembly step starts converging after 204 increments. The number of increments used for this step was therefore 336; the difference between 336 and 1000 increments is less than 0.2% whilst the computational time significantly increases.
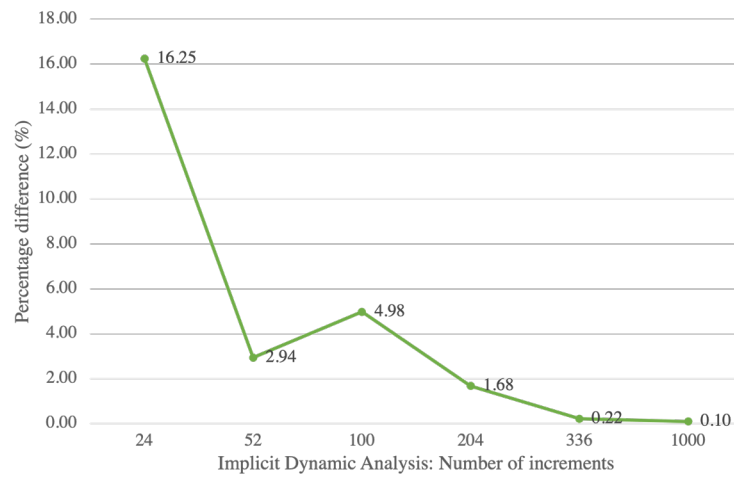
Figure 3.8. Convergence study for percentage change as a function of number of increments for maximum von Mises at the end of the assembly phase.

3.5 Mesh development

Femoral and trunnion 3D geometries were meshed using linear brick elements (C3D8). The number of elements in the finite mesh can affect analytical results and computational time. In this investigation, in order to reduce the number of elements used making the models more computationally efficient, the element size used is a function of the location in the 3D geometry, and the results of a converge analysis. Elements outside the contact surfaces were coarser away from the contacting surfaces.

To achieve this, 3D geometries were partitioned to generate different instances within the geometries using "Partition Cell" from Abaqus, within the Mesh Module. Geometries of the femoral head and trunnion undertook a series of partition design iterations in order to find the most efficient design for this investigation.   The following sections describe the design iterations of partitions and 3D model geometries, finalising with the model's convergence analysis.

3.5.1　Model optimisation: Trunnion 3D geometry

Stress singularities at the contact surface between the bore and trunnion components caused by sharp corners in the FE geometry model, were introduced in the initial 3D geometry design (Figure 3.8a) of the trunnion developed for this study. Trunnion designs shown schematically in Figure 3.9 were developed to find a design that would remove singularities caused by sharp edges in the trunnion geometry.
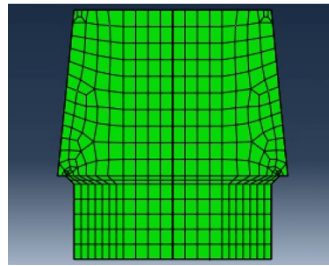
(a) No chamfer, no fillet
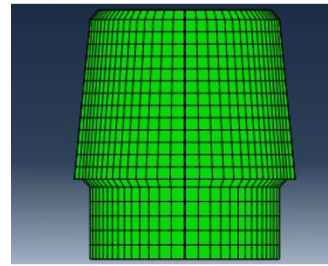
(b) Chamfer at the proximal end only
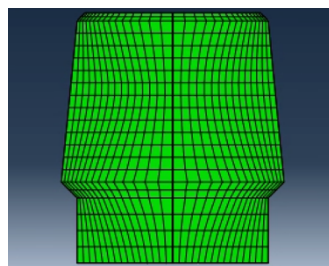
(c)　Chamfer at the proximal and distal ends
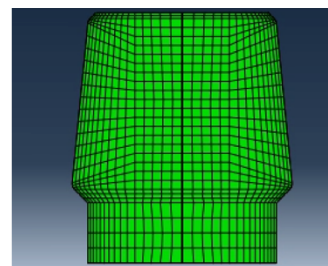
(d)　Fillet at the proximal and distal ends

Figure 3.9. Iteration of trunnion designs.

A fillet of 0.5 mm (Figure 3.10d) at the proximal and distal edges of the trunnion geometry was sufficient to smooth the sharp corners that originated singularities in the contact surface between the bore and trunnion components. This design was used throughout the remainder of this study.
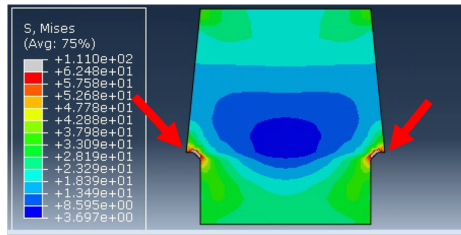
(a) No chamfer, no fillet
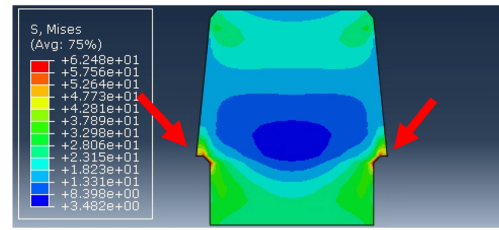
(b) Chamfer at the proximal end only
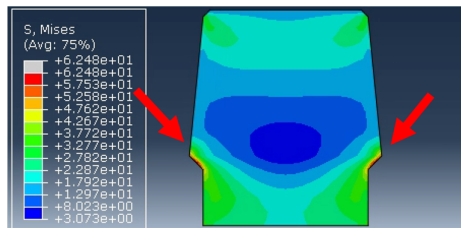
(c)   Chamfer at the proximal and distal ends
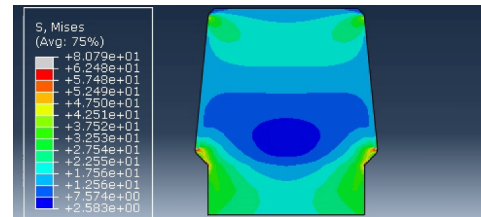
(d)   Fillet at the proximal and distal ends

Figure 3.10. Images showing high von Mises stresses developed on the trunnion after assembly phase. Sharp corners that caused singularities indicated by red arrows are shown for different trunnion designs.

3.5.2   Geometry partition design

Geometrical partitions were performed on the femoral head and trunnion models in order to utilize the same element size where the bore and trunnion are in intimate contact whilst reducing the number of elements in areas elsewhere. Bespoke partitions are represented as yellow lines in Figure 3.11. Orange dashed lines represent those partitions used to make geometries less complex allowing the shape of elements to be more homogenous.
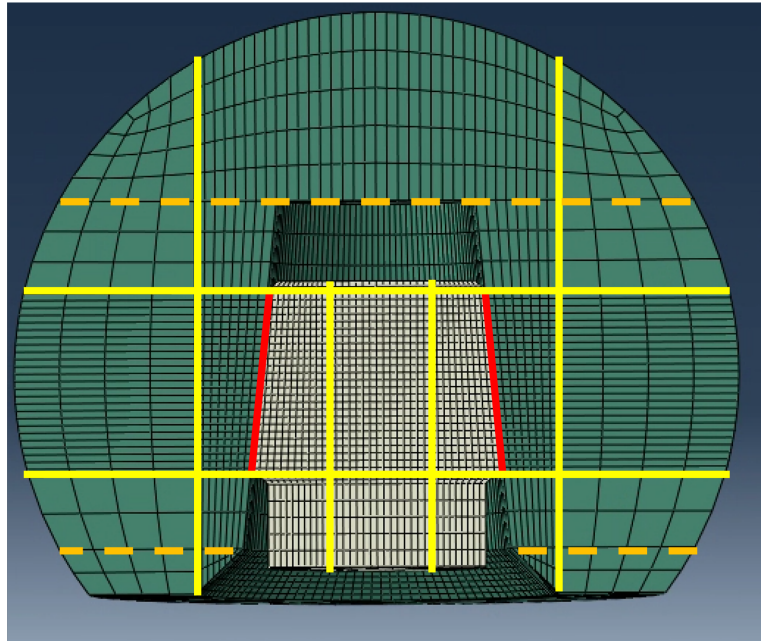
Figure 3.11. Mesh and partition distributions of the geometries used in the proposed FE model. Bespoke partitions are represented as yellow lines; orange dashed lines represent partitions used to make geometries less complex allowing the shape of elements to be more homogenous. The red lines indicate the contact regions.

3.5.3   Element size

Element size at the contacting surfaces of the trunnion and bore was determined by undertaking a convergence analysis. A higher mesh density depicts more accurately the magnitude of parameters of interest gradients in expense of more computational time, a converge analysis helps to identify a mesh density in which higher density meshes have little effect on the model's results. This analysis comprises the effect of four element sizes (0.6 mm to 0.15 mm) on the predicted maximum von Mises stress and micromotion in the taper interface at the maximum magnitude load applied during the assembly step. Figure 3.12 shows that the predicted variables of interest start converging with an element size of 0.17 mm. The percentage difference between 0.17 mm and 0.15 mm was less than 2% for all variables.
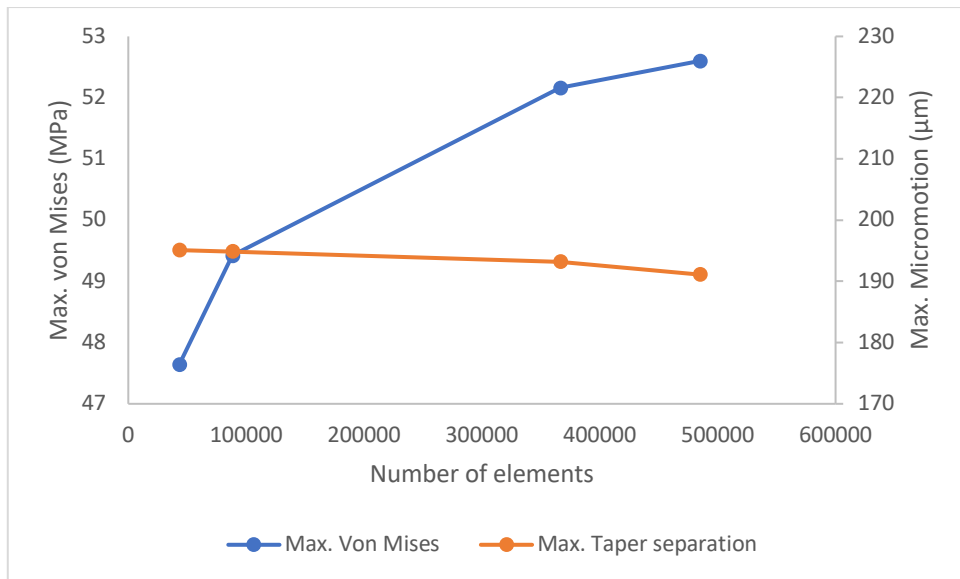
Figure 3.12. Predicted maximum von Mises and maximum accumulated micromotion as a function of element size.

3.6   Analysis

Predicted results of the contact mechanics from the FE models were post-processed for analysis, relative motion calculation at the taper interface and visualisation. Post-process scripts were developed in Python 3.0 and MATLAB 2019. This section describes the workflow to extract Abaqus data from ODB files, calculate relative motions and create contour plots used for analysis. The code for these scripts can be found in Appendix A.

3.6.1   Post-process scripts

3.6.1.1   Abaqus ODB data extraction

Taper gap opening (separation), contact areas and coordinates for all contacting nodes of the bore-trunnion interface for each increment and each phase of loading are extracted using a Python script using the Abaqus Application Programming Interface (API). For each increment, Node data (ID, coordinates, etc) is stored in a plain text file for further post-processing. Relative motions at the taper interface were calculated using coordinate data from the FE models of the bore and trunnion surfaces for each increment and phase loading.

48

3.6.1.2 Relative motion calculation

The relative motions between the bore and the trunnion surfaces were calculated following the methodology described by English et al. (2015). Extracted 3D coordinates of bore and trunnion surfaces were utilised for this calculation. Before the calculation, nodes at the trunnion interface were associated to their nearest node in the bore surface. This association procedure was performed in the first increment just before assembly, pre-load and activity phases. The resultant relative displacement ($\overrightarrow{RM}$) between the associated nodes of the trunnion and bore surfaces is rotated to align to the trunnion's circumference and surface thus obtaining $\overrightarrow{RS}$.

$$\overrightarrow{RS} = \begin{bmatrix} U \\ V \\ W \end{bmatrix} = \overrightarrow{RM} R_x R_y R_z \qquad \text{Equation 3.2}$$

Components of the relative motion $\overrightarrow{RS}$ are named after the type of relative motion that they represent, namely pistoning (U), normal (V) and tangential (W) displacements as described in Figure 3.13a. Equations 3.2, 3.3, and 3.4 are the matrix rotations in X,Y,Z axis used to align relative motions to the trunnion's surface, where θ and φ are the half of the trunnion's angle and angle normal to its circumference, respectively (Figure 3.13b).

(a)   Relative motions

(b) Trunnion angle (θ) and normal angle to the trunnion circumference (φ)
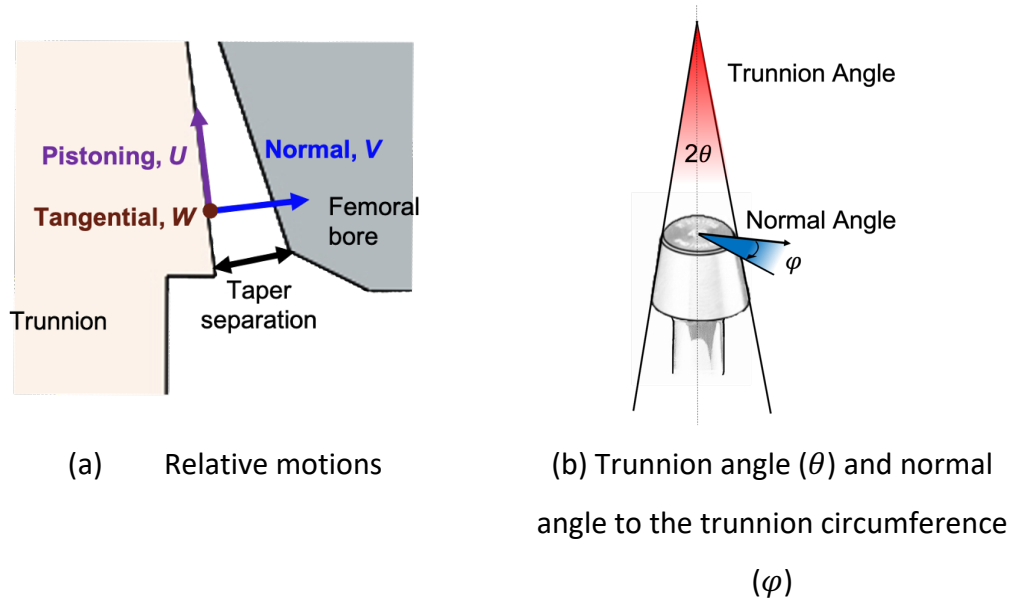
Figure 3.13. Schematic showing a) relative normal (V), tangential (W) and pistoning (U) motions, and b) trunnion angles.

$$R_x = \begin{bmatrix} 1 & 0 & 0 \\ 0 & \cos(\theta\cos\varphi) & -\sin(\theta\cos\varphi) \\ 0 & \sin(\theta\cos\varphi) & \cos(\theta\cos\varphi) \end{bmatrix} \qquad \text{Equation 3.3}$$

$$R_y = \begin{bmatrix} \cos(\theta\sin\varphi) & 0 & \sin(\theta\sin\varphi) \\ 0 & 1 & 0 \\ -\sin(\theta\sin\varphi) & 0 & \cos(\theta\sin\varphi) \end{bmatrix} \qquad \text{Equation 3.4}$$

$$R_z = \begin{bmatrix} \cos(\varphi) & -\sin(\varphi) & 0 \\ \sin(\varphi) & \cos(\varphi) & 0 \\ 0 & 0 & 1 \end{bmatrix} \qquad \text{Equation 3.5}$$

Wear damage occurs when surfaces in intimate contact move relative to each other, therefore only contacting nodes in the taper interface were considered for the analysis. Furthermore, the absolute magnitude (modulus) of the accumulated relative motions over the whole of the activity phase (phase 3) was determined.

3.6.1.3 Visualisation script

In order to have a better understanding of the relative motions occurring in the taper interface during the activity phase, further scripts were developed to aid with the

visualisation of these motion mechanics. The first script plots the magnitudes and components of the accumulated relative motions in a 2D representation of the trunnion's surface. Figure 3.14 illustrates the trunnion's frame of reference used to create the 2D surface representation. It should be noted that this created a rectangular framework where the horizontal axis represents an angle rather than a distance.
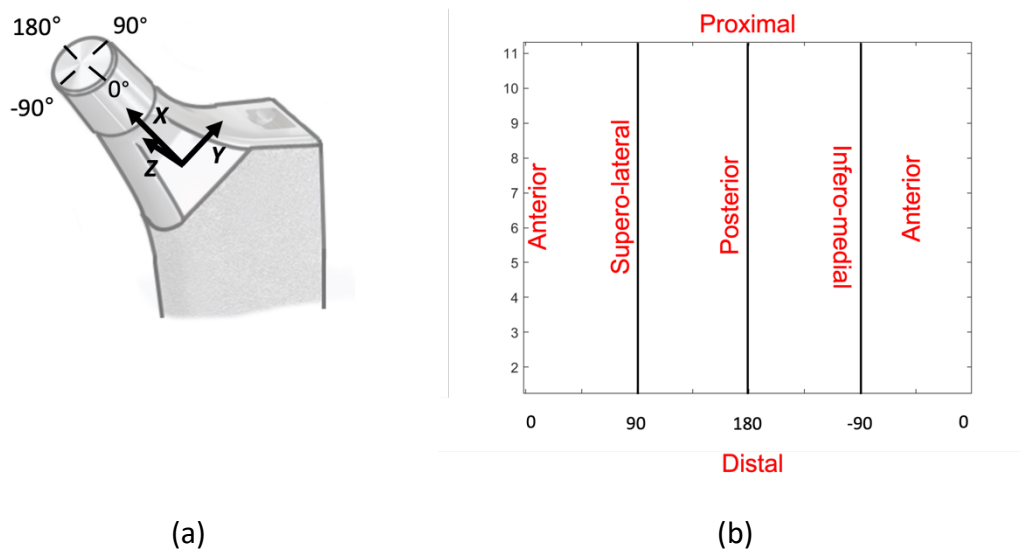
Figure 3.14. (a) Trunnion frame of reference used to create (b) the axis of the trunnion's 2D surface representation.

The second script involves the maximum distance between paired nodes at the entry point of the trunnion into the femoral head bore; named called taper separation in this study. The predicted results of this variable are plotted in a polar representation of the taper entry (Figure 3.15), taking into consideration the trunnion's frame of reference as described in Figure 3.14b.
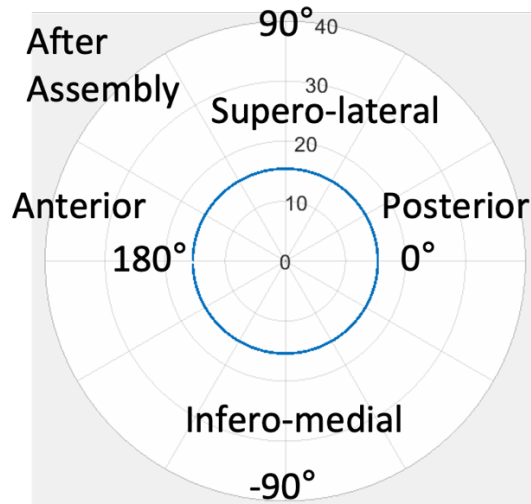
Figure 3.15. Schematic showing polar representation of the taper separation after assembly, with the separation distance (μm) between the trunnion and bore surfaces in blue.

3.7   Relevant taper design parameters and assembly conditions

A sensitivity analysis of coefficient of friction, taper clearance, and assembly force on the taper contact mechanics was performed to focus the study on the parameters that had a significant effect on the taper contact conditions during walking. Accumulated relative motions, taper separations and contact areas originated at the bore-trunnion interface for two taper clearances (0, 0.12°), two coefficients of friction (0.3, 0.21) and two assembly forces (2 kN, 4 kN) were analysed. Taper clearance changed with the trunnion angle, as the femoral bore taper angle (5.65°) was kept constant. Taper clearances, coefficients of friction and assembly forces were selected according to values that have been previously reported in the literature (Ashkanfar et al., 2017a; Bitter et al., 2016; Donaldson et al., 2014; English et al., 2015). This study showed that the taper clearance followed by the assembly force have the largest role on the contact mechanics in the taper interface. Magnitudes of contact areas and taper separation throughout a single walking cycle are shown in Figure 3.16 and 3.17, respectively. Contact areas and taper separation magnitudes were closely related to external applied forces and had a strong resemblance to the loading profile of a walking cycle (Figure 3.6), due to some of the

forces being applied perpendicular to the taper axis. Values of contact area and taper separation were at a maximum at heel-strike and toe-off, and minimum at the beginning and end of the cycle.

Interestingly, the relationship between the loading profile and predicted values in tapers with no clearance was negative, whereas the other relationships were positive. As expected, the taper with clearance angle of 0° (red lines) presented a larger contact area (414.77 mm^2) than the taper with a 0.12° clearance (black lines). For a zero-clearance taper, the minimum value occurred at heel-strike (15%) and toe off (50%) which decreased as the coefficient of friction increased and the assembly force decreased. Conversely, tapers with 0.12° clearance, the maximum and initial contact area values decreased with decreasing assembly forces and increasing coefficient of friction.
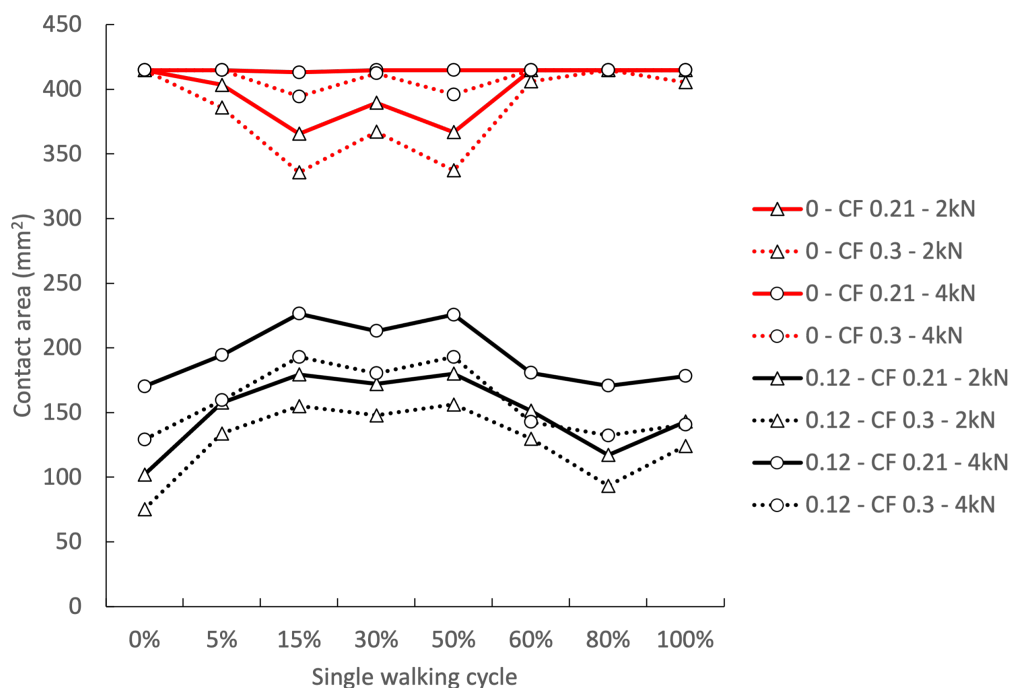
Figure 3.16. Contact area values throughout a single walking cycle. Tapers with 0° clearance are in red, and tapers with 0.12◦ clearance in black. Values from tapers with a coefficient of friction of 0.21 are represented with a solid line, and tapers with a coefficient of friction of 0.3 with a dotted line. Triangle markers represent tapers assembled with 2 kN, Circle markers those assembled with 4 kN.

Predicted values of the contact area at the taper interface at heel strike had a greater difference compared to taper clearance with an average percentage difference of 68.91%, followed by assembly force 16.47% and finally, coefficient of friction with an average difference of 10.19%. Differences of both assembly force and friction coefficient, became greater when a taper clearance was introduced.

Taper separation values, in contrast to contact area, had a positive relationship with the loading profile in all taper design parameters and assembly conditions, Figure 3.16. Similar to contact area, throughout the gait cycle the largest taper separation happened at heel-strike. Where the largest separation (17.9 μm) occurred in a $0.12°$ clearance taper with 0.3 coefficient of friction assembled using 2 kN. The maximum and initial taper separation were increased with increasing taper clearance and coefficient of friction and decreasing assembly force. Average differences between parameters had similar order of magnitude from the contact area difference, on the first-place angle of clearance had a difference of 95%, assembly force 43.1% and coefficient of friction 17.65%.
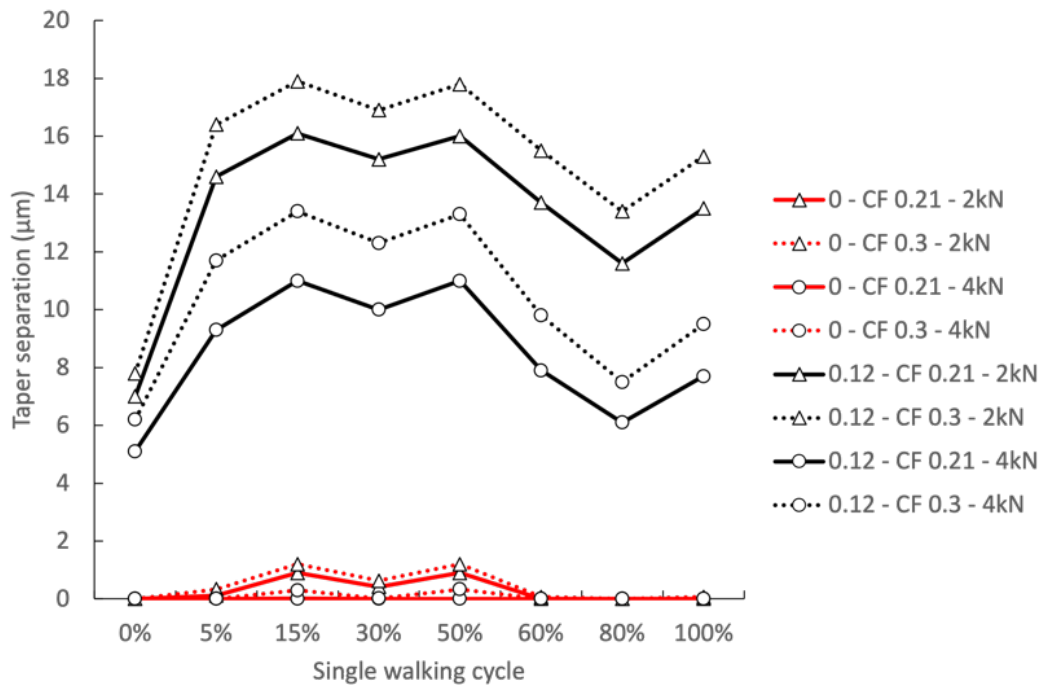
Figure 3.17. Taper separation values throughout a single walking cycle for all taper designs and assembly conditions. Tapers with 0° clearance are in red, and tapers with 0.12° clearance in black. Values from tapers with a coefficient of friction of 0.21 are represented with a solid line, and tapers with a coefficient of friction of 0.3 with a dotted line. Triangle markers represent tapers assembled with 2 kN, Circle markers those assembled with 4 kN.

The absolute values of the maximum relative motion at the most distal part the taper were determined as an accumulated value throughout a single gait cycle. The absolute values were used to remove the direction represented as a negative or positive value, otherwise the sum of the accumulated motions would result in 0. Figure 3.18 shows the predicted accumulated relative motion for all taper designs and assembly conditions. Similar to contact area and taper separation, it is noticeable that accumulated relative motions are more sensitive to changes on the clearance angle than changes in assembly force and coefficient of friction. Particularly, coefficient of friction had little effect on the predicted accumulated motion values, and only became more relevant when angle clearance was introduced.
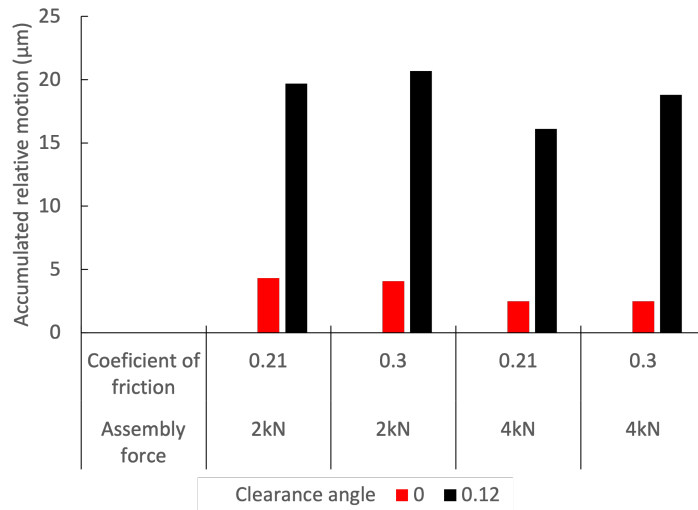
Figure 3.18. Accumulated relative motions for all tested COF and assembly forces.

Observations on the sensitivity of the predicted values for taper contact areas, separation and accumulated relative motions are supported by correlation values. Figure 3.19 shows that angle clearance has the strongest correlation with predicted values with colours in function of correlation value, a red represents a negative correlation, and blue a positive relationship. However, when clearance angle is not considered in the correlation analysis, assembly force and coefficient of friction relationship values increase, although only assembly force reaches values greater than 0.7 to be considered to have a strong relationship with the associated predicted values (Figure 3.20).

Based on this analysis, the current study on the taper contact mechanics for round and oval tapers will consider the variation of taper clearance and assembly force while coefficient of friction remains constant with a value of 0.21.
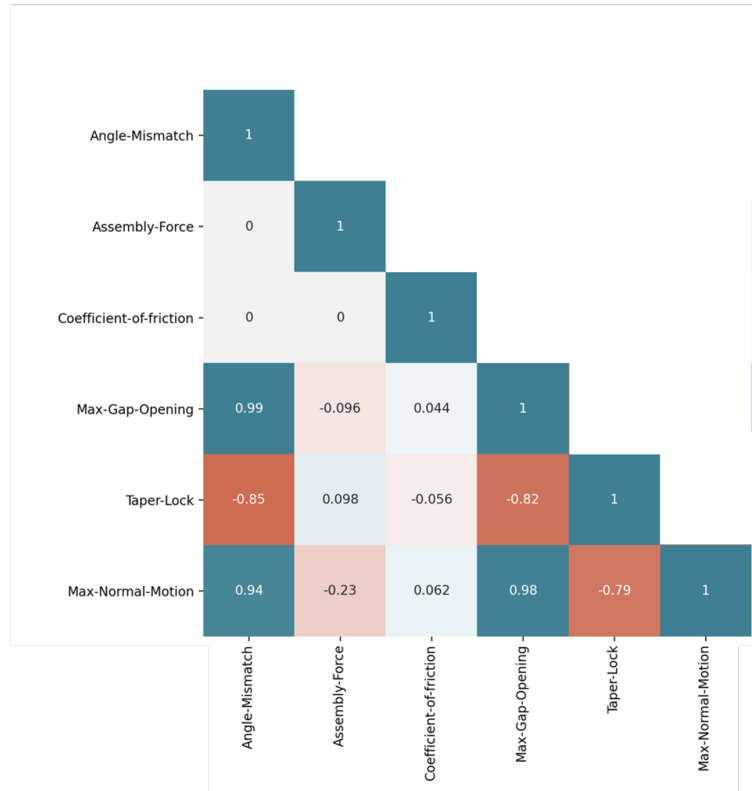
Figure 3.19. Correlation matrix of taper design parameters, assembly force, initial contact area, taper separation and relative motions.

(a) 0° clearance   (b) 0.12° clearance

Figure 3.20. Correlation matrixes for 0° and 0.12° clearances.

3.8 Validation

Validation of the current study takes place by comparing the resultant relative motions generated along the trunnion length at the inferior medial side of the trunnion from the current FE model with previous experimental and *in silico* studies. In the first validation study, relative motions generated on the proposed FE model of a perfectly cylindrical smooth trunnion with a taper clearance of 0.18° under forces and frictional moments representative of the walking activity are compared with a previous established and verified three-dimensional finite element model developed by Farhoudi et al. (2017). The difference 15 mm along the trunnion was found to be 7% with smaller differences more proximally as shown in Figure 3.21. Differences might be explained by the use of slightly different taper designs; the taper clearance and trunnion angle used in the present study, of 0.18° and 5.65°, where Farhoudi et al. study, used a smaller angular clearance of 0.024° with a trunnion angle of 5.692°.
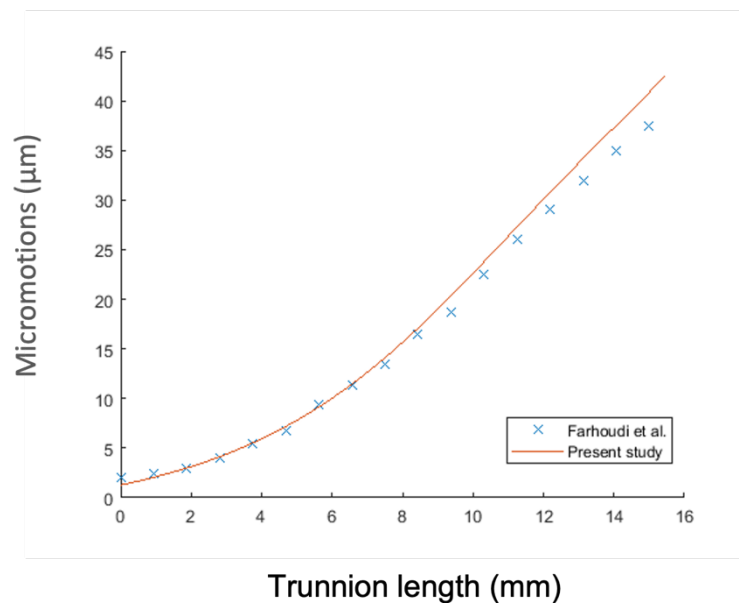
Figure 3.21. Comparison of Farhoudi et al. (2017) and the current model of the maximum predicted relative motions along the trunnion of a taper loaded with forces and moments.

In the second validation study, the taper model was subjected to a simulated fretting test with loading conditions as described by Falkenberg et al. (2019). To fully simulate the experimental loading conditions, after the assembly phase, two sinusoidal load sequences (0 to 5 kN) were applied to a reference point at the centre of the femoral head coupled with the femoral head outer surface, oriented at 35° to the taper-neck axis simulating a valgus loading. The base of the trunnion is restrained in all directions. The predicted pistoning micromotions at the distal end of the taper are compared with the reported experimental results, using a smooth taper with valgus uniaxial load and a 0 mm offset Falkenberg et al. (2019). Falkenberg et al. (2019) analysed recorded images of the trunnion surface throughout a loading sequence to measure relative movements between the trunnion and bore; images were taken through two drilled windows on the femoral head located at the distal and proximal ends of taper interface. Both the experiment and the proposed FE model generated similar relative motions during the loading cycle. Falkenberg et al. (2019) recorded pistoning micromotions values of 5.9±4 µm in the window located at the distal end of taper which are similar to the maximum pistoning relative motions (6.2 µm) generated on the distal end of the contact region of the proposed FE model.

The next chapter of this thesis describes and discusses the predicted contact areas, taper separation values, and accumulated relative motions for all taper designs and activities obtained by using the validated FE model and analysis described in this chapter.

4 Contact conditions developed for round and oval tapers

4.1 Introduction

The use of tapers for total hip replacements is well established. There are defined standards about the precision of the manufacturing of conical workpieces such as Morse tapers, however standards for taper design remain as recommendations (Hernigou et al., 2013; ISO 1947, 1973; Morlock et al., 2020). It has been established that all tapers may not perform in an ideal manner throughout their implanted lifetime. Understanding how tapers may perform under non-ideal, real conditions, whether it is through the manufacturing processes creating clearances or shape changes, in combination with the physiological loads that the tapers are exposed to, or the generation of corrosion products through the ingress of fluid to the taper interface, is important. The form of taper surfaces has not typically been considered when studying the main factors that influence the corrosion and wear processes that tapers may undergo after implantation (Dransfield et al., 2021; Wade et al., 2020). Recent studies have reported that taper surfaces differ in shape and surface topography despite being considered the same nominal design (Bitter et al., 2018; Wade et al., 2020). The impact of these variations on the contact mechanics in the taper interface and the generation of micromotions resulting in wear and mechanical assisted crevice corrosion is not well understood. The present study investigates how the shape of trunnions affects the contact with the bore and how it affects the taper mechanical response when it is loaded under different loading conditions representative of daily activities such as walking, standing-up, stairs up, jogging and cycling. Furthermore, the micromotions generated at the taper interface are characterised to identify those motions that might damage the taper surface, and how the magnitude of these motions is affected by taper design and shape.

This chapter describes the analysis and discussion of predicted results obtained from 3D FE models of a round trunnion coupled to a round femoral head bore as well as an oval trunnion coupled with a round femoral head bore. The current investigation on perfectly round and oval tapers aims to identify relevant taper design parameters that have a major role in the taper contact mechanics, and to characterise the type

of relative motions that could generate wear and/or allow fluid ingress into the taper interface. Considering these aims the investigation can be divided into a series of studies:

- Taper micromotions and contact conditions in round tapers
    - Influence of clearance
    - Influence of different activities
- Taper micromotions and contact conditions in oval tapers
    - Influence of clearance
    - Influence of out-of-roundness magnitude
    - Influence of ovality orientation

4.2 Methodology

Loading and boundary conditions of the developed FE model, and post- processing of the generated data for this study are described in Chapter 3. Contact areas, taper separation, and accumulated relative motions are analysed at the end of the preloading phase, and over each activity cycle for tapers.

4.2.1 Taper clearance for round tapers

The contact area, taper separation and relative displacements generated at the bore-trunnion interface for three angle taper clearances of a 12/14 taper (0°, 0.06°, and 0.18°), and three assembly forces (2, 4, 6 kN) were evaluated during a single cycle of standard walking (Bitter et al., 2019; English et al., 2015). The femoral head bore angle of 5.65° was kept constant in all taper designs (Dyrkacz et al., 2015; Kocagöz et al., 2013) with the taper clearance generated by changing the trunnion angle. Taper clearances and assembly forces were selected to be representative of commercially available design variables for tapers (Hothi et al., 2017; Porter et al., 2014b).

4.2.2 Activity

The mechanical contact behaviour of a taper with a proximal contact (0.18° angle clearance), assembled with an impact force of 4 kN is evaluated under the four different loading conditions that simulate daily activities namely, jogging, cycling,

stairs up, and sit-to-stand. Forces and frictional moments of these activities were obtained from instrumented hip joint replacements (Bergmann et al., 2016; Damm et al., 2013).

4.2.3   Oval tapers

Models of 12/14 round femoral bores and trunnions with different taper angles and out of roundness circumferences were generated on Abaqus CAE. The contact parameters generated at the bore-trunnion interface for three angle taper clearances of a 12/14 taper (0°, 0.06°, and 0.18°), three assembly forces (2, 4, 6 kN) and three out-of-roundness distances (6, 12 and 50 μm) were evaluated during a single cycle of standard walking (Bitter et al., 2018; English et al., 2015). Out-of-roundness distances were selected according to the taper manufacturing tolerances and those values recently reported in geometrical variations found in commercially available taper components (Bitter et al., 2019; Wade et al., 2020). The out-of-roundness position was generated along two the anterior-posterior (AP)$(0° - 180°)$ or (SI)$(- 90° - 90°)$ axes (Wade et al., 2020).

4.3   Results

4.3.1   Round tapers

In the studies of round tapers, FE models predicted that at the end of the assembly phase, the trunnion engaged at the proximal region of the bore and there is separation between the taper components for all designs which was influenced by the taper clearance and assembly force. Furthermore, these two parameters are shown to influence the separation at the entrance of the taper as well as the micromotions generated during walking.

4.3.1.1   Effects of taper design and assembly conditions

Predicted values of contact areas, taper separation and relative motions accumulated over a walking cycle were affected by taper clearance and assembly force, although with different magnitudes. As the trunnion angle decreases, representing an increasing clearance, the contact area reduces and moves

proximally. Taper contact contours between the trunnion and the bore for tested taper clearances are shown in Tables 4.1 to 4.3 showing where there was any contact over a walking cycle. As shown in these tables, no contact areas (in blue) in the taper interface increased throughout the walking cycle when the taper was assembled with lower assembly forces. Furthermore, non-contacting areas even appeared in zero clearance taper in the distal region for the lowest assembly force.

Table 4.1. Contact areas contours throughout a single walking cycle for a 0° clearance taper assembled with 2 kN, 4 kN and 6 kN. The blue colour represents no contact and red indicates contact between the bore and the trunnion. The horizontal axis goes from -2π to 3/2π and the vertical from 0 to 15 μm, representing the circumference and length of the trunnion respectively.
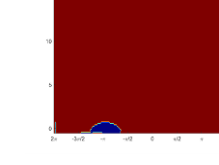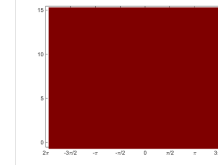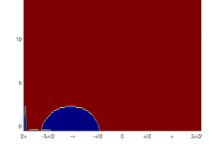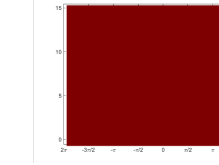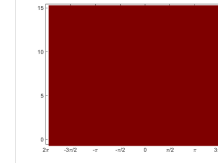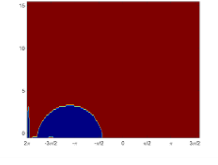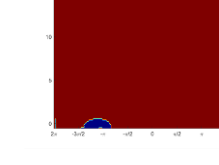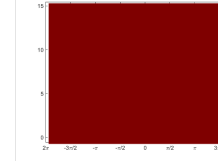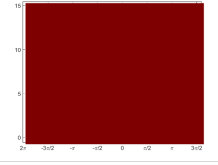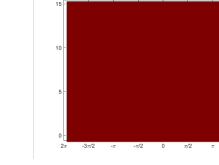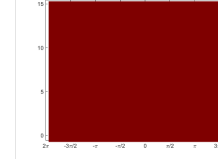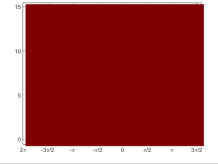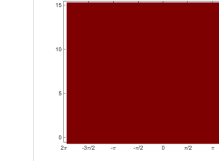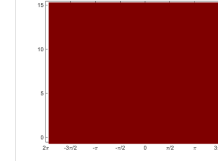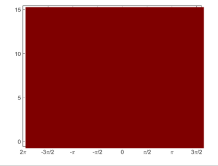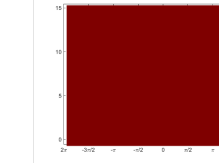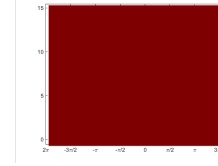
Walking cycle	2 kN	4 kN	6 kN
0%			
15%			
30%			
50%			
65%			
90%			
100%			

Table 4.2. Contact areas contours throughout a single walking cycle on a 0.06° clearance taper assembled with 2 kN, 4 kN and 6 kN. The blue colour represents no contact and red indicates contact between the bore and the trunnion. The horizontal axis goes from -2π to 3/2π and the vertical from 0 to 15 μm, representing the circumference and length of the trunnion respectively.

Walking cycle	2 kN	4 kN	6 kN
0%			
15%			
30%			
50%			
65%			
90%			
100%			
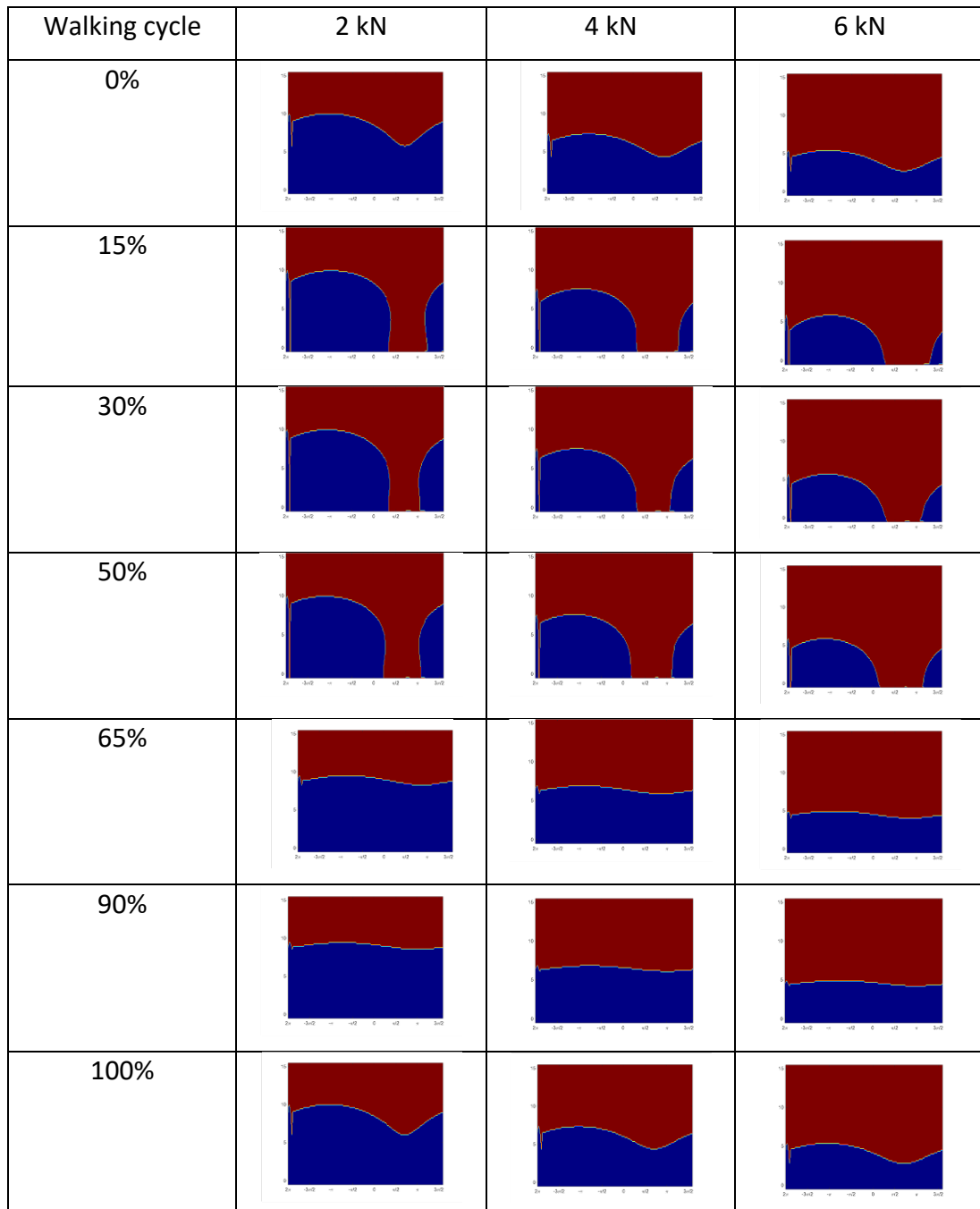
Table 4.3 Contact areas contours throughout a single walking cycle on a 0.18° clearance taper assembled with 2 kN, 4 kN and 6 kN. The blue colour represents no contact and red indicates contact between the bore and the trunnion. The horizontal axis goes from -2π to 3/2π and the vertical from 0 to 15 μm, representing the circumference and length of the trunnion respectively.

Walking cycle	2 kN	4 kN	6 kN
0%			
15%			
30%			
50%			
65%			
90%			
100%			
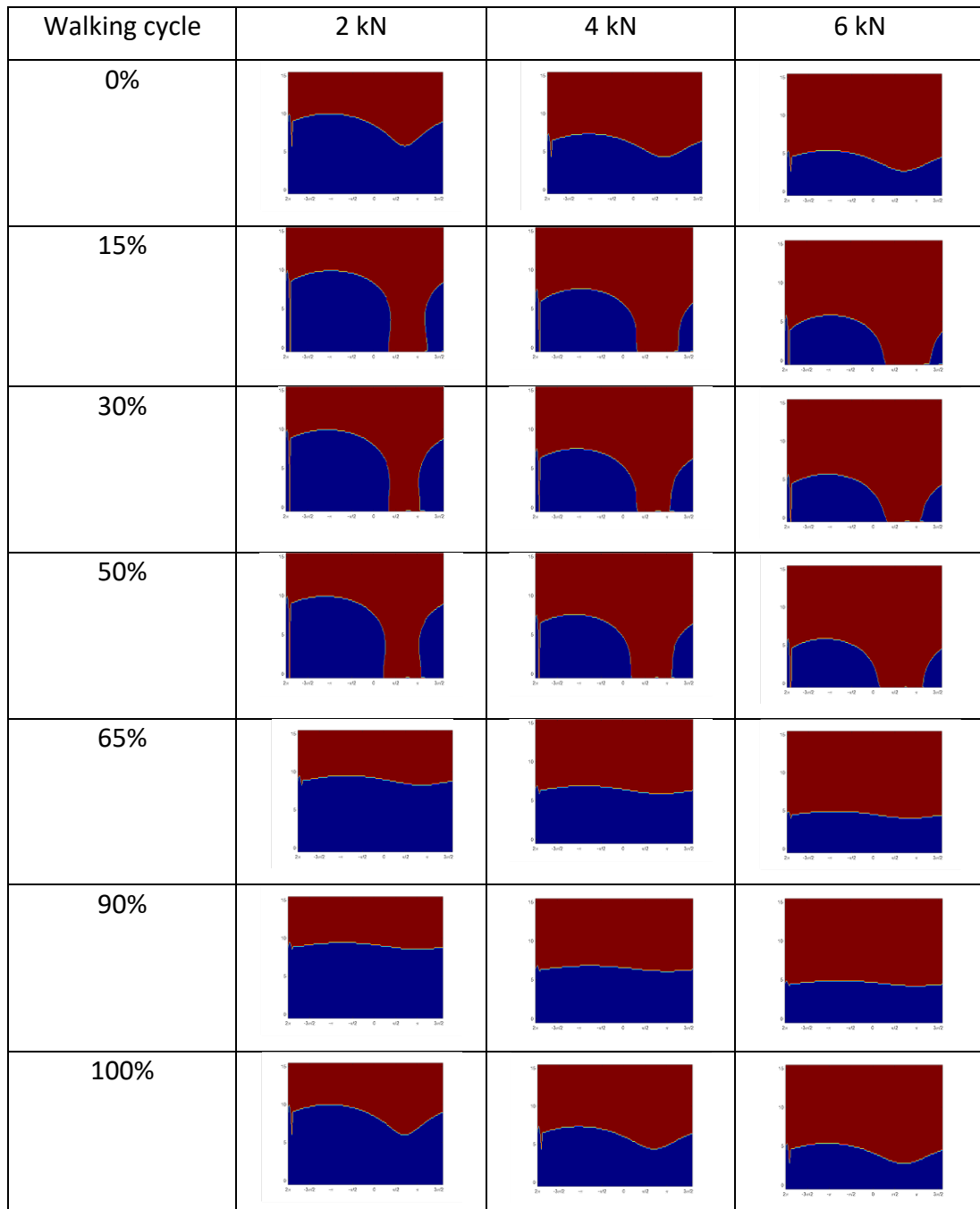
Contact area between the bore and the trunnion was greatly influenced by the applied external loads representing the gait cycle (Figure 4.1). Contact area values

had a positive relationship with the applied forces when the taper clearance was larger than 0, while tapers with no clearance produced a negative relationship between applied forces and contact area. Maximum contact area values were generated at heel-strike and toe-off, where the minimum values were at the start and end of the cycle. Maximum values and ranges of contact area and maximum taper separation for all test conditions are detailed in Table 4.4. It is evident that both these parameters are more influenced by the taper clearance than the assembly force during walking. Motions are larger when the taper has been assembled with lower assembly force and increase with clearance.
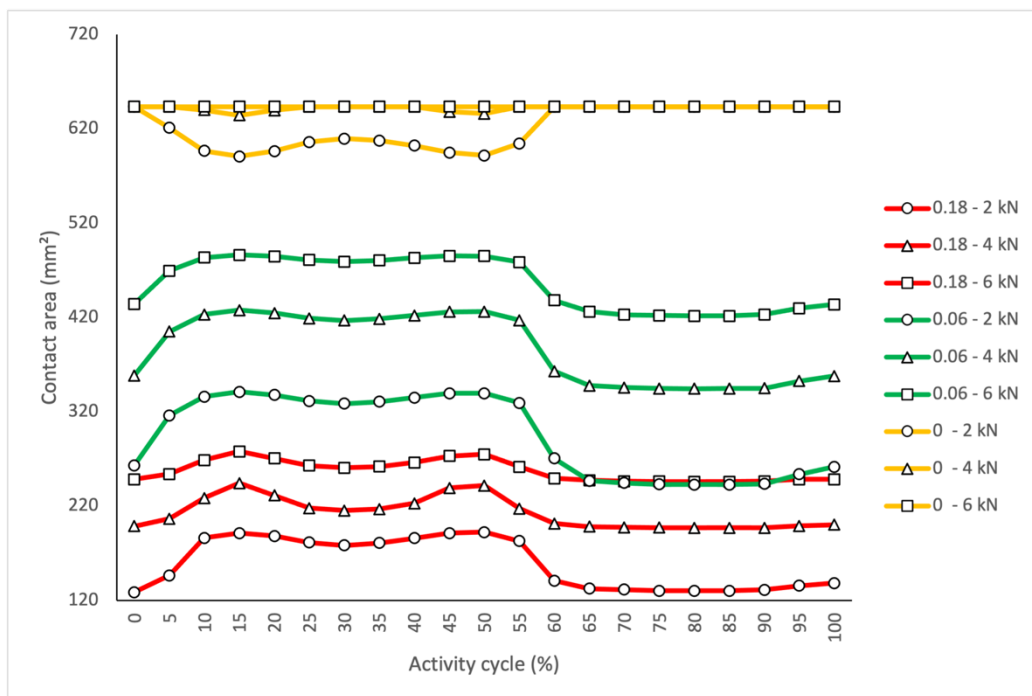
Figure 4.1. Contact area values for all tested taper clearances and assembly conditions during walking cycle. Line colours indicate clearance angle (red indicates 0.18°, green 0.06° and yellow 0°) and symbols indicate taper assembly force (Circle indicates an assembly force of 2 kN, triangle 4 kN and square 6 kN).

Table 4.4 Taper contact area and taper separation maximum and range values during a single walking cycle for all taper designs and assembly forces.

Taper clearance (°)	Assembly force (kN)	Contact area (mm)		Taper separation (mm)	
		Maximum	Range	Maximum	Range
0	2	643.7	52.8	1.1	1.1
0	4	643.6	9.2	0.1	0.1
0	6	643.6	0	0	0
0.06	2	341.1	98.3	10.9	5.8
0.06	4	427.6	83.2	7.8	4.3
0.06	6	486.3	64.5	5.6	3.2
0.18	2	192.4	63.8	38.2	13.8
0.18	4	244.3	47.3	30.9	14.0
0.18	4	278.0	32.0	25.9	11.6

The increased taper clearance created an increase in separation at the distal end between the bore and trunnion surfaces, Figure 4.2 shows the distribution of the taper separation around the distal end of the taper both after assembly for a 0.18° taper assembled with 4 kN. This initial separation also increased with lower assembly forces. As the assembly force aligned with the taper axis the separation is uniform around the circumference with a magnitude of approximately of 16 μm.
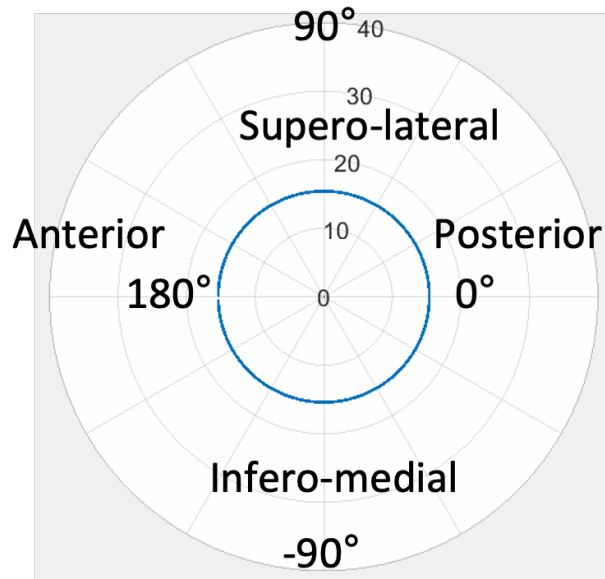
Figure 4.2. Taper separation at the taper distal end of a round taper interface shown in μm, around the circumference at the distal end of the taper following assembly using 4 kN.

Figure 4.3 illustrates the maximum taper separation throughout the walking cycle and Table 4.5 shows the taper separation distribution at heel-strike (15% of gait cycle) for all tested conditions. At heel strike, the separation is smallest in the superolateral and greatest in the inferomedial region. During the stance phase both the taper separation and contact areas demonstrate similar profiles to the reaction forces while the bore and trunnion come into contact in the superolateral region.
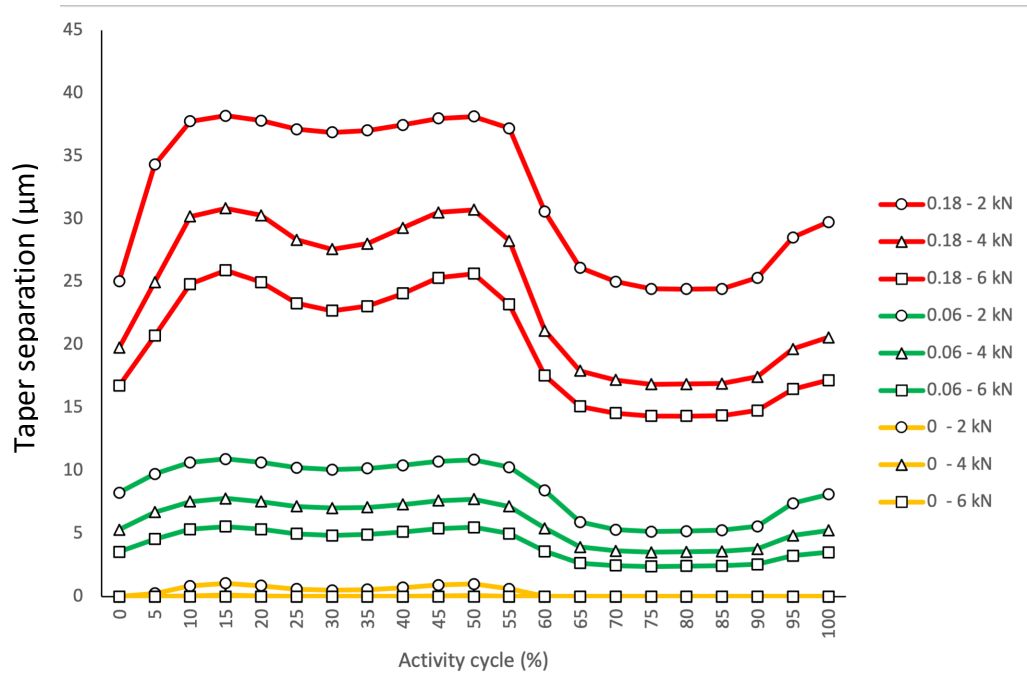
Figure 4.3: Taper separation values for all tested taper clearances and assembly conditions during walking cycle. Line colours indicate clearance angle (red indicates 0.18°, green 0.06° and yellow 0°) and symbols indicate taper assembly force (Circle indicates an assembly force of 2 kN, triangles 4 kN and squares 6 kN).

Table 4.5. Taper separation distances at heel-strike for all tested taper clearances and assembly conditions in walking.

	2 kN	4 kN	6 kN
0°			
0.06°			
0.18°			
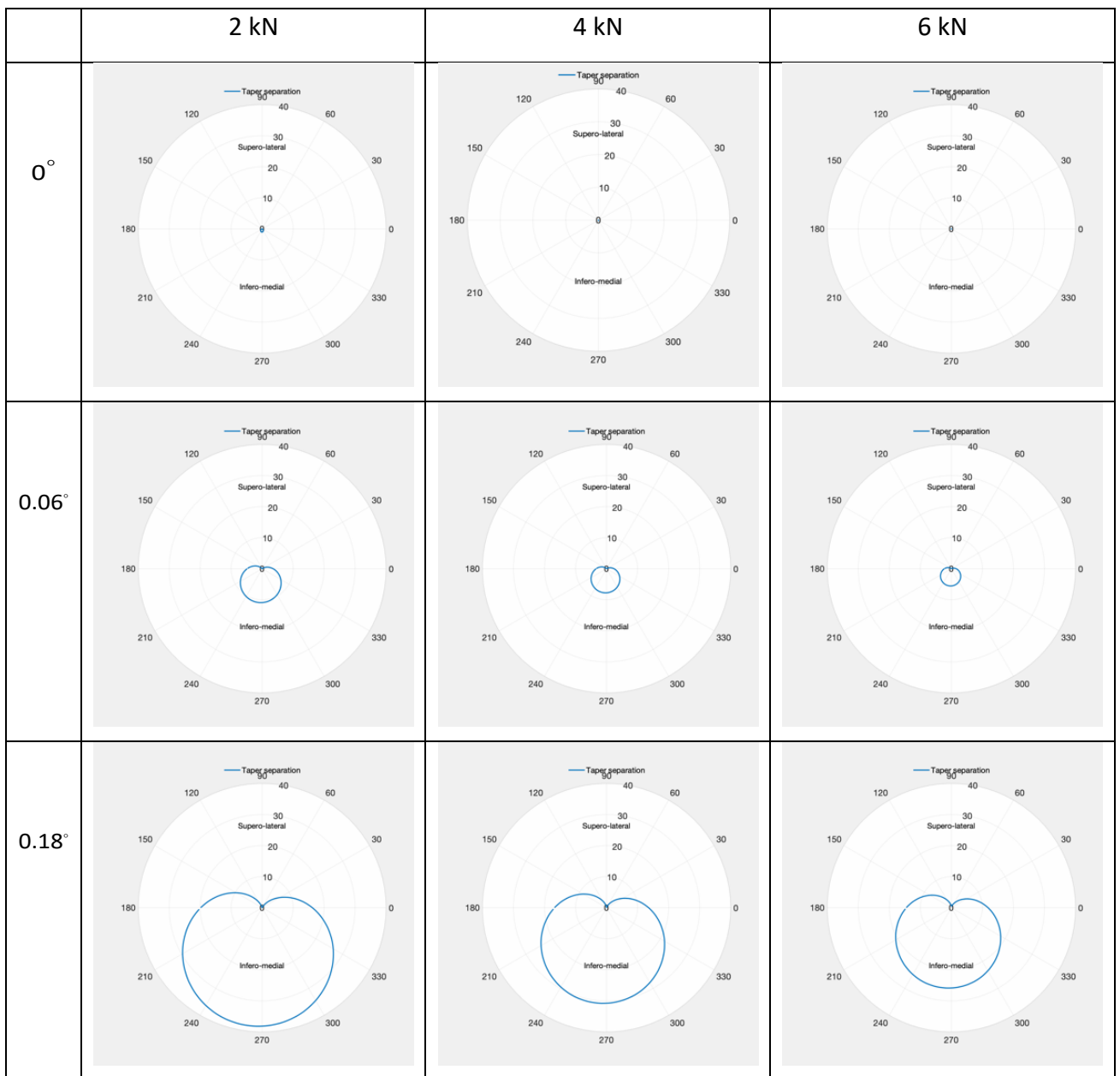
Relative motions between the taper surfaces were determined only where contact between the bore and the trunnion occurred during the activity cycle; the non-contacting areas are illustrated as uncoloured areas. The magnitude of accumulated micromotions values located at the distal end of the taper interface were influenced by taper clearance and assembly force where the maximum resultant value of 41.57 μm was established in the 0.18° clearance taper assembled with 4kN. The components of the micromotion were considered in three orthogonal directions, namely pistoning, normal and tangential.

The predicted accumulated micromotions in both the resultant and its individual components (normal, tangential and pistoning), the greatest values occurred at the distal end of the taper contact, as illustrated in Figure 4.4. In all cases, tangential motions are greatest on the supero-lateral region at the distal end of taper, while the maximum normal, pistoning and resultant motions occur at the distal end along the taper edge. The location on the taper of these relative motions coincides with the transient narrowed taper contact area during the stance phase of gait.

Cleareance (°)	Normal	Tangential	Pistoning	Resultant	Relative motion (μm)
0					
0.06					
0.18					
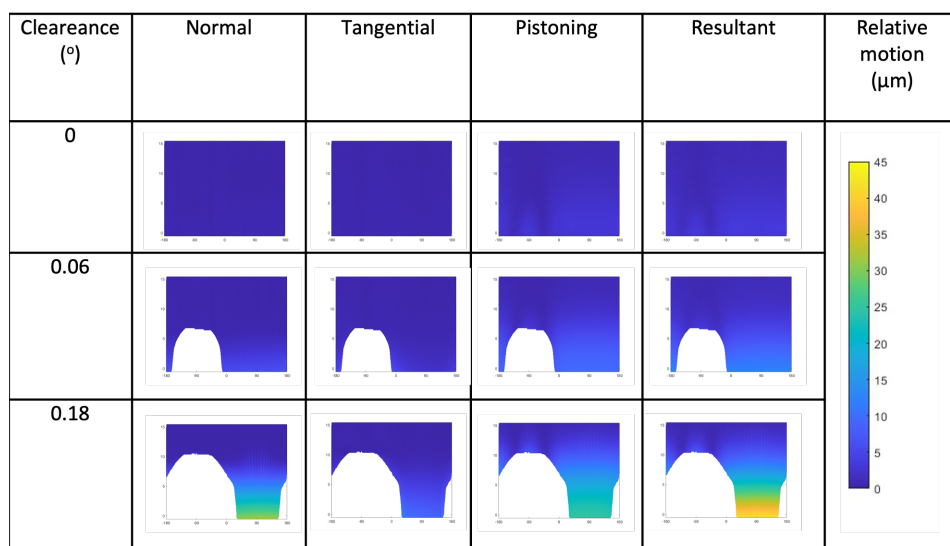
Figure 4.4. Distribution of accumulated, normal, tangential and pistoning relative motions in contacting nodes for a range of taper clearance values over a walking cycle. The horizontal axis goes from -180° to 180° and the vertical from 0 to 15 μm, representing the circumference and length of the trunnion respectively.

In addition to relative motion magnitudes, taper clearance also affected the distribution of the resultant components of the separation (Figure 4.5). The predominant relative motion component in tapers with zero clearance was pistoning, as there was no space for normal motions. As the trunnion angle decreased (increased clearance), the tangential relative motions became more predominant.
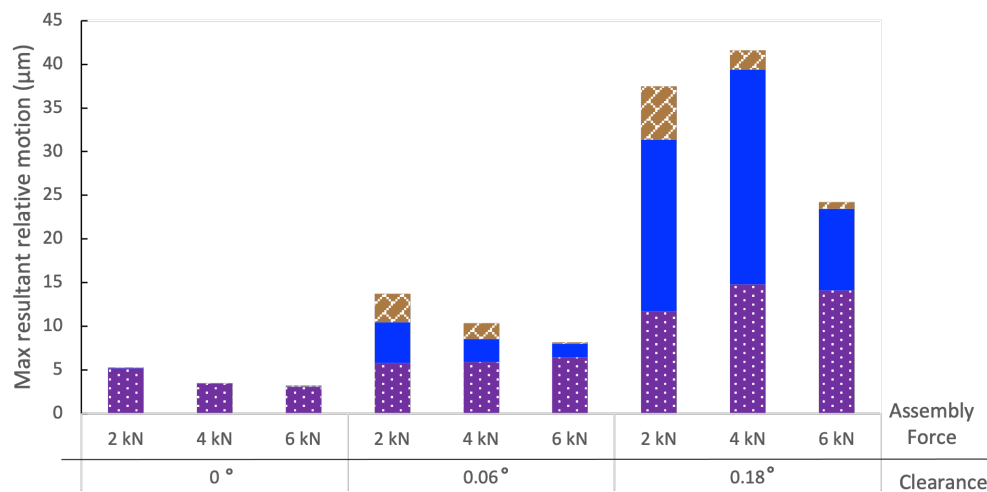
Figure 4.5. Component distribution of pistoning (purple), normal (blue), and tangential (yellow) accumulated relative motions in contacting nodes for different clearance values and assembly forces over a walking cycle.

4.1.1 Influence of activities on taper contact mechanics

The high sensitivity to external forces and moments of the taper contact mechanics generated unique contact conditions and relative motions between the trunnion and the bore. Contact area and taper separation values were intimately associated with the activities' resultant force profiles as illustrated in Figures 4.6 and 4.7.
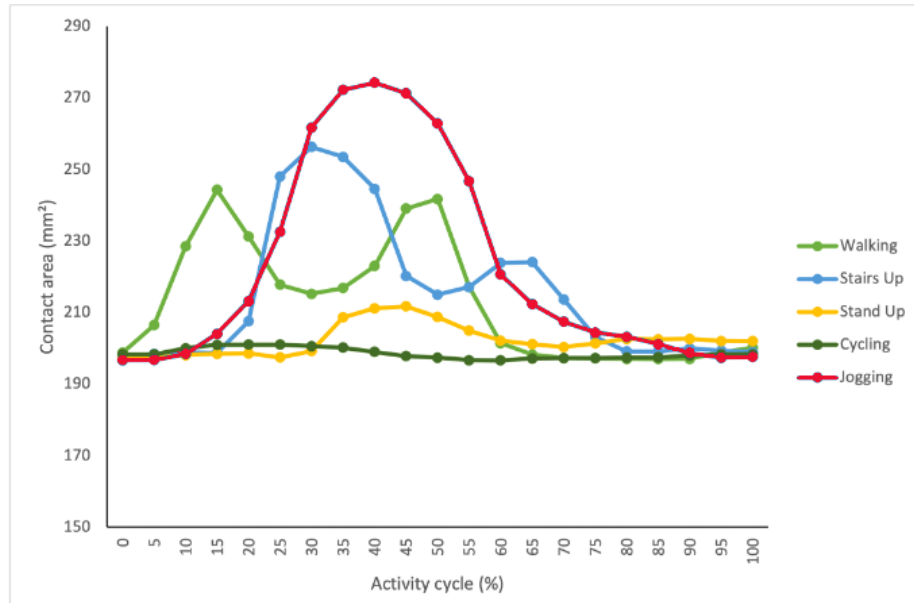
Figure 4.6. Contact area at the taper interface for round tapers with a 0.18° clearance for different activities.
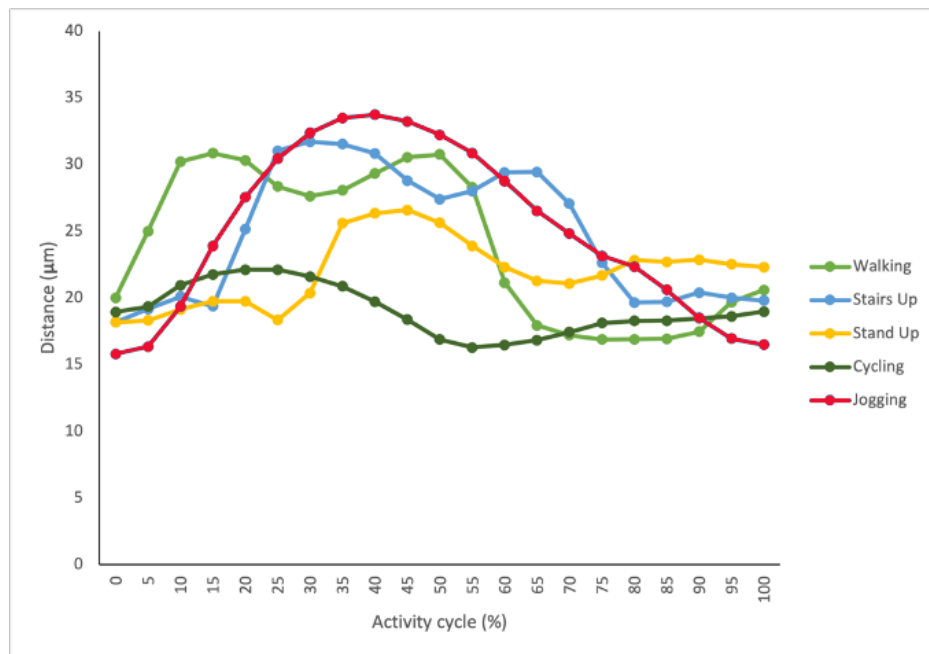
Figure 4.7. Distribution of accumulated relative motions in contacting nodes for round tapers with a 0.18° clearance for different activities.

The contact area, in the superolateral region of the trunnion, is greatest for walking, jogging and stairs up corresponding to the highest resultant forces (Table 4.6). Contact area and taper separation values for stairs up and jogging are similar to walking, but larger than both sit to stand and cycling activities. Close examination

reveals that jogging had the largest range in both contact area (77.6 mm^2) and maximum taper separation (17.9 µm), when assembled at 4 kN with a taper clearance of 0.18°.

Table 4.6. Taper contact area and taper separation maximum and range values during different activities.

Activity	Contact area (mm^2)		Taper separation (µm)	
	Maximum	Range	Maximum	Range
Stairs up	256.3	58.9	31.7	13.5
Jogging	274.3	77.6	33.7	17.9
Sit-to-stand	211.7	14.5	26.6	8.4
Cycling	201	4.4	22.1	5.8

Table 4.7 illustrates the contact between the trunnion and the bore surfaces at different activity stances. Similar to walking, stairs up and jogging also generated an intermittent contact area at the distal end of the taper interface, the circumferential distance of this contact was 37 µm, 11 µm, and 249 µm for walking, jogging and stairs up activities, respectively.

Table 4.7. Contact areas contours throughout a single activity cycle in a 0.18°
clearance taper assembled with 4 kN. Colour blue represents no contact between the
bore and the trunnion. The horizontal axis goes from -2π to $3/2\,\pi$ and the vertical
from 0 to 15 μm, representing the circumference and length of the trunnion
respectively.

	Walking	Stairs up	Jogging	Sit-to-stand	Cycling
0%					
15%					
30%					
50%					
65%					
90%					
100%					
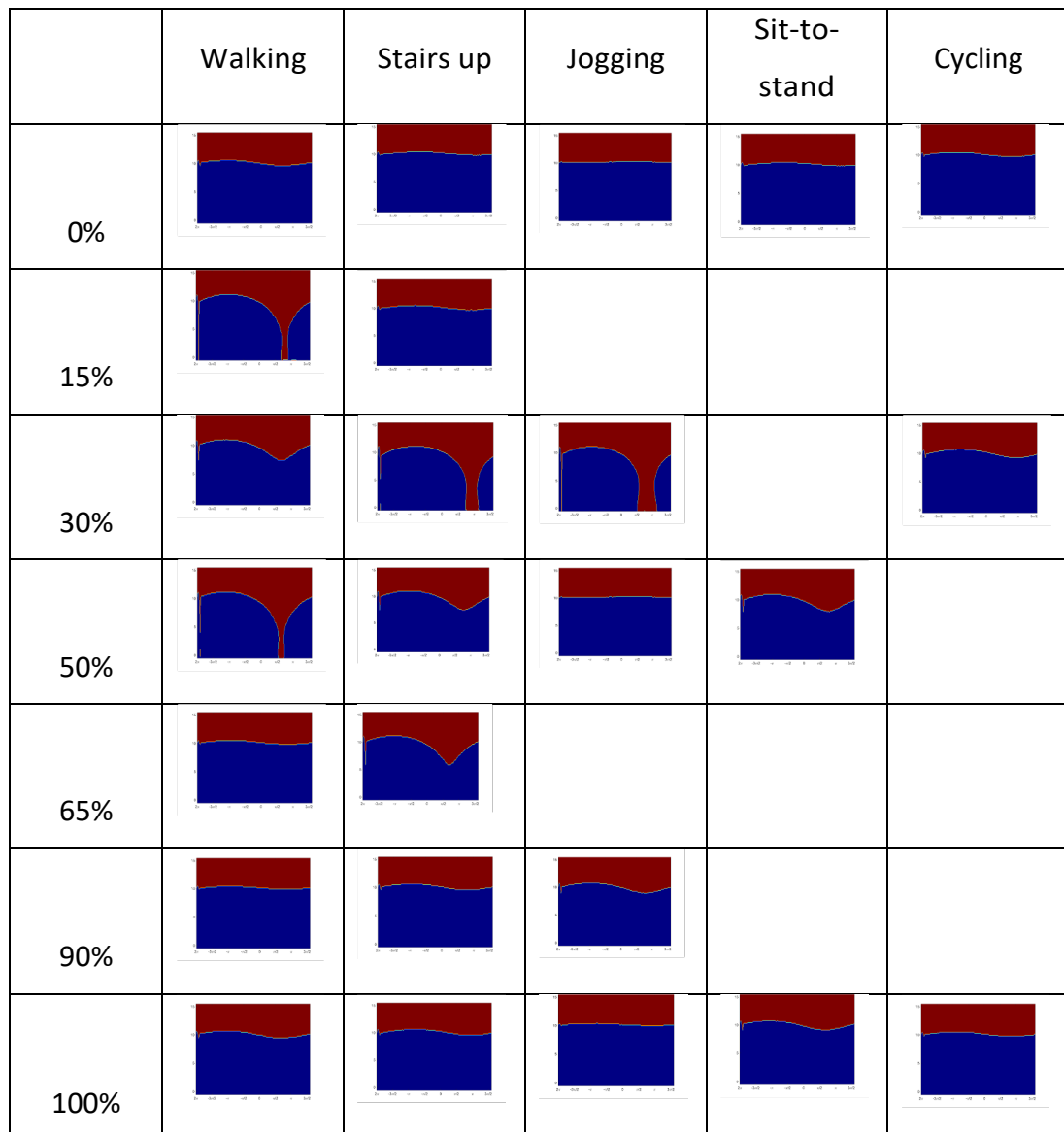
Separation distances at the taper entrance in round tapers changed throughout the
activities cycle (Figure 4.8). Sit-to-stand and cycling activities separation distances did
not experience significant changes throughout the activity's cycle in contrast to
walking, stairs-up and jogging activities. In these activities, separation distances at

the inferior-medial part of the taper increased while distances at the supero-inferior

region decreased during the peak resultant force of the activity.

Table 4.8. Taper separation throughout a single activity cycle on a 0.18∘ clearance tapers assembled with 4 kN for different activities.

	Walking	Stairs-up	Jogging	Sit-to-stand	Cycling
0%					
15%					
30%					

50%					
65%					
90%					
100%					
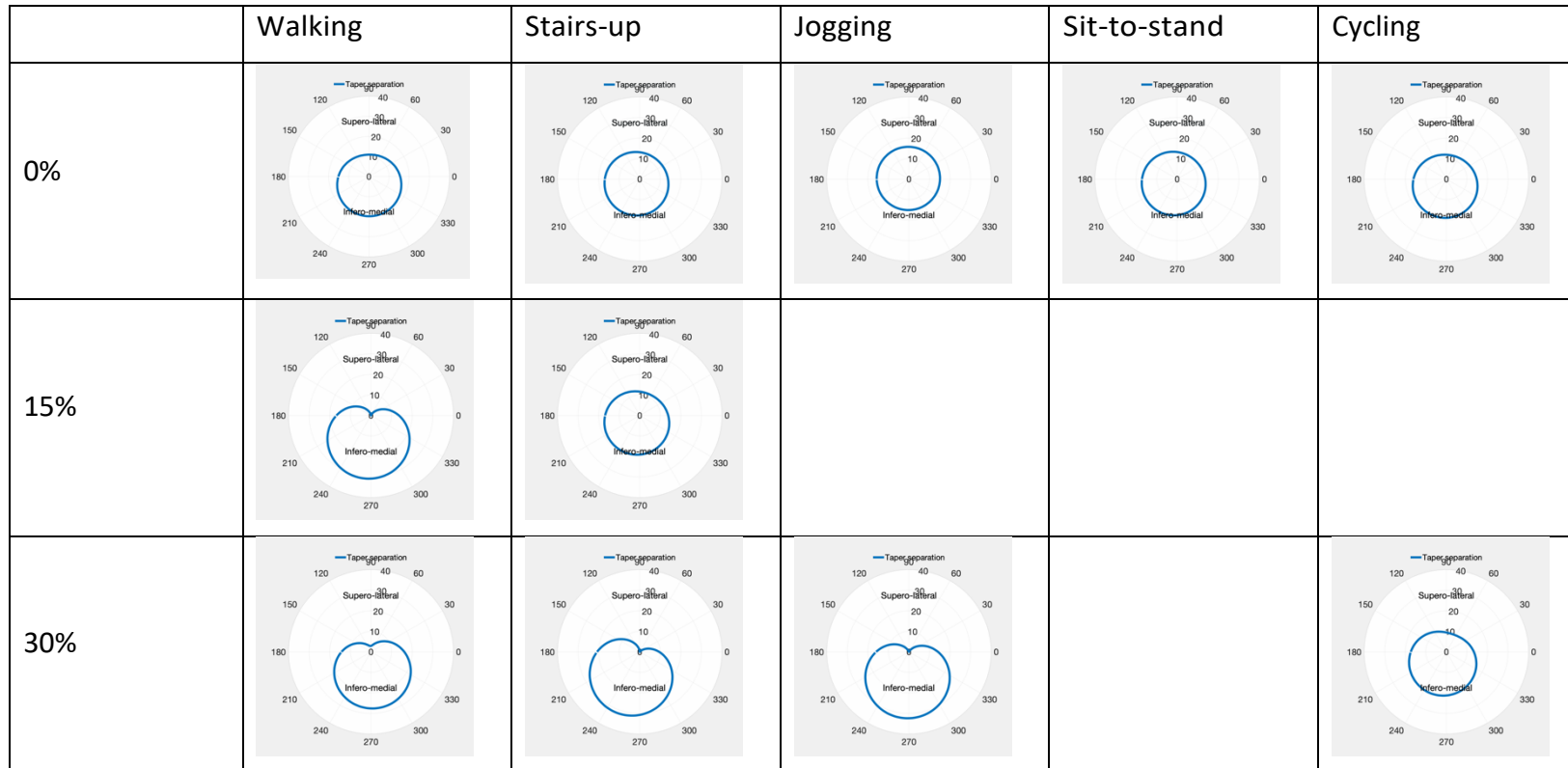
Micromotions and their component distribution are distinctive for each activity (Figures 4.8 and 4.9). Sit-to-stand and cycling activities are associated with significantly smaller accumulated maximum micromotions than walking, jogging and stairs up. Although jogging and stairs up activities presented similar micromotions to walking, the distribution of the components vary between each of the activities. For example, while jogging is associated with considerable pistoning motions, the tangential motions for jogging, and stairs up are similar but greater than those generated during walking, cycling and sit-to-stand; interestingly, walking activity presented the highest normal motion of all activities (Figure 4.9).

Activity	Cleareance (°)	Normal	Tangential	Pistoning	Resultant	Relative motion (μm)
Walking	0.18					
Jogging	0.18					
Stairs Up	0.18					
Sit-to-stand	0.18					
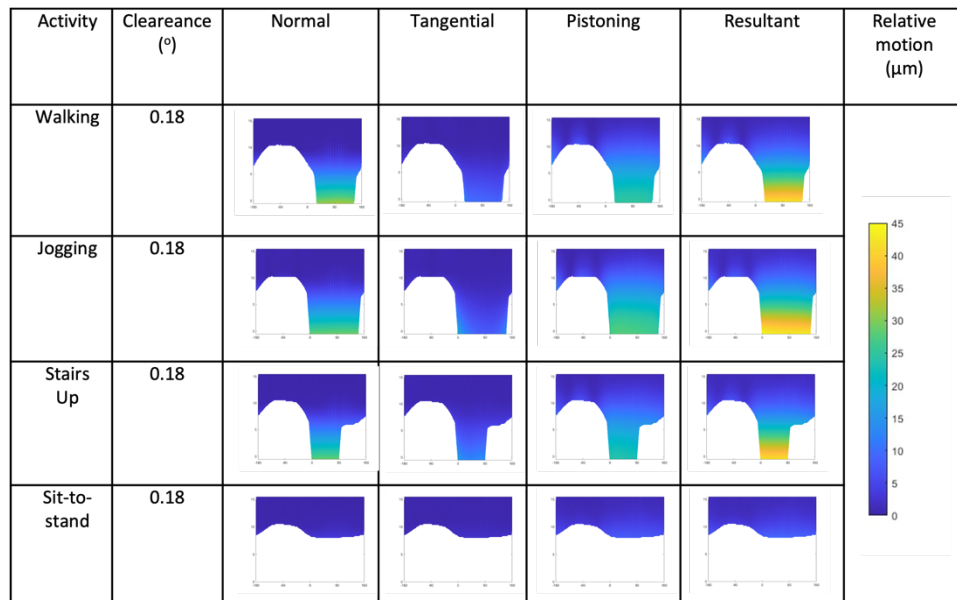
Figure 4.8. Distribution of accumulated relative motions in contacting nodes over different activities. The horizontal axis goes from -180° to 180° and the vertical from 0 to 15 μm, representing the circumference and length of the trunnion respectively.
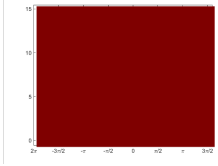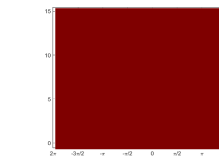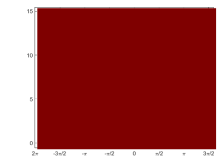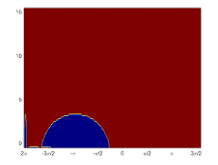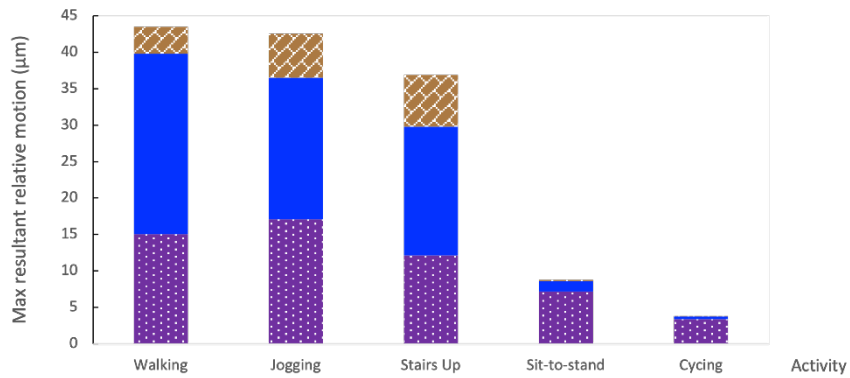
Figure 4.9. Component distribution of pistoning (purple), normal (blue), and tangential (yellow) accumulated relative motions in contacting nodes over different activities.

4.1.2 Oval tapers

Oval trunnions significantly affect the contact mechanics and micromotions at the taper interface after assembly and during a single walking cycle. Moreover, the orientation of the ovality influenced how the oval trunnion interacted with the round bore during walking. Ovality augmented the influence of taper clearance and assembly force on the mechanical response of the taper during walking.

4.1.2.1 Taper separation and contact area

Contact conditions in the taper interface of oval trunnions were influenced by the magnitude of ovality and its orientation. Ovality oriented along the AP axis, showed that increasing the ovality magnitude decreases the maximum and range of contact areas, and increases the maximum taper separation distance for tapers with 0° and 0.6^o clearances (Table 4.9). However, when increasing the taper clearance to 0.18^o a different pattern in the contact response is obtained. A 12 µm ovality results in the smallest contact area (139.4 mm^2) and smallest maximum taper separation at the taper entrance (5.9 µm). When the ovality is oriented in the SI direction, contact conditions in the taper interface are lower than those tapers with an ovality in the AP axis. In these tapers the ovality in the SI direction reduces the maximum contact area and range, however for tapers with a 12 µm ovality the maximum taper

separation distance showed a similar value to the taper with 6 µm ovality (27.7 and 23 µm respectively).

Table 4.9. Predicted contact areas and maximum taper separation in the bore-trunnion interface for all variables examined. The taper clearances, assembly forces and out of roundness results were determined on tapers loaded by a walking cycle.

	Taper clearance / °	Ovality magnitude / µm	Assembly force / kN	Ovality direction	Contact area / mm²		Max taper separation / µm	
					Max	Range	Max	Range
Out of roundness	0	6	4	AP	419.7	81.5	5.3	2.7
		12	4	AP	355.7	21.3	11.6	3.8
		50	4	AP	157.4	3.1	57.7	15
	0.06	6	4	AP	376.1	20.9	16.2	6.7
		12	4	AP	239.7	7.9	19.1	6.2
		50	4	AP	130.4	3.36	59.1	13.8
	0.18	6	4	SI	270.3	41.4	23	6.3
				AP	313.5	84.1	34.1	13.8
		12	4	SI	82.6	4.4	27.5	1.6
				AP	139.4	59.3	5.9	16.6
		50	4	SI	150.5	0.8	48.5	0.8
				AP	161.9	10.5	73.7	19.3

Taper separation distribution is affected by both the external loading and the ovality of the trunnion. The out-of-roundness generated specific taper separation distribution to the ovality magnitudes, where the distance between the bore and trunnion at the taper entrance is reduced, and sometimes resulting in full contact between the bore and trunnion surfaces at the out-of-roundness in 50 µm oval tapers (Figure 4.10). The distributions of the taper separation for 6 and 50 µm oval tapers through a single walking cycle are illustrated in Figures 4.11, 4.12, respectively.
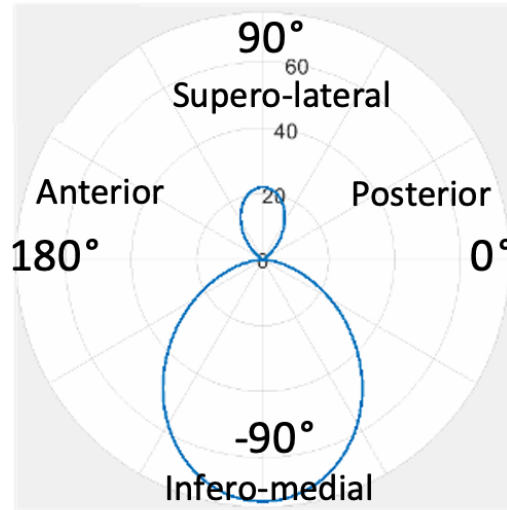
Figure 4.10. Taper separation at the distal end of a 50 μm oval taper with SI direction assembled with 4 kN at heel strick shown in μm, around the circumference at the distal end of the taper interface. Contact between the bore and trunnion is present at the anterior and posterior regions of the taper interface.

Both maximum taper separation and taper contact area profiles through the single walking cycle are similar to the applied external profile. For the taper with 6 μm of ovality, the maximum taper separation is 10.3% higher and the contact area 28.3% higher than for a round taper, although the contact continues to occur between 15% and 50% of the gait cycle. However, for the taper with 50 μm of ovality, the taper contact patterns are very different. In particular, the contact areas are smaller but remain in contact throughout the entire gait cycle (Figure 4.11 and 4.12).
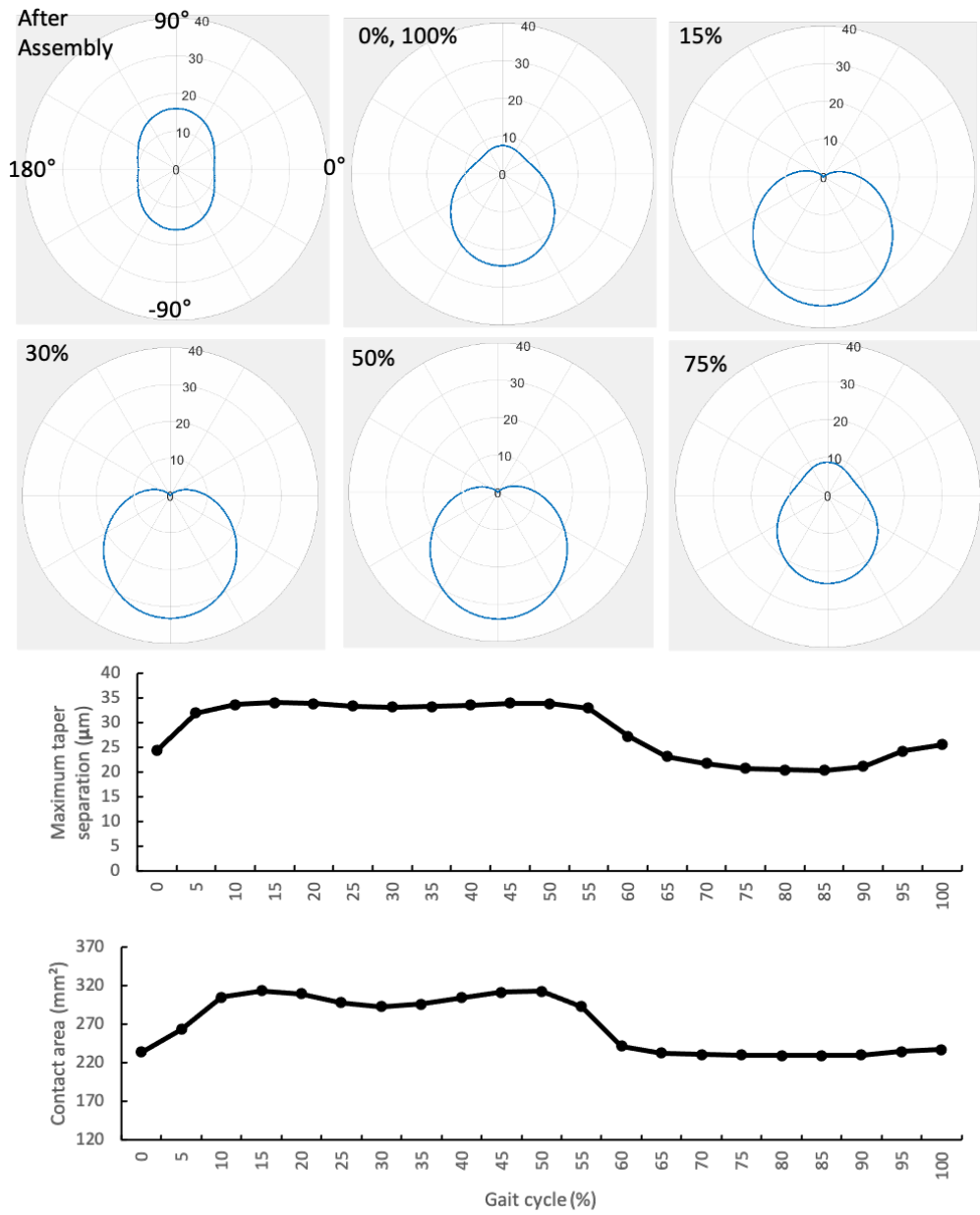
Figure 4.11. Distribution of taper separation recorded at the distal end of the bore-trunnion, taper separation and contact area throughout the gait cycle for a 6 µm oval taper with AP direction and a taper clearance of 0.18°.
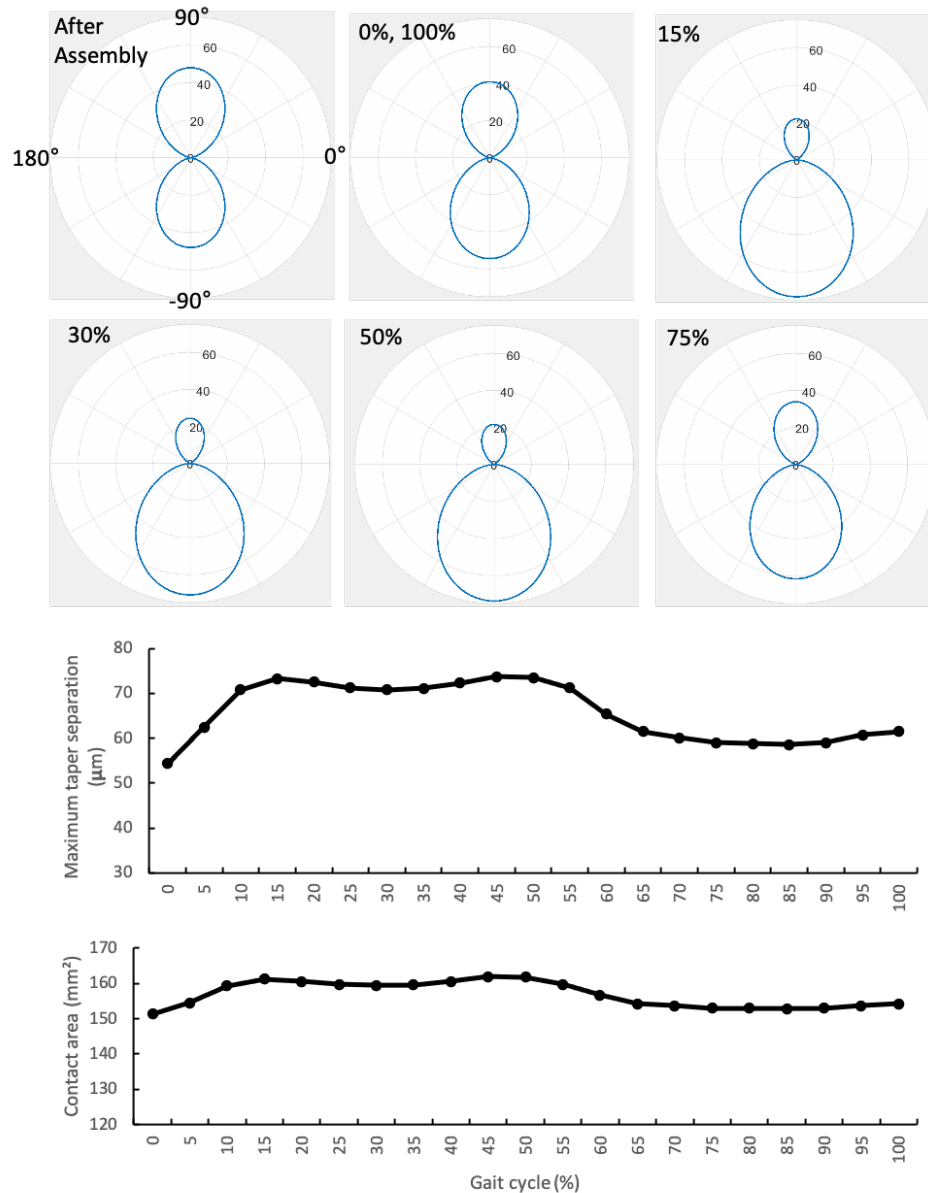
Figure 4.12. Distribution of taper separation recorded at the distal end of the bore-trunnion, taper separation, and contact area throughout the gait cycle for a 50 μm oval taper with SI direction and a taper clearance of 0.18°.

Separation distances generated at the distal entrance of the taper throughout a single walking cycle are shown in Table 4.10. Ovality orientation determined the location and distribution of the separation distances generated at the taper interface of oval tapers. Ovality in the SI direction caused fewer changes throughout the walking cycle as the resultant load coincided with the ovality orientation. Whilst in tapers with the ovality in the AP direction, presented wider changes throughout the

85

cycle. Regarding taper separation distances around the taper, oval tapers oriented in the SI direction generated a symmetrical distribution where the maximum distances were on AP direction. Inversely, oval tapers in the AP direction, maximum distances were generated in the SI direction.

Table 4.10. Taper separation at the distal entrance of the taper interface of different ovality magnitudes and orientations during a single walking cycle.

	50 um (SI)	50 um (AP)	6 um (SI)	6 um (AP)
0%				
15%				
30%				

50%				
65%				
90%				
100%				
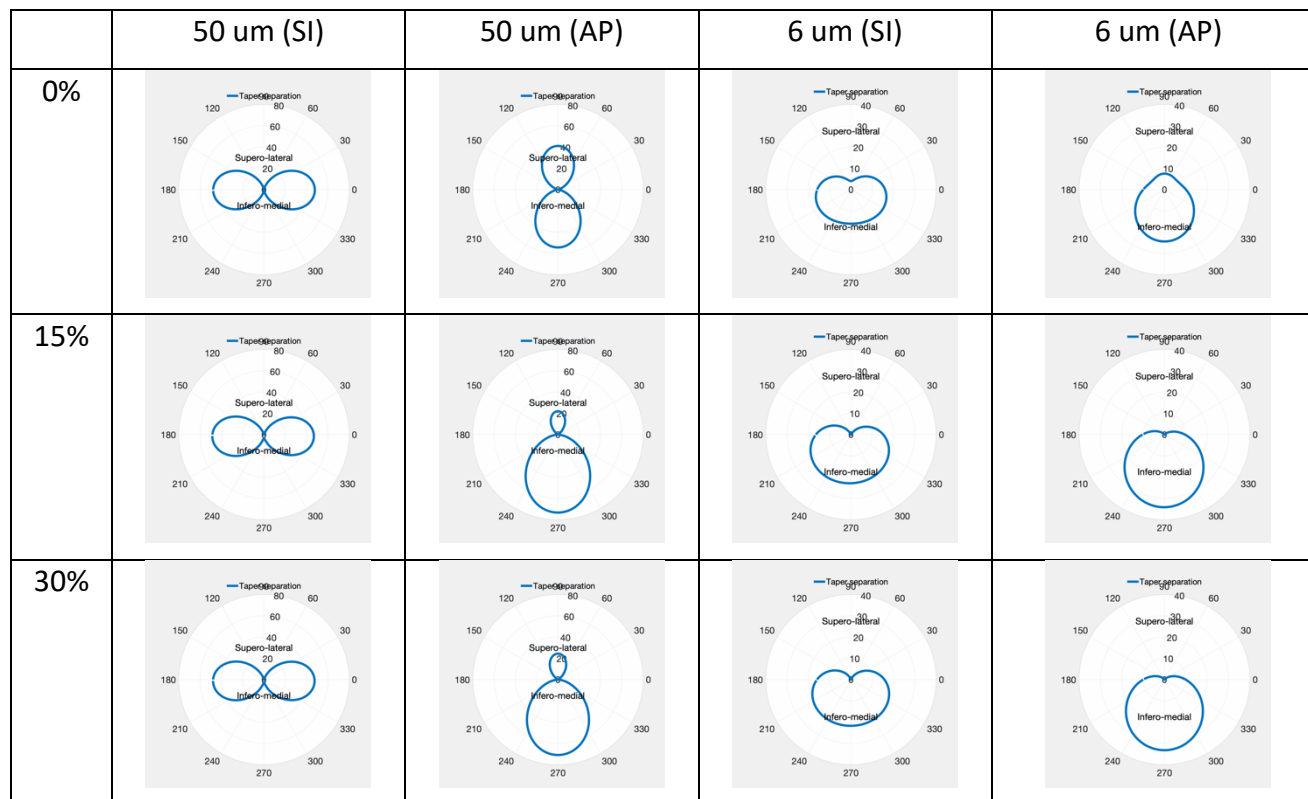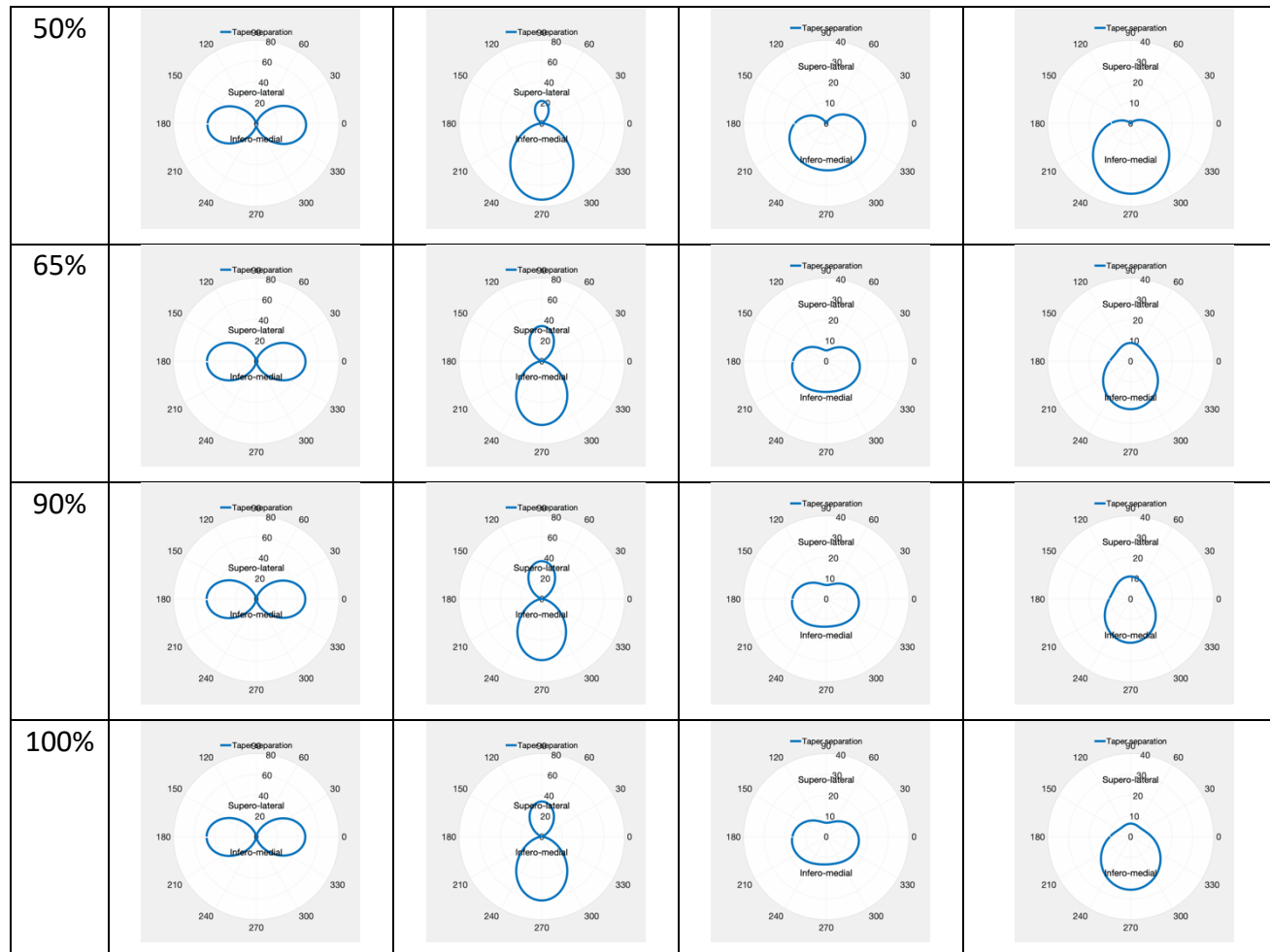
4.3.3.2. Micromotion distribution and taper contact patterns

The micromotion distribution for different ovalities (Figure 4.14) and contact areas are influenced by the extent of the magnitude of the ovality for each clearance. The model predicts that the orientation and extent of the ovality plays a major role in the development of relative movement as shown in Figure 4.13. In particular small changes in the out- of-roundness greatly influence the contribution of pistoning to the overall motion due to an irregular contact between the trunnion and bore surface. Comparisons of the influence of assembly force, ovality and taper clearance are shown in Figure 4.13, which highlights that tangential motion tends to increase with ovality, that the normal motion increases with taper clearance and that pistoning motion is a complex interaction of the variables once a firm assembly force of 4 kN is applied.

Clearance (°)	Ovality	Normal	Tangential	Pistoning	Resultant	Relative motion (µm)
0	6 um					
	12 um					
	50 um					
0.06	6 um					
	12 um					
	50 um					
0.18	6 um					
	12 um					
	50 um					
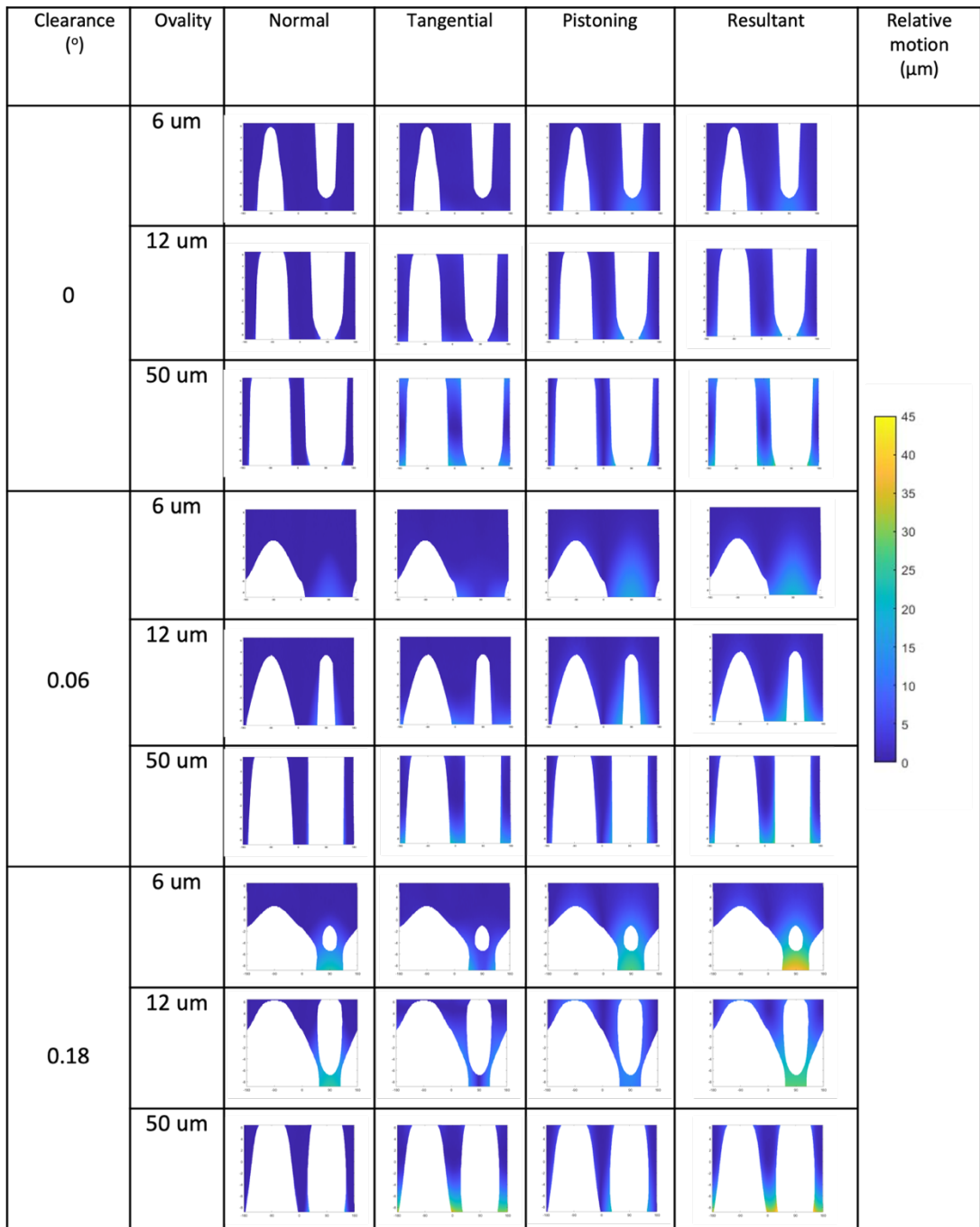
Figure 4.13. Distribution of accumulated relative motions in contacting nodes for different out of roundness values over a walking cycle. The horizontal axis goes from -180° to 180° and the vertical from 0 to 15 µm, representing the circumference and length of the trunnion respectively.
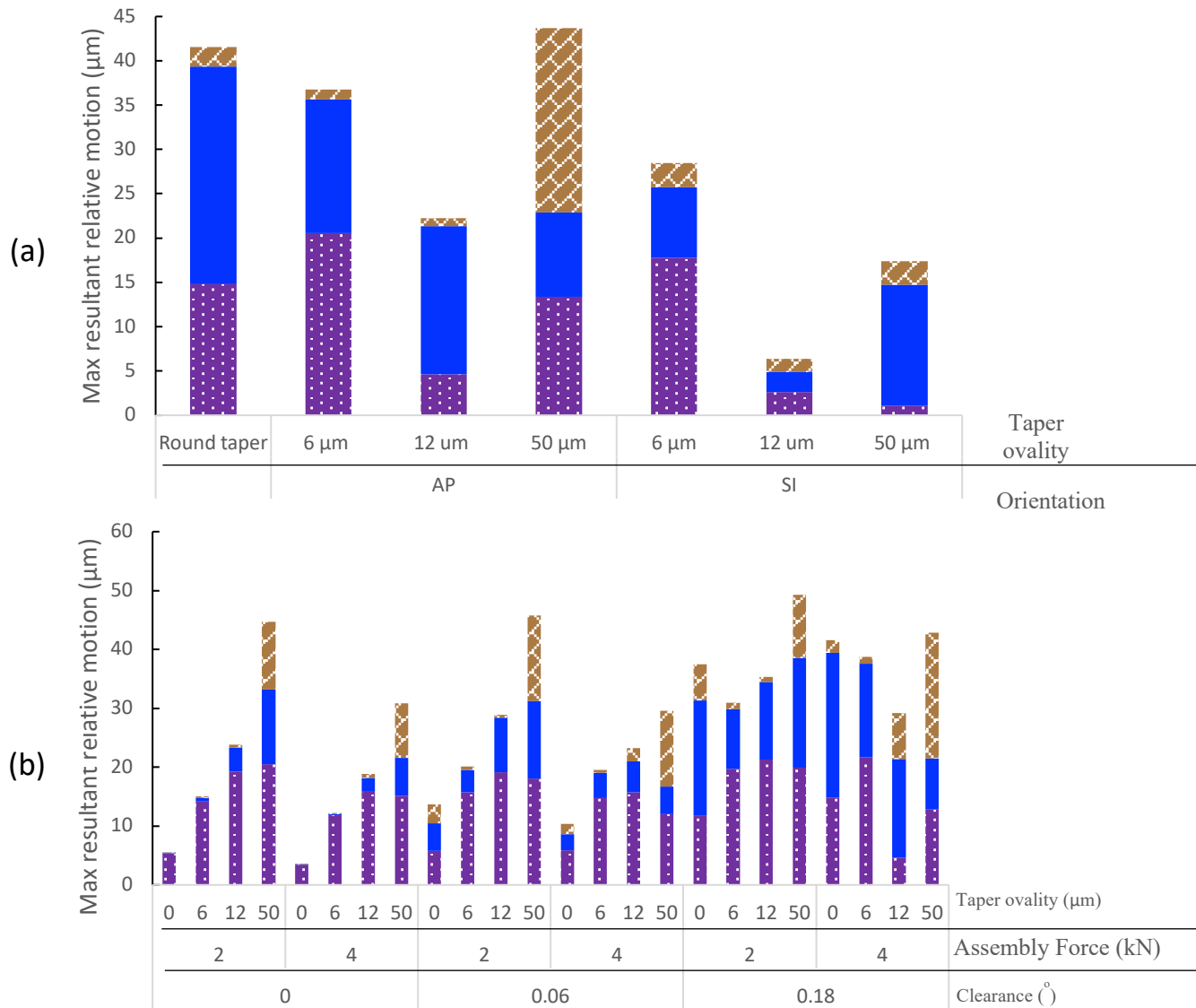
Figure 4.14. Maximum resultant relative motion and the tangential (mustard), normal (blue) and pistoning (purple) components' distribution for a) different taper ovalities and orientations, and b) taper ovalities, clearance angles and assembly forces up to 4kN.

Contact between the bore and trunnion was highly dependent to the extent of out-of-roundness ovality and the orientation determined the contact changes throughout the walking cycle (Table 4.11). Tapers with an ovality of 50 μm and a clearance of 0.18° did not engage on the distal part of the trunnion, instead the engagement of the taper was found on the lateral sides where the major axis of the oval circumference was located. In oval tapers with 6 and 12 μm the engagement occured at the distal end of the taper, where it was expected, however, additional

contact areas due to the out-of-roundness ovality were observed. The extent of these additional contact areas in the taper interface were a function of the ovality magnitude. Orientation of the out of roundness changed the location of the additional contact areas presented in 6 and 12 μm oval tapers, and the engagement location for the 50 μm oval taper but maintained the same shape of the contact areas (Figure 4.13). However, ovality orientation did affect the contact area evolution throughout the walking cycle, in which oval tapers oriented along the SI axis presented small changes throughout the cycle due to the limited motion occurring at the taper interface, in contrast to those oval tapers oriented along the AP where larger areas of intermittent contact between the bore and trunnion occurred throughout the gait cycle, similar to round tapers.

Table 4.11. Contact area at the taper interface of different ovality magnitudes and orientations during a single walking cycle. The horizontal axis goes from -2π to 3/2 π and the vertical from 0 to 15 µm, representing the circumference and length of the trunnion respectively.

	50 um (SI)	50 um (AP)	6 um (SI)	6 um (AP)
0%				
15%				
30%				
50%				
65%				
90%				
100%				
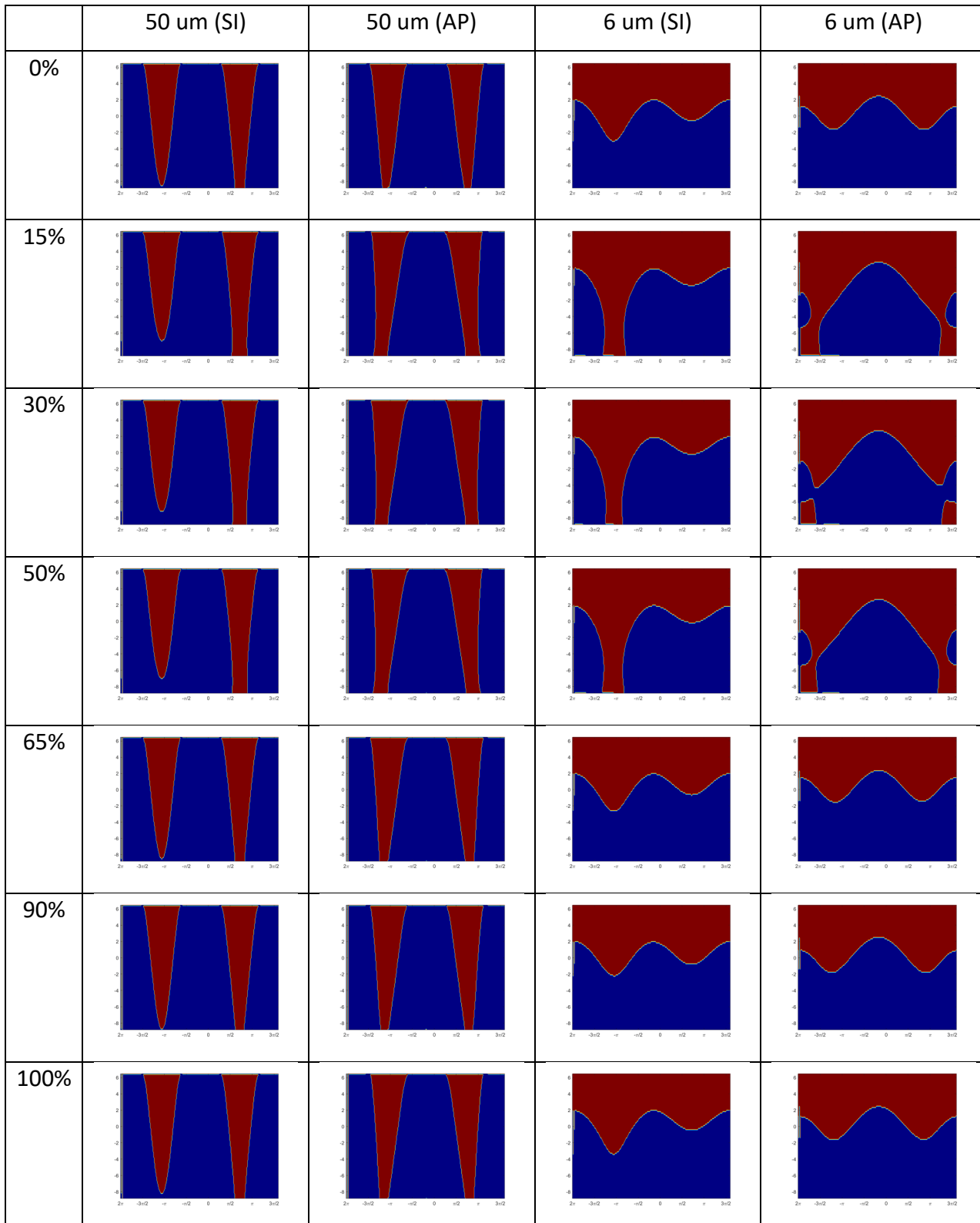
4.4 Discussion

3D models of a femoral head and different trunnion designs were developed to investigate the contact mechanics of tapers under a range of loading conditions. The present study was developed to provide insight into the possible mechanisms that generate the different types and magnitude of taper damage reported in retrieval and experimental studies. In this section, findings on the contact mechanics and micromotions on round and oval tapers are discussed.

4.4.1 Round tapers

Relative micromotions, taper separation and contact area at the taper interface through different forces and frictional moment profiles representative of different activities were examined. Observations from this investigation showed that the mechanical response between the trunnion and the bore can be affected by taper design as well as the type of activity. These findings can be associated with previous clinical and experimental studies.

In this study, taper clearance and assembly forces were shown to influence the magnitudes of the micromotions, where the taper clearance was the most significant design variable followed by assembly force. Increasing taper clearance resulted in an increase in the micromotions' magnitude; micromotions in round tapers ranged from 3 to 42 µm with the largest micromotions generated in a taper with a clearance of 0.18° assembled with a 4 kN force. Interestingly when the same taper was assembled with a 2 kN force, the maximum resultant micromotions generated in the taper interface was lower than 4 kN as the preloading phase allowed the trunnion to move significantly due to the poor initial taper fixation. The model results demonstrate that higher impact forces can reduce the micromotions magnitudes; the models have shown that the effect of impact assembly force on micromotions is more significant as taper clearance increase, which has not been previously reported.

Previous experimental and *in vitro* studies (Bitter et al., 2016; English et al., 2016; Fallahnezhad et al., 2017; Mroczkowski et al., 2006; Panagiotidou et al., 2017; Pennock et al., 2002) have highlighted the importance of the assembly force on the taper contact in order to reduce the micromotions magnitude generated at the taper interface thus reducing damage in the taper interface. Higher assembly forces reduce the risk of disrupting the passive surface layer by maximizing the local radial press-fit and thereby improving the initial taper connection stability reducing the reported clinical fretting corrosion rate. Assembly forces in combination with taper design parameters have previously been reported to have a role in taper connection stability (Mueller et al., 2021); results of the present study agree with this observation. Furthermore, results also showed that assembly forces affect the relationship between taper clearance and generated micromotions in the taper interface which has not been reported previously. Higher impact forces are required in taper clearances with a proximal engagement than in tapers with lower clearances in order to reduce the micromotions generated in the taper interface.

Previous FE studies (Bitter et al., 2019; English et al., 2016), have concluded that increased assembly forces result in lower relative motion magnitudes. However, one study has presented a contradicting finding showing that higher assembly forces increase the contact pressure in the bore-trunnion interface and have concluded that this thereby increases wear damage (Fallahnezhad et al., 2017). None of these FE studies include topographical features of the bore nor the trunnion suggesting that contact conditions and micromotions may not fully represent the mechanical performance of real tapers.

FE investigations have also studied the role of taper clearance, suggesting that the taper clearance plays an important role in the location and depth of wear damage as well as the extent of material loss (Bitter et al., 2019; Fallahnezhad et al., 2017). Micromotions and wear damage associated with fretting at the taper interface has been found to correlate with three key parameters, namely angular clearance, centre offset and body weight (Donaldson et al., 2014). Furthermore, in the same study, it has been suggested that an appropriate combination of small angular clearance and

centre offset may be sufficient to significantly reduce fretting at taper interfaces. Indeed the taper clearance has been found to play an important role in the integrity of the junction of the bore and the trunnion (Ashkanfar et al., 2017a; Dyrkacz et al., 2015). Observations with respect to the taper clearance in the current study agree with the role of taper clearance on the mechanical response of tapers when subjected to external loads. In the present study, when taper clearance increased, the contact between the bore and trunnion reduced, whilst micromotions and gap opening increased.

The nature of external loads can affect the micromotions generated at the taper interface. Raising the implanted leg has been identified to generate greater micromotions thus resulting in more wear damage (Fallahnezhad, Oskouei, et al., 2018). In the current study stairs up, as well as, jogging present similar maximum relative motions to walking, 40 and 42 µm, respectively and are significantly higher than sit-to-stand and cycling, that generated micromotions up to 8 and 3 µm, respectively. Taking a closer examination of jogging, walking and climbing stairs, these activities generate higher forces than sit-to-stand and cycling suggesting that the present results are driven by forces applied to the taper rather than joint angles alone.

Taper separation provides information about the likelihood of fluid ingress into the taper interface due to the separation between the bore and trunnion surfaces. Results of taper separation between the trunnion and femoral bore of round tapers of the present study are affected by taper parameters as well as the external forces and moments applied to the taper. The maximum taper separation can be usually located at the inferolateral part of the trunnion, and the range during the gait cycle varied with taper design and activity. In round tapers, the maximum taper separation ranged from 0 to 33.7 µm; for tapers assembled with a 4 kN load the separation increased with taper clearance. Stairs-up activity develop the largest taper separation up to 31.7 µm on a taper with 0.18° angle clearance. A previous study (Raji & Shelton, 2019), suggested that stairs-up activity would generate the largest taper separation (67 µm), suggesting that climbing stairs will increase the chances of fluid

ingress into the taper interface resulting in crevice corrosion. It has previously been reported than taper openings of 1 μm allow the ingress of cells (Gilbert, Sivan, et al., 2015). Even for round tapers with no angle clearance, assembled with a low assembly force of 2 kN, gaps were generated of 1.1 μm, which indicate that there would be risk of fluid ingress into the taper interface, reinforcing the importance of assembly impact force. Furthermore, tapers with taper clearances (0.06° and 0.18°) show taper separations greater than 5 μm, indicating that cell ingress would be possible.

Micromotions in the taper interface are the resultant vectors of different relative movements happening at the interface between the bore and trunnion at the same time. Movement normal to the taper surface provides information about the likelihood of fluid flow happening in the taper interface. Whereas tangential and pistoning movements may cause damage if they occur when the taper surfaces are in contact. In this study, the proportion of the relative motion components are found to be affected by taper geometry and load vector magnitude and direction within the load cycle, which would lead to different damage mechanisms occurring at the taper interface. For example, the reduced normal motion and larger pistoning proportion observed in lower taper clearances suggest that they are not only in risk of fretting damage but also to MACC due to the negligible normal motion. On the other hand, in larger taper clearances normal motions predominate in the relative motion vector, suggesting toggling at the taper interface triggering fluid ingress/egress and increasing corrosion susceptibility (Haschke et al., 2019). Despite stair climbing and jogging having similar relative motions to walking, the proportion of their components are different. Jogging presents larger pistoning motions than walking and stair climbing. Stairs-up activity produced the largest tangential motions in the tested activities. This finding can be associated with experimental observations, where stairs-up activities have been described as more detrimental to the taper interface than walking due to greater moments acting on the hip (Toh et al., 2023). The combination of moments and forces caused a circumferential motion along the trunnion's edge, where the largest distance of up to 249 μm, is observed during stairs up. The significant circumferential distance difference between stairs-up compared to the other activities can be explained by the distinctive moments on X and Y axes

(My and Mx), and forces in Z (Fz) during this activity. These observations indicate that patients' activities may define the type of taper damage.

4.4.2   Oval tapers

A 3D FE model of an oval trunnion and femoral head bore was developed to investigate the physical response of tapers with different ovality magnitudes and orientations, as well as taper clearances in order to provide insight into how they influence those relative motions associated with taper damage reported in retrieval and experimental studies. The mechanical response and contact parameters at the taper interface, namely micromotions, taper separation and contact area through a single walking cycle for different taper ovality magnitudes and orientations were analysed and associated with previous clinical and experimental studies. The main finding of the current study is that taper clearance combined with out-of-roundness ovality influences the relative micromotions at the taper interface, where tangential and pistoning motions have the greatest contribution in the resultant relative motions, indicating the likelihood of fretting wear. This finding also suggests that tapers with a larger clearance and oval surfaces generate a weaker taper interlock.

Previous parametric FE studies regarding tapers performance and design, have considered taper macro geometry parameters such as taper angle, length, and diameter with an idealised flat surface resulting in an ideal cone, although it has been shown that tapers are away from being ideal showing different roundness deviations of up to 6 µm (Falkenberg et al., 2019; Wade et al., 2020). ISO 2768-1:1989 allows a tolerance of up to 50 µm, resulting in highly oval tapers. In the current study, the out-of-roundness deviations in the taper interface as small as 6 µm influences the contact mechanics and micromotions generated at the taper interface. When the out-of-roundness orientation is considered, oval tapers oriented along the AP axis show larger micromotions than those oriented along the SI axis, due to the load vector during walking being perpendicular to the trunnion's out-of-roundness' major axis. Furthermore, toggling in the oval tapers was exacerbated when ovality orientation was in the AP direction due to the load direction being perpendicular to the ovality. This observation confirms a previously reported finding that oval tapers along the AP

axis generate larger wear rates in comparison to those oriented along the SI axis due to larger relative motions in the taper interface (Bitter et al., 2018). Fretting corrosion is likely to occur when surfaces at the taper interface experience relative motions ranging from 5 to 12 µm (Mali, 2016; Mali & Gilbert, 2015). Observations in the current study suggest that oval tapers, regardless of the assembly force and clearance angle, are at risk of developing fretting corrosion damage, as indicated by the increase in tangential and pistoning relative motions. Furthermore, the magnitude of these potential damaging relative motions increases with the extent of out-of-roundness. Taper separation for oval tapers is also influenced by the extent of the ovality and has a more significant effect when ovality orientation is considered; a taper with an ovality of 50 µm is predicted to develop the largest taper separation magnitudes. However, a 50 µm oval taper with the long axis positioned along the SI axis exhibits a range of 0.8 µm (47.7 to 48.5) separation over a walking cycle, Table 4.9, suggesting that this taper exhibits little relative movement increasing the risk of fluid stagnation, which would lead to a more aggressive corrosion environment (Gilbert, 2012; Gilbert, Mali, et al., 2015).

4.5 Limitations

The current study has a number of limitations that are recognised; the most significant being the lack of surface features that influence the contact conditions after assembly thus affecting the predicted values of contact area, micromotion and contact pressure. It is well known that commercially available trunnion and bore tapers exhibit different surface topographies (Lundberg et al., 2015; Munir et al., 2015; Royhman et al., 2021), that undergo plastic deformation changes on their surface topography after assembly. The current study, along with the previously published models, has not generated plasticity at any stage, even during assembly, despite plasticity having been reported from experimental findings (Gustafson et al., 2022; Lundberg et al., 2015). The relative motions may therefore be underpredicted due to larger contact areas and lower contact stress at the taper interface generated due to the ideal cone surface used to generate the current model. Due to the simplification of the surface, a wear model was not included in the present study, so

the evolution and impact of those micromotions that can cause wear damage, namely pistoning and tangential motions, has also not been studied. Micromotions at an asperity level, where plasticity and fatigue damage leading to wear are likely to occur, were not investigated and adaptive FE meshes were not implemented, as the surface roughness has not been modelled, preventing the study of wear, and the true effect and evolution of pistoning and tangential relative motions on the taper surface. The influence of chemical corrosion, which would affect material removal and subsequently change these output parameters was considered as variables including taper contact stress, and electrochemical processes associated with surface features on the tapers, would need to be considered for a useful approximation of damage.

4.6   Conclusions

The present findings involving accumulated micromotions of contact nodes in the taper interface during different activities suggests that the distal end of the taper is at greater risk of wear damage due to the combination larger relative motions and contact between taper surfaces. Taking into consideration the different contact areas determined by taper design and ovality suggests that wear damage location may be influenced by these factors.

The present study has shown that geometrical variations of the trunnion significantly affect the contact conditions in the taper interface resulting in increased micromotion magnitudes and taper separation. Similar to previous studies, when taper clearance and assembly force are considered, relative motions increase as they affect the interlock strength generated during assembly. The increased taper separation generated in oval tapers may facilitate the ingress and egress of fluid into the taper interface. Also, orientation of ovality plays a role in the micromotion generation, as if the ovality is oriented on the same direction of the resultant external force micromotions are considerable reduced, though this can lead to fluid stagnation in the taper interface. Furthermore, during walking, stair climbing and jogging the taper interface can simulate a pump-like action that is a function of taper

separation and contact area; this movement may allow fluid ingress and egress both into and away from the taper interface.

5   Surface topography study: Finite element model development, analysis and validation

5.1   Introduction

Micromotions at the taper interface are influenced by multiple factors. Retrieval studies have investigated the main taper design parameters that can affect the generation of micromotion, including the design parameters, manufacturing tolerances as well as pre and post-assembly conditions, namely taper length, taper angle, femoral head size, material combination, surface finish, patient biometrics, surface finish, and implantation time with the extent and location of corrosion damage (Goldberg & Gilbert, 2003; Hothi et al., 2015, 2017; Kocagöz et al., 2013; Nassif et al., 2014; Pourzal et al., 2018; Tan et al., 2015). These studies have established that THR devices using larger femoral heads as typically have been found in metal-on-metal bearings, along with the use of high taper clearance and longer tapers, assembled with a lower assembly force and are more likely to fail due to trunnionosis. However, the role of the taper surfaces on fretting and corrosion processes has not previously been widely investigated. The issues associated with taper surface topography on reducing the rate of trunnionosis, has produced contradictory conclusions. Retrieval studies of commercially available tapers have found a significant variation in both of trunnion and bore surfaces between manufacturers, in both geometry and surface finish (Mueller et al., 2017; Munir et al., 2015; Pourzal et al., 2016; Whittaker et al., 2017); such differences have been found even in tapers with the same nominal taper design (Mueller et al., 2017). Manufacturing methods that are utilised to produce trunnion and bore components can differ between manufacturers resulting in deviations and designs in shape and surface topology. Table 5.1 presents studies that have reported changes due to manufacturing effects.

Table 5.1. Retrieval studies that have described deviations in taper components.

Reference	Finding	Deviation dimension
(Wade et al., 2020)	Oval trunnion	Major axis 12 µm
(Wade et al., 2020)	Barrelling in female bore	Barrelling height 2 µm
(Walton et al., 2019)	Barrelling in female bore	No information
(Racasan et al., 2015a)	Barrelling in female bore	No information
(Dransfield et al., 2021)	Barrelling in female bore	No information

Surfaces of bore and trunnions are classified into two groups namely, rough and smooth, depending on their roughness parameters Ra and Rz. Taper surfaces are described as rough if their topographical roughness (Ra) parameter is greater than 2 µm and Rz is greater than 5 µm, and smooth if their Ra and Rz values are below these values. Most rough trunnions surfaces have a characteristic threaded surface comprised of microgrooves of around 11 -30 µm height with a spacing of 150 and 300 µm that can be observed by the naked eye (Hall et al., 2018; Lundberg et al., 2015; Whittaker et al., 2017). Microgrooved trunnions were developed to reduce the contact stresses at the taper interface for coupling with ceramic heads; however, these trunnions are also now widely coupled with metal heads. The implications of using threaded surfaces in metal-to-metal taper interfaces requires further investigation. Experimental (Witt et al., 2015) and observational (Pourzal et al., 2016) studies on the contact conditions and taper topography have shown that rough tapers undergo plastic deformation, and that contact conditions are different from smooth tapers (Arnholt et al., 2017; Ashkanfar et al., 2017b). The most recent FE models (Bechstedt et al., 2020; Gustafson et al., 2020a, 2022) studied the contact mechanics when threaded and smooth taper surfaces are in contact using a single sinusoidal wave function to simulate a rough taper surface. These models have predicted that the magnitude of plastic strains in microgrooved peaks of the trunnion surface are similar to those obtained experimentally (Godoy et al., 2022). However, the trunnion and bore surfaces are conformed by a set of topographic different peak sizes and scales that results in a non-homogenous contact of the trunnion with the bore surface (Witt et al., 2015), namely form, waviness and roughness as illustrated in Figure 5.1 and are different from a single sinusoidal wave. The purpose of this

study is to investigate if idealised taper surfaces can predict the taper contact mechanics by studying the effect of topographic features at both macro and micro scales.
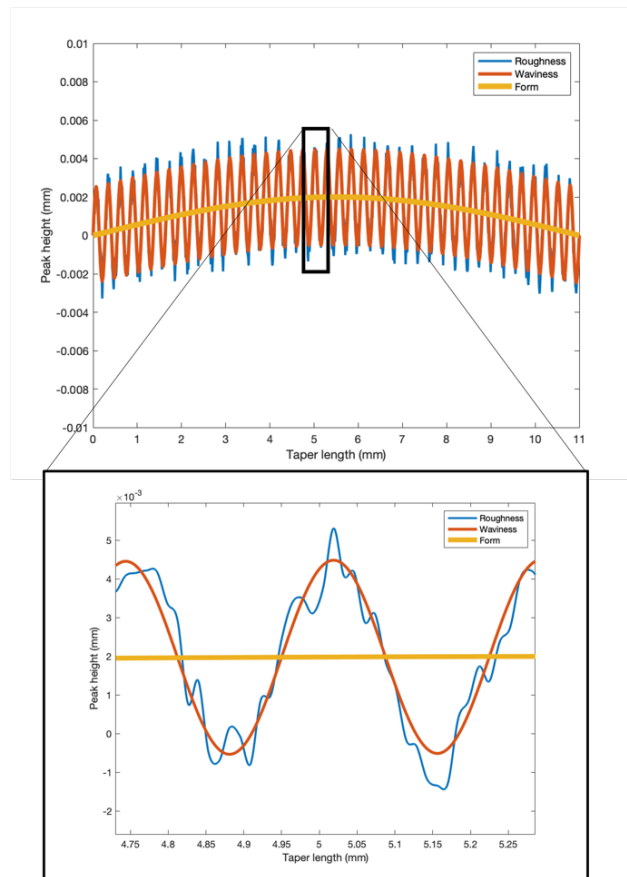
Figure 5.1. Schematic showing form, waviness, and roughness regions in a surface of a taper at low and high magnification.

For this purpose, surfaces of five trunnions and three femoral head bores were characterised, and roughness parameters were measured. Using the obtained surfaces of these taper components, FE models were developed to study the macro and micro surface taper regions. In the first study, the macro surface study, features that include surface form of the taper are investigated. Form variations at the bore surface are usually seen as a surface with a concave shape as shown by the yellow line in Figure 5.1 (Cartner et al., 2017; Racasan et al., 2015b; Wade et al., 2020). The second study, the micro topography surface study, investigates the effect features at the micro scale in tapers, namely waviness and roughness as shown by the orange

and blue lines respectively, of both trunnion and bore surfaces on the contact mechanics.

The aim of this study is to test the hypothesis that taper surfaces can be simulated as flat lines, for smooth tapers, and single sinusoidal functions, for rough tapers, when investigating the contact mechanics within the taper interface. The research questions to be investigated include whether:

- Surface form has an effect on the overall taper contact mechanics.
- Sine waves can appropriately simulate features found on manufactured, rough trunnion surfaces.
- The surface topography is the same in nominally similar trunnions
- The peak contact mechanics in sinusoidal waves are similar to measured profiles.
- Surface variations at different scales should be considered when modelling taper interfaces.

The study of the macro features of the taper topography, namely the form, will cover the first research question and part of the last question. Investigations about the features at the micro scale of the taper surface components will address the remaining questions.

5.2 Materials and methods

5.2.1 Surface characterisation and roughness parameters

12/14 taper components, including five Ti6Al4V trunnions (four from measured data where three were obtained from (Witt et al., 2015) and the one obtained by the author of this thesis, and one simulated with a sinusoidal function) and three CoCrMo femoral head surfaces (two surfaces measured by the author of this thesis, one simulated with a single line) were characterised, and roughness parameters namely, Ra, Rz, Power Spectrum Density (PSD) and peak height variation before assembly, were determined.

The surface profiles of the idealised trunnion and one bore were created utilising a sinusoidal wave and line functions, respectively. Sinusoidal waves were created taking into consideration the median wavelength and peak-height of commercially available trunnions for the function´s frequency and amplitude (Gustafson et al., 2020a, 2022; Pourzal et al., 2018).

Trunnion surface profiles of three trunnions (Trunnions 1 – 3) were obtained from a previous experimental study. Surface profiles of the remaining trunnion (4) and two bores (1 and 2) (Figure 5.2a) were measured using a contact profilometer (Dektak system (Figure 5.2b), 0.1 nm vertical resolution, 12.5 µm radius tip). For the femoral head bore surfaces, the femoral heads were cut in half while taking care to not damage the bore surfaces. Before measuring the surfaces, they were thoroughly cleaned using industrial wipes and ethanol. A pressure-sensitive putty adhesive was used to attach taper components onto the base of the profilometer to prevent motion during surface measurement. The surfaces were aligned with the probe's axis and the taper's central axis camera interface. A stylus force of 9 mg was used as recommended (DektakXT user manual) for hard-metal surfaces.

Figure 5.2. (a) Femoral stem and femoral heads used to characterise taper roughness. (b) Measuring the trunnion surface using Bruker DetaktXT contact profilometer.

5.2.2 Measurement accuracy and precision

Measurements were taken along the entire length of trunnions and bores. Vertical measurement resolution was set to 0.47 µm by changing the time needed to measure the length, this resolution generated approximately 23,128 data points for an 11.5 mm length. Representative surface profiles for Bore 1, Bore 2 and Trunnion 4 were determined by comparing the surface profiles at anterior and posterior sides of the component (Figure 5.3 and 5.4) making sure that peak heights and wavelengths were similar.
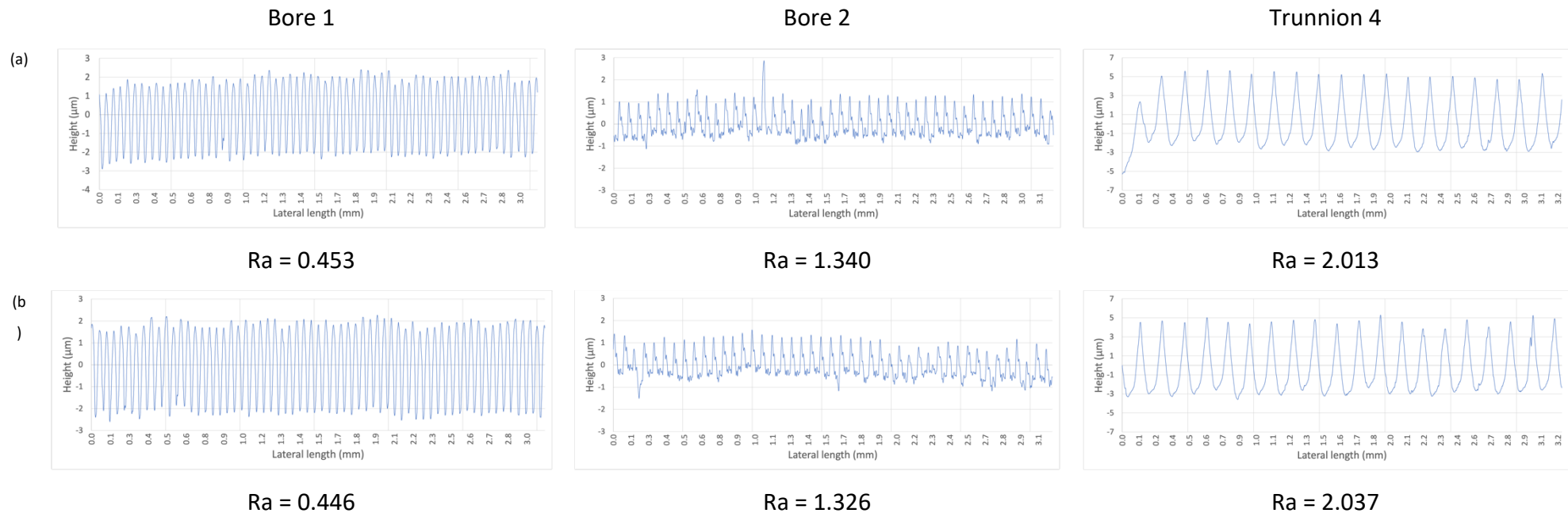
Figure 5.3. Three mm sections of bore 1, bore 2 and trunnion 4 surface profiles at (a) lateral posterior and (b) lateral anterior surfaces.

Bore 1 — Ra = 0.453

Bore 2 — Ra = 1.340

Trunnion 4 — Ra = 2.013

Bore 1 — Ra = 0.446

Bore 2 — Ra = 1.326

Trunnion 4 — Ra = 2.037
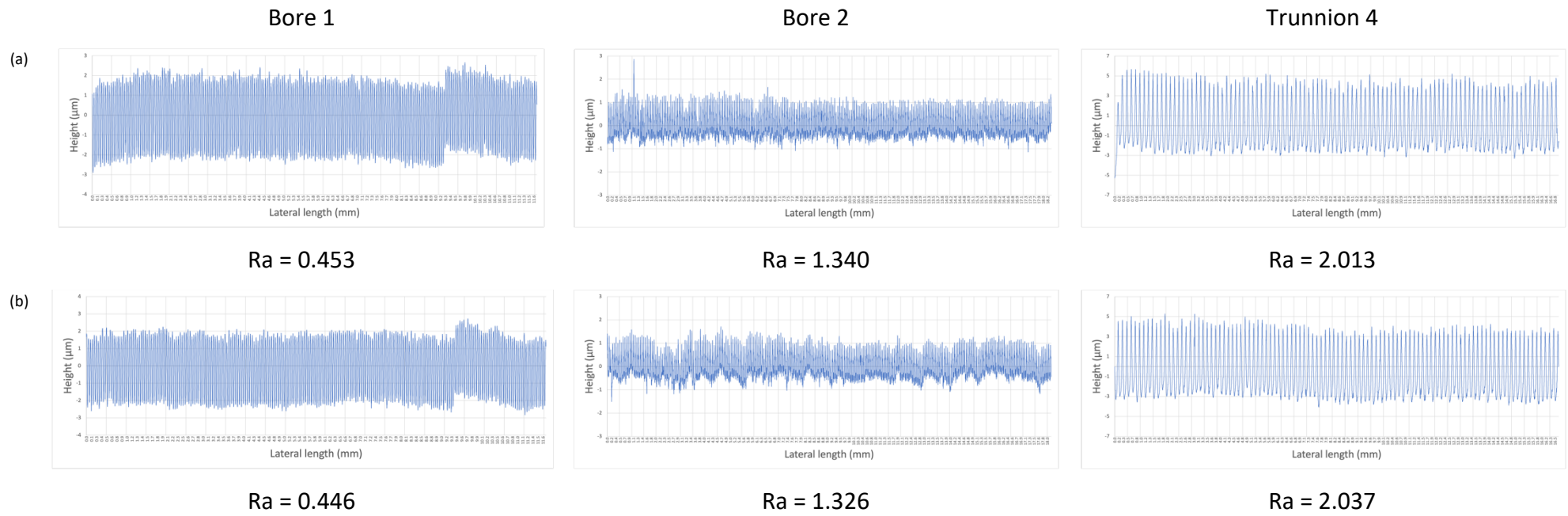
Figure 5.4. Full component length sections of bore 1, bore 2 and trunnion 4 surface profiles at (a) lateral posterior and (b) lateral anterior surfaces.

Measurement accuracy was evaluated by repeating the surface measurement on the same surface location up to 4 times. The highest deviation along each of the surfaces was of 0.689 nm. Form and taper angles were removed from all the experimentally derived taper components' roughness profiles, before using in the FE models.

5.2.3 Roughness analysis

Surface roughness analysis of the trunnions surfaces was performed using a standardised metrology software (MountainsMap 9). Amplitude roughness parameters, Ra, Rz, peak height variation, and frequency roughness parameters, Power Spectrum Density (PSD), were determined from the trunnion and bore profiles.

5.2.4 Finite element model

5.2.4.1.1 Model geometries

Due to the relatively small features making up the taper surfaces, in order to reduce the complexity of the FE model, axisymmetric 2-dimensional geometries were considered for both the macro and micro scale studies.

5.2.4.2 Loading conditions

Loading conditions simulated the assembly of a femoral head into a trunnion following the experimental work performed by Witt et al (Witt et al., 2015). The bespoke experimental setup assembles the femoral head into the trunnion by applying a displacement of 0.04 mm s^{-1} as suggested by ISO 7206-10 to determine compressive or disassembly loads required to cause failure of modular head systems. To simulate the experimental loading conditions the outer surface of the femoral head is coupled to a reference point (RP-1) at the centre of the femoral head as presented in Figure 5.5. This reference point, thus the outer surface of the femoral head as well, is only allowed to move in the direction of the trunnion axis. The base of the trunnion is constrained such that it does not translate nor rotate in any direction. Reaction forces parallel to the applied displacement orientation were obtained from nodes at the base of trunnion (Red striped line). Contact conditions

between the bore and trunnion were analysed when the sum of the reaction forces at the base of the trunnion reached 0.5, 2 and 4 kN.
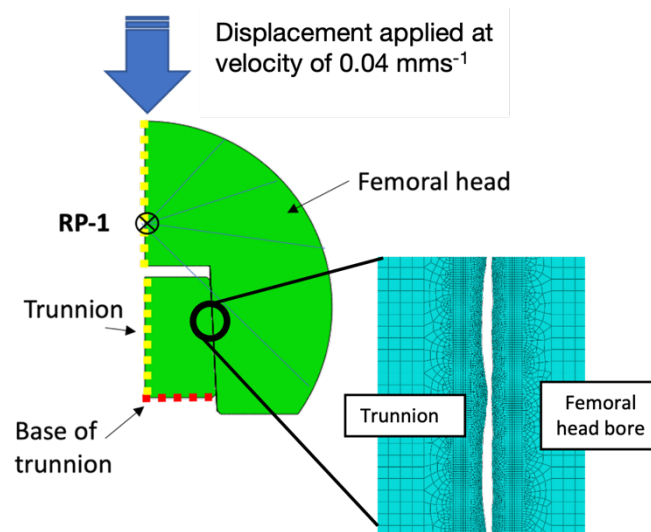
Figure 5.5. Schematic of an axisymmetric 2D geometries of a femoral head and trunnion, boundary and loading conditions.

5.2.4.3   Material properties

Material properties, as described in Chapter 3, associated with a Ti6Al4V alloy were assigned to the trunnion and CoCrMo alloy to the femoral head.

5.2.4.4   General boundary conditions

Contact between the bore and the trunnion was modelled using a surface-to-surface discretisation with a finite sliding formulation and a contact interaction with a penalty method using a coefficient of friction of 0.21. Models were created, assembled, and meshed in Abaqus CAE Standard 2020 using four-node linear hexahedral (CAX4) elements.

5.2.5   Macro surface study

5.2.5.1   FE model geometries

FE models of Ti6Al4V trunnion/CoCrMo bore pairs were developed that include five taper clearances (-0.18, -0.07, 0, 0.07, 0.18°) and four barrelling surface heights (0 (flat), 0.1, 0.2, 0.4 μm) were considered, Figure 5.6. These models only considered

the form surface, without including the surface waviness and roughness when creating the trunnion and bore surfaces.
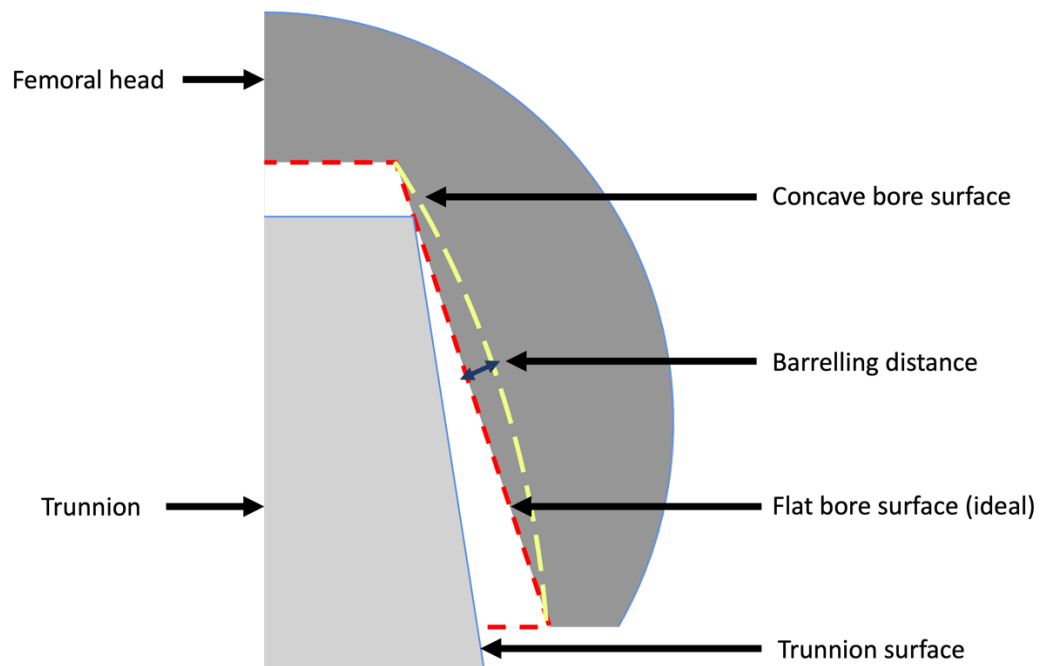
Figure 5.6. Schematic of a trunnion assembled into a femoral head. Dashed lines represent flat (red) and concave (yellow) bore surfaces.

5.2.5.2   Specific boundary conditions

FE model simulations were developed and carried out using Abaqus/Standard and "NLGEOM" nonlinear geometry options were used.

5.2.5.3   Mesh density analysis

The macro surface study mesh analysis was performed on tapers comprising of a flat bore and trunnion surface. The model used to study the macro features did not reach plastic deformation, so von Mises stress was considered instead for this analysis. A mesh density analysis was performed using 4 different element sizes of 100, 50, 10 and 1 μm. The model showed convergence at an element size of 10 μm. 1 μm element size generated a 10.3% difference in von Mises stress and 0.46% for contact pressure while the number of elements difference was approximately 57 times greater as shown in Figure 5.7.

112

(a)

(b)
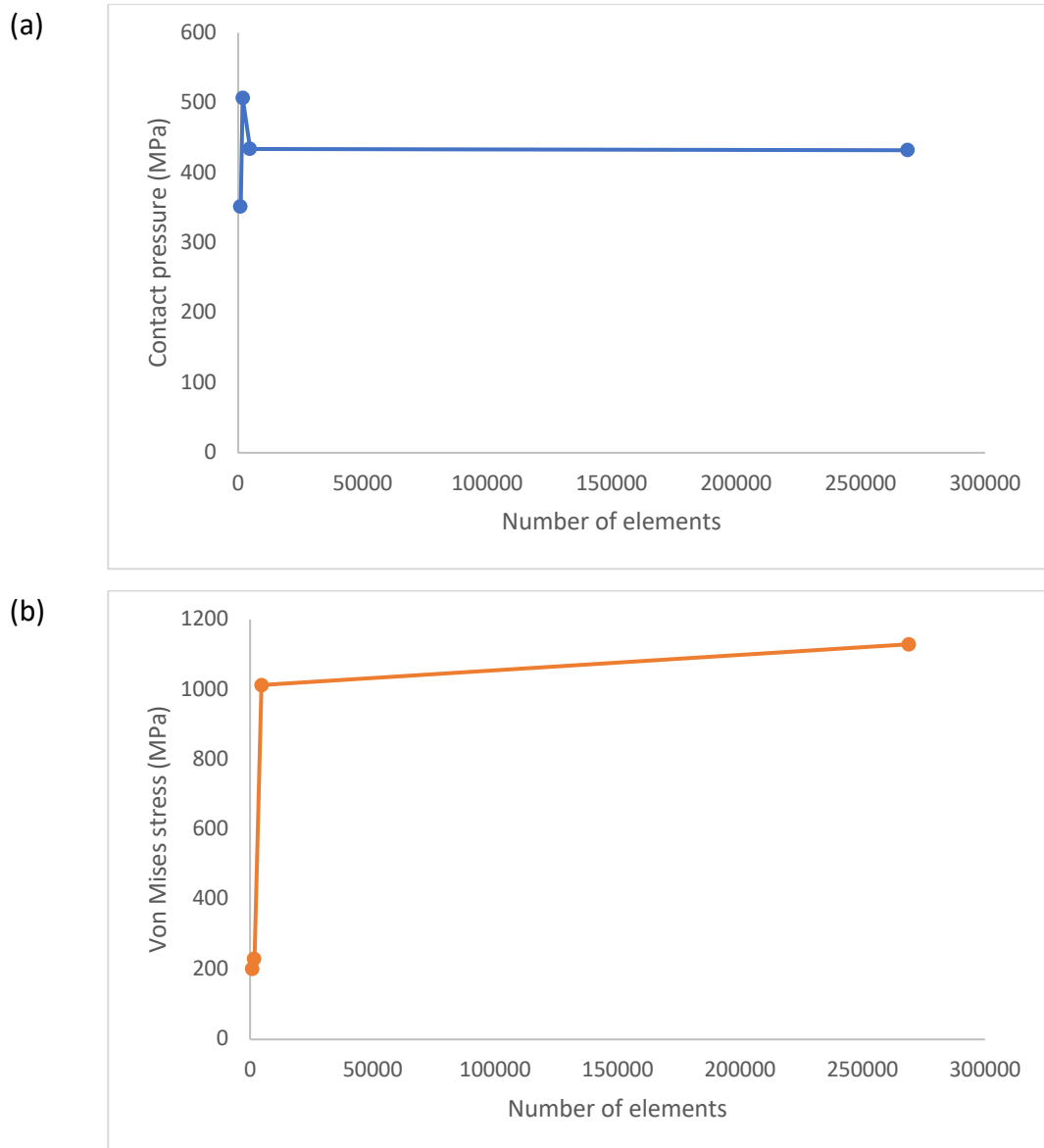
Figure 5.7. Mesh sensitivity analysis for macro topography features study. (a) Contact pressure and (b) von Mises stress converge at an element size of 10 μm.

5.2.5.4   Model validation

Figure 5.8 shows a relationship between the % length of the taper in contact as a function of the taper clearance after assembly at 4 kN. The resulting relationship of the predicted contact length and taper clearance is similar to those reported in a previous *in silico* study (Raji & Shelton, 2019). The results show a 1% difference at a taper clearance of -0.07°, whilst at +0.07° the difference was estimated to be 8%. At larger clearances the differences were estimated to be 5% and 7% for -0.18 ° and +0.18 ° respectively. Differences in the extent of the predicted contact regions from these studies may be due to simulated assembly conditions and different taper

designs considered such as taper diameter. However, with a mean difference of approximately 5%, the model was validated.
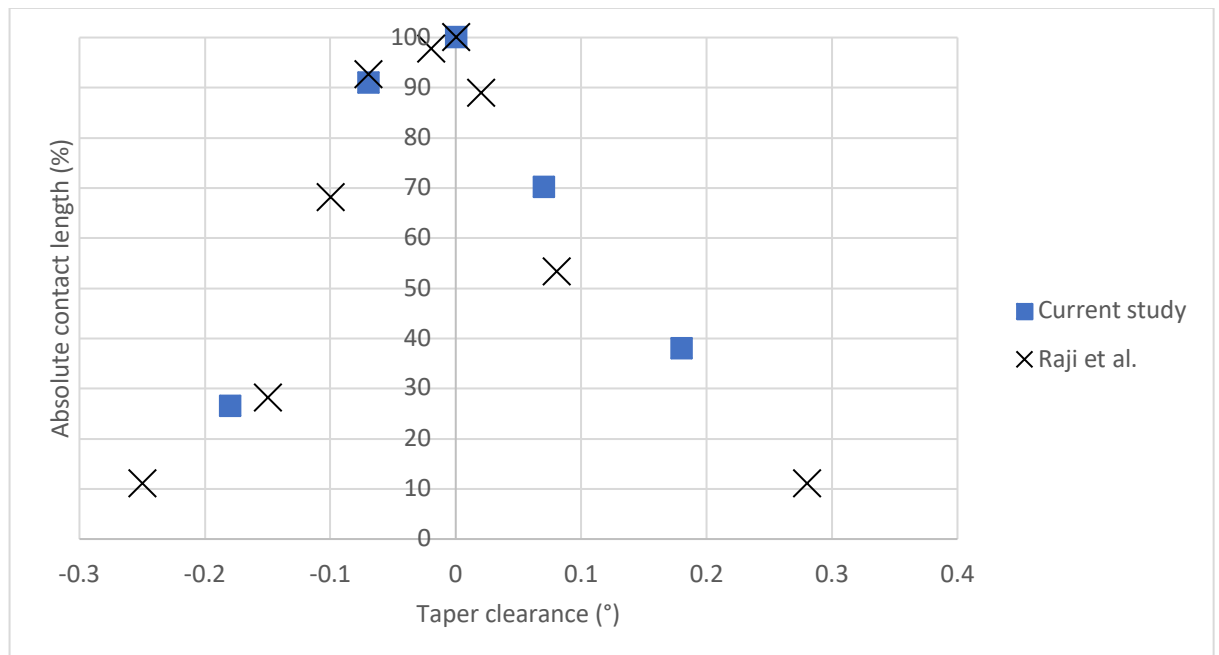
Figure 5.8. Predicted relationship between absolute contact length and taper clearance in this study and Raji et al., 2019.

5.2.6   Micro features surface study

5.2.6.1   FE model geometries

Six axisymmetric FE models of a taper junction involving the femoral head bores and trunnions were generated. Table 5.2 shows how the trunnion and femoral head bores coupled. The taper angles of all trunnions were 5.67° and were matched with bore tapers with the same angle, resulting in taper components with very small clearance angles. The entire trunnion surface seated within the femoral head bore. To create the surface of the trunnion and bore, peak height data points of the measured profile surfaces were used. Trunnion surfaces were created from four trunnion roughness profiles measured before assembly and one using a sinusoidal function.

Table 5.2. Taper bore, trunnion and clearance angles.

	Clearance (°)	Trunnion	Bore
Taper 1	-0.01	1 (Witt et al.)	3 (Flat)
Taper 2	0.0	1 (Witt et al.)	3 (Flat)
Taper 3	0.0	1 (Witt et al.)	3 (Flat)
Taper 4	0.0	4 (Measured)	1 (Measured)
Taper 5	-0.01	1	2 (Measured)
Taper 6	-0.01	5 (Sine wave)	3

Bore surfaces were created using 2 bore roughness profiles and one flat surface. Trunnions 1, 2, 3, and 5 had a taper length of 11 mm, trunnion 4 had a length of 17 mm. The profile surface trunnion data had the component´s taper angle removed; accordingly, a MATLAB script was developed to rotate the surface data into the trunnion angle orientation. Coordinate data was imported into Abaqus using a Python 2.7 script where the axisymmetric 2D model was generated. The trunnion surface was generated by 'stitching' coordinate data points with a spline function generating peaks within the roughness and waviness regions. In this cohort, trunnions were assembled with a bore modelled with flat surface representing a smooth taper surface. The bores for tapers 4 and 5 were characterised experimentally and were matched with appropriate trunnions. Taper 6 used a sinusoidal wave for the trunnion and a flat surface for the bore.

5.2.6.2 Specific boundary and contact conditions

In order to overcome excessive distortion of mesh elements due to the detailed roughness profiles considered, Arbitrary Lagrangian-Eulerian (ALE) mesh formulation was applied on the trunnion section where surface roughness was considered. For tapers 4 and 5, in order to reduce computational power in their corresponding FE models the femoral head was defined as a rigid body. Furthermore, taper 5 FE model simulation was developed using Abaqus/Explicit due to the large plastic deformation occurring in the trunnion's surface. In explicit FE models, increments time steps are determined by the mesh size and density, therefore the time increments for taper 5 model are in the scale of $1x10^{-35}$. The experimental setup of the assembly of the taper

is considered static, meaning that it takes place relatively slowly and that inertia can be ignored. Solving the model considering this, would take a more than 20 million steps increasing errors and computing time. Therefore, in order to reduce computing time, time increments can be increased by artificially increasing the mass of the model (mass scaling) and the load rate increased to reduce the simulation length. However, the energy ratio of internal and kinetic energy must be no more of 0.1 throughout the simulation to be considered static when using Abaqus/Explicit. A time increment of 5 x10^{-7}and a load rate of 1 mm/s resulted in the kinetic energy being than 5% of the internal energy throughout the simulation as shown in Figure 5.9.
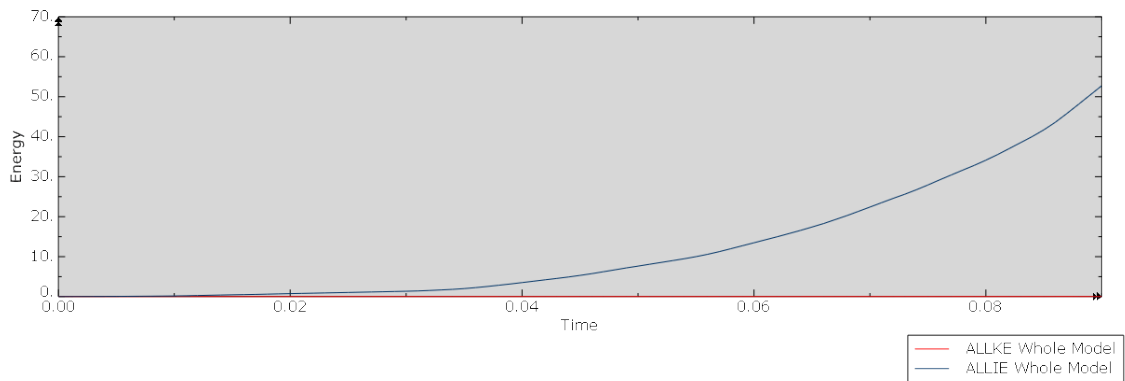
Figure 5.9. Internal energy (Blue) and kinetic energy (red) of taper 5 using Abaqus/Explicit.

5.2.6.3 Mesh density analysis

Contact pressure, and plastic strain (PEEQ parameter in Abaqus) were analysed at an assembly reaction force equivalent to 4 kN for 4 element sizes (1.25, 0.75, 0.5 and 0.25 μm). Mesh sensitivity analysis was performed in taper 1 as the topography surface of this trunnion presented the largest number of dominant spatial frequencies generating smaller peaks compared to the other trunnions in this study. Figure 5.10 shows the change of contact pressure and plastic strain in the trunnion surface as the element size increases. This model showed convergence at an element size of 0.5 μm. During the assembly step, peaks in the roughness region of the trunnion surface where the amplitude was larger than the wavelength at the top of

the microgroove peak stopped the model converging during the first increments of the assembly step due to large deformations. Therefore, the element size within these peaks were manually reduced to 0.1 μm. Taper1, presented 2 such occurrences, whilst taper 2 and 3, had just 3 such occurrences. There were approximately 1.1 million elements for each femoral head and trunnion combination model in the micro topography features study.

(a)

(b)
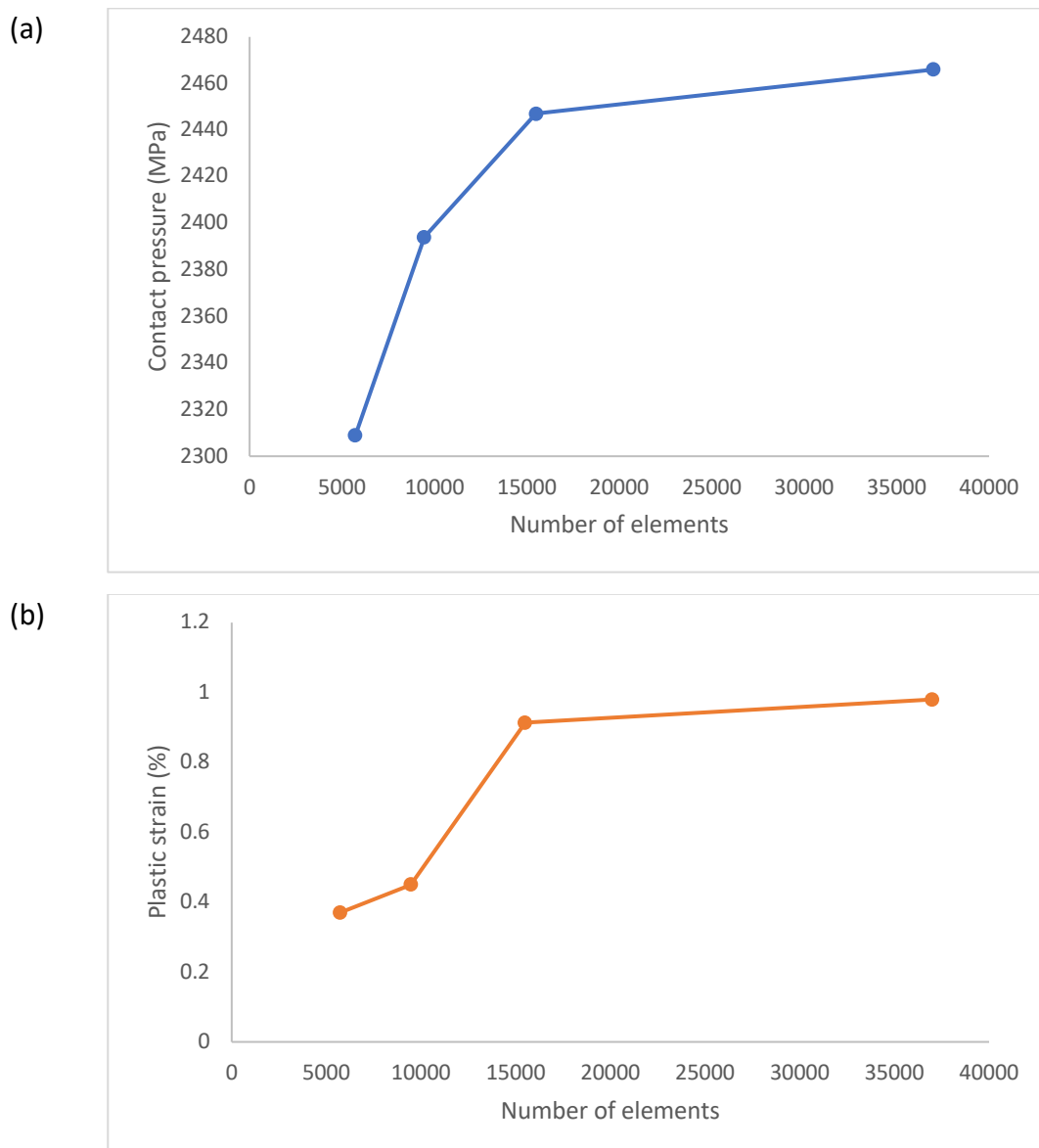
Figure 5.10. Mesh sensitivity analysis for micro topography features study. (a) Contact pressure and (b) plastic strain converge at an element size of 0.5 μm.

5.2.6.4 Model validation

Results were validated by comparing the predicted percentage of microgrooved peaks in contact with the bore surface at assembly reaction forces of 0.5, 2, 4 and 6 kN against experimental data of the same surfaces experimentally assembled for tapers 1, 2 and 3. The FE model and experimental contact data for tapers 1, 2 and 3 were similar as shown in Figure 5.11; approximately 20% of microgrooved peaks were in contact at 500 N increasing for FE the models and experiment to approximately 65% at 2 kN and 80% and 90% respectively, at 4 kN. Differences between the FE models and experimental results may occur due to surface variations on the bore surface used experimentally and variations in the orientation of the bore and the trunnion present experimentally during assembly/disassembly which are not considered in the FE model. These results validate that the contact conditions at the taper interface can be predicted using the current FE model.
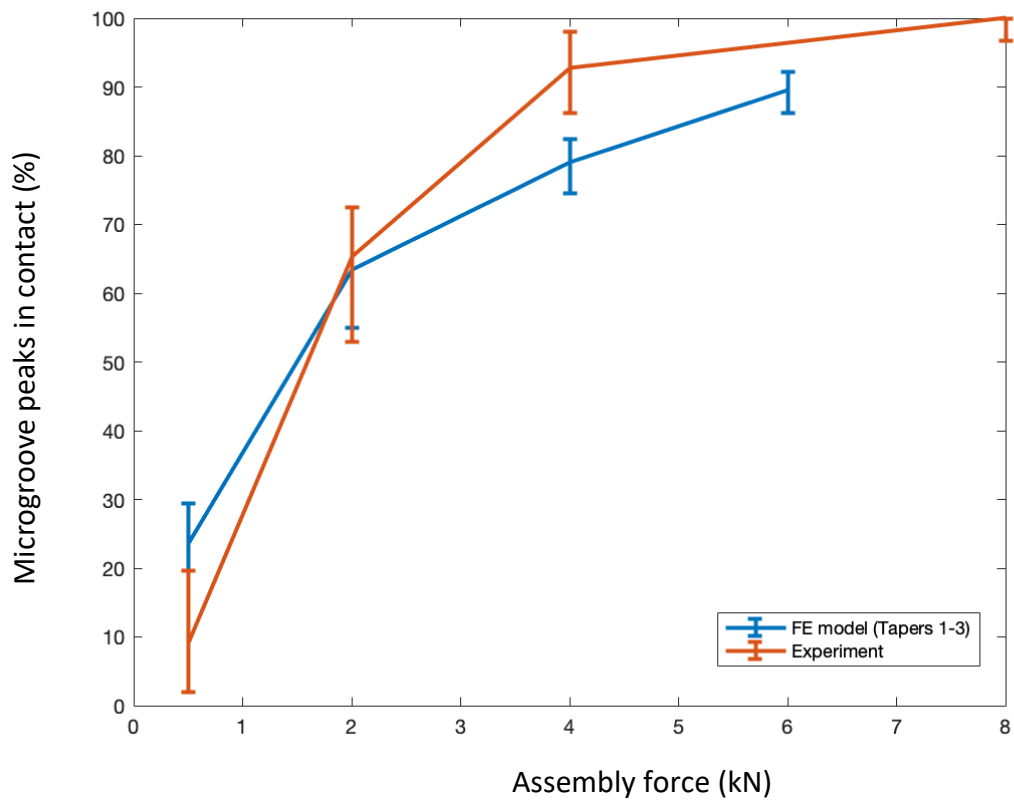
Figure 5.11. Mean percentage of number of microgroove peaks in contact in the taper interface obtained experimentally (orange) and predicted from FE models of the measured surfaces used experimentally before assembly (blue). Error bars indicate the range of values obtained experimentally and computationally for all tested subjects at each assembly force.

5.3   Results

5.3.1   Study of macro features in the taper surface topography
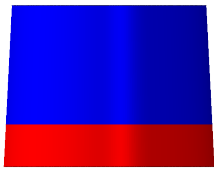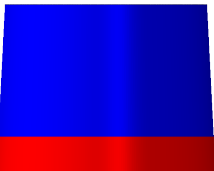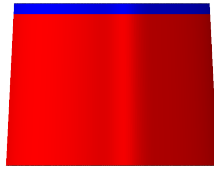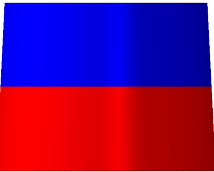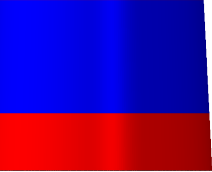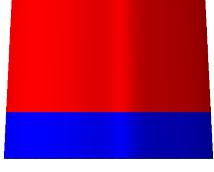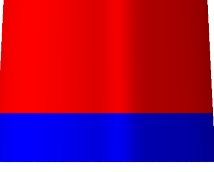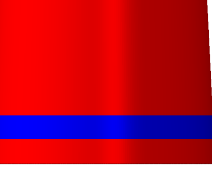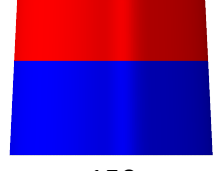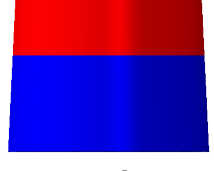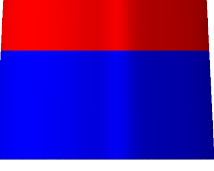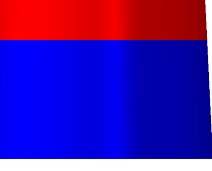
Predicted maximum contact pressures and contact areas magnitudes and regions determined from the FE models of the surface form study are presented in Tables 5.2 and 5.3 respectively. Taper clearance determined the extent and location of contacting regions between the bore and trunnion. When introducing a barrelling form on the bore surface, the contact area in the taper interface was slightly affected. Increasing the height of the concave bore surface, increased the maximum contact pressure generated in the taper interface, and reduced the extent of the contact area between the bore and trunnion (Table 5.3 and Figure 5.11).

Table 5.3. Maximum contact pressure (MPa) at the taper interface at 4 kN for different barrelling heights.

		Barrelling height (µm)			
		0	0.1	0.2	0.4
Clearance angle (°)	-0.18	2545	2693	2897	2531
	-0.07	1941	2789	2482	3105
	0	1050	1712	1787	2055
	0.07	1680	2029	2783	2743
	0.18	2579	3318	3587	3044

The contact regions in the taper interface for each taper clearance were greatly affected by the barrelling-surface height in the bore as shown in Table 5.3. Negative clearance angles generated a contact at the distal end of the taper interface, whilst positive angles generated contact at the proximal end of the taper. The effect of barrelling in bore surfaces on the extent of the contact area in the taper interface is clearly seen in Table 5.4. This effect was more pronounced in taper clearances of 0.07 ° and -0.07 °, than those with higher taper clearances.

Table 5.4. Contact regions 3D representations and contact area (mm^2) at the taper interface at 4 kN for different barrelling heights. Where red indicates contact between the bore and the trunnion, and blue no contact.

		Barrelling height (µm)			
		0	0.1	0.2	0.4
Clearance angle (°)	-0.18	105	95	86	71
	-0.07	360	229	202	138
	0	395	395	395	395
	0.07	277	277	278	285
	0.18	150	143	132	117
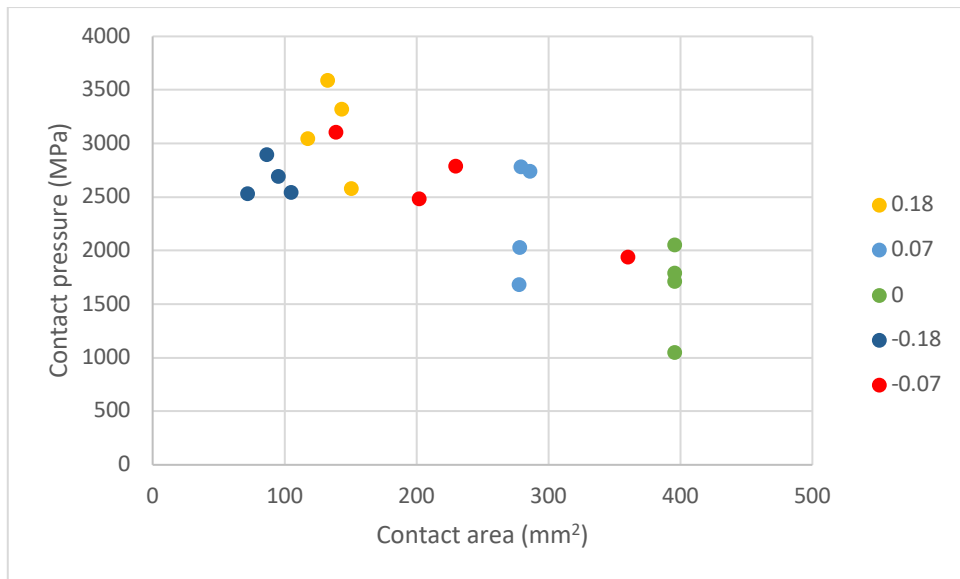
Figure 5.12. Relationship between contact area and maximum pressure for a range of taper clearance angles with a concave bore surface of 0, 0.1, 0.2, 0.4 µm.

The relationship between contact area and contact pressure is shown in Figure 5.12 for all the taper clearances and barrelling heights tested. This demonstrates the sensitivity of the -0.07° clearance taper to the effective of very small non-linearity in the taper form.

5.3.2 Study of micro features in the taper surface topography

5.3.2.1 Surface analysis

Surface profiles, PSD and peak-height distributions are presented in Figure 5.13. Ra and Rz roughness parameters, and spatial frequencies magnitudes for measured and idealised bore and trunnion surfaces are shown in Table 5.4. All of the tested bore and trunnion surfaces generated Ra and Rz parameters representative of smooth (Ra <=2.0 µm; Rz <=5.0 µm) and rough (Ra >2.0 µm; Rz >5.0 µm) taper surfaces, respectively. The trunnions exhibited mean values for Ra of 3.036 µm and Rz of 12.992 µm, while the bore group generated lower mean values of 0.883 µm and 3.363 µm, excluding bore 1 as it was flat.

Estimated PSD (Figure 5.13b and Table 5.5, spatial frequencies) values for trunnion and bores surfaces showed that these surfaces are conformed by a number of superimposed waves of different frequencies and amplitudes. Analysing the number

of dominant spatial frequencies (X axis in Figure 5.13b), trunnions exhibited up to seven dominant frequencies ranging from 15 to 259 μm, while bore surfaces exhibited up to two dominant wavelengths ranging from 30 to 6 μm. No association between the number of spatial frequencies in the trunnion and bore surfaces and manufacturer was observed. Trunnions from the same manufacturer (Trunnions 1, 2 and 3), presented different numbers of dominant spatial frequencies, trunnions 1 and 3 comprised of seven frequencies, whilst trunnion 2 comprised of only 5 frequencies. These three trunnions with a similar Ra and Rz of approximately 3.30 and 15.5 μm, presented their largest dominant spatial frequency of 3.86 mm^{-1} equivalent to a wavelength of the microgrooves of 259 μm. In contrast Trunnion 4, which was less rough with an Ra of 2.037 μm, showed an elevated dominant spatial frequency of 6.49 mm^{-1}, generating shorter and smoother microgroove peaks separated by approximately 154 μm and presented only three frequencies. Trunnion 5 was designed to exhibit similar roughness parameters (Ra, Rz) to trunnions 1, 2 and 3; nonetheless a single spatial frequency was present, contrasting with the multiple frequencies found in real surfaces. The bore surfaces measured in this study despite representing Ra and Rz values of smooth surfaces, showed different Ra values where bore 2 was smoother than bore 3. In both bore surfaces, the spatial frequency following the largest dominant frequency was approximately half the magnitude of the most dominant frequency.
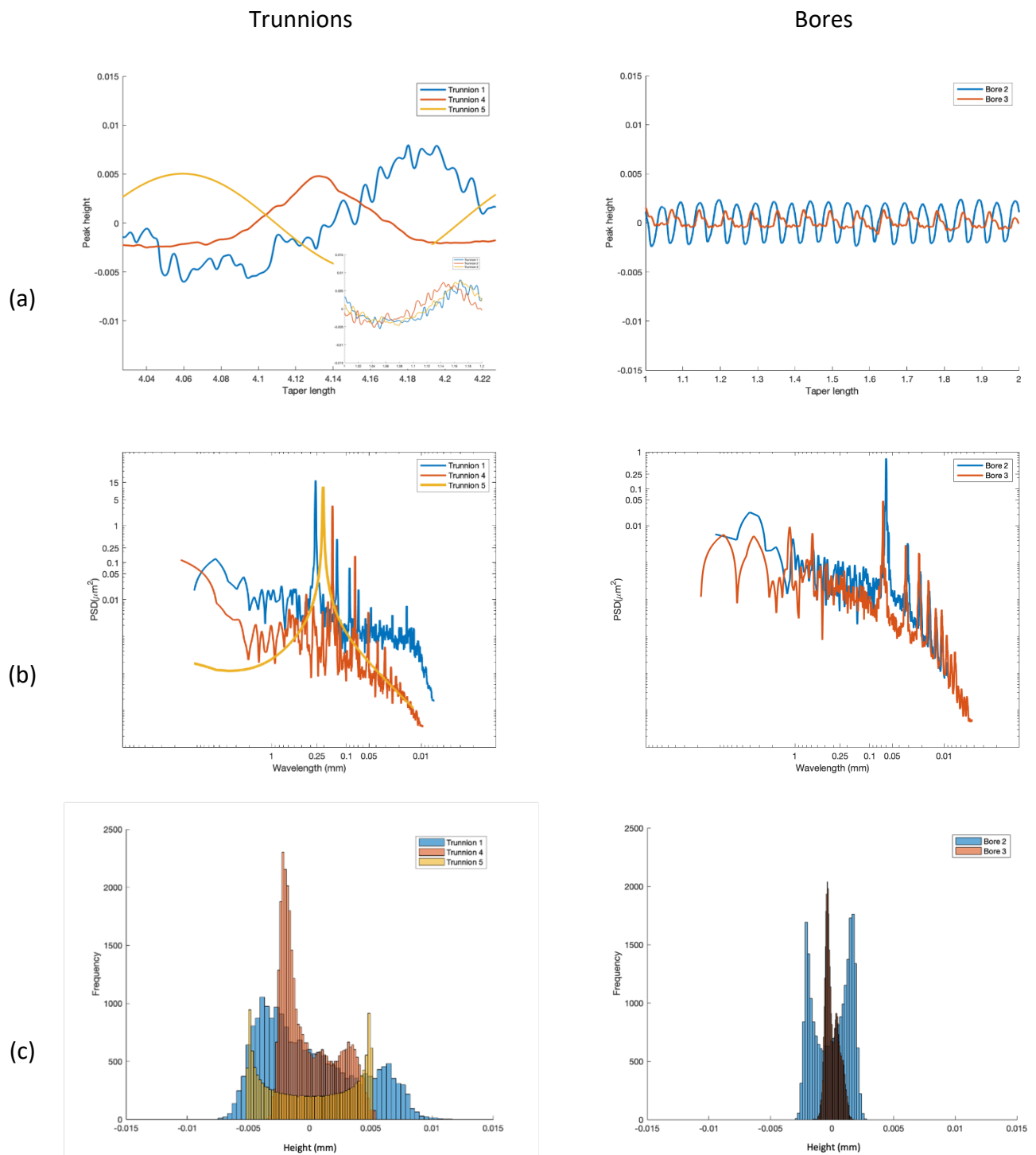
Figure 5.13. Bore and trunnion surface roughness analysis. (a) roughness surface profile, (b) estimated PSD for trunnion and (c) peak-height histograms.

Table 5.5. Amplitude and wavelength parameters of the tested bores and trunnions.

	No. of peaks	Ra (µm)	Rz (µm)	Spatial frequencies (mm)						
Trunnion 1	51	3.303	15.79	0.259	0.133	0.091	0.068	0.046	0.024	0.015
Trunnion 2	51	3.332	15.95	0.259	0.134	0.091	0.069	0.041	-	-
Trunnion 3	51	3.327	15.51	0.259	0.133	0.091	0.068	0.046	0.024	0.015
Trunnion 4	102	2.037	7.730	0.154	0.076	0.051	-	-	-	-
Trunnion 5 (sinusoidal)	51	3.184	9.981	0.259	-	-	-	-	-	-
Bore 1 (flat)	-	-	-	-	-	-	-	-	-	-
Bore 2	-	1.32	4.602	0.066	0.031	-	-	-	-	-
Bore 3	-	0.446	2.125	0.060	0.030	-	-	-	-	-

Surface peak height variation for all tested surfaces of trunnions and bores are shown in Figure 5.13c. Trunnions 2 and 3 were similar to 1 and are not included in Figure 5.12c for clarity. Surfaces of bore and trunnions presented a bimodal distribution with different levels of skewness that were associated with the nature of the surface. Measured surfaces of trunnions 1-4 presented a similar negative skewness, while the idealised surface of taper 5 did not introduce any skewness.

5.3.3 Global stress conditions

von Mises stresses in the bulk region of the trunnion for all tested taper pairs maintained similar stress distributions despite of the topography of the respective taper components. At lower assembly forces, stresses were generated in the surface region by the trunnion microgrooved peaks in contact with the bore surface. As the assembly force increased, the number of trunnion peaks in contact with the bore also increased and the stresses within the bulk region of the trunnion appeared, Figure 5.14. At assembly forces larger of 4kN for all tested tapers local stresses concentrations at the distal and proximal regions in the trunnion can be observed,

but these do not influence the stresses developed in the bulk region of the trunnion, as can be seen from the relatively uniform blue colour, with stresses away from the surface ranging from 5 to 40 MPa as shown in figure 5.14.
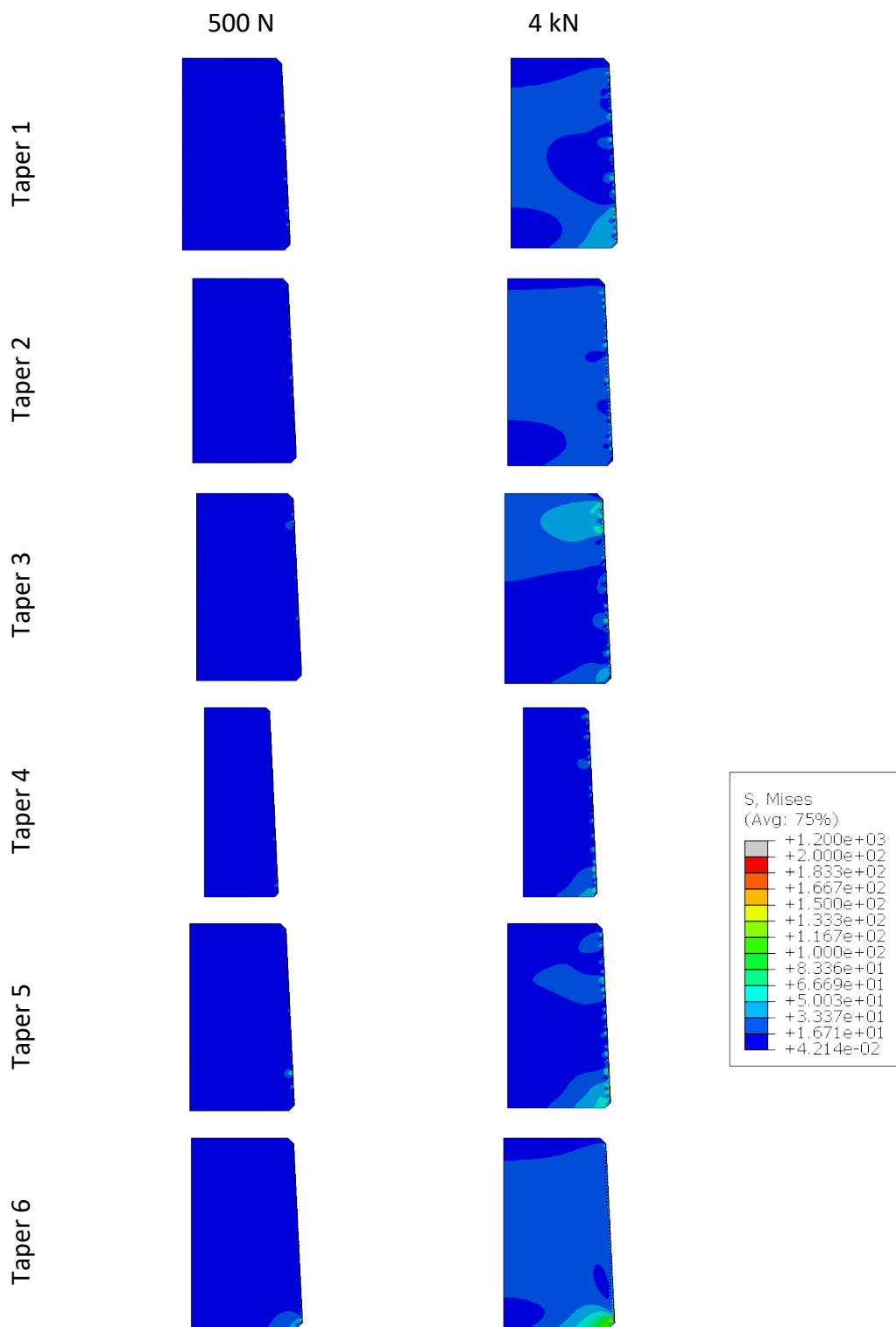
Figure 5.14. Global von Mises stress (MPa) of half-tapers contour map for all tested tapers 1 at 500 N and 4 kN.

5.3.4 Contact conditions along the trunnion

Evolution of contact conditions along the trunnion as the assembly force increased were studied by determining contact pressures as well as their respective surface profiles at the taper interface for all modelled taper pairs; these are shown in Tables 5.6 and 5.7. Taper models generated using measured surface profiles of trunnion and bore components generated a non-homogenous contact in their interface. In tapers 1, 2 and 3, contact pressure was mostly determined by the peak height of the trunnion's surface profile due to the flat bore surface; taper 1 generated the largest contact pressure of 3.02 GPa. In tapers 4 and 5, where the topography of the bore surface was also considered in the taper model, contact pressures generated within the taper interface were not solely determined by the trunnion's surface peak height. The predicted contact pressures between the bore and trunnion surface for these tapers were up to 2.5 and 3.46 GPa for tapers 4, and 5, respectively. In tapers where the bore surface roughness was included, contact pressures along the trunnion length changed as the femoral head bore moved into the trunnion during assembly. Contact conditions in taper 6 model were homogenous compared to the other trunnions and predicted lower contact pressures of up to 1.8 GPa.

Table 5.6. Contact pressure at assembly forces of 500 N, 2 kN and 4 kN for all tested tapers.

	500 N	2 kN	4 kN
Taper 1			
Taper 2			
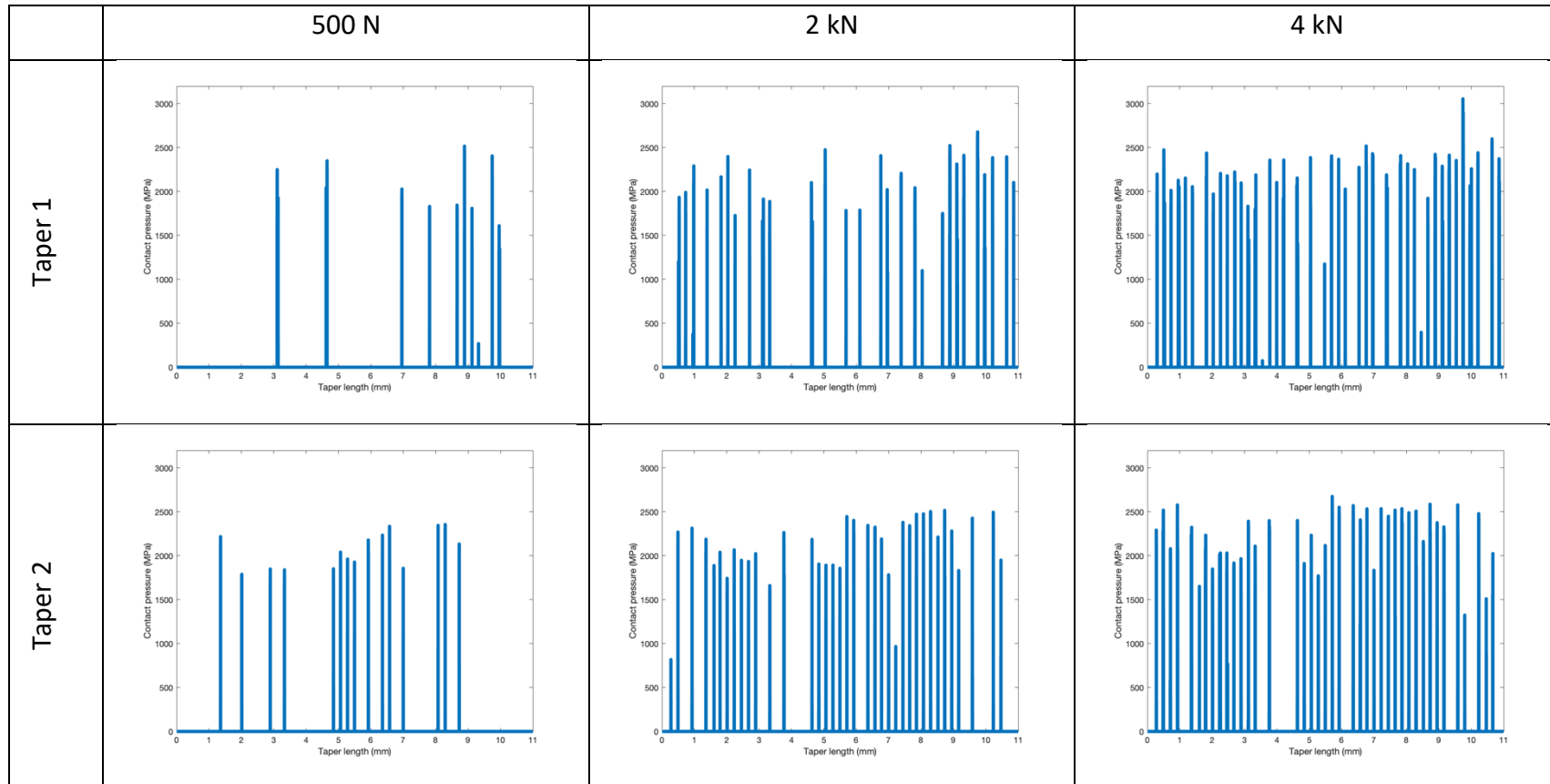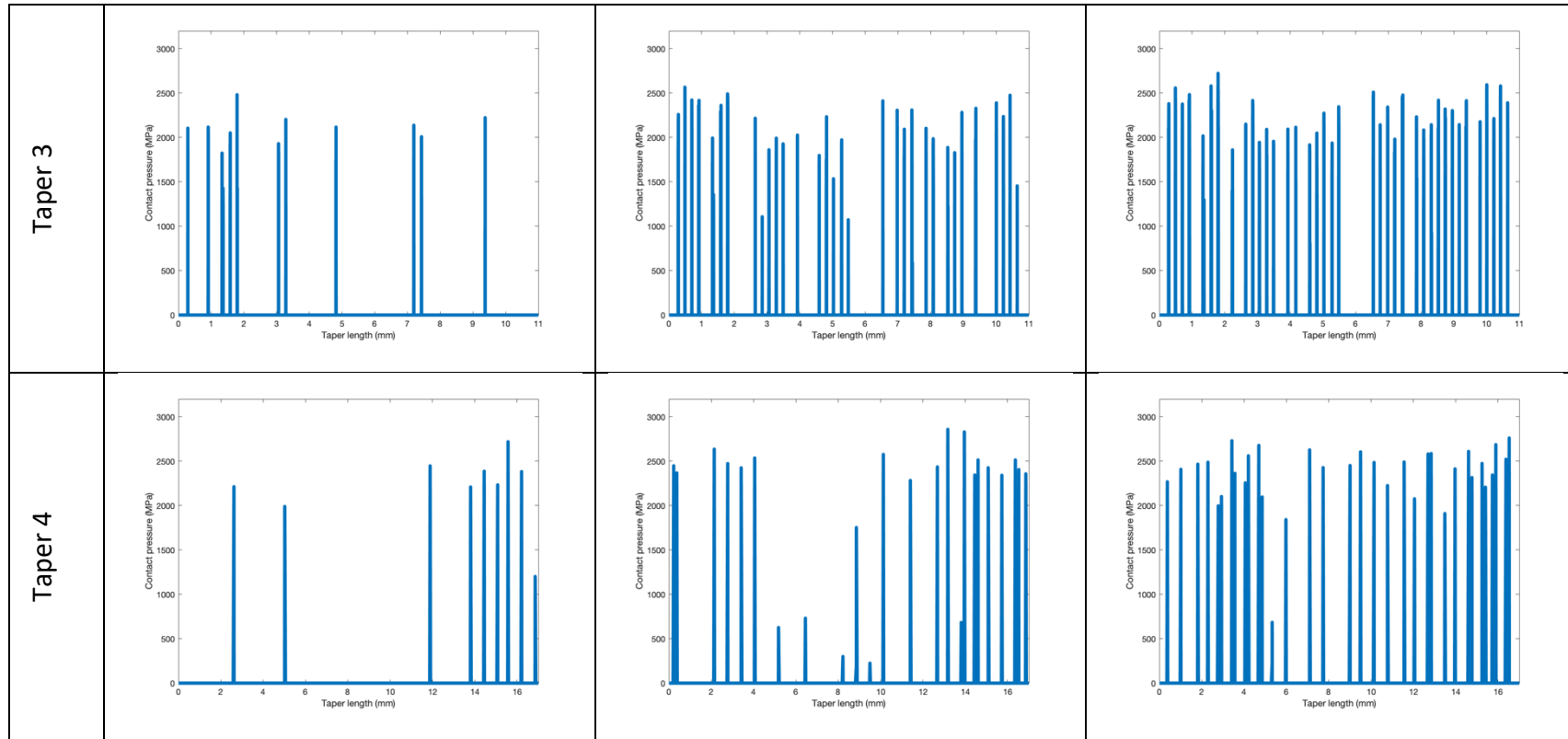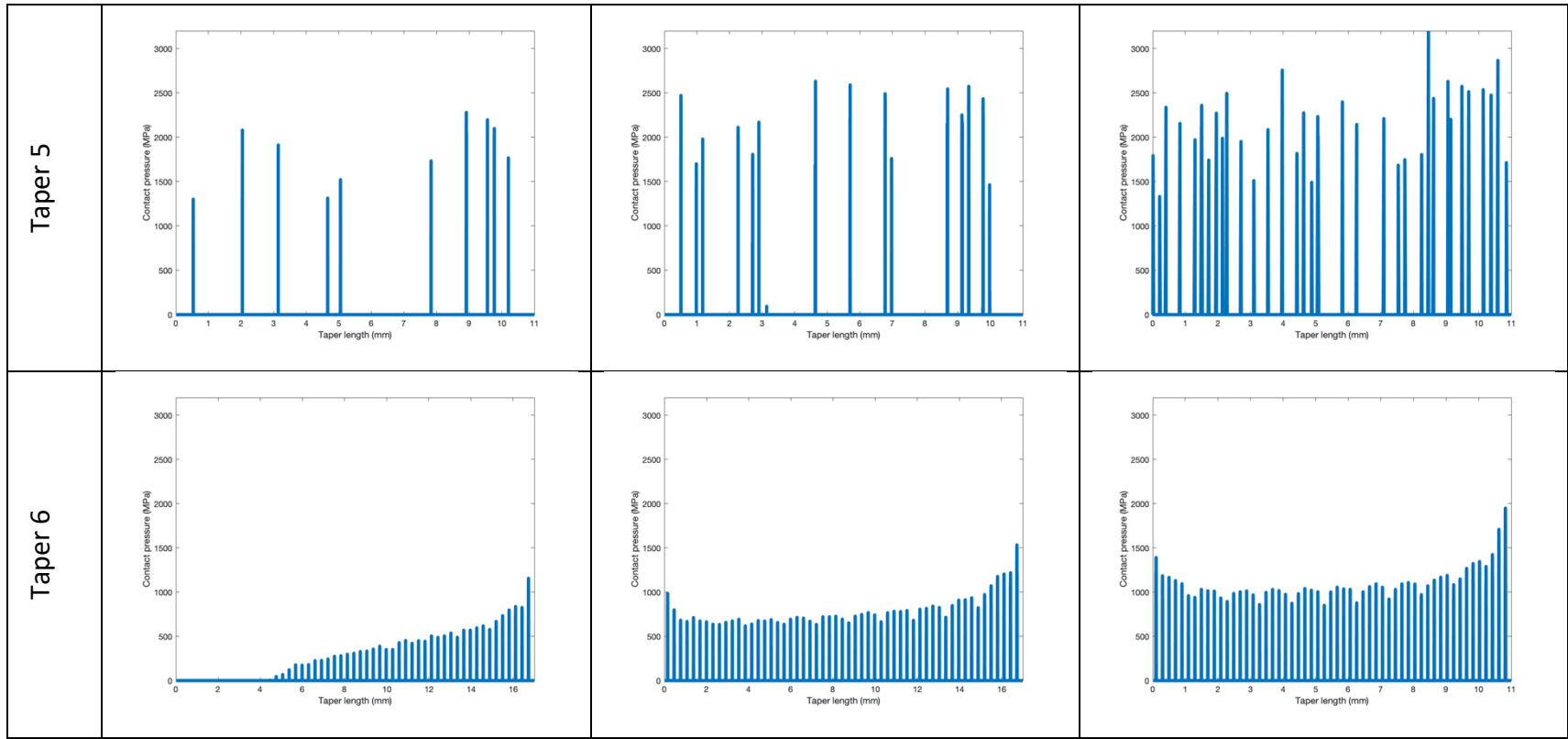
Table 5.6 presents the deformed surface profile (orange) superimposed over the undeformed surface profile (blue) of the taper. The bore surface determined the way the trunnion peaks deformed as the assembly increased. When the bore surface was considered perfectly flat all deformed microgrooved peaks maintained relatively the same height as it can be seen in tapers 1, 2, 3 and 6. The imprinting of the flat surface of the bore becomes more evident in higher assembly forces. In contrast, for tapers 4 and 5, each of the microgrooved peaks deformed by different amounts.

Table 5.7 Taper contact surface profiles at assembly forces of 500 N, 2 kN and 4 kN for all tested tapers. Surface profile column shows the peak height before (blue) and after assembly (orange).

	500 N	2 kN	4 kN
Taper 1			
Taper 2			

Taper 5			
Taper 6			
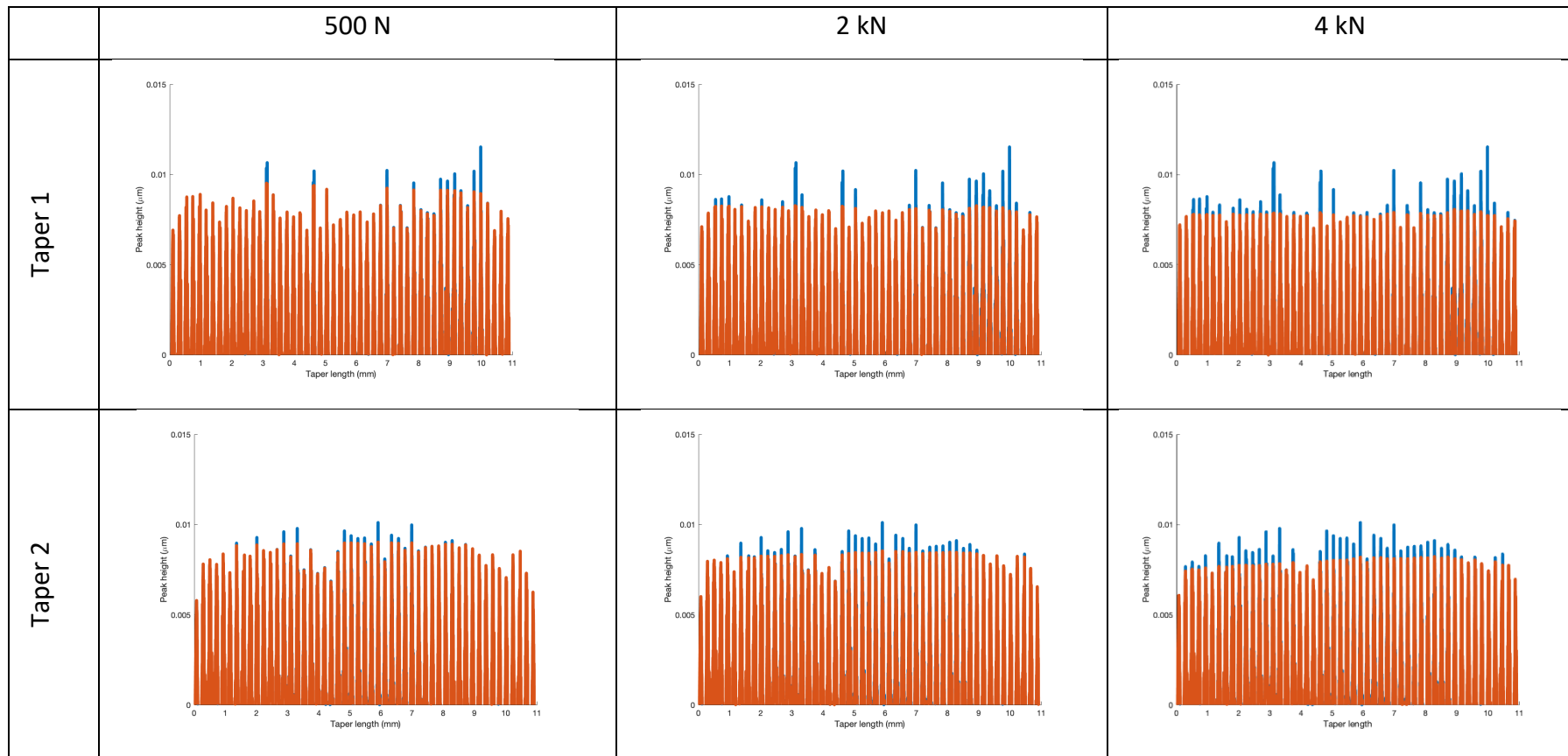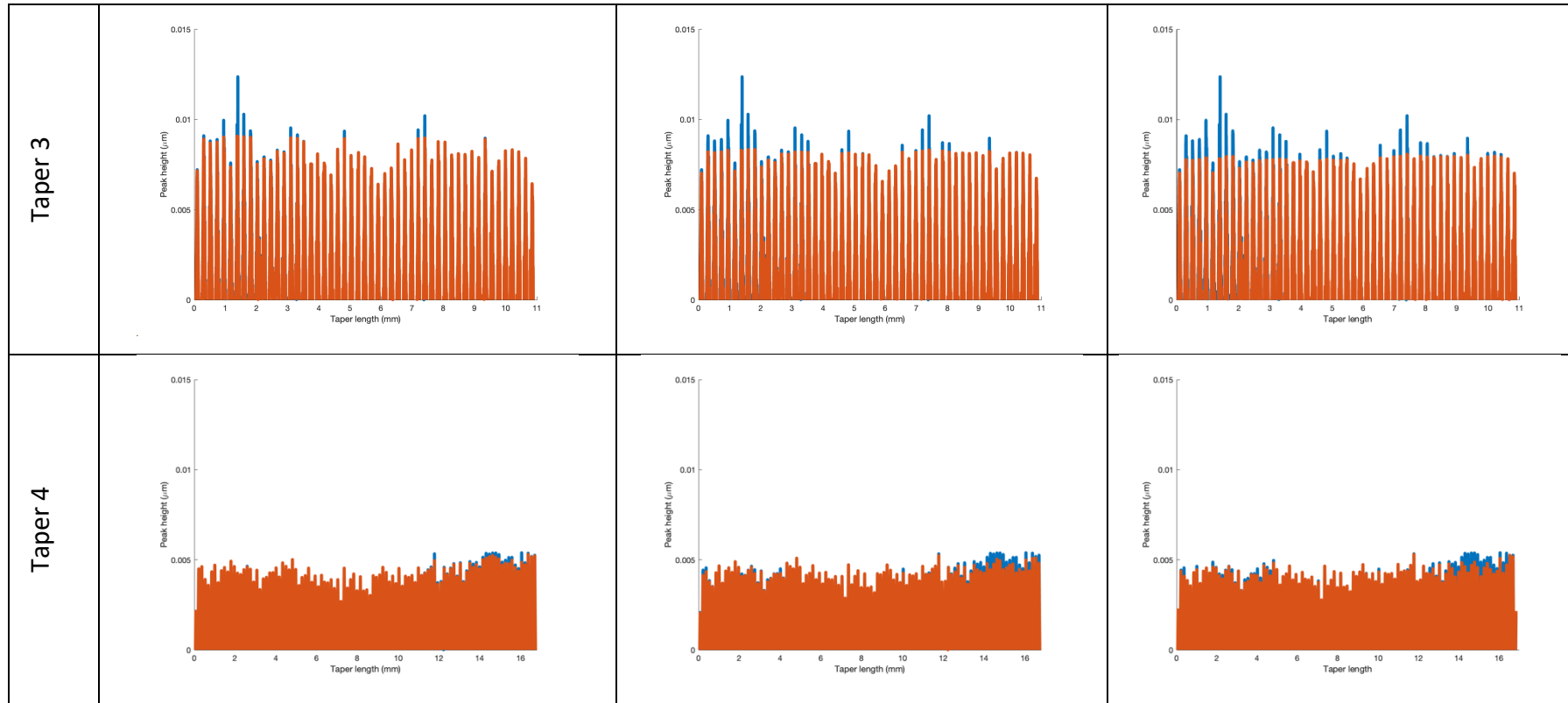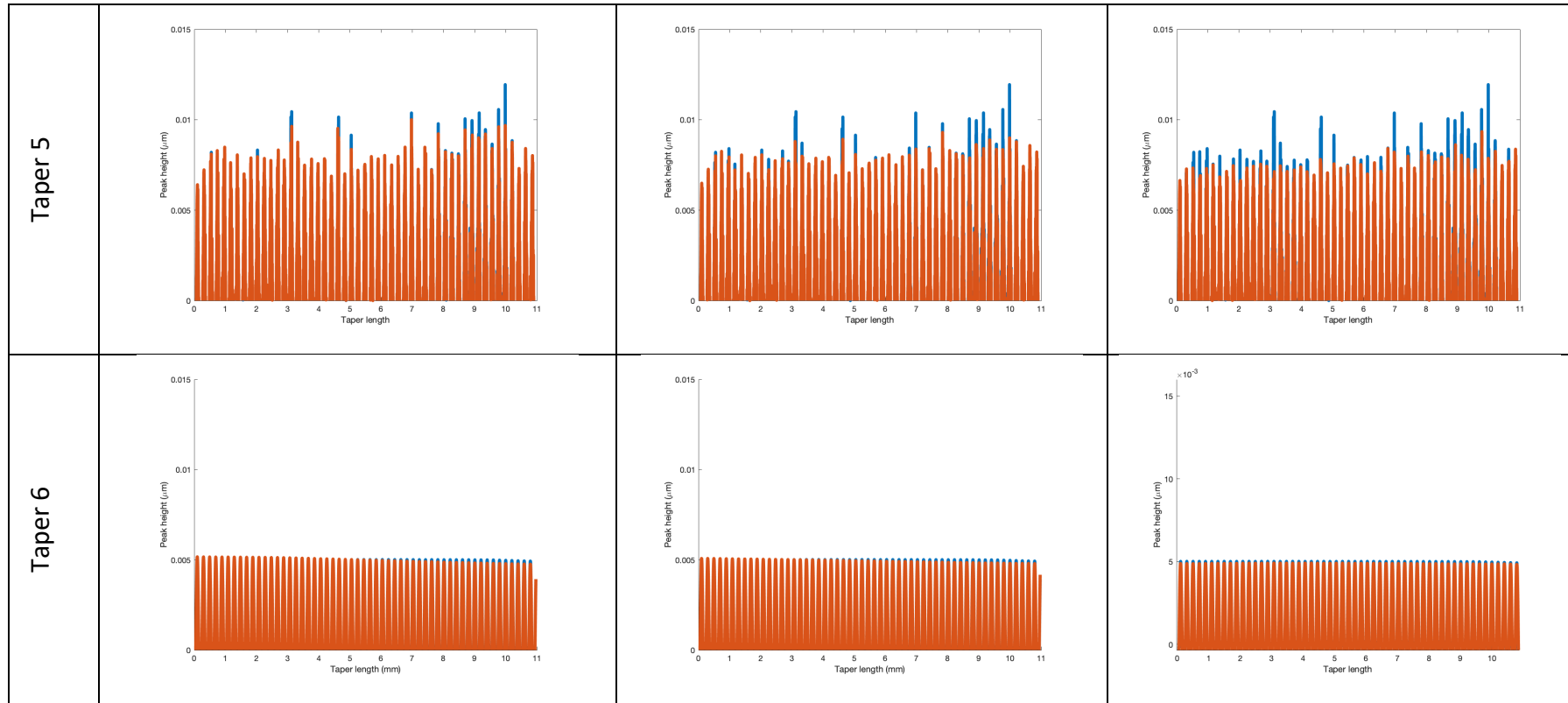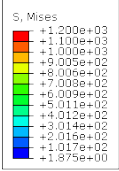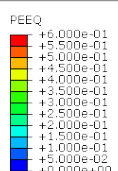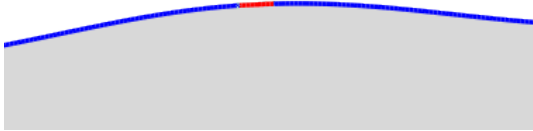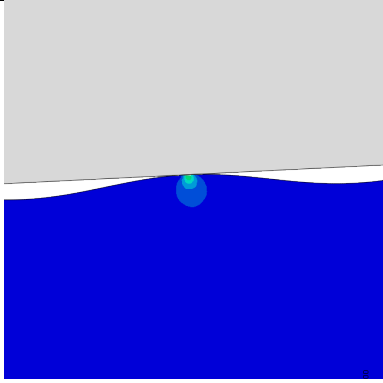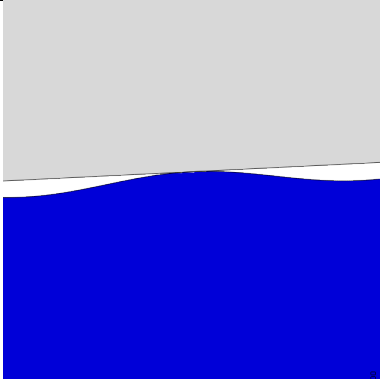
5.3.5 Local contact conditions

Different local contact conditions at the trunnion's microgrooved peaks surface regions were observed along the trunnion length as shown in Table 5.8. Contact condition cases were defined according to the number of contact points within a single microgrooved peak, these cases range from one to three-point contact between the trunnion's surface and the bore. In all tapers, regardless of the surface of topography the number of the trunnion's microgroove peaks in contact with the bore increased as the reaction assembly force increased. Local conditions within trunnion's microgrooved peak region were determined by the peak form, bore topography, and assembly force. Figure 5.15 presents the number of trunnion microgrooved peaks in contact with the bore surface and its contact case as well as the stresses and plastic strains occurring at that point. In tapers 1-5, as assembly force increased, the bore and trunnion surface became closer increasing the number contact points within the trunnion's microgrooved peak. Tapers 1, 2 and 3 generated the largest number of point contacts, with up to a three-point contact at 4 kN due to the flat bore surface which allowed a larger region of the rough trunnion microgrooved peak to interact with the bore surface. In these tapers, assembly forces larger than 4 kN, the majority of cases were two-point contact followed by one, three-point contacts. Two- and four-point contacts would become one point as the peak plastically deformed. Furthermore, in tapers 4 and 5, up to two-point cases were observed due to the bore's surface topography, which reduced the interacting regions with the trunnion surface but increased the stresses and plastic strains generated in the local region of the microgrooved peak. In these tapers, the number of peaks in contact could be reduced as the assembly force increased due to the topography of the bore, peak-height variation and the advancing motion of the femoral head. On the other hand, taper 6 only generated one-point contact cases due to the smooth microgrooved peak of the trunnion interacting with the flat bore surface.

Table 5.8 Local contact conditions between the trunnion and bore developed at the microgrooved surfaces of the trunnion. Red in the wave surface indicates contact with the bore surface.

	Contact area	von Mises stress	Plastic strain
Idealised contact (single point)			

Single-point contact			
Two-point contact			
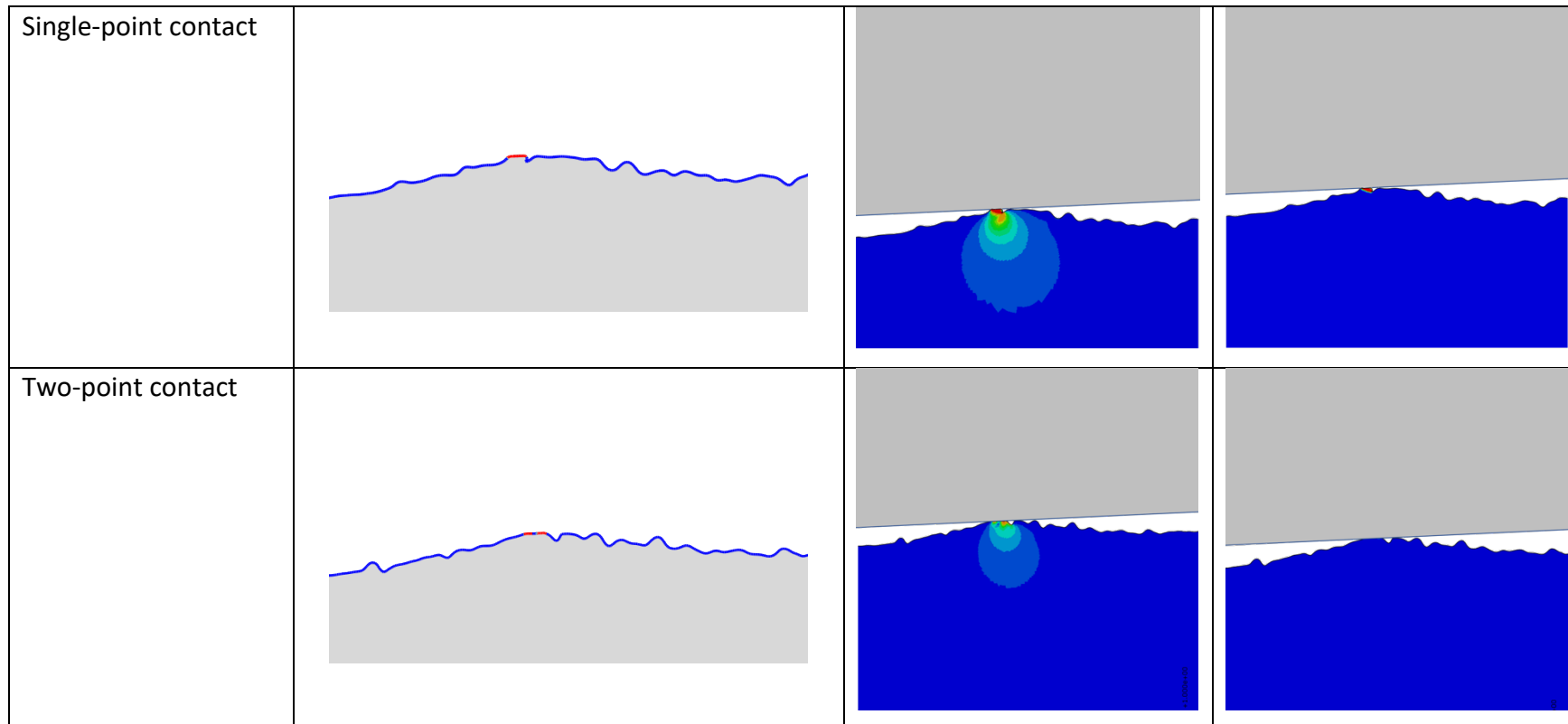
Three-point contact			
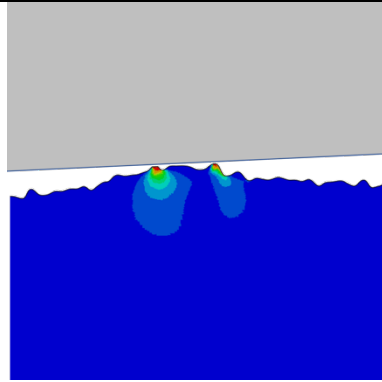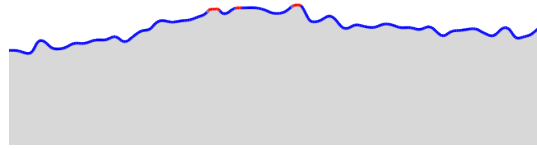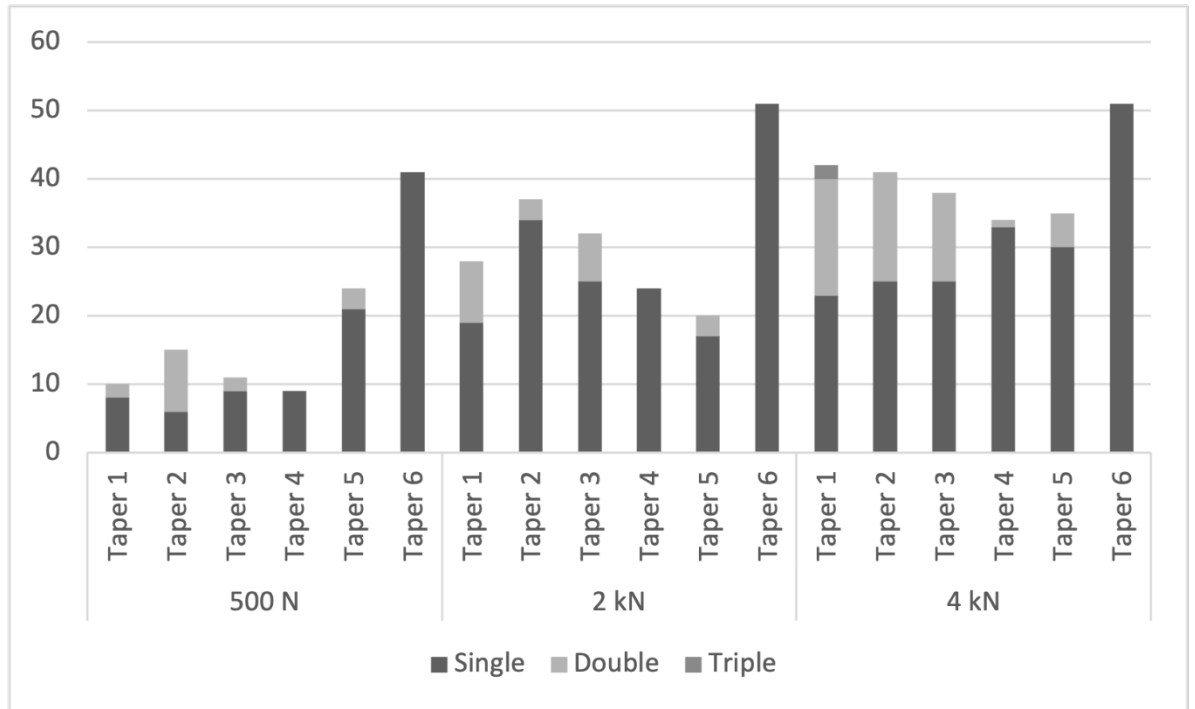
Figure 5.15. Number of accumulated types of contact along the microgrooved peaks of the trunnion surfaces resulting in the total number of peaks in contact with the bore at different assembly surfaces.

The microgrooved peaks generated different von Mises stresses and plastic deformation magnitudes at the trunnion surface. All the trunnion surfaces reached at least one region of plastic deformation, however the respective magnitude of the plastic strain was determined by the nature of the surface topography. Taper 6 generated the lowest level of plastic deformation within the cohort of tapers modelled with an equivalent plastic strain (PEEQ) up to 0.02, while the rest of the models reached plastic deformation with strains that are associated with material failure (0.6). Failure levels of plastic strains did not occur in all microgroove peaks in contact along the taper length. The absolute number of trunnion microgrooved peaks in contact with bore and the number of peaks with plastic strain larger that 0.6 for all tested tapers at different assembly forces are shown in Table 5.9. Taper 1-3 despite having similar trunnion surfaces generated different number of contacting and failing trunnion microgrooved peaks.

Table 5.9 Microgrooved peaks in contact and peaks with a plastic strain larger than 0.6 for all tested tapers at different reaction assembly forces.

	Number of peaks in contact (Peaks with >0.6 plastic strain)		
	500N	2 kN	4 kN
Taper 1	10 (8)	28 (24)	42 (22)
Taper 2	15 (4)	37 (11)	41 (19)
Taper 3	11 (6)	32 (14)	38 (20)
Taper 4	9 (0)	24 (5)	34 (9)
Taper 5	24 (16)	20 (12)	35 (25)
Taper 6	41 (0)	51 (0)	51 (0)

5.3.6 Evolution of contact conditions

Evolution of the contact conditions in the taper interface resulted from the trunnion microgrooved peaks changing their contact condition with the bore surface as the femoral head moves along the taper axis, closing the gap between the trunnion and bore surfaces, generating an increase in the reaction assembly force. Changes in the contact conditions in the taper interface were determined by the waviness and roughness surface regions of the interacting taper components. The number of trunnion microgrooved peaks in contact with the bore increased with the assembly force and remained in contact with bore throughout the assembly in taper pairs (1, 2, 3 and 6) where the bore surface was simulated as a flat surface. This is shown for the von Mises stresses in Tables 5.10 - 5.12, and the plastic strains in Tables 5.15 - 5.18). Tables 5.13 and 5.14 show the von Mises stresses developed and Tables 5.19 and 5.20 show the plastic strains developed in tapers 4 and 5 respectively, where the bore was rough.

In tapers where a rough bore surface was included, the height of microgrooved peaks in the trunnion changed as the femoral head advanced, flattening the microgrooved peak and changing the trunnion's surface. In some cases, due to the trunnion peak flattening the number of peaks in contact with bore decreased as the femoral head moved. At an assembly force of 4 kN in taper 4 and 5, around 6% and 10%, respectively, of the total number of microgrooved peaks in the trunnion surface were plastically deformed but were not finally in contact with the bore surface. These changes in the flattened microgrooved peaks not in contact can be associated with

the number of dominant spatial frequencies that include the taper components surfaces as smaller spatial frequencies represent the smaller peaks at the roughness region of the surface topographies. Small peaks of the roughness surface region at the top of the microgrooved peaks are the first peaks to enter contact and be deformed by the bore surface. These flattened peaks may stop interacting with the bore as the femoral head advances during the assembly of the taper, due to the undulation of the bore surface. In flat bore surfaces the deformation was constant, whereas in bore surfaces from measured data the deformation was intermittent, and in some cases produced higher deformation as observed in Table 5.14 for peaks 2, 3 and 4.

Table 5.10. Evolution of von Mises stresses within the five highest microgrooved peaks for taper 1.
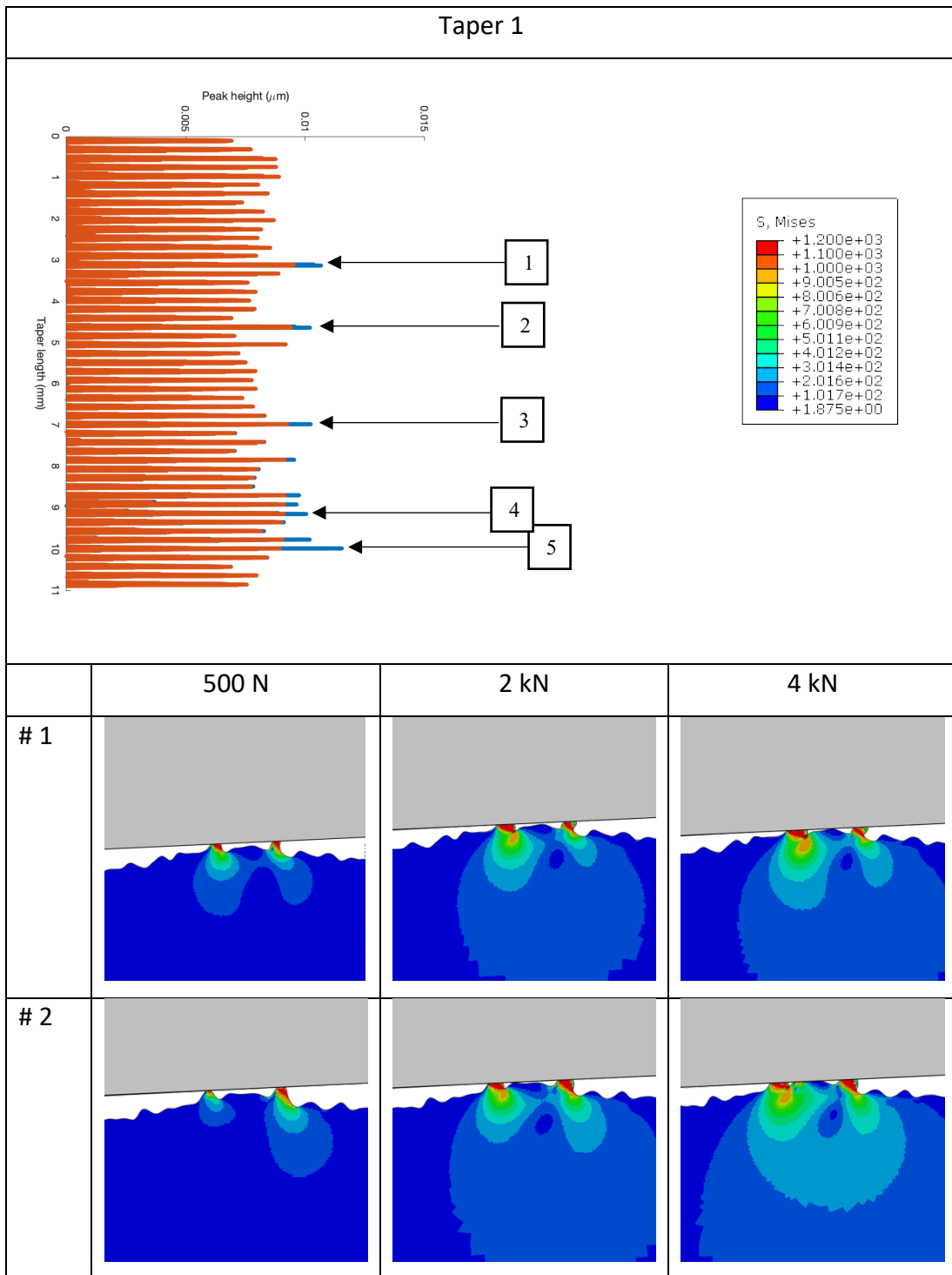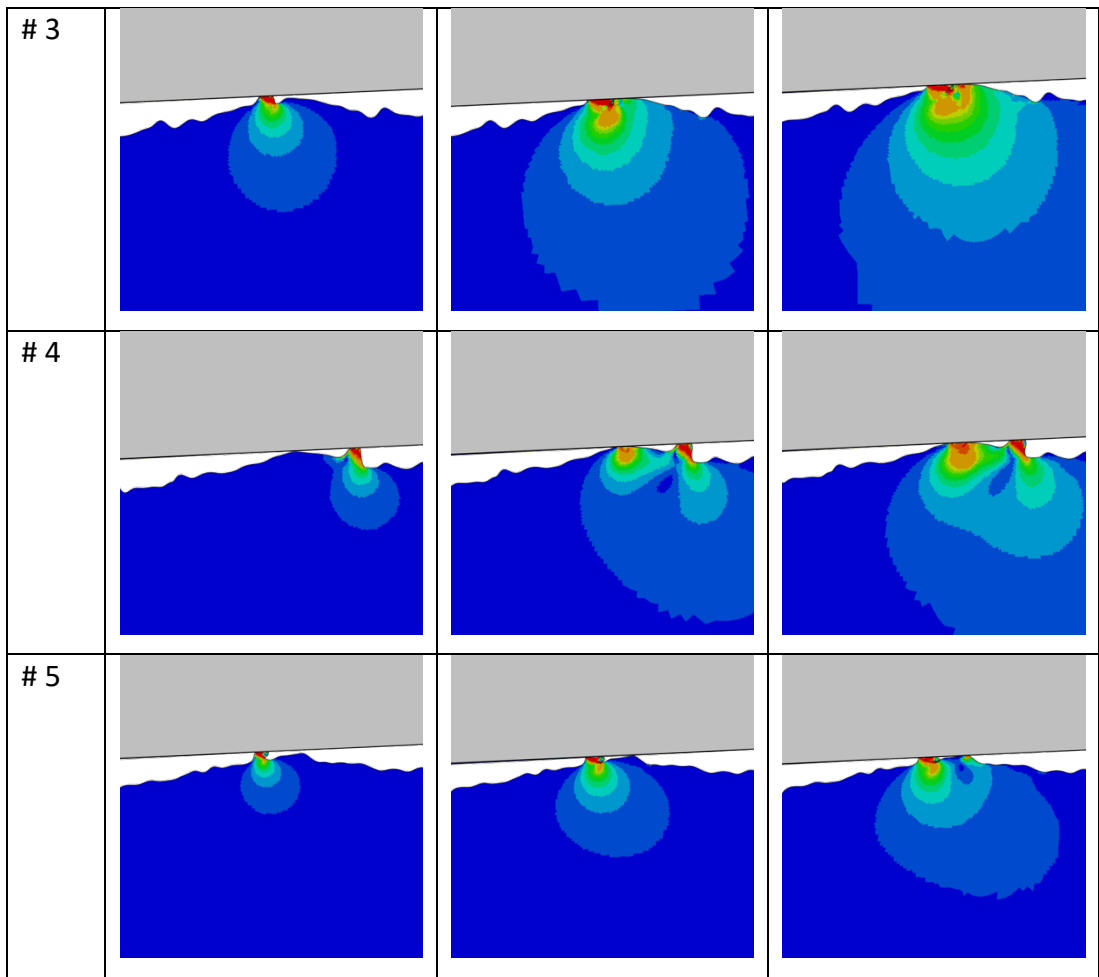
Table 5.11. Evolution of von Mises stresses within the five highest microgrooved peaks for taper 2.

# 3			
# 4			
# 5			
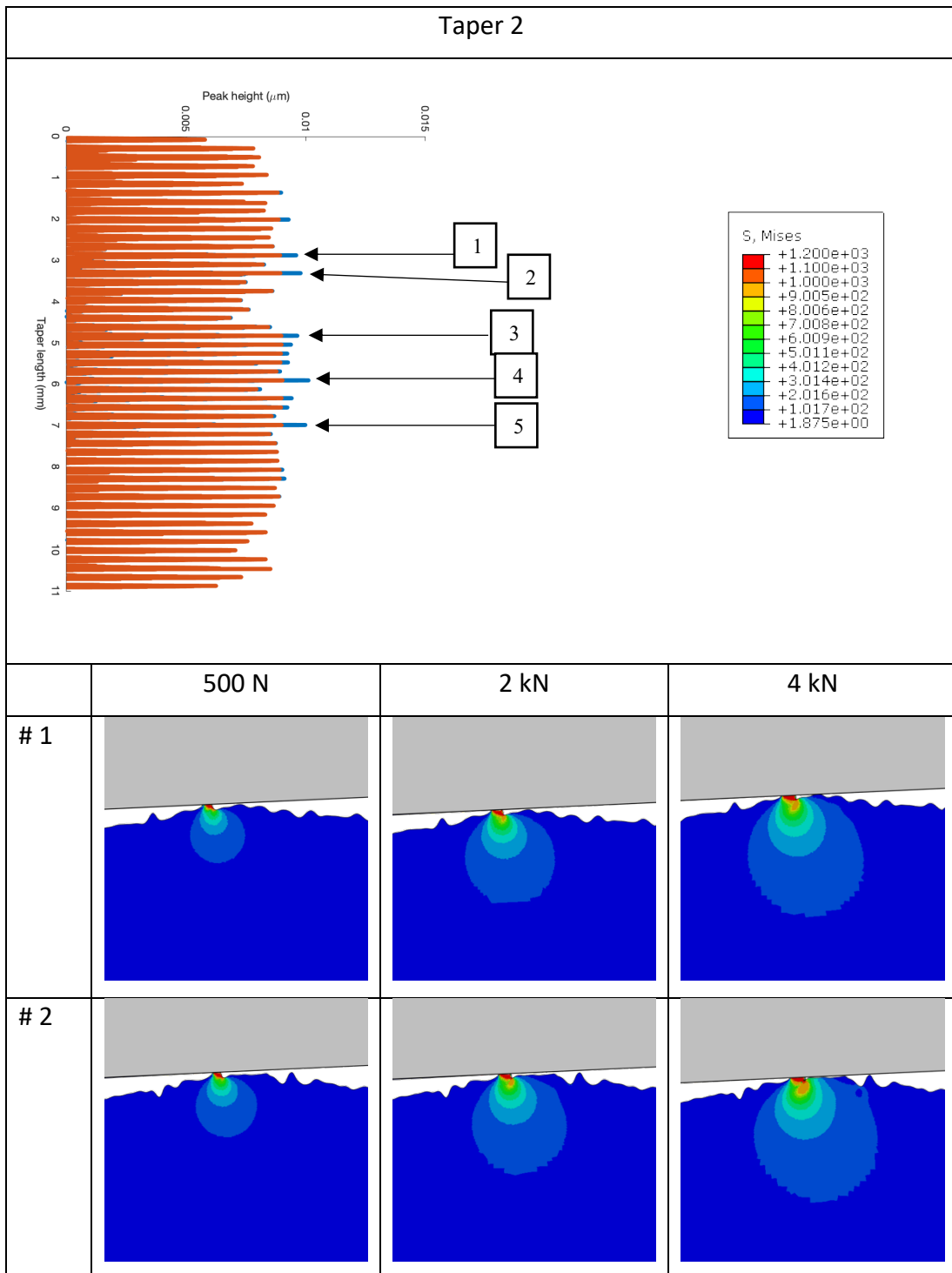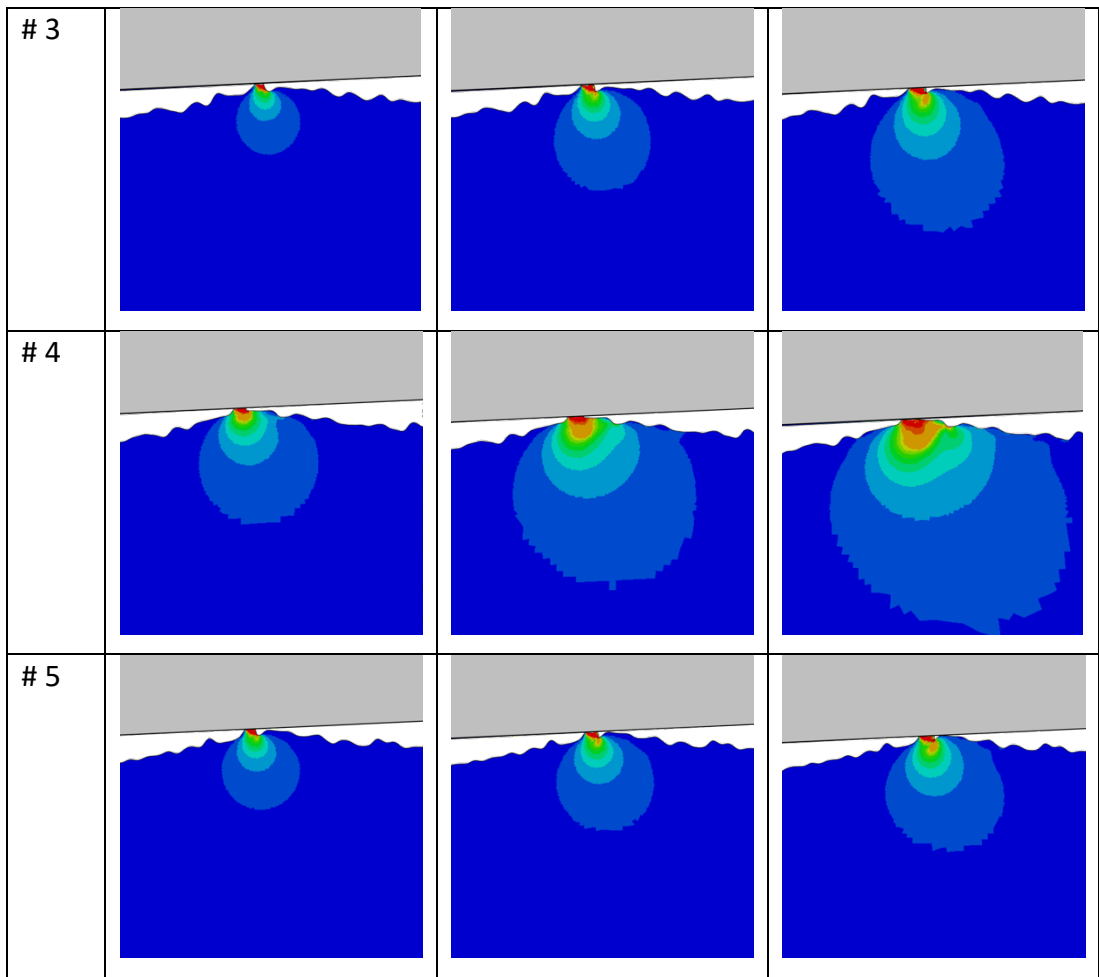
Table 5.12. Evolution of von Mises stresses within the five highest microgrooved peaks for taper 3.
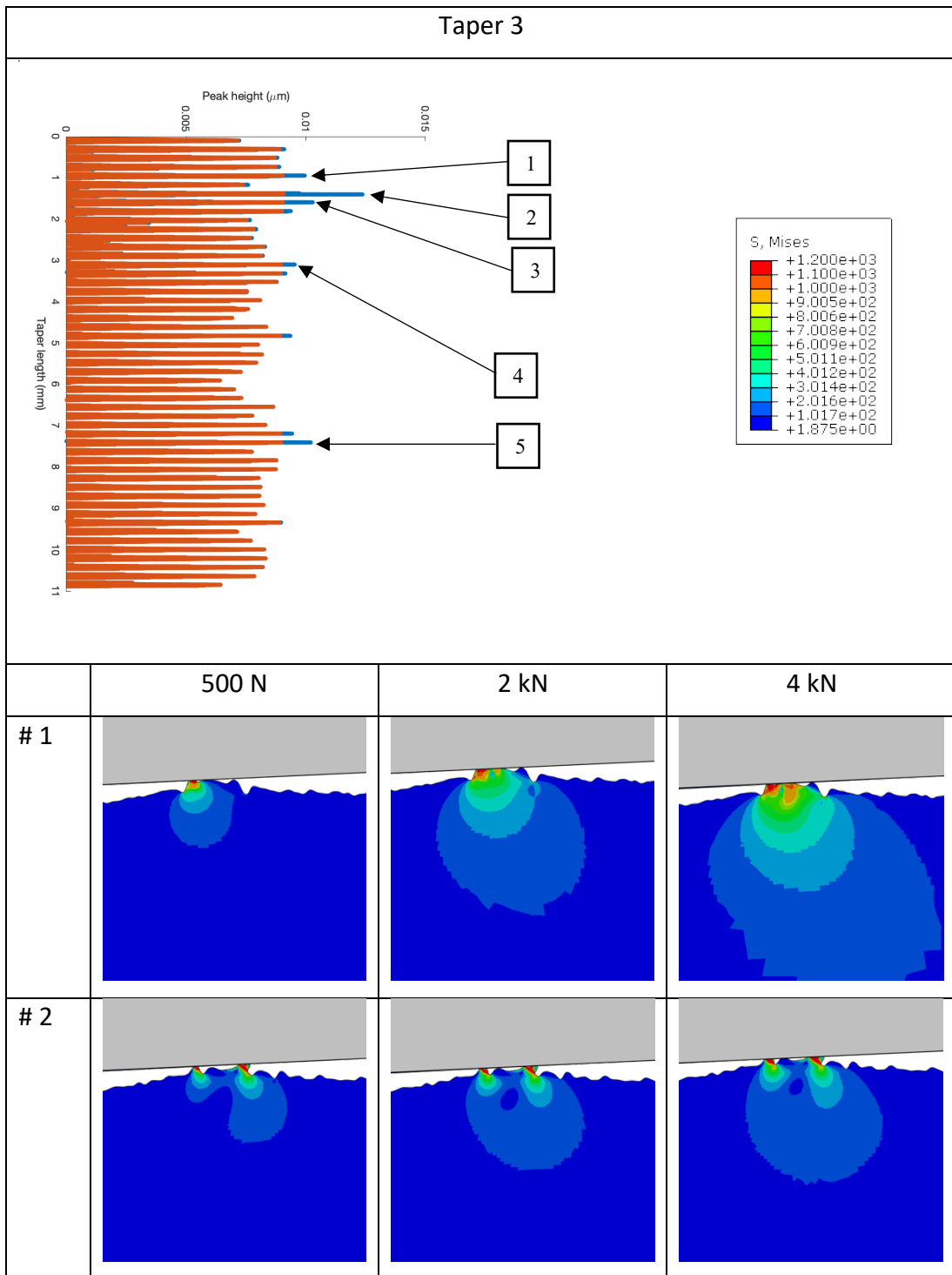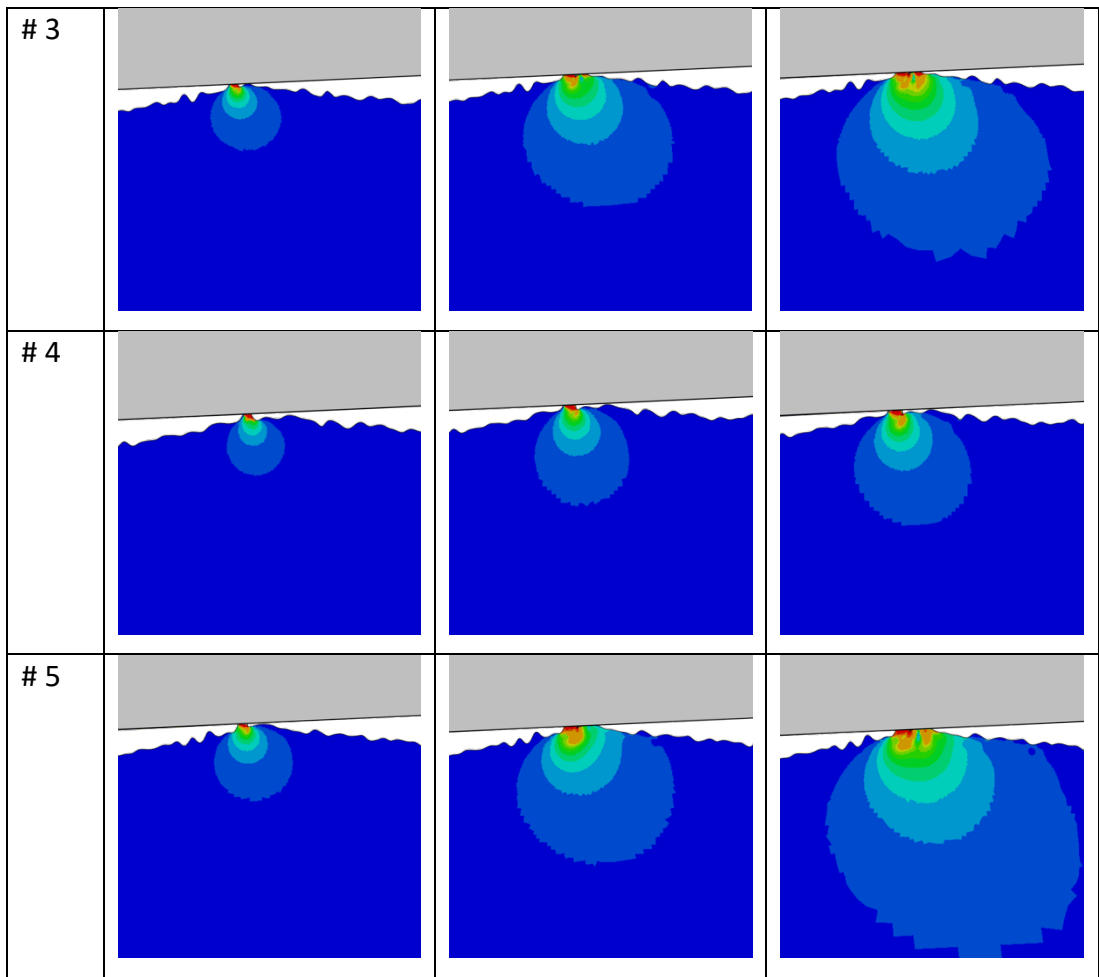
Table 5.13. Evolution of von Mises stresses within the five highest microgrooved peaks for taper 4.
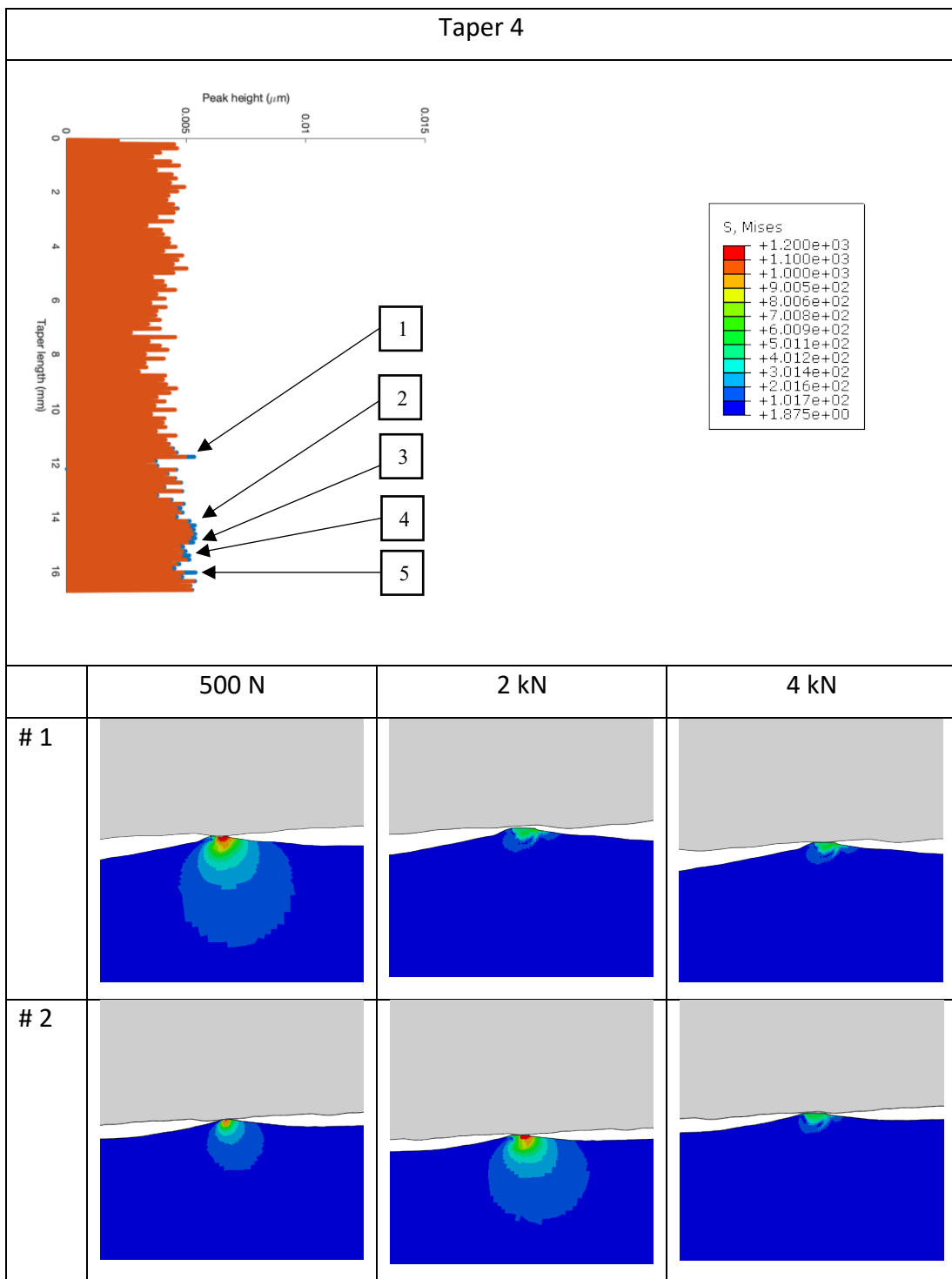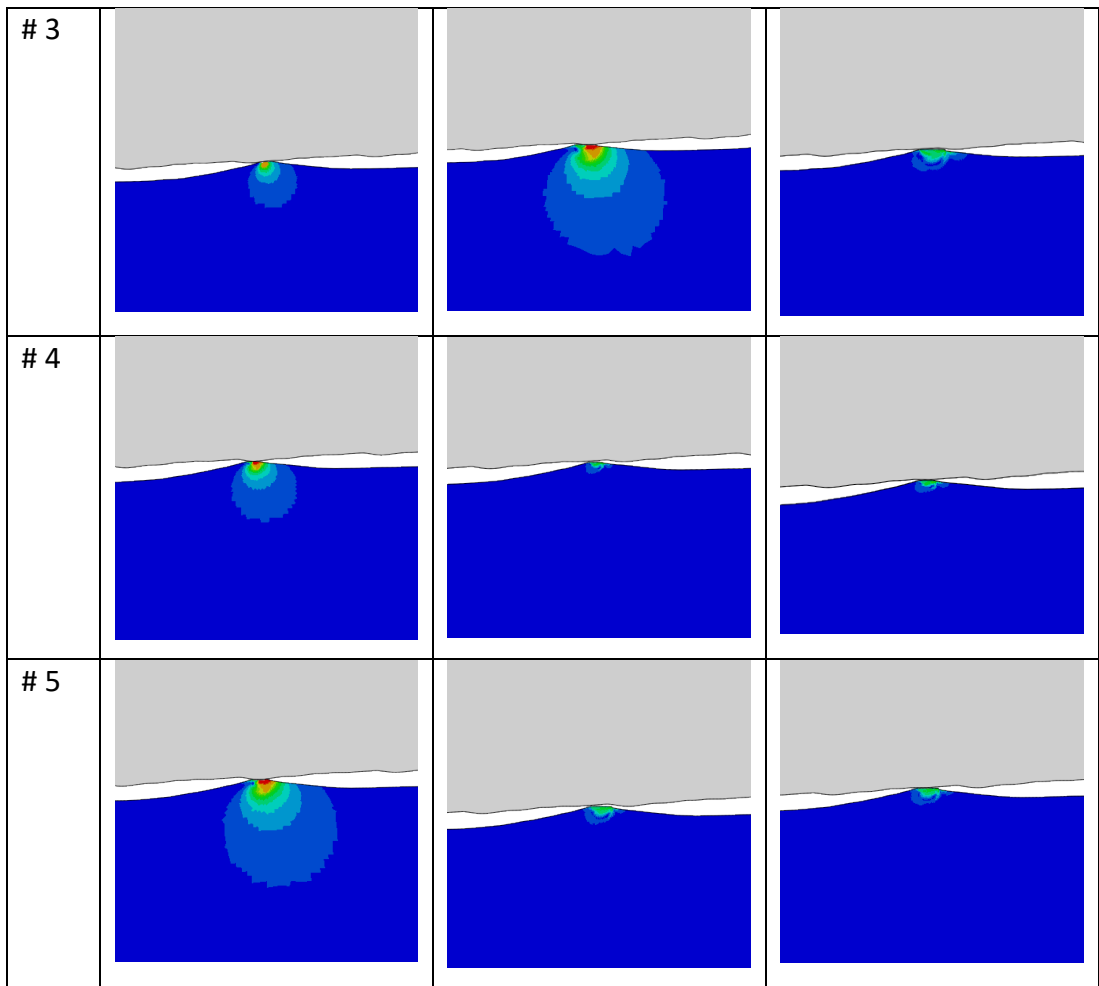
Table 5.14. Evolution of von Mises stresses within the five highest microgrooved peaks for taper 5.
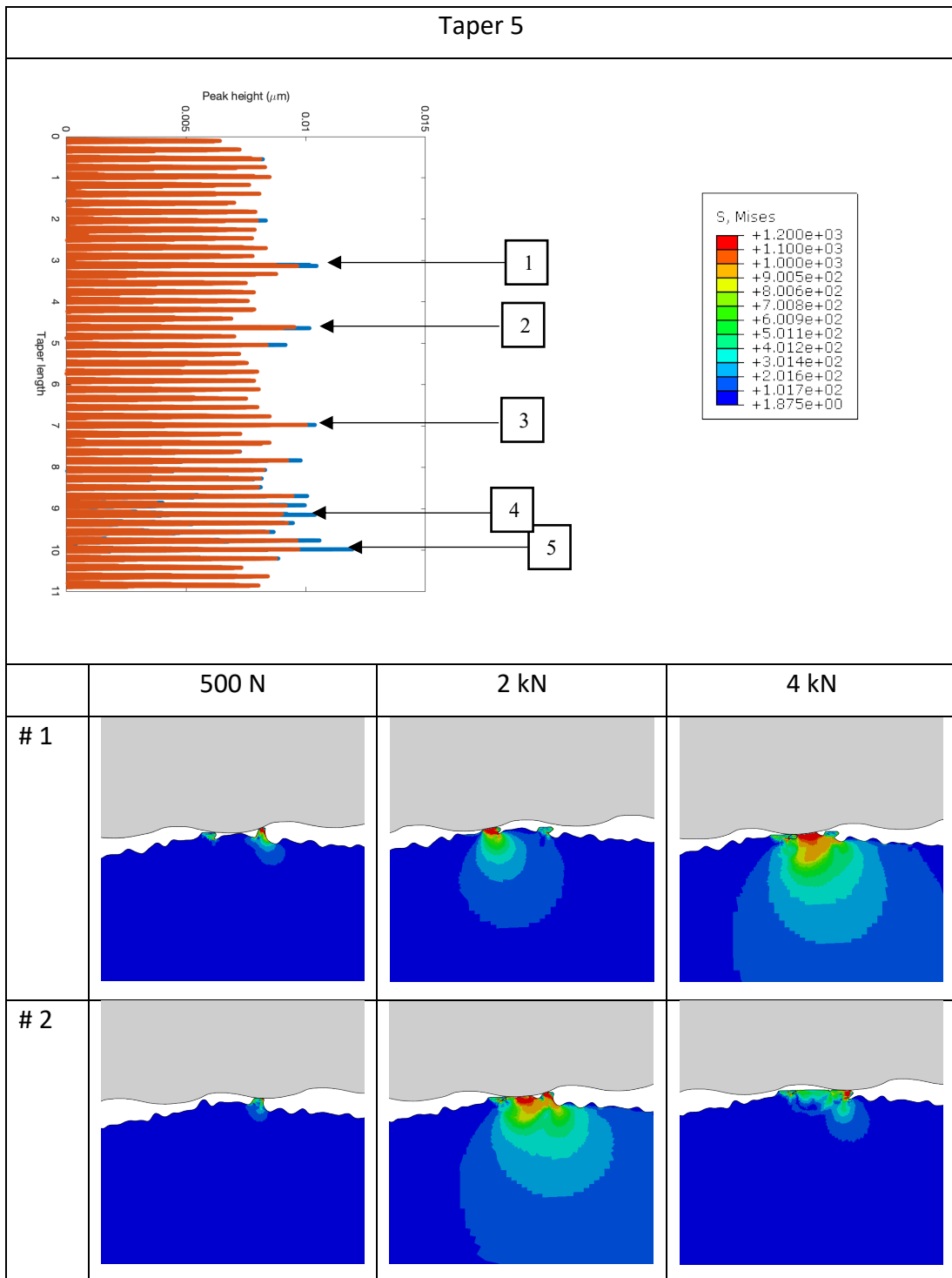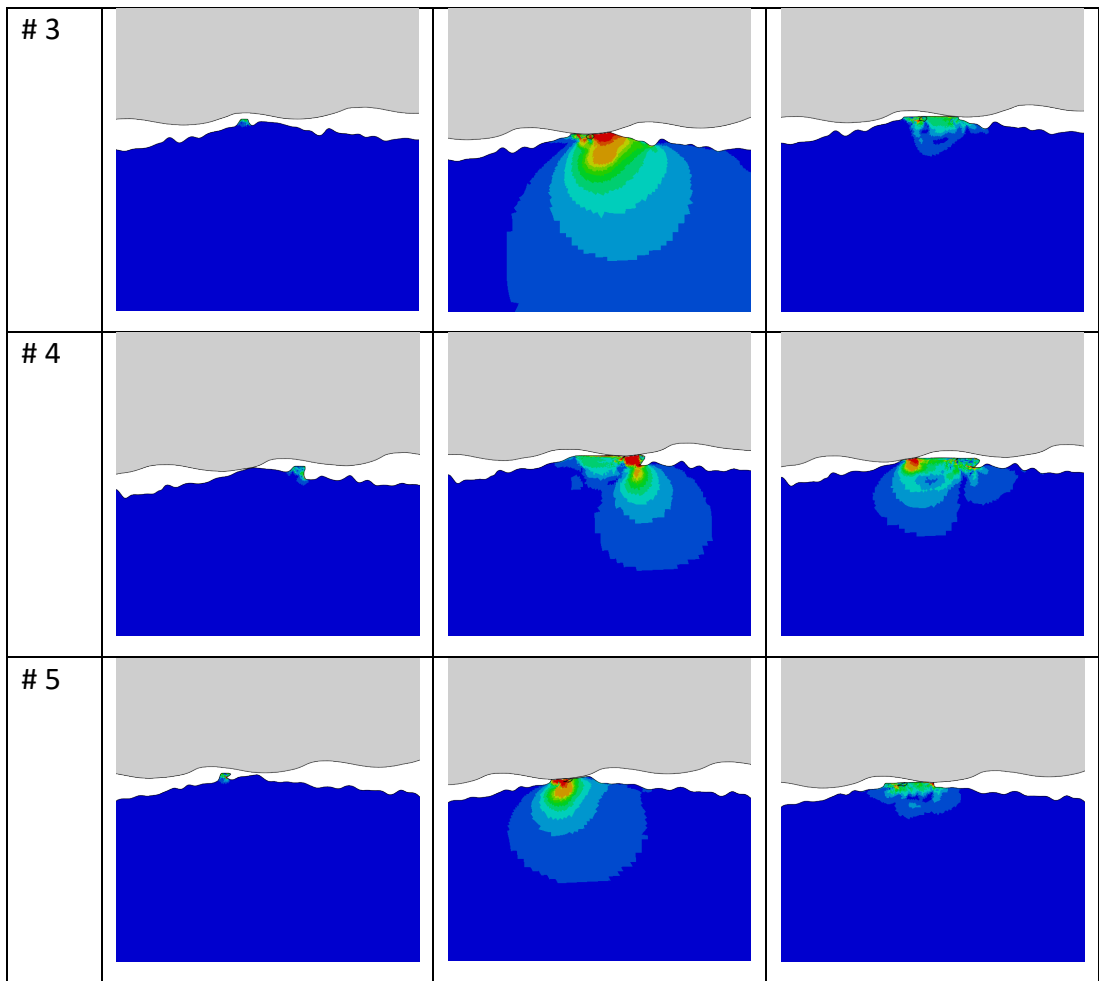
Table 5.15. Evolution of von Mises stresses within two microgrooved peaks located at the proximal and distal regions of taper 6.
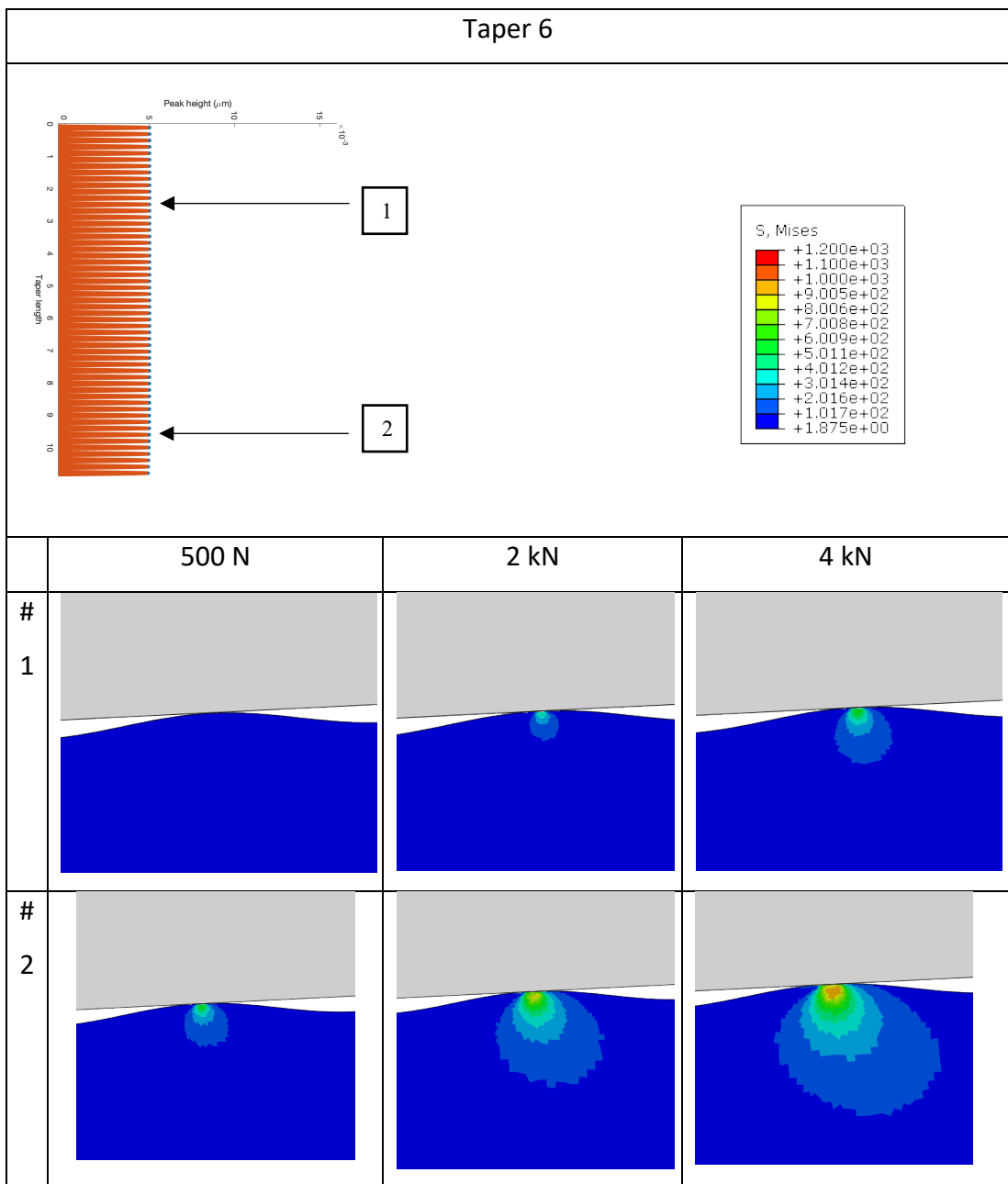
Table 5.16. Evolution of plastic strains within the five highest microgrooved peaks for taper 1.
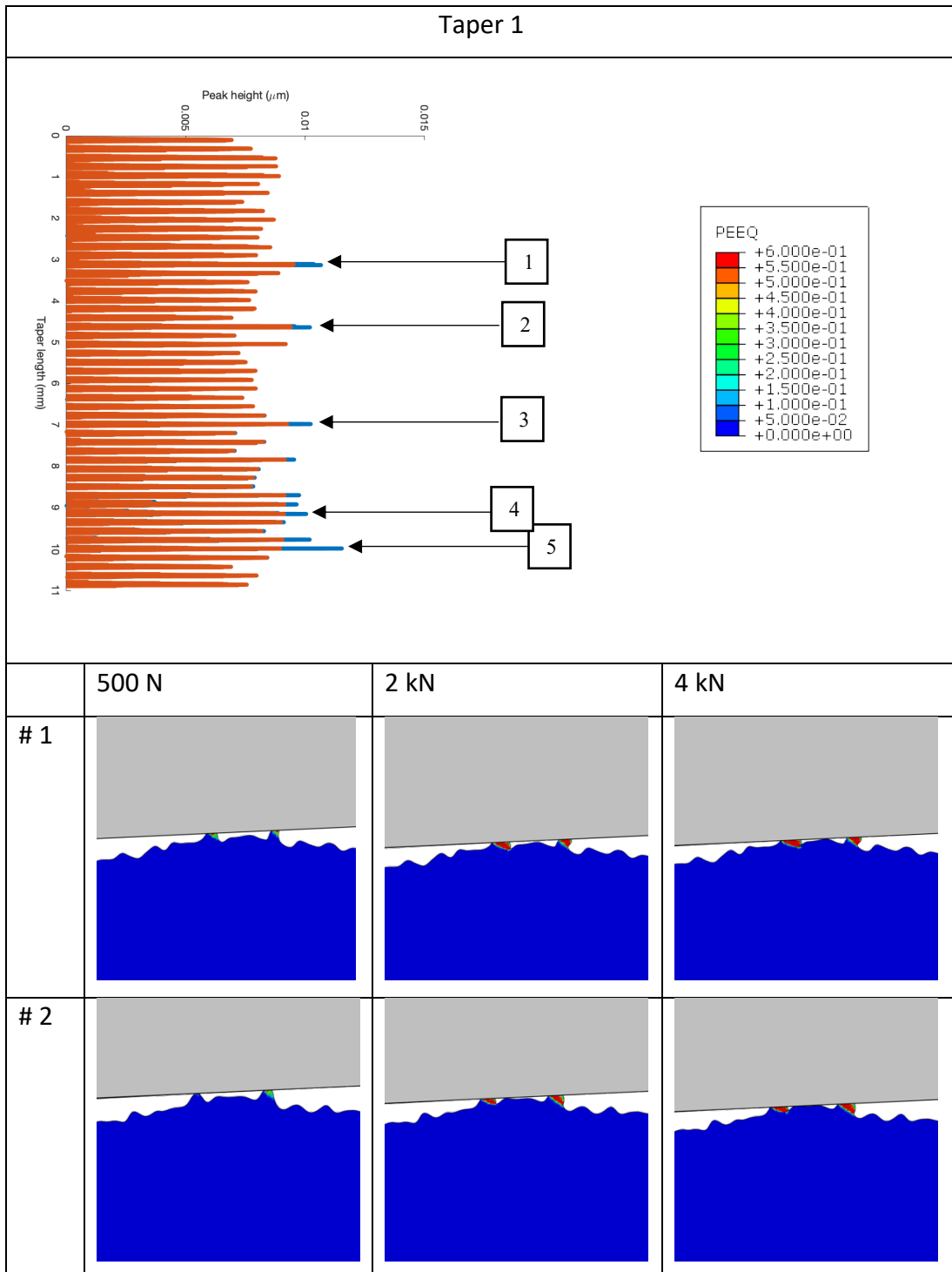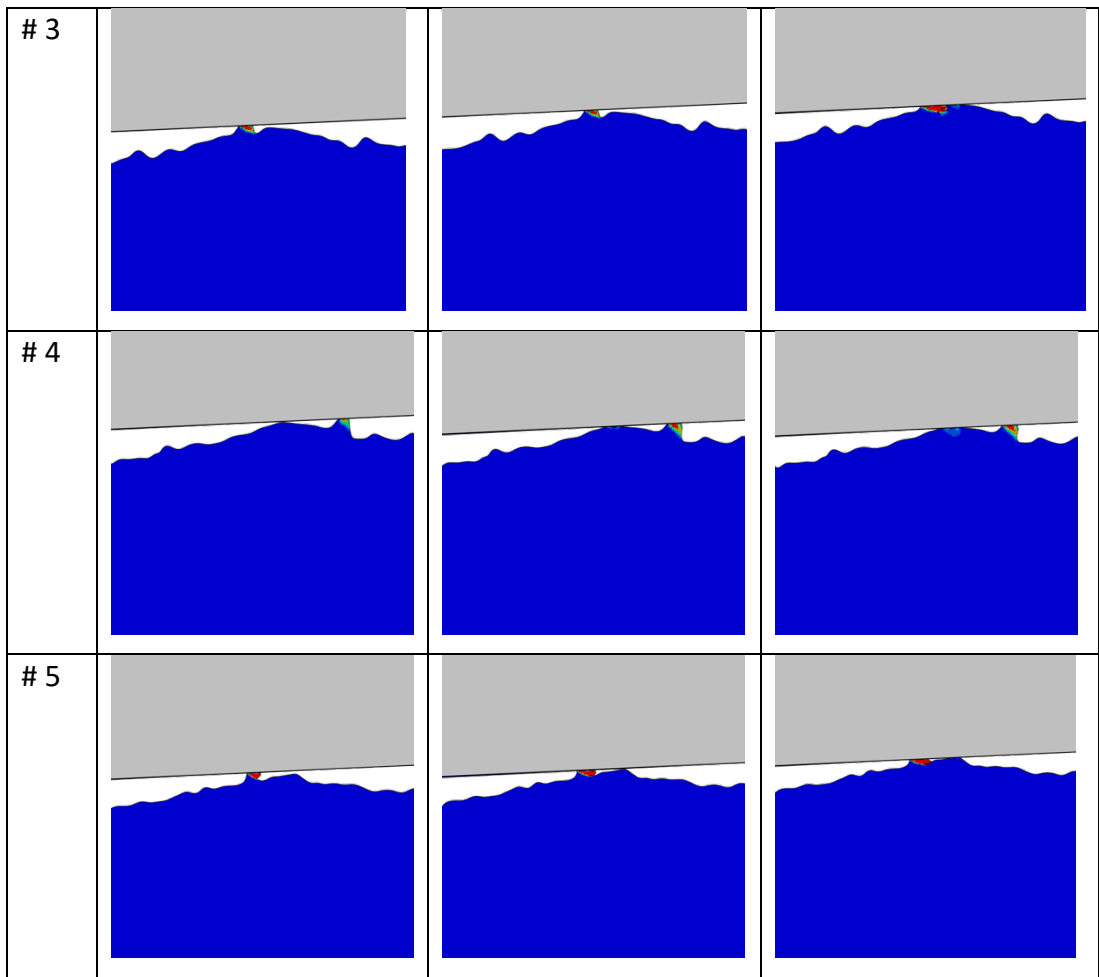
Table 5.17. Evolution of plastic strains within the five highest microgrooved peaks for taper 2.

# 3			
# 4			
# 5			
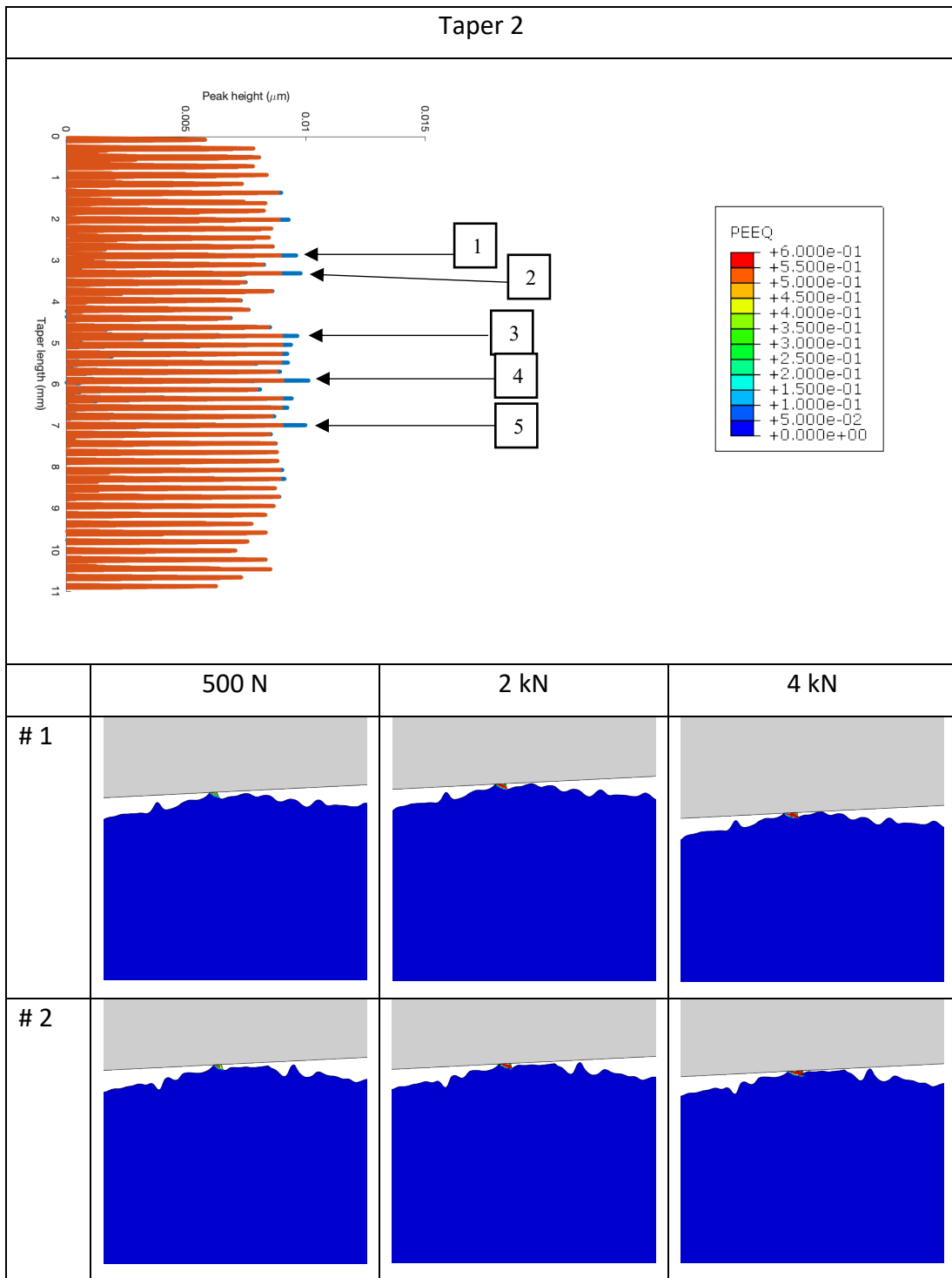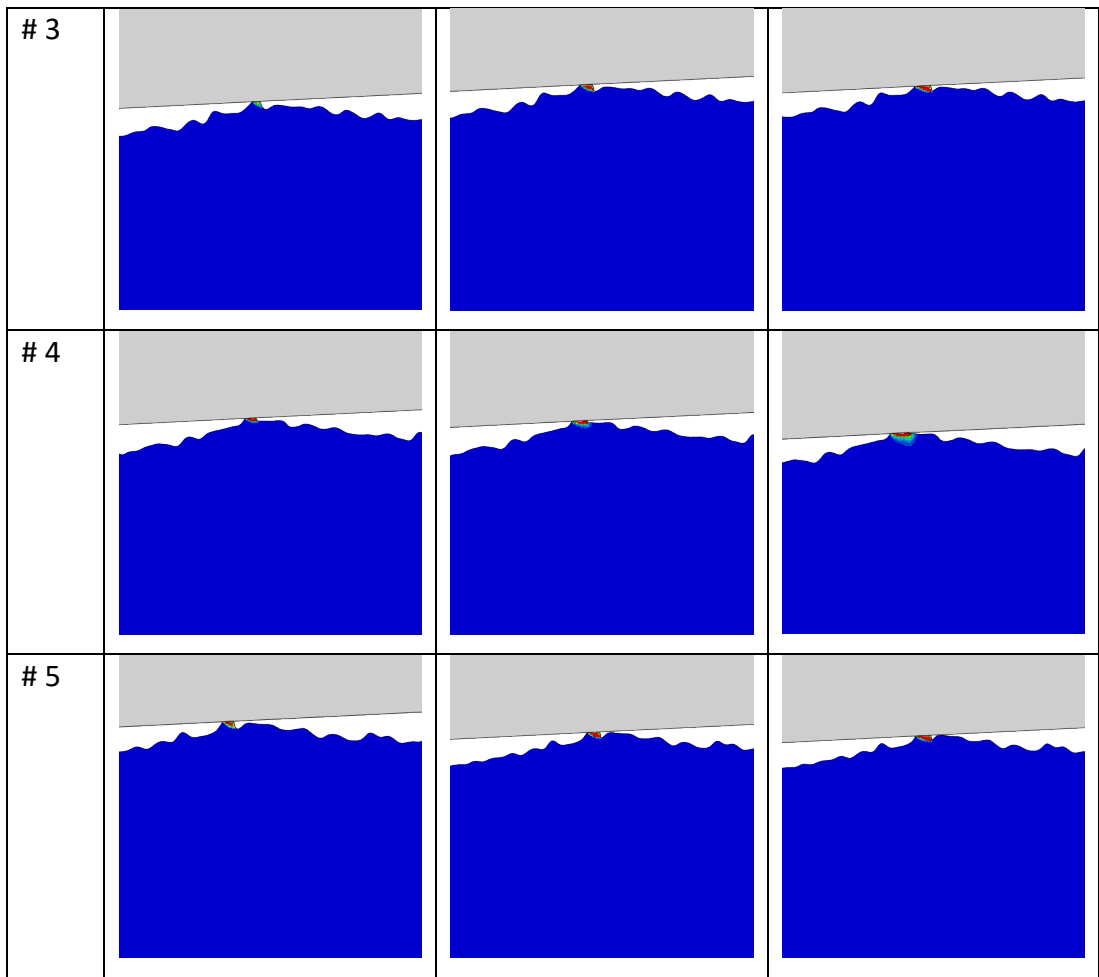
Table 5.18. Evolution of plastic strains within the five highest microgrooved peaks for taper 3.

	500 N	2 kN	4 kN
# 1			
# 2			

# 3			
# 4			
# 5			
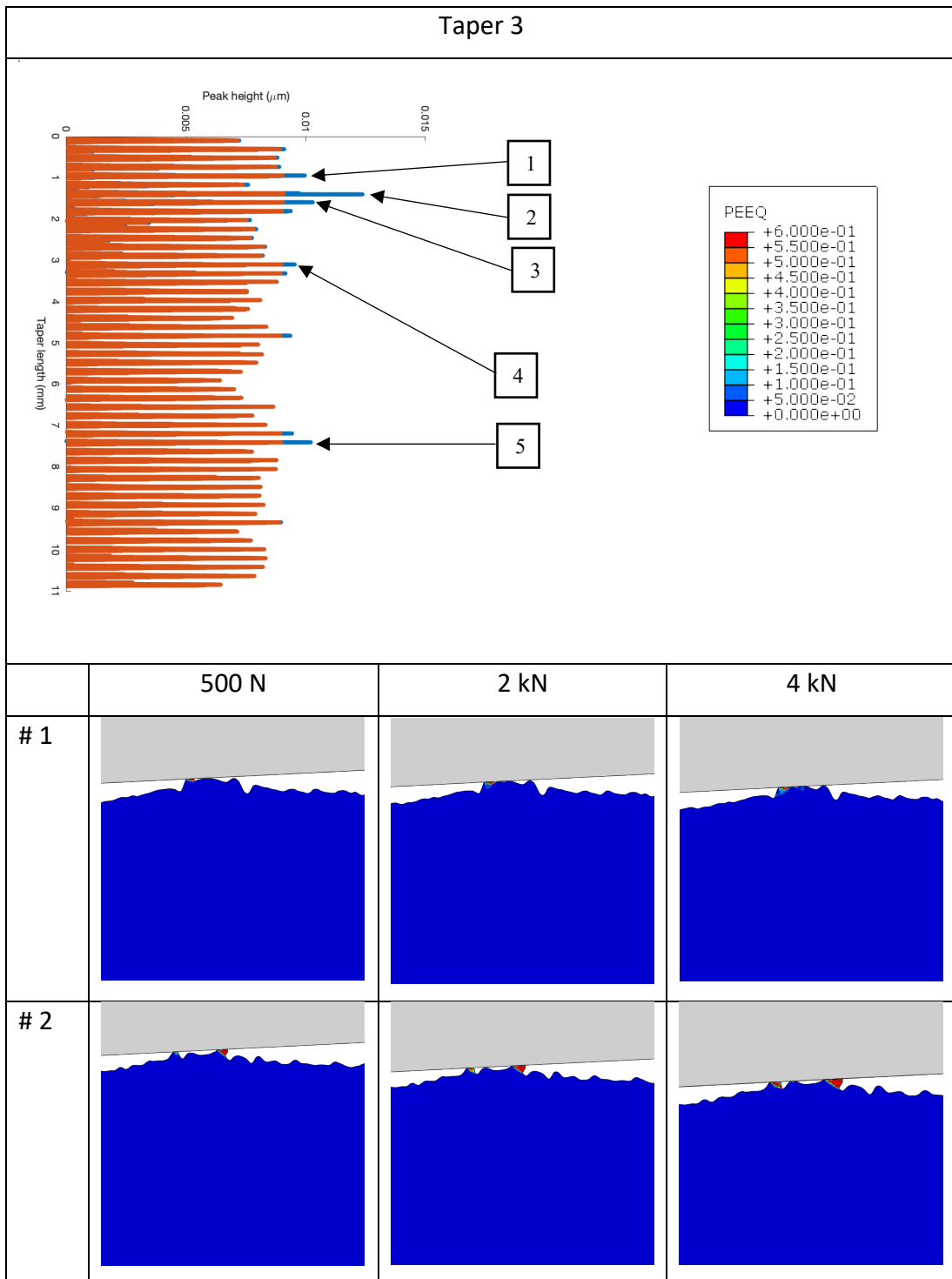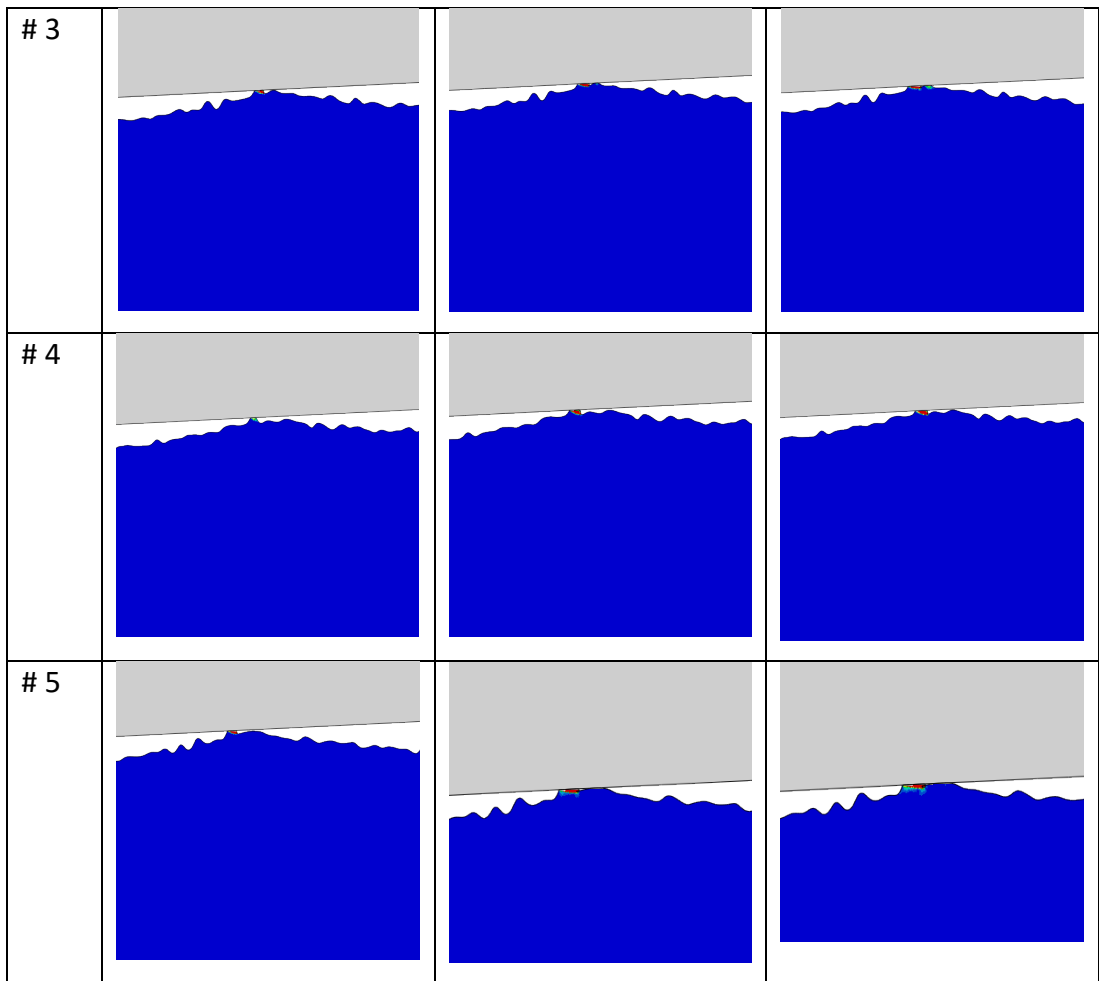
Table 5.19. Evolution of plastic strains within the five highest microgrooved peaks
for taper 4.

	500 N	2 kN	4 kN
# 1			
# 2			
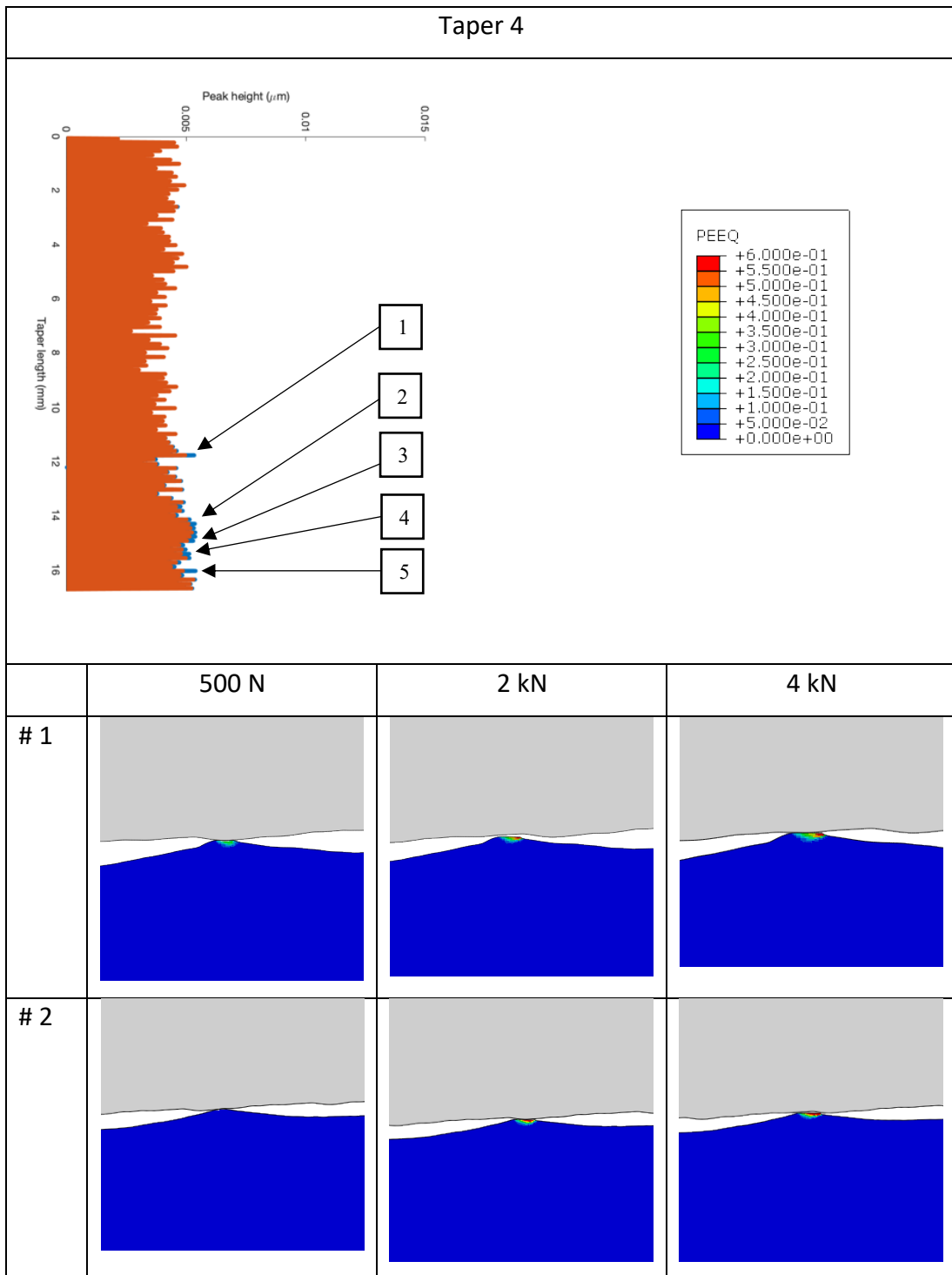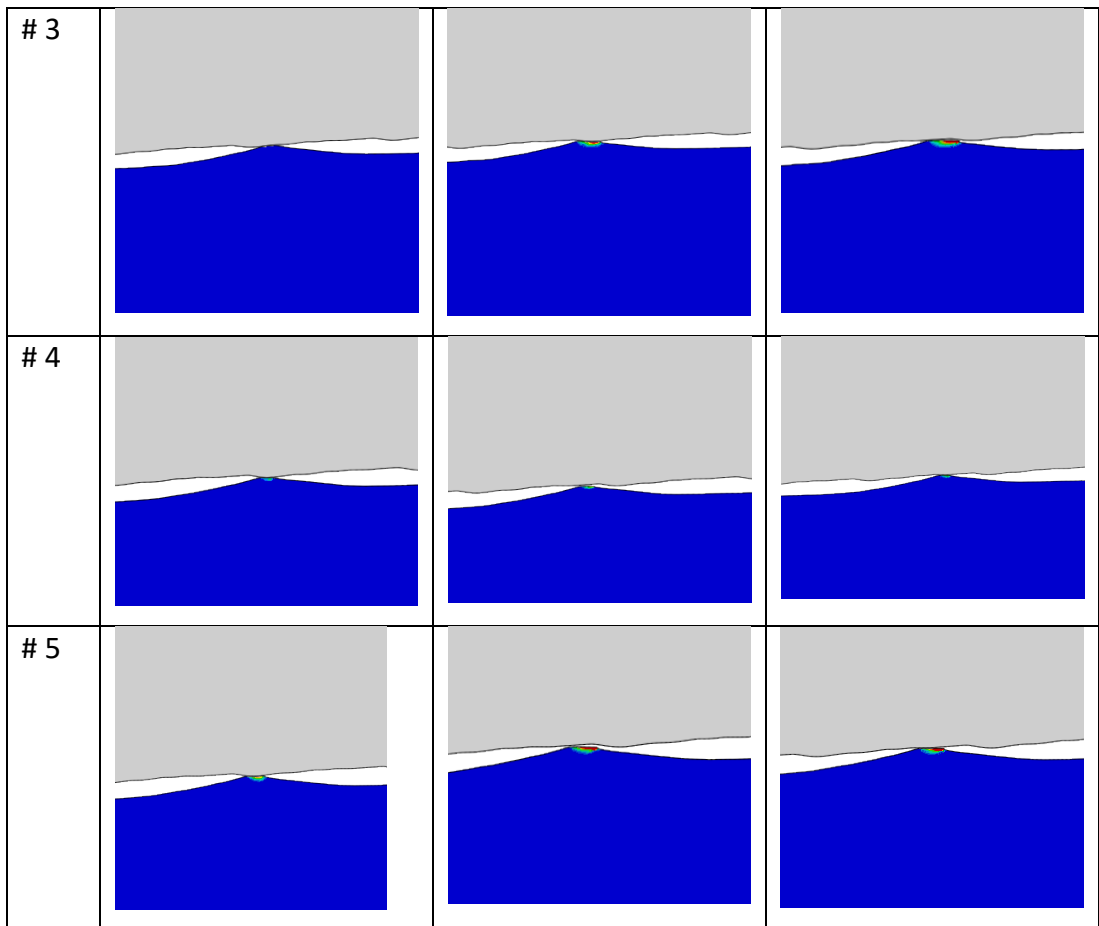
Table 5.20. Evolution of plastic strains within the five highest microgrooved peaks for taper 5.
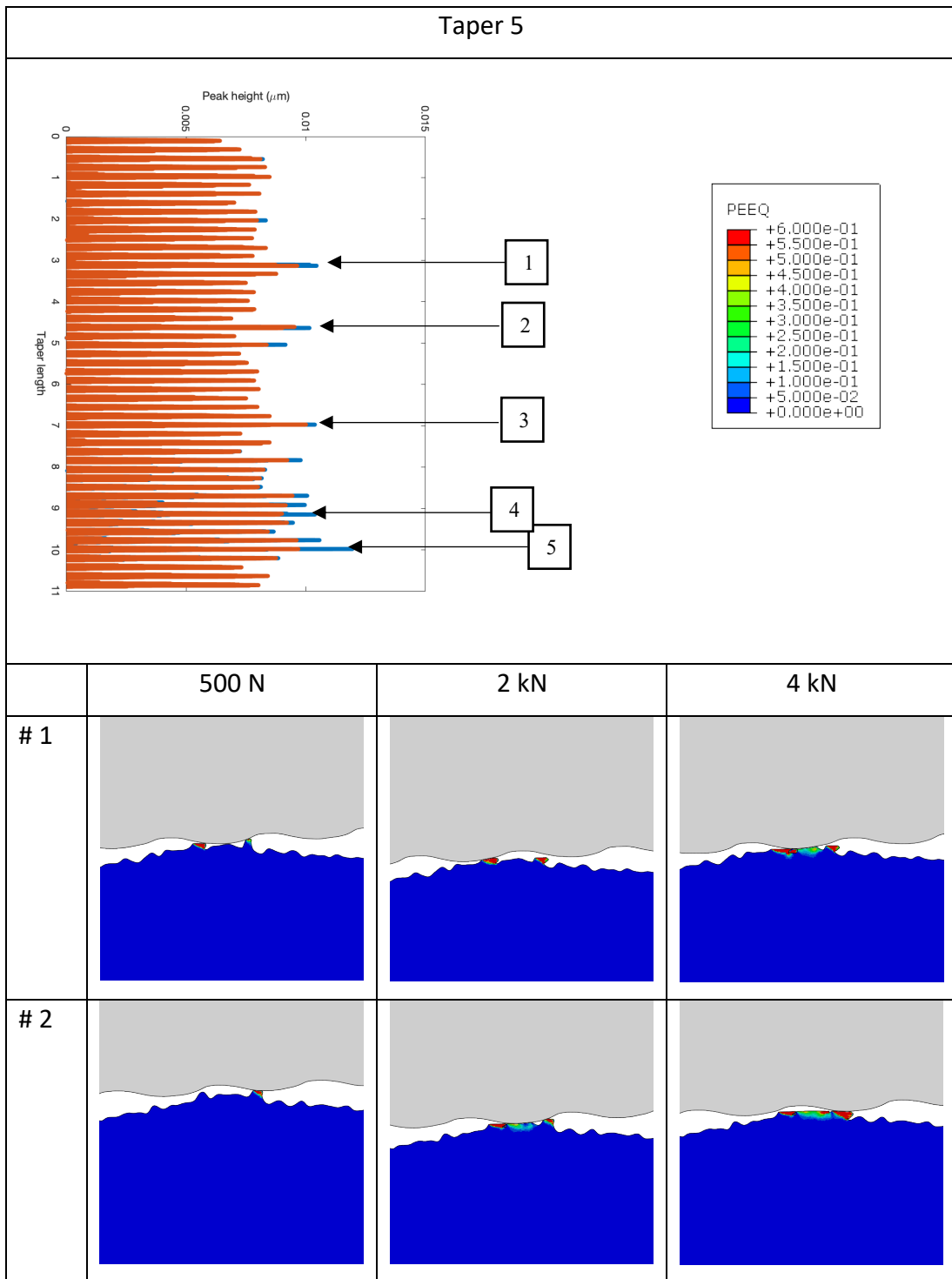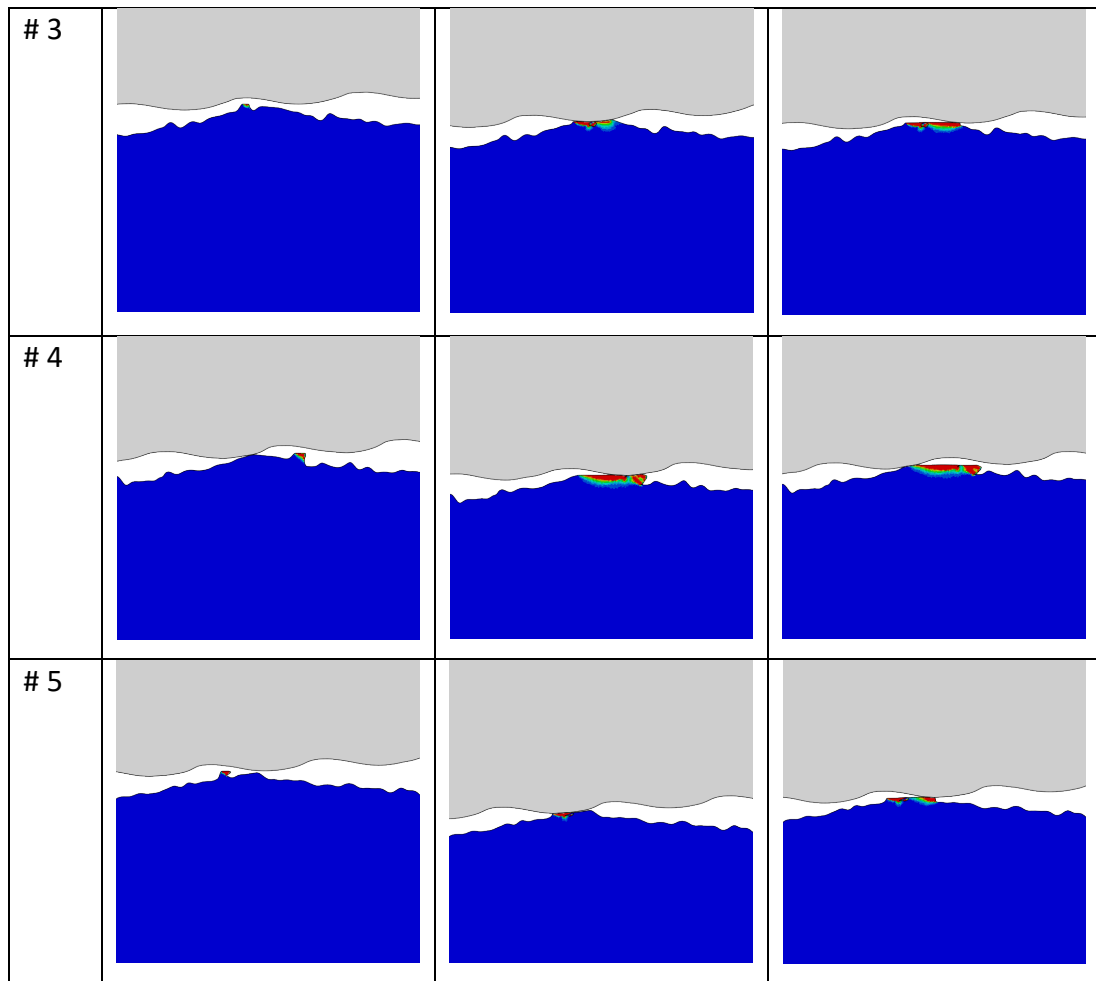
5.4   Discussion

A two-dimensional model of the taper assembly in a total hip replacement that included form, waviness and roughness region in its components' surface has been developed. This is the first time that all these parameters have been reported. The effect of the surface variations at different surface scales in the contact mechanics of the taper interface after assembly showed, for the first time, that noticeable different contact conditions when form, waviness and roughness were considered. The current study confirmed that contact conditions generated in taper interfaces with idealised surfaces are significantly different from those tapers where form, waviness and roughness were considered.

Currently, surface finish in bore and trunnion surfaces is not prescribed by regulation (Dransfield et al., 2021). Typically, the form is removed when investigating the taper surface topography, despite this parameter influencing the outcome of material loss

estimation in wear studies (Dransfield et al., 2021; Racasan et al., 2015a; Walton et al., 2019). Barrelling of the bore surface has been identified to affect the taper angle (Wade et al., 2020), and the current study of the form of tapers supports this observation. As shown in Tables 5.2 and Figure 5.12 the locking area after assembly decreases as the barrelling height of the bore increases, even by very small amounts. The effects of this type of form variation increases with the taper clearance angle, decreasing the contact area and increasing the contact pressure. For tapers with no clearance, despite no changes in the contact area in the taper interface, an increase of contact pressure at the distal and proximal ends from approximately 1 GPa to 2 GPa was observed in tapers with a concave bore. Form barrelling deviations not only affect the material loss estimations, but also enhance the influence of taper clearance in wear and corrosion generation as they affects the parameters of contact pressure and contact area (Fallahnezhad et al., 2017; Kocagöz et al., 2013).

In the study of the contact mechanics in tapers when features of taper components at micro scale regions are included, contact pressures and von Mises stresses were obtained using profile data, including waviness and roughness, of trunnion and bore surfaces. The magnitude of these contact parameters was higher in taper pairs where the trunnion surface was generated from a measured surface profile. Local conditions of microgrooved trunnion peaks of measured profiles in contact with the bore surface comprised up to three-points of contact; in these tapers, plastic deformation was high due to the smaller surface details considered in the model and plastic deformation exceeded plastic strain values of 0.6, which represents the point where the titanium alloy would fail. Surface parameters (Ra, Rz) from the trunnion were not related to the evolution of the contact conditions and plastic deformation along the taper and microgrooved peak regions. For example, in Tapers 1 and 3 similar contact conditions at different assembly forces were found to be different from those conditions in a nominally identical taper (Taper 2). Stresses in the bulk area of the trunnion were not significantly affected by the surface topography (Figure 5.14); stresses distribution were somewhat similar because form and original clearance were removed from the geometries.

Recent FE studies where the waviness of the taper components have been considered (Ashkanfar et al., 2017b; Bechstedt et al., 2020; Godoy et al., 2022; Gustafson et al., 2020a, 2022), have simulated surfaces generated utilising a single sinusoidal function. These models have predicted a uniform contact and plastic deformation in the microgrooved peaks. In the current study peaks with wavelengths as small as 15 μm were found in the taper surface, and it has been shown that not considering frequencies lower than the most dominant spatial frequency will lead to an underestimation of contact pressures and plastic deformation locally. This underestimation would have the consequence of underestimating wear damage in extended studies. Due to the small geometry of peaks represented by smaller dominant spatial frequencies in the PSD of a taper surface, larger contact pressures and plastics strains can be generated when in contact with the opposing taper surface. These small peaks at the top of the microgrooved peak of trunnion surfaces are the first parts to enter in contact with the bore surface. These may stop interacting with the bore as the femoral head advances due to the peak height variation at the bore surface. Results from the current study show that tapers with a higher number of dominant spatial frequencies, generated a higher percentage of microgroove peaks with plastic strains that would lead to damage on the surface than those tapers with fewer spatial frequencies. The clinical relevance of the number of spatial frequencies in taper component surfaces needs to be further studied, as they could be explanation behind the contradicting conclusions regarding the advantages of utilizing microgrooved tapers in the literature (Mai et al., 2022; Mueller et al., 2021; Munir et al., 2015; Panagiotidou et al., 2013; Pourzal et al., 2016; Stockhausen et al., 2021). In the present study it was observed that including the bore's real surface topography significantly changes the contact mechanics in the taper interface, supporting recent FE studies regarding the importance of bore surface details (Gustafson et al., 2022; Lundberg et al., 2015).

Predicted contact conditions generated by the interaction of different taper topographies in this study resulted in an irregular development of contact conditions as the femoral head was assembled into the trunnion (Figure 5.15), contradicting previous studies where contact in the taper interface steadily increases with

assembly force (Donaldson et al., 2014; English et al., 2015; Farhoudi et al., 2017; Raji & Shelton, 2019; Witt et al., 2015). The uneven evolution of contact conditions is due to the flattening of microgroove peaks that trunnions experience as the femoral head bore moves along the trunnion axis during assembly. This flattening/damage process in the taper surface has been previously suggested to occur during disassembly of tapers in retrieval studies or during *in vivo* loading (Arnholt et al., 2017; Higgs et al., 2016; Kocagöz et al., 2013; Whittaker et al., 2017; Witt et al., 2015), however the present results suggest that this occurs during taper assembly. This has the implication that counting the number of peaks plastically deformed after assembly and disassembly will result in an over estimation of the contact conditions of experimental and retrieval studies (Arnholt et al., 2017; Brock et al., 2015; Dransfield et al., 2019; Kocagöz et al., 2013; Witt et al., 2015).

Contact conditions within the taper interface can be linked to the surface details found in the waviness and roughness regions of the taper components. For example, in tapers 1 and 5 the same trunnion surface profile was used to generate their trunnion geometry and were assembled with different bore surfaces: a flat line (taper 1), simulating a smooth surface, and a measured bore surface (taper 5). This generated distinct contact conditions for each taper; in taper 5 the number of trunnion peaks in contact with the bore at 4 kN was 35 peaks compared to 42 peaks in contact for taper 1. Interestingly, peak height profiles at 4 kN of the trunnions for these tapers were similar despite having different numbers of peaks in contact with the bore (Table 5.7) due to the peak flattening during the assembly process of the taper.

Commonly used roughness parameters to describe the surface of roughness in tapers such as Ra, Rz and largest peak wavelength were different between the trunnion and bores used for this study. Specifically, the contribution of peak wavelengths in the taper surface components. Measured surfaces are evidently different from the surface created with a single sinusoidal wave. In the current study, PSD estimations of bore and trunnion surfaces showed that trunnions present more dominant spatial frequencies than the bore surfaces, recognising that only 2 bores were scanned. This

characterisation of the surface roughness can predict the functionality of these surfaces and contact mechanical properties, such as friction, wear, and lubrication (Jacobs et al., 2017). The effect of the number of dominant spatial frequencies in the taper surface can be seen when comparing tapers 1 and 3 against taper 2, the former presented up to seven dominant frequencies and generated similar contact conditions at different assembly forces, in contrast to taper 2 that only had five dominant peak frequencies and its predicted contact response was different. Smaller spatial frequencies with a relatively higher PSD power represent smaller peaks in the taper component surface profile; these smaller peaks will generate smaller contact areas when in contact with the bore surface increasing the local contact pressure in both surfaces. This difference in the number of spatial frequencies found in the PSD estimation of taper surfaces can be associated with different surface finishes and manufacturing methods (Krolczyk et al., 2016; Podulka, 2022). Furthermore, polished and unpolished smooth and rough surfaces have been associated to different corrosion and wear processes highlighting the importance of surface finish in tapers (Fischer et al., 2023). A polished surface finish will remove smaller peaks associated to smaller wavelengths increasing the contact area between the bore and trunnion, and reducing contact stresses that can damage the trunnion surface. More investigations are needed to find out if these spatial frequencies are normal in commercially available taper components and how these frequencies affect their mechanical response during and after assembly.

The obtained roughness parameters in the present study agree with the literature in retrieval studies, in which a large variation in taper geometries and topographies have been reported between and within manufacturers (Hothi et al., 2015; Munir et al., 2015; Stockhausen et al., 2021; Whittaker et al., 2017). Despite the small population of tapers used to generate the FE model for the current study, it has established a better understanding on the role of surface details at different scales. Future studies should consider a roughness analysis which is sufficiently detailed, including PSD estimations, to better describe the taper surfaces when investigating the contact mechanics and tribocorrosion in taper interfaces. Taper surface variations caused by different manufacturing methods and manufacturers have not

been previously considered, and further investigation on the implications in the topography of taper components is required. From this initial work, the characterisation of *both* contacting surfaces has been shown to be important to understand the damage mechanisms that have been observed in retrieval and experimental studies, in particular those that involve contact conditions such as fretting wear and fretting corrosion.

The FE model used for this study can be further developed to include a material failure model that can remove those elements that reach material failure. Fretting-corrosion and crack propagation processes are dependent on the microstructure of the surface material which is determined by the surface finish method (Liu et al., 2022; Mai et al., 2022). As this study has shown, variations in the waviness and roughness regions have a considerable influence in the local mechanics in the interface between the bore and trunnion surfaces and should be considered when developing wear and fretting-corrosion models in tapers. Measured surface profiles of trunnions and bores can also yield information on the role of waviness and roughness regions on the coefficient of friction in the taper interface (Bitter et al., 2016; Mulvihill et al., 2011); the coefficient of friction has been identified to affect the overall taper performance (Donaldson et al., 2014; English et al., 2015, 2016). Relating a coefficient of friction to the interacting surface profiles would provide information on the taper performance resulting in the improvement the taper surface design. The mechanical response of the taper during cyclic loading and loading conditions representative of the patient's activities such as walking, when measured surfaces of the taper components are considered, needs to be investigated. As highlighted throughout the present study, waviness variations and roughness regions of taper surfaces play a significant role in the taper local contact mechanics.

5.5   Conclusions

The current study has established that idealised surfaces generated with a single sine wave do not fully represent real taper surfaces and generate smaller contact stresses and different contact conditions when assembled with a femoral head. A more

realistic simulation of the taper assembly and contact conditions in the taper interface is important when studying the mechanical response of a taper as they affect taper interlock mechanics and overall strength of the taper. This study showed that idealised surfaces significantly underestimate the contact mechanics of the taper. Surface variation in roughness and waviness regions of measured surfaces need to be considered when studying and modelling taper micromotions, wear and fretting-corrosion. Understanding the role of surface topography in THR devices will enable optimal taper design parameters for material combinations to be established with a view to reducing the propensity of modular tapers to fretting-corrosion.

6 Static coefficient of friction modelling for taper interfaces in THRs

6.1 Introduction

The contact environment in the taper interface is determined by the topology of the interacting surfaces of the bore and trunnion components, as in shown in Chapter 5. Contact parameters such as contact area, contact pressure and stresses generated in the taper surface are of interest as they can be used to predict the tapers stability as well as to estimate wear and corrosion damage that may occur once assembled. Corrosion and fretting in the tapered junction between the femoral head and femoral stem has been identified as one of the causes of the failure of THR devices as they can introduce metal particles into the body which adversely interact with the body causing inflammation and loosening of the implants (Dyrkacz et al., 2013; Friedebold, 1976; Jaekel et al., 2014; Mueller et al., 2021; Wiklund & Romanus, 1991). The extent of damage and severity originating from fretting-corrosion in the taper interface has been associated with many factors related to taper design, implantation technique and patient's biometrics and activities (Wight et al., 2017). Retrieval, experimental, and *in vitro* studies have associated femoral head size, taper mismatch, implant alignment, assembly force, assembly conditions and surface finish with the generation of relative motions and contact conditions. Modelling using the finite element method has been used to study how these factors affect the mechanical response of tapers as an alternative to experimental setups that can be costly and time consuming (Ashkanfar et al., 2017a; English et al., 2015; Gustafson et al., 2022). *In silico* studies also allow the investigation of parameters that can be hard to obtain experimentally without interfering with the taper contact environment or geometry such as contact parameters between the femoral head bore and trunnion and stresses in the taper device (Falkenberg et al., 2019; Witt et al., 2015).

In FE models, contact conditions are simulated by defining parameters which include the contact algorithm, frictional model, and coefficient of friction (COF). The coefficient of friction determines the contact environment and mechanical response at the taper interface. Indeed, FE studies of tapers have identified that the COF in the

taper interface influences the micromotions that generates wear; as a higher value generates lower relative motions (Donaldson et al., 2014; English et al., 2015, 2016; Farhoudi et al., 2015; Mueller et al., 2021). Despite understanding the effect of the COF on the wear damage in taper interfaces, its value assigned to the taper surfaces has varied, ranging from 0.15 to 0.55; in other applications friction coefficients can be found in range from 0.3 to 0.8 in similar couple materials (Bitter et al., 2016; Mulvihill et al., 2011). The COF is known to be affected by lubrication, material properties of the interacting surfaces, adhesion of the materials, and loading conditions (Green, 1955; Mulvihill et al., 2011; Patil & Eriten, 2014). In the current application, due to the sliding loading conditions (the femoral head sliding into the trunnion) during assembly of the taper, two factors contributing to the coefficient of friction will be considered in the current study, namely adhesion and deformation.

The deformation mechanism stems from energy dissipation during the plastic deformation experienced by surface asperities, thus the surface conditions and mechanical properties of the interacting surfaces play an important role. The dominant mechanism of friction can change with the extent of penetration of the two surfaces at the roughness/waviness/form scales. The penetration increases the deformation mechanism during sliding, while decreasing the influence of adhesion (Green, 1955; Malyshev, 2014; Mulvihill et al., 2011). Adhesion can be assumed as a 'cold-welded' junction as a result of the bonding of the two material surfaces. Considering the role of surface conditions on the global COF, it is however, not surprising to find that a wide range of coefficient of friction values in commercially available taper devices have been used as there is a large variation of taper surface finishes in both bore and trunnion surfaces. Currently, the global COF in tapers is obtained experimentally rather than predicted, and the role of the taper surface topography and taper contact mechanics in the determination of a global COF is not well defined.

The coefficient of friction is defined as the ratio of the tangential force to the normal force acting on the bodies of interest. FE models have been used to model the COF of Ti-alloys surfaces using single asperities modelled as wedges based on Green

observations on sliding friction (Green, 1955; Hu et al., 2021; Mulvihill et al., 2011). The current study presents a novel methodology to estimate the global coefficient of friction in interacting measured taper surfaces and, and thereby, predict the mechanical response of tapers. The effect of adhesion, simulated by including a local coefficient of friction in the contact definition, and topography surface on the generation of tangential forces in taper surfaces was studied. Surface pairs of different surface roughnesses were characterised, assembled and then translated; the tangential and normal forces generated were used to estimate a global coefficient of friction of the surface pair. In the second part of the study, the resulting global COF was introduced into a 3D FE model of a whole taper loaded over a single walking cycle and the predicted relative motions analysed to study the sensitivity of the global coefficient of friction in the generation of micromotions in the taper interface.

The following research questions were tested in the present study:

- Deformation of surfaces and surface adhesion, represented by local COF in FE models, influence the estimated global COF in taper surface pairs.
- FE models of rougher surfaces will generate smaller relative motions.

Part 1 – Estimation of global COF

6.2   2D Finite element method

6.2.1   Materials and methods

Roughness parameters (Ra, Rz) and surface profiles of three bore and three trunnion surfaces were used to generate 2D FE models and COF was estimated at 400 N, 800 N and 1600 N normal forces. The contact pressures generated due to the interaction of the surfaces is also analysed.

Surface profiles from Tapers 4, 5 and 6 (Idealised) as described in Chapter 5 were used for the present study. In tapers 4 and 5 both surfaces were measured from commercially available trunnions and bores, while the surfaces of taper 6 were generated using a linear (bore surface) and sinusoidal (trunnion surface) function.

Ra, Rz roughness parameters of tested surfaces were obtained as described in Chapter 5. Surface characteristic and methodology for those surfaces measured and artificially generated are also described.

6.2.2   Loading and boundary conditions and calculation of COF - COF model

A two-dimensional model of two interacting surfaces representative of a femoral head bore and 12/14 trunnion surfaces was developed using Abaqus 2020 Explicit. Model boundary and loading conditions were based on experimental work to obtain the static COF of taper surfaces (Bitter et al., 2016). Two rectangular geometries of 2.5 mm height and 5 mm length were created, and surfaces profiles of the tapers were included along the length of the geometries. The blocks were assembled so the surface profiles faced each other (Figure 7.1). A global coefficient of friction was included in block's surface interaction as a proxy for the adhesion between surfaces. Contact between the bore and trunnion blocks, and their respective mesh sizes were defined as described in Chapter 5 using global COFs ranging from 0 to 1. Explicit model's kinetic energy was ensured to be less than 10% of the internal energy throughout assembly and sliding steps for all models so they can be considered static.
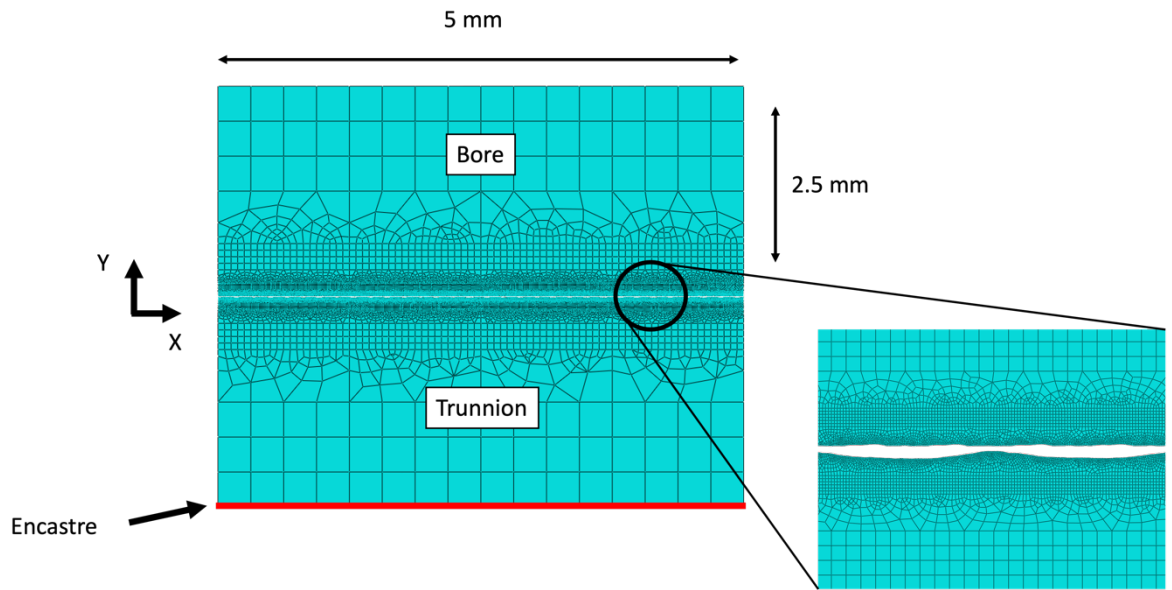
Figure 6.1. Schematic showing the geometries utilised in the 2D FE model to estimate COF.

The model consists of two steps namely assembly and sliding, in both steps the base of the trunnion surface geometry (bottom geometry), the red line in Figure 6.1, is restrained to prevent rotation and translation. To decrease computation time of the model, the bore surface geometry was defined as a rigid geometry. In the first step the bore is displaced against the trunnion surface at a speed of 0.5 mm s^{-1} in the Y direction reaching a reaction normal force of 400 N, 800 N, and 1600 N. During the following sliding step, the bore surface geometry is translated in the X direction relative to the trunnion surface geometry at a velocity of 130 μm s^{-1} for 2.5 s. The distance is equivalent to approximately 1.8 peak wavelengths established in the analysis of the trunnion surfaces. Once the normal reaction at the trunnion encastre reached the desired magnitude, the bore rigid block was only allowed to move along the X-axis. Velocity was introduced into the rigid body in a smooth step. To study the adhesion contribution in global COF in measured surfaces, another set of FE models for a normal force of 1600 N were generated and a frictionless contact interaction was defined. The tangential and normal forces throughout the sliding step are recorded and an estimated transient coefficient of friction is obtained utilising Equation 1.

$$COF = \frac{Q_i}{P_i}$$ <div style="text-align: right">Eq. 1</div>

Where Q is the tangential force, and P is the normal force and i is the current increment (total increments = 200) in the sliding step.

6.3 Results

6.3.1 Surface analysis

Roughness surface analysis for taper 4, 5 and idealised surfaces (taper 6) are presented in Chapter 5 section 5.5.1.

6.3.2 Effect of normal force and adhesion in global COF.

6.3.2.1 Contact conditions during assembly and sliding steps

von Mises stresses generated in the trunnion surface of taper 5 were different between assembly, and the sliding steps shown in Figure 6.2. An irregular contact between the bore and trunnion surfaces was generated due to the waviness of the taper surfaces in both assembly and sliding steps. The plastic deformation threshold (von Mises stresses > 1200 MPa) was reached in all conditions and all tested taper pairs. During the assembly step, Hertzian stress distributions were generated due to the contact interaction between the bore and trunnion surface topography, distributions were symmetrical around the contact of the trunnion peaks with the bore surface along to the Y axis. von Mises stresses values increased as the normal force increased and were not affected by the local COF. During the sliding step, Hertzian stress distributions slightly rotated around the contact origin due to frictional forces and reaction forces generated due to the topography interaction between the bore and trunnion surfaces (Figure 6.2c). Indeed, when a friction coefficient was not included on the taper 5 model, Hertzian stress distributions still experienced a slight rotation due to the topographies' interaction of the bore and trunnion surfaces.

a)

400 N	
Assembly	Sliding
800 N	
Assembly	Sliding
1600 N	
Assembly	Sliding

b)

0	
Assembly	Sliding
0.21	
Assembly	Sliding
0.57	
Assembly	Sliding
0.8	
Assembly	Sliding

c)
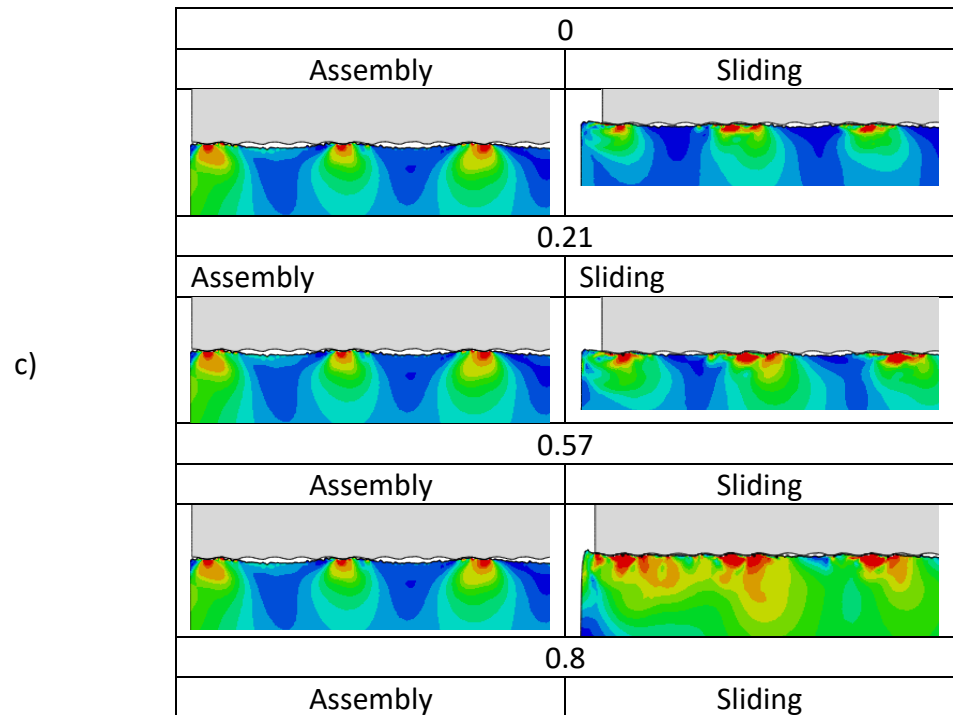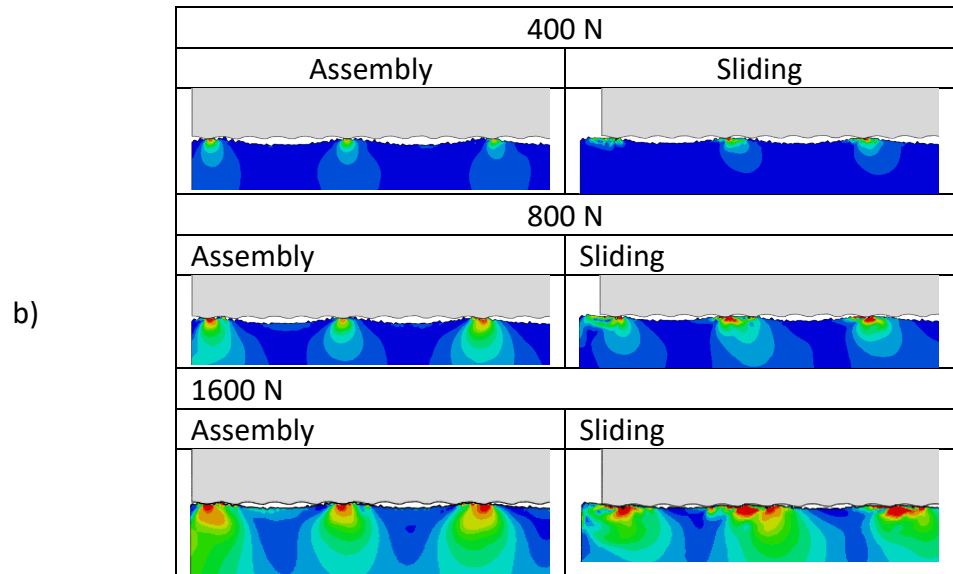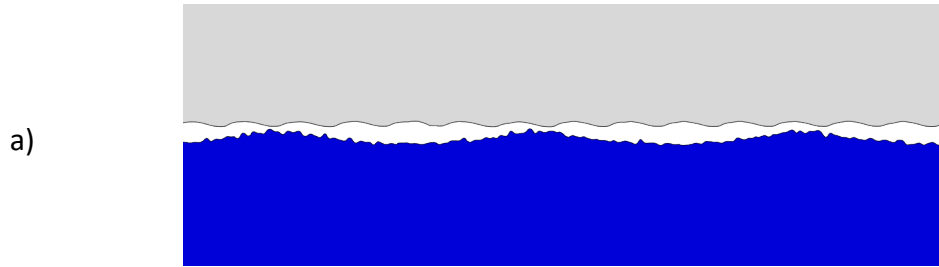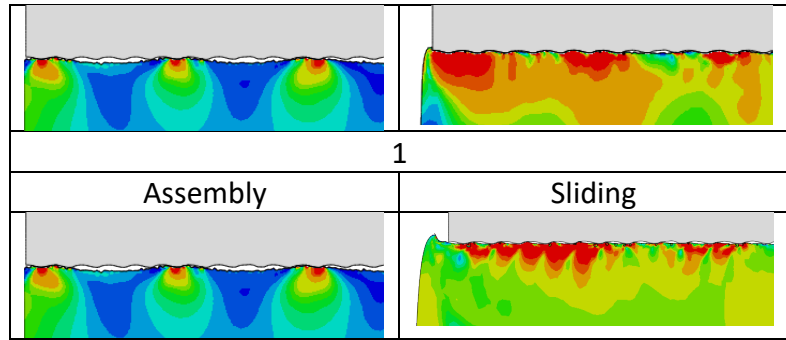
Figure 6.2 Taper 5 bore and trunnion surfaces (a) before assembly, (b) von Mises stresses generated at 400 N, 800 N, 1600 N assembly forces assuming a local COF of 0.21 during sliding step, (c) von Mises stresses generated at different local COF values at assembly and during sliding steps at an assembly force of 1600 N.

The generated contact pressures between the surface pairs at the end of the assembly step, Figure 6.3, show that contact pressures increased as the normal reaction force increased in all tested tapers. Different pressures were generated between tested tapers where tapers with measured surfaces generated larger contact pressures of up to 3.02 kN at 1600 N compared to the taper with idealised surfaces (1.29 kN). The contact pressures did not increase linearly with the reaction normal force in tapers with measured surfaces. Local COF did not affect the contact pressure after the assembly of the surfaces.
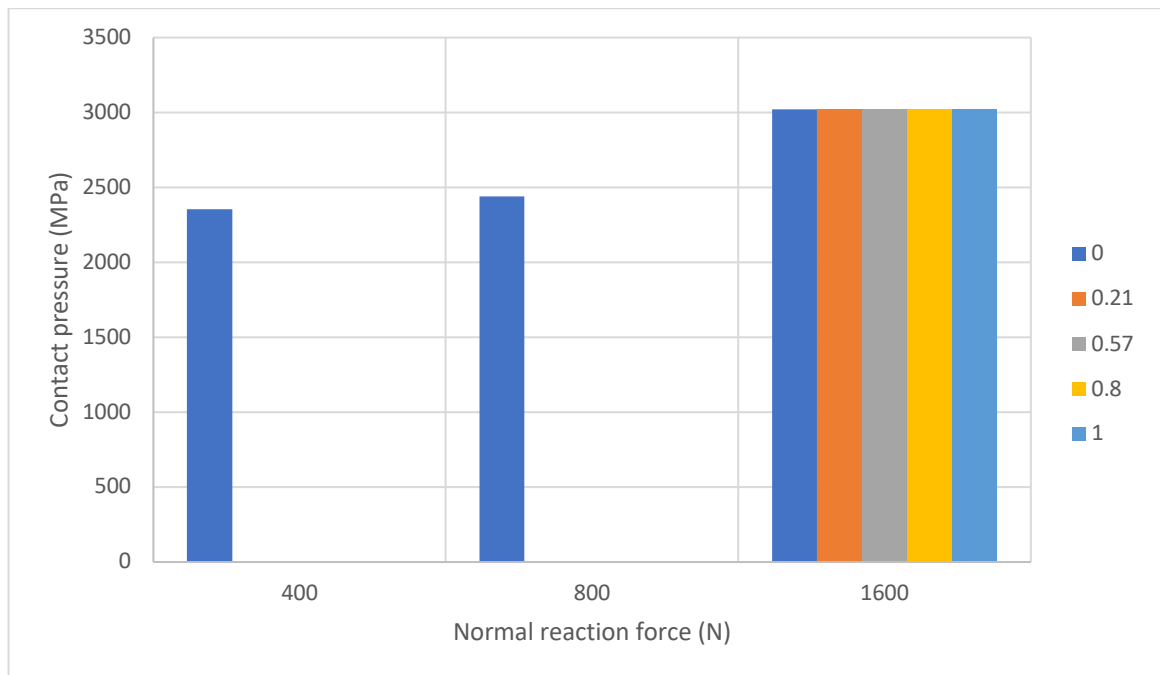
Figure 6.3 Contact pressure at the end of the assembly step at 400 N, 800 N and 1600 N and different local COF normal reaction forces for taper 5.

6.3.2.2 Estimated global COF

Obtained normal, tangential, and estimated transient COF for taper 5 at different normal reaction forces and local COF during the sliding step are presented in Figure 6.4. Normal force decreased slightly during the sliding step due to the bore surface sliding away from the trunnion surface causing the plastically deformed trunnion microgrooved peaks to stop interacting with the bore surface geometry. Tangential force was influenced by local COF and normal reaction forces. Tangential force throughout the sliding step was generated in a series of waves with a decreasing amplitude and wave height influenced by normal force. This behaviour was originated by the interaction of the different spatial frequencies that conform the trunnion and bore topographies.

a)

400 N		
Normal force	Tangential force	Estimated transient COF

800 N		
Normal force	Tangential force	Estimated transient COF

1600 N		
Normal force	Tangential force	Estimated transient COF
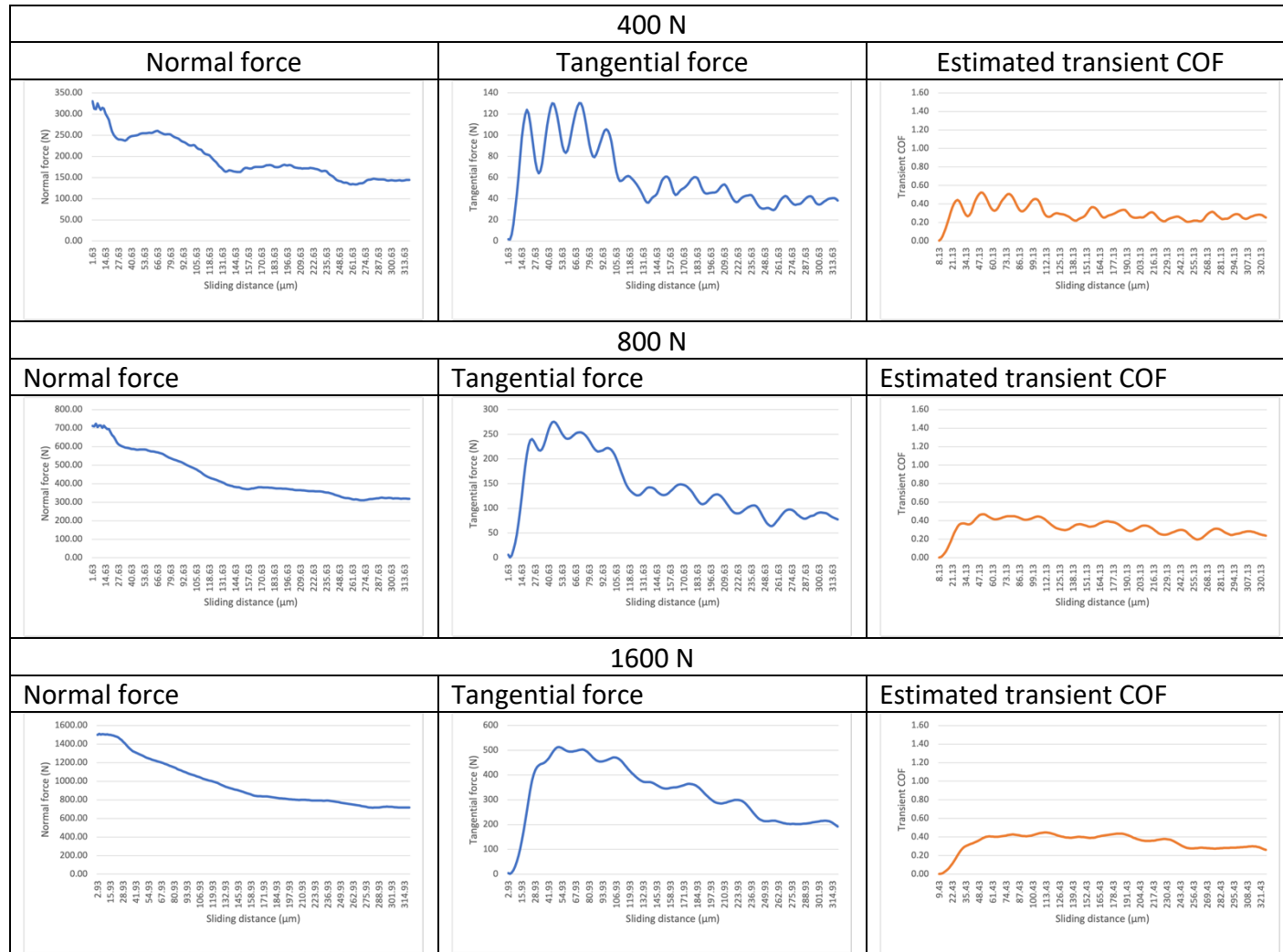
b)
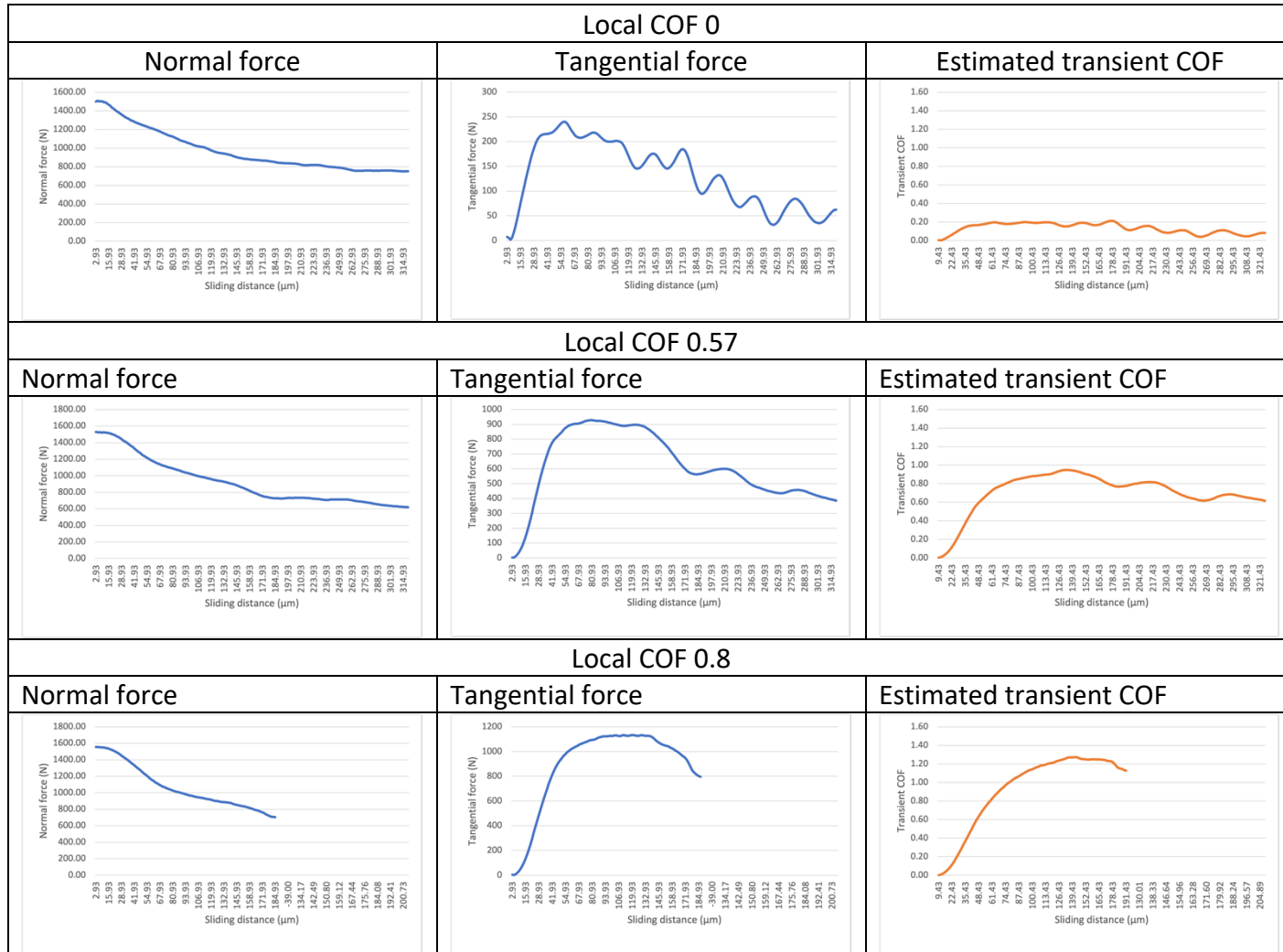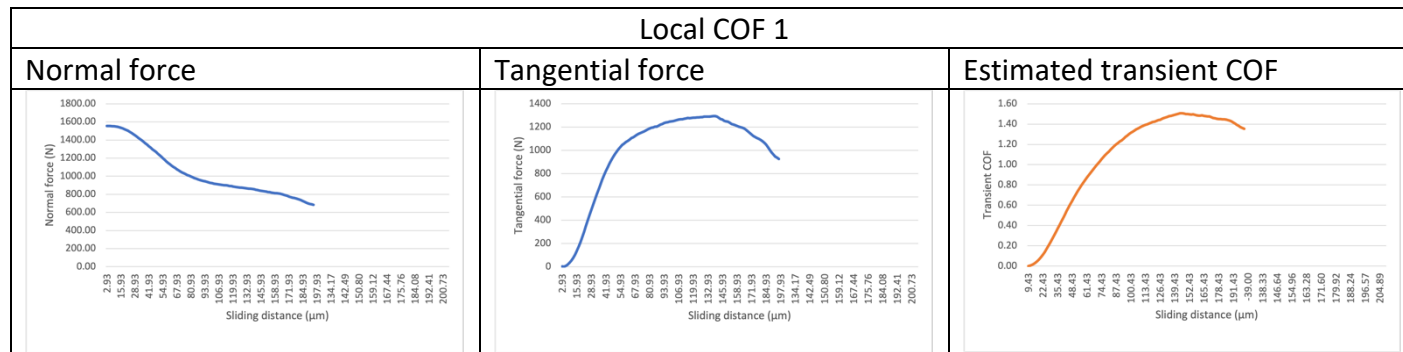
Figure 6.4. Normal and tangential forces and estimated transient COF for taper 5 at (a) normal forces of 400 N, 800 N, 1600 N and (b) at different local COF values at 1600 normal force. Models with * did not reach the final sliding position due to convergence issues produced by the large deformations.

Transient coefficient of friction during the sliding step was determined by tangential forces. A global estimated COF was determined by using the maximum transient COF over the sliding step, as the transient COF values after the maximum represent the interaction of deformed trunnion peaks with the bore which are no longer representative of the roughness parameters of the surface pairs; these peaks will continue to flatten as the bore surface advances as shown in Figure 6.5. The global estimated COF was not affected by normal force. However, local COF influenced the global COF reaching up to 1.44 when a local COF of 1 was considered (Figure 6.6). Removing the coefficient of friction in the contact definition of the surface contact interaction between the FE models of the bore trunnion did not affect predicted normal forces; indeed, however, tangential, and estimated COF were affected.
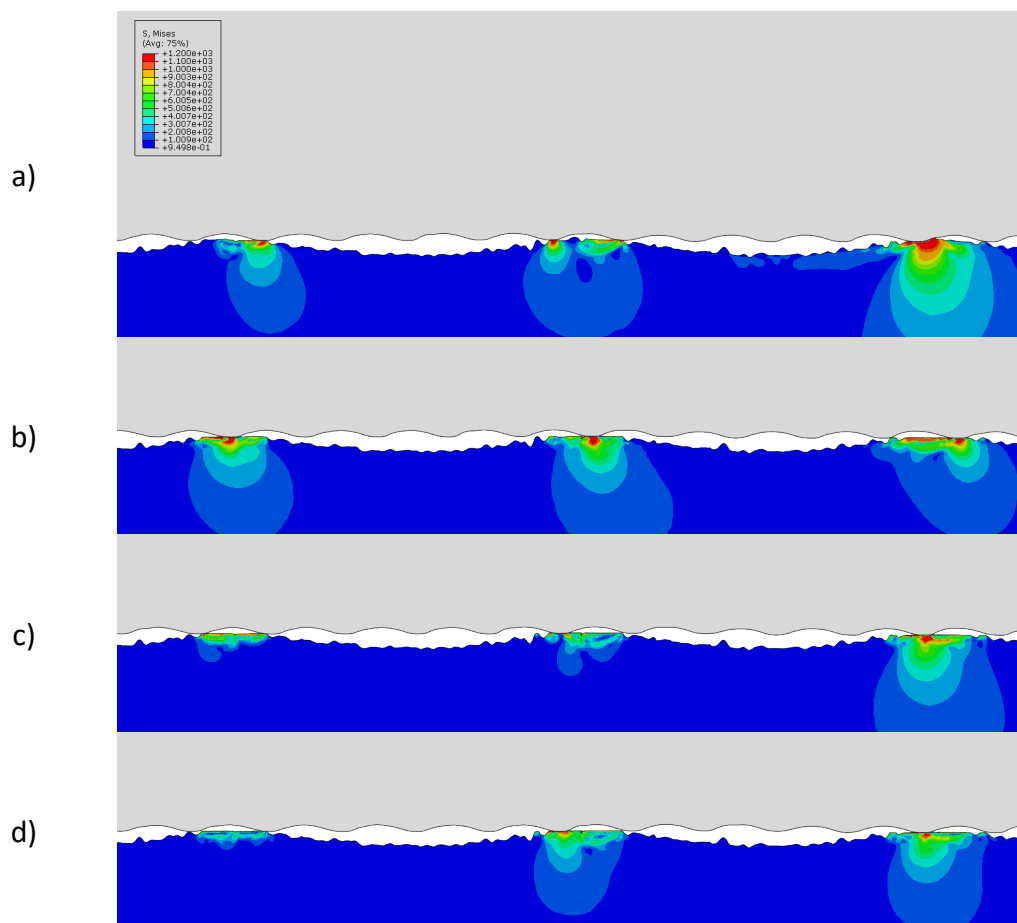
Figure 6.5. Flattening of the microgrooved peaks during sliding step in Taper 5 at sliding distances of (a) 52 µm, (a) 104 µm, (a) 208 µm, and (a) 320 µm.
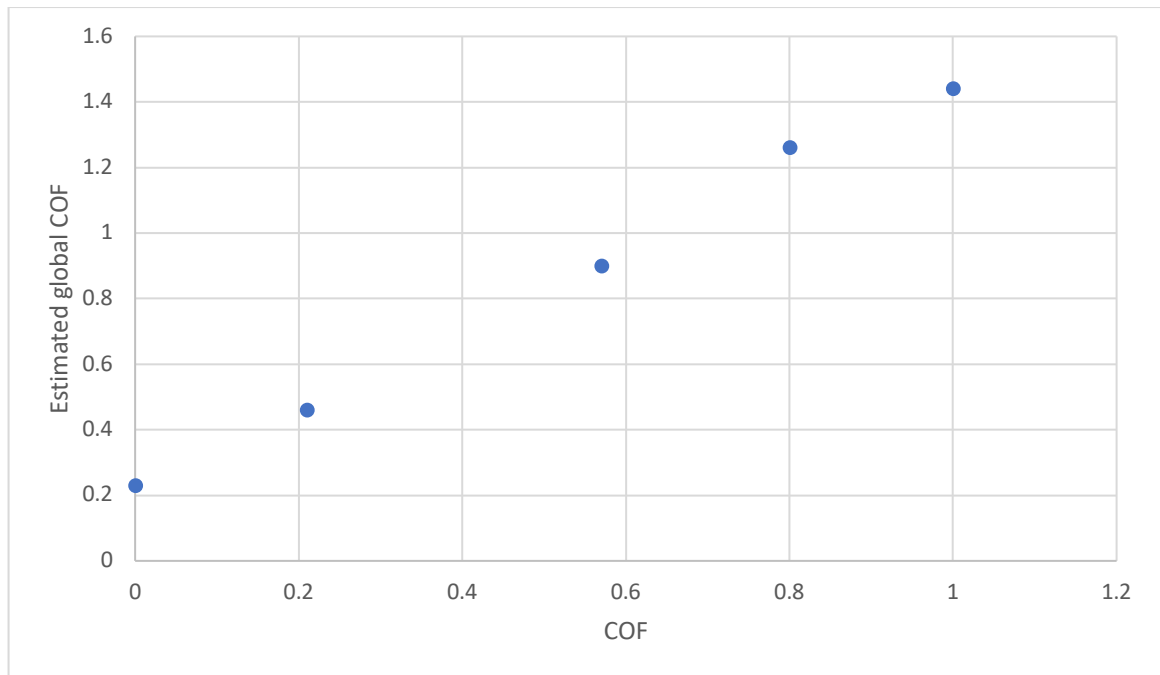
Figure 6.6. Global estimated COF determined from maximum transient COF at different local COF in taper 5 surface pair.

6.3.3   Effect of surface topography of taper components in COF

When considering surfaces with different topographies for the bore and trunnion geometries, the global COF was determined by the surface roughness and local COF. Contact pressure generated in the interface of the taper components was determined by the coupled topographies; tapers 5 and 4 generated greater maximum contact pressure compared to those generated by the idealised taper (Figure 6.7). For all taper couplings, contact pressure generated at the end of the assembly step increased as the normal reaction force increased. von Mises stress distributions were influenced by features that make up the surface topographies. Tapers 4 and 5 generated irregular stress concentration and contact areas between trunnion and bore surfaces at assembly and sliding steps, whilst in the idealised surface pairs, the stress concentrations were the same along the surface.

183
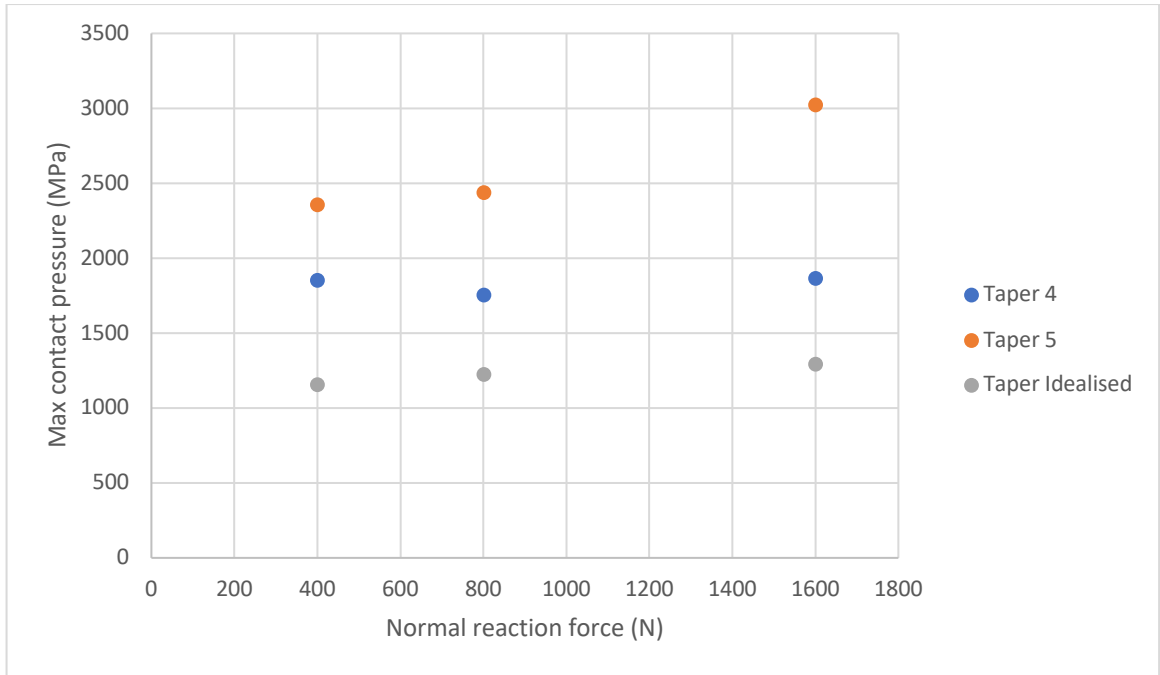
Figure 6.7. Contact pressure at the end of the Assembly step at 400 N, 800 N and 1600 N normal forces for all tested taper pairs.
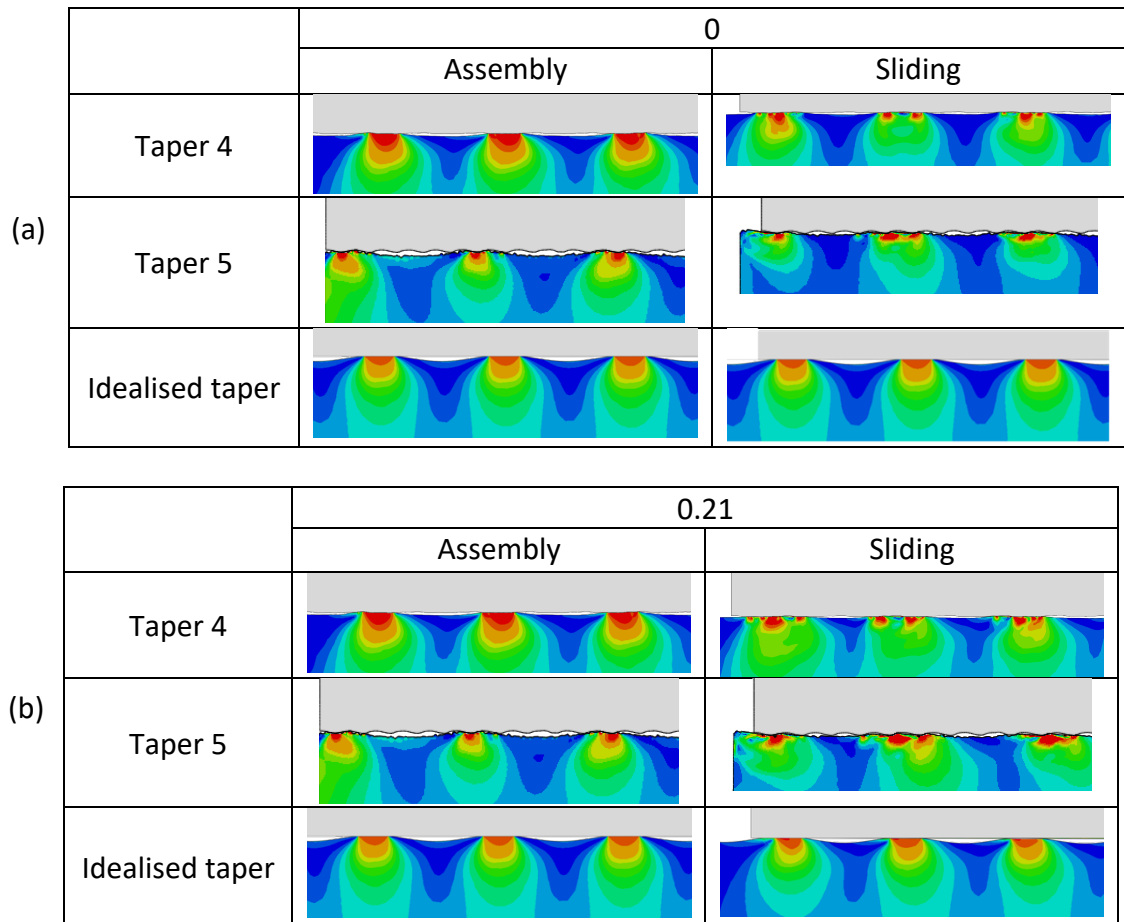
Figure 6.8. von Mises stresses distributions at the end of assembly and sliding steps at (a) 0 and (b) 0.21 local COF for taper 4, 5 and idealised surface pairs.

During the sliding step, rotation of the Hertzian stress distributions was observed in all the tested tapers. The extent of the rotation was determined by the local COF and taper topography, where the idealised taper experienced no rotation of its stress distributions. The normal reaction force magnitude decreased as the bore advanced due to the irregular shape of the topographies. Indeed, in the idealised taper this reduction of the normal force was significantly smaller in comparison to the other tested tapers. Behaviour of the tangential force throughout the sliding step was specific to the surface coupling. In all taper couplings, an abrupt increase of the tangential force was observed at the beginning of the sliding step, followed by a decay with a characteristic sinusoidal-like frequency. The frequency of this sinusoidal wave was specific to the taper couplings, where the idealised taper did not present such decay and variable tangential behaviour (Figure 6.10). The predicted magnitude

of tangential forces was significantly smaller by almost a half compared to those tangential forces obtained in surface couplings where COF was considered in their contact definition, thus estimated COF decreased as well.

Estimated global COF was influenced by local COF conditions and surface roughness. The greatest global COF of 0.46 was generated by taper 5 with a local COF of 0.21, while the lowest global was of 0 by the idealised taper under frictionless conditions (Figure 6.9). Rougher surfaces generated larger global COF compared to smooth surfaces.
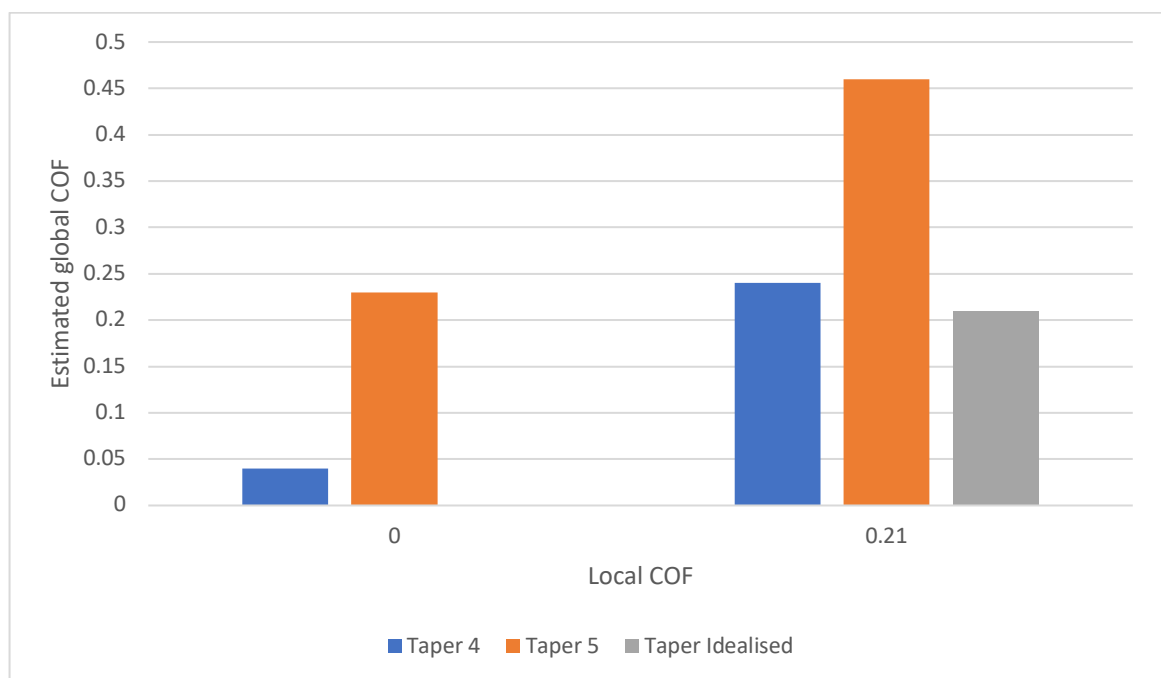
Figure 6.9. Estimated global COF at different normal forces for all tested surface couplings at 0 and 0.21 local COF.

a)

187
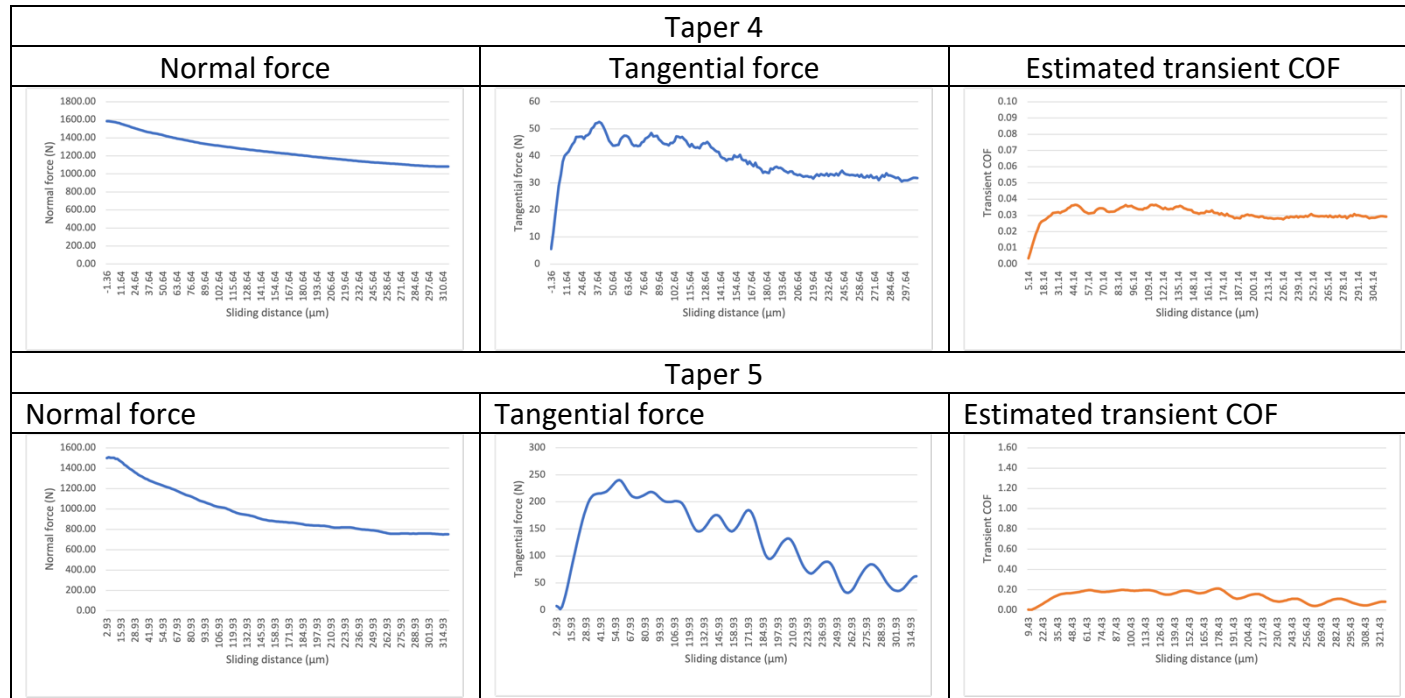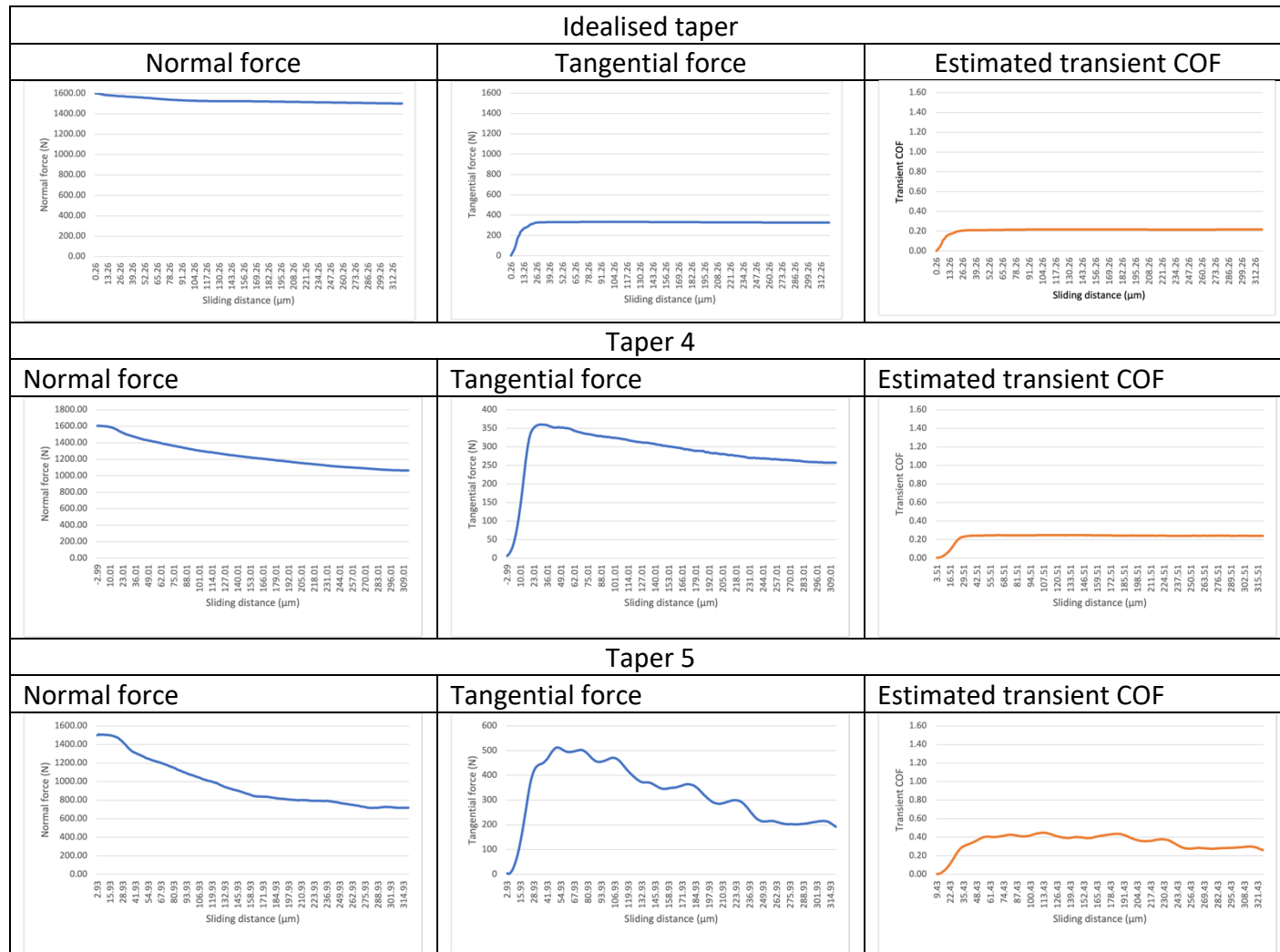
Figure 6.10. Normal and tangential forces and estimated transient COF for all tested taper pairs at local COF of (a) 0 and (b) 0.21.

A function to estimate the global COF as a function of surface deformation and adhesion factors can be obtained with the methodology presented in Part 1 as shown in Figure 6.5. Local COF values used in Part 1 were used to investigate the adhesion contribution on generating a global COF. For illustration purposes, 0.21 was chosen for the second part of this study; It is worth noting that any arbitrary local COF value will generate a global COF that will be influenced by the surface topographies.

Part 2 – Effect of COF in the taper mechanical response

6.4   Materials and methods

A three-dimensional model of a 11 mm long 12/14 taper with 0.18º clearance was developed. Boundary, loading conditions and contact formulation with their respective estimated COF were assigned to the models as described in Chapter 3. Tapers were assembled with a 4 kN assembly force.

Material properties, as described in Chapter 3, associated with Ti6Al4V alloy were assigned to trunnion geometries, and CoCrMo alloy to the femoral head geometries. Element type and sizes, loading and boundary conditions associated with walking activity for the FE models of the current study were assigned as described in Chapter 3 and Chapter 5, respectively. Global COF values in function of local COF and surface coupling (Table 6.1) were introduced to the 3D taper model and generated micromotions and contact conditions were analysed. Surface couplings refers to surface combination representing the bore and trunnion components as described in Chapter 5, Table 5.2. Taper 5, 4 and idealised taper couplings were chosen as tapers 4 and 5 bore and trunnion components were designed to be coupled together and the idealised taper was chosen to compare its predicted mechanical with those taper couplings that their surfaces have not been idealised.

Table 6.1. Estimated global COF values function of taper surface coupling and local COF.

Surface coupling	Local COF	Estimated global COF
Taper 4	0.21	0.23
Taper 5	0.21	0.45
Idealised taper	0.21	0.21

6.5 Results

6.5.1 Contact conditions

Contact area and contact pressure in the taper interface was greatly influenced by the applied external loads representing the gait cycle and coefficient of friction (Figure 6.11). Maximum contact area and contact pressure values were generated at heel-strike and toe-off, where the minimum values were at the start and end of the cycle. As global COF increased the contact area decreased, however due to a weaker frictional force the trunnion penetrated further into the femoral head bore increasing maximum contact pressures in the taper interface. Maximum contact pressures in the taper interface were observed at the proximal end of the trunnion and ranged from 798.52 to 933.27 MPa.
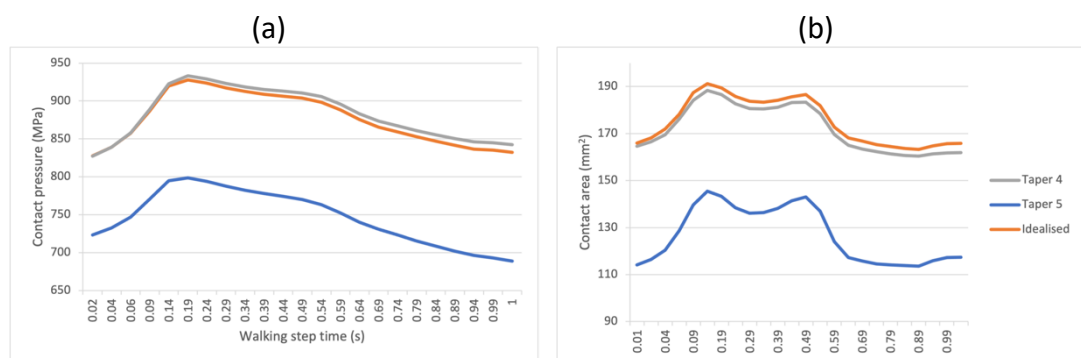
Figure 6.11. Contact area in the taper interface for all tested tapers over a single walking cycle.

6.5.2 Accumulated micromotions

Global estimated coefficient of friction associated with different trunnion and bore surface topographies generated different accumulated micromotions in the taper interface. Figure 6.12 shows accumulated resultant, normal, tangential and pistoning relative motions in contacting nodes between the bore and trunnion throughout a single walking cycle. Global COF did not affect the location where maximum relative motions occurred; however, the magnitude and contribution of these motions were significantly affected. Maximum resultant, normal and pistoning relative motions were located at the distal end of the contacting nodes, while tangential maximum motions were generated on the lateral edges of the contacting nodes.

191

	Accumulated micromotions				
	Resultant	Normal	Tangential	Pistoning	
0.21					
0.24					
0.46					
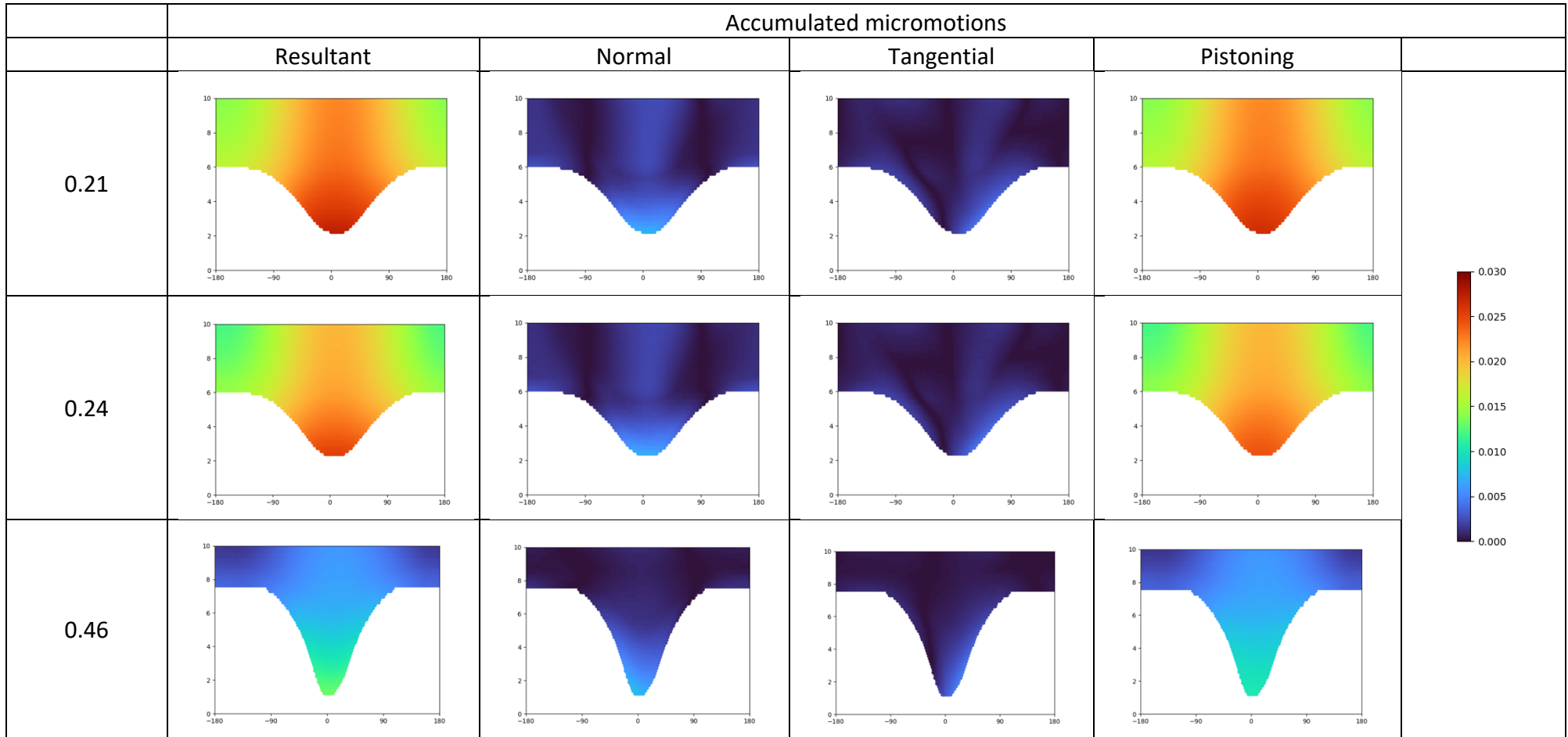
Figure 6.12. Accumulated resultant, normal, tangential and pistoning relative motions of contacting nodes in the taper interface for all tested tapers.

Figure 6.13 summarises the predicted maximum resultant, normal, tangential and pistoning motions for all tested global COF. A global COF of 0.46 predicted the least micromotions, below 13.1 µm. Global COF affected the weight distribution of resultant micromotions, higher COFs in taper interface produced larger normal and tangential relative motions but shorter pistoning motions in comparison to smaller global COF.
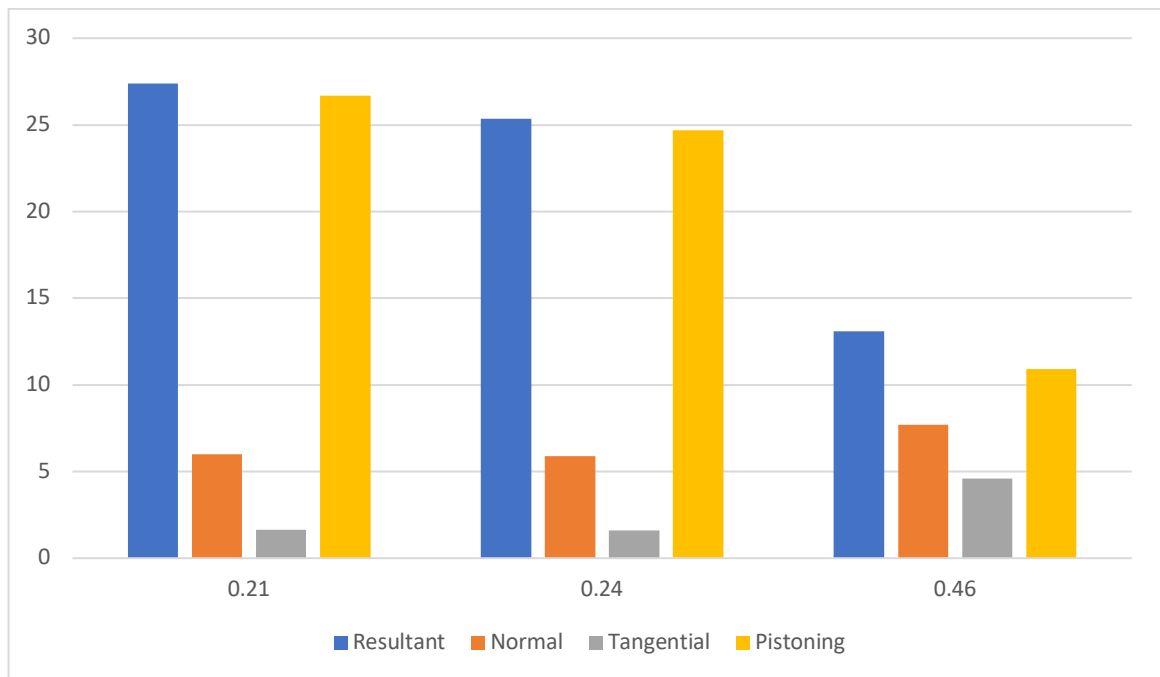
Figure 6.13. Maximum accumulated resultant, normal, tangential and pistoning relative motions generated in the taper interface using three global COF.

6.6   Discussion

A novel methodology was developed to estimate a coefficient of friction that is associated with the surface interaction of taper components in THR devices. The obtained coefficient of friction was implemented into 3D models of a femoral and trunnion under a single walking cycle and the resultant contact conditions were studied. The present investigation was developed to predict the contact environment and mechanical response of coupled bore and trunnion components including the contact pressures and von Mises stresses generated at the trunnion surface, and normal, tangential, and pistoning movements from the interaction of surface

couplings representative of different taper surface finishes were examined. The estimated global COF from this investigation showed that it was affected by the surface roughness of interacting surfaces and surface tangential resisting forces. These findings support previous observational, modelling and experimental studies in determining the coefficient of friction for Ti-alloys (Bitter et al., 2016; Green, 1955; Mulvihill et al., 2011).

In the present study the interaction of different surface profiles resulting from different surface roughness led to significant different coefficient of friction values regardless of any tangential resisting forces. The coefficient of friction was highly dependent on the roughness features of the sliding surfaces; interacting trunnion and bore surfaces with a higher roughness Ra parameter generated higher coefficient values compared to those sliding surfaces with lower roughnesses. The obtained COF ranged from 0 to 0.23 when no local COF was considered; 0.21 to 1.6 when a local COF of 0.21 was introduced. In taper 5, where the bore surface was composed of slightly higher and shorter wavelength peaks, a large variation of tangential forces at the base of the geometry was generated thus generating a large variation of estimated COF values during the sliding phase. A decrease of tangential force magnitude during the sliding phase in this taper occurred due to the flattening of the surface peaks as the rough bore surface advanced. Shorter flattened trunnion peaks generate smaller moments thus reducing the reaction tangential forces. In contrast, taper 4 and the idealised taper where the bore surface was comprised of peaks of the same height, tangential forces steadily increased with the normal force.

A wide range of COF values (0.15 – 0.58) in taper surfaces experimentally obtained and used in FE models of taper interfaces can be found in the literature (Bitter et al., 2016; Donaldson et al., 2014; Fessler & Fricker, 1989; Swaminathan & Gilbert, 2012; Zhang et al., 2013). This broad range of values is attributed to the different conditions where the COF was obtained, namely material combination, surface topography, and experimental techniques. The predicted COF values in this study are within this range when no local COF was considered. In the present study, rough surfaces generated higher COF in comparison to smooth surfaces which contradicts with previous

reported experimental results in which smooth taper surfaces were associated with higher COF values up to 0.29, and 0.19 for rough surfaces (Bitter et al., 2016). The explanation for this finding does not consider the adhesion processes that taper surfaces may experience, which has been reported to occur in unlubricated interacting metal surfaces (Mueller et al., 2021). Indeed, this adhesion process, which in this study was simulated by including friction in the contact definition of the local region of the models, has been shown to have a significant effect on the estimation of COF in tapers in addition to that generated by the plastic deformation of the surfaces. Adhesion processes are important when modelling an effective COF of surfaces together with surface material properties, normal load, and roughness parameters (Mulvihill et al., 2011; Patil & Eriten, 2014). In order to estimate a more accurate COF of taper surfaces and have a better understanding on the role of surface topography in the contact mechanics in taper interfaces more experimental and surface characterisation of taper components is needed. Furthermore, in the present study transient COF reached values higher than 1. Values higher than 1 imply that the force required to slide an object along the surface is greater than the normal force of the object on the surface, however it does not mean that the surface material will withstand the shear stresses that the interaction will generate. In previous studies, material surface combinations of silicone rubber and aluminium under dry conditions have been shown to generate COF values greater than 1 (Barrett, 1990; Malyshev, 2014).

The contact response in the taper interface due to different COFs from the present study indicates that the COF influences the micromotions, contact area and pressures generated at the taper interface. A higher coefficient of friction reduced the micromotions and the influence of its components namely, normal, tangential and pistoning motions generated in the taper interface during walking. However, contact area and pressure increased with smaller COF values. Weaker tangential resistant forces allowed the trunnion to slide further into the femoral head bore. This supports the finding that a low COF can be detrimental to taper interfaces by increasing micromotions (Donaldson et al., 2014; English et al., 2016; Fallahnezhad, Oskouei, et al., 2018; Mali & Gilbert, 2015; Stockhausen et al., 2021; Swaminathan & Gilbert,

2012). However, the current results showed that a higher COF generated larger normal relative motions suggesting that tapers may experience more fluid ingress-egress which increases the chances of releasing metal ions into the body. This effect would be particularly high in tapers with a mismatch at the proximal end and an oval trunnion (Diaz-Lopez et al., 2022). The present study associates rougher surfaces with lower micromotions generated at the taper interface supporting the observation that rougher surfaces in tapers increase the wear damage generated in the taper interface (Brock et al., 2015; Royhman et al., 2021; Stockhausen et al., 2021).

Nonetheless, when comparing predicted contact pressures in the surface interfaces in the COF and walking models, it is evident that surface features significantly change the contact environment in the interfaces. Contact pressure in COF models were predicted to be up to 3.2 GPa almost three times larger than those generated in the global model of the taper interface during walking. Such under estimation of the contact environment due to the oversimplification of taper surfaces in FE models significantly change the mechanical response between the bore and trunnion surfaces and would impact the estimation of wear damage (Gustafson et al., 2022; Lundberg et al., 2015; Zhang et al., 2013).

6.7   Conclusions

A novel methodology to estimate the mechanical response of two interacting surfaces representing a bore and trunnion surface components was developed. The present findings involving estimated static COF suggests that rougher surfaces will generate larger COF, that will decrease the micromotions generated in the taper interface. These findings suggest that smooth taper surfaces are at risk of fretting corrosion damage, and rough taper tapers will generate relative motions that can allow fluid ingress. Findings also indicated that adhesion processes in taper interface have a considerable effect on the estimation of an effective static COF. Further investigation on the strength of interatomic bonding generated by taper surface finishes is needed.

7 Final discussion, conclusions and recommended future work

7.1 Discussion

The objectives of the series of studies presented in this thesis were to characterise the micromotions generated in the interface of a Morse taper in a THR under different loading conditions and investigate how taper design parameters, surface finish and assembly conditions influence the generation of micromotions. Micromotions associated with fretting wear have been previously described to be influenced by factors related to patient activities (Bergmann et al., 1993), weight (Anakwe et al., 2011; Falkenberg et al., 2019), anatomy (del Balso et al., 2021; Wiklund & Romanus, 1991), implant design, surface roughness (Hothi et al., 2017; Pourzal et al., 2018), taper diameter (Donaldson et al., 2014; Panagiotidou et al., 2013), angular mismatch (Ashkanfar et al., 2017a; Kocagöz et al., 2013; Raji & Shelton, 2019), length (Brock et al., 2015; Jauch-Matt et al., 2017; Raji & Shelton, 2019) and flexural rigidity (Haschke et al., 2019), material combination (Gilbert, Mali, et al., 2015; Ouellette et al., 2019) as well as surgeon controlled factors such as implantation technique (assembly force (English et al., 2016; Mroczkowski et al., 2006), surface cleanness (Gilbert et al., 2009)).

3D FE models of a femoral head and trunnion in this work were developed to characterise the micromotions generated in the taper interface under a range of loading conditions, trunnion geometries, and contact conditions. Results of the investigation in Chapter 4 showed for the first time that micromotion components and their magnitudes are determined by the nature of the external loading, in particular those loadings associated with raising the implanted leg as they generate high moments. Activities such as stair climbing, and jogging generated similar relative motions to walking, and were significantly larger than those activities that do not required raising of the leg such as sit-to-stand and cycling. Furthermore, a pump-action type of relative movement namely an opening and closing around the circumference of the taper was observed in the taper interface during those activities that involved leg raising. This type of action may stimulate the fluid ingress-egress to

the junction's interface by increasing/decreasing the taper's opening at the distal part of the taper, combined with circumferential motion around the trunnion's circumference. The largest distance of up to 249 μm was observed during walking up stairs.

Higher assembly forces are recommended to reduce damage associated with fretting corrosion (Farhoudi et al., 2017; Mroczkowski et al., 2006; Mueller et al., 2021; Panagiotidou et al., 2017; Pennock et al., 2002). Findings regarding assembly conditions in Chapter 4 agree with this recommendation; predicted micromotions in this study were influenced by taper clearance and assembly force. Increasing taper clearance resulted in an increase in the micromotions' magnitude and an increase on the effect of impact force on micromotions, suggesting that that larger taper clearances require higher assembly forces. Nevertheless, higher assembly forces increase the contact pressure in the bore-trunnion interface (Ashkanfar et al., 2017b), particularly if the surfaces are made up of threaded grooves.

Micromotions in the taper interface are the resultant of three types of relative motions, namely, pistoning, tangential and normal. If pistoning and tangential motions occur where there is contact between the trunnion and bore fretting damage can take place, while normal relative motions allow the fluid ingress into the taper surface. Analysing these 3 components separately it was identified that the contribution of the micromotion components on the resultant micromotion were also affected by assembly force followed by taper clearance. Furthermore, different activities also generated different micromotion component distribution where jogging presented the largest pistoning motion of 16 μm followed by walking and stairs up in tapers with a clearance angle of 0.18°. These findings bring an insight on the influence of loading conditions and fretting damage generation, where a simplification of the loading conditions would result on different damage patterns at the taper interface.

Looking at the effect of taper form in the generation of relative motions in the taper junction, the ovality of a trunnion influenced both micromotions and contact

conditions developed in the taper's interface. Tangential and pistoning motions were the greatest component contributions in the resultant micromotion in tapers with an oval trunnion which at the same time were affected by taper clearance, increasing the motion magnitude with clearance angle. A roundness deviation of 6 μm in the trunnion was enough to significantly affect the contact conditions in the taper interface. Ovality orientation played a key role on the generation of micromotions; when the ovality's major axis was parallel to the anterior-posterior axis, micromotions were considerably smaller compared to when the major axis was parallel to the superior-inferior axis. However, both orientations were at risk of developing wear damage due to increased tangential and pistoning motions in comparison to round tapers.

The strength of the Morse taper junction is determined by the engagement area between the male and female conical surfaces that originates due to geometrical and surface differences of the taper components. Commercially available metal tapers surfaces are manufactured with a surface finishing to protect the surface from corrosion damage and also to improve contact engagement in the taper interface. Trunnion and bore taper surfaces can be classified into smooth and rough, depending on their surface finish, defined by the roughness parameters such as Ra and Rz (Hothi et al., 2015; Jauch-Matt et al., 2017; Whittaker et al., 2017). There are no standards or recommendations on the use of a particular surface finish depending on the material, or taper geometry. Manufacturing methods may lead to undesired variations on the taper's surface affecting its shape and form resulting in oval components and 'barrelling' of the surfaces (Bitter et al., 2019; Wade et al., 2020).

Bore and trunnion surfaces, measured and computer generated, were characterised and 2D FE models were developed to study the effect of surface form, waviness and roughness of trunnion and bore surfaces. The study in Chapter 5, investigates how non-ideal real surfaces in taper components affect the contact environment generated between the trunnion and bore during assembly. This study is divided into macro and micro studies. In the macro study, concave surface bores were assembled with ideal conical trunnions. Due to the nature of the manufacturing process for the

production of femoral bores, the bore surface can be concave, known as barrelling, affecting the engagement point with the trunnion, as well as decreasing the contact area between the bore and trunnion. In the present study, models showed for the first time that an increase of the barrelling height up to 0.4 µm would reduce the contact area by approximately 28 % on tapers with a clearance angle of 0.18°. A reduce contact between the bore and trunnion can affect the head-neck junction strength and increase the risk of higher micromotions in the taper interface (Bechstedt et al., 2020; Donaldson et al., 2014). Furthermore, the engagement point design considers ideal geometries of the bore and trunnion surfaces; deviations of the assumed engagement point may affect the intended femoral off set resulting in an increase of both frictional moments at the THR bearing and micromotions magnitudes in the taper interface (Wade et al., 2020).

The micro surface study investigated the contact environment in taper interfaces that included waviness and roughness in the surface of the taper components, a novel 2D FE model using surface data was utilised to create the models' geometries. Roughness analysis of the bore and trunnion surfaces, and FE results show for the first time that trunnion and bore surfaces are comprised of several superimposed spatial wave frequencies and that contact conditions are sensitive to the features present in the surface in addition to taper geometry design and assembly conditions. The measured bore and trunnion surfaces are intrinsically different from idealised surfaces. Power spectrum density (PSD) analysis showed that the surfaces comprise up to seven spatial frequencies for trunnion and three for the bore surfaces. These trunnion surfaces which were made up of more than one spatial wave frequency generated higher contact pressures and experienced larger plastic strains, which in some cases reached the failure threshold which did not occur in single frequency surfaces. Commonly used surface parameters (Ra, Rz) to describe trunnion and bore surfaces were not associated with the change of contact conditions generated in the taper interface during assembly. Moreover, measured and idealised surfaces produced different contact patterns during the assembly of the femoral head into the trunnion. During assembly, the model showed that all the tested taper couplings experience flattening of the surface peaks, which resulted in a changed of the contact conditions as the bore surface advanced, particularly in tapers that considered

measured surfaces in both the trunnion and bore components. Peak height variations in measured surfaces generated irregular contact between the bore and trunnion surfaces, and due to peak flattening the trunnion stops interacting with the bore at some points. Such contact behaviour in the taper interface during assembly has been shown for the first time in this study and was not present in idealised taper surfaces. These observations on the role of surface topography in the taper interface are in agreement with recent studies which highlight the importance of the trunnion surface topography when studying the contact mechanics in the taper interface (Bechstedt et al., 2020; Gustafson et al., 2020a, 2022).

In experimental studies the extent of contact area between the bore and trunnion may be overestimated due to the flattening peaks in the trunnion surface during assembly (Witt et al., 2015). The experimental overestimation of the contact conditions in the taper interface can lead to the underestimation of the recommended assembly forces. Further investigation is needed to understand if the spatial frequencies described in this study are common in other commercial taper junctions used in THR devices and how these frequencies affect fretting and corrosion damage generation in the taper interface.

The surface variations found at different length scales on the taper component surfaces generate different fretting and corrosion damage patterns at the trunnion and/or bore surfaces. This is due to the specific contact environments result of the interaction of surface shape, form, waviness and roughness scales (Mai et al., 2022; Stockhausen et al., 2021; Witt et al., 2015). Despite the significant effect that surface finish has on the contact environment, and probably on the evolution of wear and corrosion damage as well, studies on the taper performance and wear damage have previously focused on the design of the taper geometry assuming a perfect conical round surface (Falkenberg et al., 2019; Haschke et al., 2019; Krull et al., 2018).

Furthermore, previous *in silico* studies have used a smooth round conical surface to investigate wear damage and taper performance (Ashkanfar et al., 2017a; Bitter et al., 2018; English et al., 2016; Fallahnezhad, Oskouei, et al., 2018; Farhoudi et al.,

2017; Raji & Shelton, 2019; Toh et al., 2023). The current literature on taper surfaces is limited to the geometry characterisation of commercially available bore and trunnion components. However, the role of the taper surfaces themselves on the junction performance has not previously been studied in detailed. Understanding how surface features found at different scales influences performance is important as these will determine the contact environment in tapers when assembled. Recent FE studies have investigated the effect of rough surfaces by artificially generating surface machined threads with a single sinusoidal function and showed that using this simplified smooth and rough taper surfaces generated different contact conditions (Bechstedt et al., 2020; Gustafson et al., 2020a, 2022).

The202ualityy of contact between the bore and trunnion surfaces determines the junction's stability and thereby affects wear and corrosion damage caused by the surfaces' relative motions (Falkenberg et al., 2019; Krull et al., 2018; Morlock et al., 2020). The resistive force to sliding during relative movements, referred to as friction determines the interlocking of the taper interface (Dransfield et al., 2019; Gustafson et al., 2020a; Mroczkowski et al., 2006) and the junction's mechanical response during external loading that directly influences the magnitude of micromotions generating lower relative motions in higher coefficient of friction (COF) values (Donaldson et al., 2014; English et al., 2016). A novel methodology was developed in this work to study the adhesion and surface deformation contributions in COF values and estimate a global COF under sliding loading conditions for different trunnion and femoral head bore surface pairs. Results showed that the global COF is sensitive to the taper's topography and adhesion forces, which were simulated by including a local COF in the surface definition. Rougher surfaces, particularly those surfaces with more than one spatial frequency, generated higher global COF. Idealised surfaces with no local COF generated no tangential reaction forces, therefore generating a global COF of zero as there was no surface friction. Estimated global COF values for all tested conditions and surfaces ranged from 0 to 1.6, and the global COF ranged from 0 to 0.23 was estimated when only the deformation factor of the interacting surfaces alone was considered, whereas ranges of the global COF was from 0.21 to 0.46 when a local COF of 0.21 was introduced in the surface interaction. Peak

flattening in the trunnion surface was observed when the bore surface slid parallel to the trunnion surface causing a reduction in the tangential reaction forces and resulting in a reduction in the transient COF. Adhesion is determined by the surface finish of the taper components (Mueller et al., 2021). COF values in taper junctions modelled in THR devices are varied, ranging from 0.15 to 0.55, due to the diverse surface finishes for commercial THRs (Mueller et al., 2017; Whittaker et al., 2017). Nonetheless the surface contribution in generating a COF is not well understood nor have recommendations for taper surface finish uses been developed. The present results indicate that an adhesion factor has a significant role in the estimation of a global COF in addition to the surface deformation and suggests that surface finish has an important role in predicting the performance of the taper junction.

Introducing approximated global COF of three taper surface pairs corresponding to tapers 4, 5 and 6 from Chapter 5 with a local COF of 0.21 into a 3D model of a taper with 0.18° clearance angle under walking loading conditions showed that predicted micromotions, and the normal, tangential and pistoning components were sensitive to the COF values, assembly forces, taper clearance, trunnion's ovality extent and orientation, as well as the external loading associated with patient activities. A higher coefficient of friction between a bore and a round taper reduced the micromotions during walking, in the present study a taper with a 0.18° clearance angle reduced the micromotions magnitude by 48% when increasing the COF from 0.21 to 0.46. This supports the assumption that a low COF can be detrimental to taper interfaces by increasing micromotions (Donaldson et al., 2014; English et al., 2016; Fallahnezhad, Oskouei, et al., 2018; Mali & Gilbert, 2015; Swaminathan & Gilbert, 2012). However, inspecting the surface profiles and contact conditions in Chapter 6, taper couplings with higher COF values present a higher number of smaller spatial wave frequencies. This means that despite these tapers with higher COF values presenting lower micromotions at their interface, they will experience greater contact pressures and plastic strains thus generating more debris. Rougher taper components increase the wear damage at the junction interface (Brock et al., 2015; Royhman et al., 2015; Stockhausen et al., 2021). Findings from this investigation suggest that when estimating the wear damage, macro and micro features in the taper junction's

surface components need to be considered as ignoring either of these factors will interfere the accuracy of this estimation.

This current multi-scale study of the contact mechanics in the taper interface, draws attention to the topographical features found at the waviness scale of trunnion and bore surface components. Reducing the number of spatial frequencies found in rough taper components can reduce the risk of damaging the taper surface during assembly and will increase the contact between the trunnion microgrooved peak and bore surface. Furthermore, rough tapers will generate higher COF values reducing the magnitude of micromotions generated in the taper interface. The findings regarding surface finish design may significantly affect the junction's performance when loaded and further investigations could suggest significant design changes in the taper geometry that would reduce relative motions associated with fretting and corrosion damage, and thereby improve implant performance.

7.2 Conclusions

- The contact environment generated due to the interaction of the trunnion and bore surface is sensitive to variations found in the shape, form, waviness, and roughness of THR taper components.

- Different types of relative motions were identified at the taper interface during common physical activities. These relative motions were affected by taper design and assembly conditions.

- During walking, round tapers generated motions that encourage fluid ingress and egress into the taper interface.

- The ovality of the trunnion and its orientation influences the taper contact mechanics.

- Characterised bore and trunnion surfaces are comprised of up to seven spatial frequencies; when assembled, these surfaces generated larger contact pressures and plastic strains in comparison to those taper surface that were idealised with a single function.

- Flattening of microgrooved peaks at the waviness scale can occur in the taper interface during assembly affecting the number of peaks in contact between the bore and trunnion as the assembly force increases.

- Adhesion effect cannot be ignored when determining a global coefficient friction of paired taper surfaces.

- Rougher measured taper surfaces generated a larger global coefficient of friction and reduced relative motions.

7.3   Future work

The present study explored the implications of taper component surface variations on the contact mechanics that govern the interface performance and stability. In Chapter 4, different types of micromotions occurring in the taper interface during everyday activities are described. The combination of these micromotions can produce mechanisms that may allow the fluid ingress-egress into the taper interface and fretting damage at the same time. Experimentally Identifying which of these micromotions is detrimental to the stability of the taper interface will help to improve the design of the taper geometry. Currently, ISO standards (ASTM F1875-98) recommends a cyclic sinusoidal loading (300 – 3300 N) for corrosion testing of modular taper interfaces (Bingley et al., 2018). However, this cyclic loading may fail to generate the different magnitudes and types of micromotions that are generated the taper interface during *in vivo* loading. Magnitudes of the different types of micromotions described in this thesis can be used to develop cyclic loading profiles and test protocols that can reproduce the micromotions that can damage the taper components and allow fluid ingress into the taper interface.

One of the key findings of the study in Chapter 6 that supports experimental work observations (Witt et al., 2015) and recent *in silico* studies (Godoy et al., 2022; Gustafson et al., 2022) is that threaded trunnion surface will experience flattening of the trunnion microgrooved peaks during assembly and that contact the real contact regions are significantly smaller than those predicted in FE models of round smooth tapers. In this investigation, those trunnion surfaces with more dominant spatial frequencies were associated with larger roughness parameters (R_a, R_z), larger contact pressures and larger plastic strains in comparison to those trunnion surfaces with fewer dominant spatial frequencies. These predicted contact parameters suggest that dominant spatial frequencies may have an influence on the fretting and MACC rates. Further investigations of taper surfaces need to consider roughness parameters that can provide a detailed description of both amplitude and wavelength values of the peaks that comprise the taper components.

Surfaces of taper components can be conformed of several dominant spatial frequencies, which in the present study the trunnion taper surfaces were formed from three up to seven spatial frequencies. The number of tested surfaces in this study was limited to only four trunnions, and two bore components from two different manufacturers. However, spatial frequency analysis on a larger cohort of components is required to create a state of art of commercial taper components. Characterising the waviness and roughness regions of commercially available taper junctions may help to understand how fretting and corrosion damage mechanisms start and develop and possible differences between manufacturers. The significance of the spatial frequencies of different magnitudes found in taper surfaces on the generation of metal debris through fretting and corrosion should be investigated. Also, manufacturing factors that are used to generate these spatial frequencies need to be identified.

The coefficient of friction used in taper junctions is usually obtained through expensive and time-consuming experimental studies. Associating a realistic global coefficient of friction for materials and surface combinations would improve the development of FE models of tapers by simplifying the surface interaction into a contact interaction that considers the topological and adhesion effects. The present study presents a novel method to obtain a global coefficient of friction from two paired taper surfaces, however the adhesion of the peaks has not been fully explored. The adhesion mechanisms in surface finishes used in taper should be well understood in order to develop more accurate FE models, indeed the adhesion force in taper surface combinations is currently unknown. Finding the right adhesion proxy in this novel method could be established by comparing predicted global coefficient of frictions with experimental work.

In the present study, micromotions and contact parameters generated in the taper interface after assembly were studied on non-adaptive FE models and on a single activity cycle. The mean implantation time of retrieved modular THR devices is of 5.4 ± 6.0 years and throughout that time the implant can experience a large number of different activity cycles (Higgs et al., 2016). Indeed, contact parameters between the

trunnion and bore can be affected by small changes in the topography of taper components due to a weaker taper lock result of the taper surface wear thus generating larger micromotions in the taper interface producing further wear damage (Fallahnezhad et al., 2019; Fallahnezhad, Oskouei, et al., 2018; Feyzi et al., 2021a). As observed in oval tapers after a single gait cycle (Figures 4.11 and 4.12), contact conditions and taper gap opening between the bore and trunnion differ from the initial contact conditions suggesting that micromotions and contact parameters derived from the contact between the bore and trunnion will change on the following gait cycle. Implementing an adaptative mesh into the present FE models and running them through several activity cycles could help to simulate the fretting degenerative process more accurately and have a better understanding on the role of micromotions and taper surface on the degenerative process of fretting wear in the taper interface.

References

Anakwe, R. E., Jenkins, P. J., & Moran, M. (2011). Predicting Dissatisfaction After Total Hip Arthroplasty: A Study of 850 Patients. *The Journal of Arthroplasty*, *26*(2), 209–213. https://doi.org/10.1016/j.arth.2010.03.013

Arnholt, C. M., MacDonald, D. W., Underwood, R. J., Guyer, E. P., Rimnac, C. M., Kurtz, S. M., Mont, M. A., Klein, G. R., Lee, G.-C., Chen, A. F., Hamlin, B. R., Cates, H. E., Malkani, A. L., & Kraay, M. J. (2017). Do Stem Taper Microgrooves Influence Taper Corrosion in Total Hip Arthroplasty? A Matched Cohort Retrieval Study. *The Journal of Arthroplasty*, *32*(4), 1363–1373. https://doi.org/10.1016/j.arth.2016.11.018

Ashkanfar, A., Langton, D. J., & Joyce, T. J. (2017a). A large taper mismatch is one of the key factors behind high wear rates and failure at the taper junction of total hip replacements: A finite element wear analysis. *Journal of the Mechanical Behavior of Biomedical Materials*, *69*, 257–266. https://doi.org/10.1016/j.jmbbm.2017.01.018

Ashkanfar, A., Langton, D. J., & Joyce, T. J. (2017b). Does a micro-grooved trunnion stem surface finish improve fixation and reduce fretting wear at the taper junction of total hip replacements? A finite element evaluation. *Journal of Biomechanics*, *63*, 47–54. https://doi.org/10.1016/j.jbiomech.2017.07.027

Baleani, M., Erani, P., Bordini, B., Zuccheri, F., & Makosa, M. K. (2017). In Vivo Damage of the Head-Neck Junction in Hard-on-Hard Total Hip Replacements: Effect of Femoral Head Size, Metal Combination, and 12/14 Taper Design. *Materials*, *10*(7), 733. https://doi.org/10.3390/ma10070733

Barrett, R. T. (1990). *Fastener Design Manual*. NASA Reference Publication.

Baxmann, M., Jauch, S. Y., Schilling, C., Blömer, W., Grupp, T. M., & Morlock, M. M. (2013). The influence of contact conditions and micromotions on the fretting behavior of modular titanium alloy taper connections. *Medical Engineering & Physics*, *35*(5), 676–683. https://doi.org/10.1016/j.medengphy.2012.07.013

Bechstedt, M., Gustafson, J. A., Mell, S. P., Gührs, J., Morlock, M. M., Levine, B. R., & Lundberg, H. J. (2020). Contact conditions for total hip head-neck modular taper junctions with microgrooved stem tapers. *Journal of Biomechanics*, *103*, 109689. https://doi.org/10.1016/j.jbiomech.2020.109689

Bergmann, G., Bender, A., Dymke, J., Duda, G., & Damm, P. (2016). Standardized Loads Acting in Hip Implants. *PLOS ONE*, *11*(5), e0155612. https://doi.org/10.1371/journal.pone.0155612

Bergmann, G., Graichen, F., & Rohlmann, A. (1993). Hip joint loading during walking and running, measured in two patients. *Journal of Biomechanics*, *26*(8), 969–990. https://doi.org/10.1016/0021-9290(93)90058-M

Bergmann, G., Graichen, F., Rohlmann, A., Bender, A., Heinlein, B., Duda, G. N., Heller, M. O., & Morlock, M. M. (2010). Realistic loads for testing hip implants. *Bio-Medical Materials and Engineering*, *20*(2), 65–75. https://doi.org/10.3233/BME-2010-0616

Berstock, J. R., Whitehouse, M. R., & Duncan, C. P. (2018). Trunnion corrosion. *The Bone & Joint Journal*, *100-B*(1_Supple_A), 44–49. https://doi.org/10.1302/0301-620X.100B1.BJJ-2017-0569.R1

Bhalekar, R. M., Smith, S. L., & Joyce, T. J. (2019). Wear at the taper-trunnion junction of contemporary ceramic-on-ceramic hips shown in a multistation hip simulator. *Journal of Biomedical Materials Research Part B: Applied Biomaterials*, *107*(4), 1199–1209. https://doi.org/10.1002/jbm.b.34213

Bingley, R., Martin, A., Manfredi, O., Nejadhamzeeigilani, M., Oladokun, A., Beadling, A. R., Siddiqui, S., Anderson, J., Thompson, J., Neville, A., & Bryant, M. (2018). Fretting–corrosion at the modular tapers interface: Inspection of standard ASTM F1875-98. *Proceedings of the Institution of Mechanical Engineers, Part H: Journal of Engineering in Medicine*, *232*(5), 492–501. https://doi.org/10.1177/0954411918760958

Bitter, T., Khan, I., Marriott, T., Lovelady, E., Verdonschot, N., & Janssen, D. (2017). A combined experimental and finite element approach to analyse the fretting mechanism of the head–stem taper junction in total hip replacement. *Proceedings of the Institution of Mechanical Engineers, Part H: Journal of Engineering in Medicine*, *231*(9), 862–870. https://doi.org/10.1177/0954411917713774

Bitter, T., Khan, I., Marriott, T., Lovelady, E., Verdonschot, N., & Janssen, D. (2018). Finite element wear prediction using adaptive meshing at the modular taper interface of hip implants. *Journal of the Mechanical Behavior of Biomedical Materials*, *77*, 616–623. https://doi.org/10.1016/j.jmbbm.2017.10.032

Bitter, T., Khan, I., Marriott, T., Lovelady, E., Verdonschot, N., & Janssen, D. (2019). The effects of manufacturing tolerances and assembly force on the volumetric wear at the taper junction in modular total hip arthroplasty. *Computer Methods in Biomechanics and Biomedical Engineering*, 1–12. https://doi.org/10.1080/10255842.2019.1627524

Bitter, T., Khan, I., Marriott, T., Schreurs, B. W., Verdonschot, N., & Janssen, D. (2016). Experimental Measurement of the Static Coefficient of Friction at the Ti–Ti Taper Connection in Total Hip Arthroplasty. *Journal of Biomechanical Engineering*, *138*(3). https://doi.org/10.1115/1.4032446

Boese, C. K., Dargel, J., Oppermann, J., Eysel, P., Scheyerer, M. J., Bredow, J., & Lechler, P. (2016). The femoral neck-shaft angle on plain radiographs: a systematic review. *Skeletal Radiology*, *45*(1), 19–28. https://doi.org/10.1007/s00256-015-2236-z

Bone, M. C., Sidaginamale, R. P., Lord, J. K., Scholes, S. C., Joyce, T. J., Nargol, A. V., & Langton, D. J. (2015). Determining material loss from the femoral stem trunnion in hip arthroplasty using a coordinate measuring machine. *Proceedings of the Institution of Mechanical Engineers, Part H: Journal of Engineering in Medicine*, *229*(1), 69–76. https://doi.org/10.1177/0954411914567552

Brock, T. M., Sidaginamale, R., Rushton, S., Nargol, A. V. F., Bowsher, J. G., Savisaar, C., Joyce, T. J., Deehan, D. J., Lord, J. K., & Langton, D. J. (2015). Shorter, rough trunnion surfaces are associated with higher taper wear rates than longer, smooth trunnion surfaces in a contemporary large head metal-on-metal total hip arthroplasty system. *Journal of Orthopaedic Research*, *33*(12), 1868–1874. https://doi.org/10.1002/jor.22970

Callaghan, J. J. (2016). *The adult hip : hip arthroplasty surgery* (3rd ed.). Philadelphia: Wolters Kluwer.

Cartner, J., Aldinger, P., Li, C., & Collins, D. (2017). Characterization of Femoral Head Taper Corrosion Features Using a 22-Year Retrieval Database. *HSS Journal ®*, *13*(1), 35–41. https://doi.org/10.1007/s11420-016-9517-5

Clark, J. M., Freeman, M. A. R., & Witham, D. (1987). The relationship of neck orientation to the shape of the proximal femur. *The Journal of Arthroplasty*, *2*(2), 99–109. https://doi.org/10.1016/S0883-5403(87)80016-5

Damm, P., Dymke, J., Ackermann, R., Bender, A., Graichen, F., Halder, A., Beier, A., & Bergmann, G. (2013). Friction in Total Hip Joint Prosthesis Measured In Vivo during Walking. *PLoS ONE*, *8*(11), e78373. https://doi.org/10.1371/journal.pone.0078373

del Balso, C., Schemitsch, E., & Lanting, B. (2021). Trunnionosis. In *Evidence-Based Orthopedics* (pp. 179–183). Wiley. https://doi.org/10.1002/9781119413936.ch29

del Balso, C., Teeter, M. G., Tan, S. C., Lanting, B. A., & Howard, J. L. (2015). Taperosis. *The Bone & Joint Journal*, *97-B*(7), 911–916. https://doi.org/10.1302/0301-620X.97B7.35149

Denkena, B., Böß, V., Nespor, D., & Samp, A. (2011). Kinematic and Stochastic Surface Topography of Machined TiAl6V4-Parts by means of Ball Nose End Milling. *Procedia Engineering*, *19*, 81–87. https://doi.org/10.1016/j.proeng.2011.11.083

Diaz-Lopez, R. A., Wen, P. H., & Shelton, J. C. (2022). Influence of taper design and loading on taper micromotion. *Journal of the Mechanical Behavior of Biomedical Materials*, *128*, 105106. https://doi.org/10.1016/j.jmbbm.2022.105106

Donaldson, F. E., Coburn, J. C., & Siegel, K. L. (2014). Total hip arthroplasty head–neck contact mechanics: A stochastic investigation of key parameters. *Journal of Biomechanics*, *47*(7), 1634–1641. https://doi.org/10.1016/j.jbiomech.2014.02.035

Dransfield, K., Addinall, K., & Bills, P. (2021). Comparison and appraisal of techniques for the determination of material loss from tapered orthopaedic surfaces. *Wear*, *478–479*, 203903. https://doi.org/10.1016/j.wear.2021.203903

Dransfield, K., Racasan, R., Williamson, J., & Bills, P. (2019). Changes in the morphology of microgrooved stem tapers with differing assembly conditions. *Biotribology*, *18*, 100096. https://doi.org/10.1016/j.biotri.2019.100096

Drummond, J., Tran, P., & Fary, C. (2015). Metal-on-Metal Hip Arthroplasty: A Review of Adverse Reactions and Patient Management. *Journal of Functional Biomaterials*, *6*(3), 486–499. https://doi.org/10.3390/jfb6030486

Dyrkacz, R. M. R., Brandt, J. M., Morrison, J. B., O' Brien, S. T., Ojo, O. A., Turgeon, T. R., & Wyss, U. P. (2015). Finite element analysis of the head–neck taper interface of modular hip prostheses. *Tribology International*, *91*, 206–213. https://doi.org/10.1016/j.triboint.2015.01.016

Dyrkacz, R. M. R., Brandt, J.-M., Ojo, O. A., Turgeon, T. R., & Wyss, U. P. (2013). The Influence of Head Size on Corrosion and Fretting Behaviour at the Head-Neck Interface of Artificial Hip Joints. *The Journal of Arthroplasty*, *28*(6), 1036–1040. https://doi.org/10.1016/j.arth.2012.10.017

Eliaz, N. (2019). Corrosion of Metallic Biomaterials: A Review. *Materials*, *12*(3), 407. https://doi.org/10.3390/ma12030407

Elkins, J. M., Callaghan, J. J., & Brown, T. D. (2014). Stability and Trunnion Wear Potential in Large-diameter Metal-on-Metal Total Hips: A Finite Element Analysis. *Clinical Orthopaedics and Related Research®*, *472*(2), 529–542. https://doi.org/10.1007/s11999-013-3244-8

El-Zein, Z. S., Gehrke, C. K., Croley, J. S., Siljander, M. P., Mallow, M. A., Flierl, M. A., Verner, J. J., & Baker, E. A. (2021). Assessing Taper Geometry, Head Size, Head Material, and Their Interactions in Taper Fretting Corrosion of Retrieved Total Hip Arthroplasty Implants. *The Journal of Arthroplasty*, *36*(7), S386-S394.e4. https://doi.org/10.1016/j.arth.2021.02.041

English, R., Ashkanfar, A., & Rothwell, G. (2015). A computational approach to fretting wear prediction at the head–stem taper junction of total hip replacements. *Wear*, *338–339*, 210–220. https://doi.org/10.1016/j.wear.2015.06.016

English, R., Ashkanfar, A., & Rothwell, G. (2016). The effect of different assembly loads on taper junction fretting wear in total hip replacements. *Tribology International*, *95*, 199–210. https://doi.org/10.1016/j.triboint.2015.11.025

Falkenberg, A., Biller, S., Morlock, M. M., & Huber, G. (2019). Micromotion at the head-stem taper junction of total hip prostheses is influenced by prosthesis design-, patient- and surgeon-related factors. *Journal of Biomechanics*, 109424. https://doi.org/10.1016/j.jbiomech.2019.109424

Fallahnezhad, K., Farhoudi, H., Oskouei, R. H., & Taylor, M. (2016). Influence of geometry and materials on the axial and torsional strength of the head–neck taper junction in modular hip replacements: A finite element study. *Journal of the Mechanical Behavior of Biomedical Materials*, *60*, 118–126. https://doi.org/10.1016/j.jmbbm.2015.12.044

Fallahnezhad, K., Farhoudi, H., Oskouei, R. H., & Taylor, M. (2018). A finite element study on the mechanical response of the head-neck interface of hip implants under realistic forces and moments of daily activities: Part 2. *Journal of the Mechanical Behavior of Biomedical Materials*, *77*, 164–170. https://doi.org/10.1016/j.jmbbm.2017.08.038

Fallahnezhad, K., Oskouei, R. H., Badnava, H., & Taylor, M. (2017). An adaptive finite element simulation of fretting wear damage at the head-neck taper junction of total hip replacement: The role of taper angle mismatch. *Journal of the Mechanical Behavior of Biomedical Materials*, *75*, 58–67. https://doi.org/10.1016/j.jmbbm.2017.07.003

Fallahnezhad, K., Oskouei, R. H., Badnava, H., & Taylor, M. (2019). The Influence of Assembly Force on the Material Loss at the Metallic Head-Neck Junction of Hip Implants Subjected to Cyclic Fretting Wear. *Metals*, *9*(4), 422. https://doi.org/10.3390/met9040422

Fallahnezhad, K., Oskouei, R. H., & Taylor, M. (2018). Development of a fretting corrosion model for metallic interfaces using adaptive finite element analysis. *Finite Elements in Analysis and Design*, *148*, 38–47. https://doi.org/10.1016/j.finel.2018.05.004

Farhoudi, H., Fallahnezhad, K., Oskouei, R. H., & Taylor, M. (2017). A finite element study on the mechanical response of the head-neck interface of hip implants

under realistic forces and moments of daily activities: Part 1, level walking. *Journal of the Mechanical Behavior of Biomedical Materials*, *75*, 470–476. https://doi.org/10.1016/j.jmbbm.2017.08.012

Farhoudi, H., Oskouei, R. H., Jones, C. F., & Taylor, M. (2015). A novel analytical approach for determining the frictional moments and torques acting on modular femoral components in total hip replacements. *Journal of Biomechanics*, *48*(6), 976–983. https://doi.org/10.1016/j.jbiomech.2015.02.010

Farhoudi, H., Oskouei, R., Pasha Zanoosi, A., Jones, C., & Taylor, M. (2016). An Analytical Calculation of Frictional and Bending Moments at the Head-Neck Interface of Hip Joint Implants during Different Physiological Activities. *Materials*, *9*(12), 982. https://doi.org/10.3390/ma9120982

Fawsitt, C. G., Thom, H. H. Z., Hunt, L. P., Nemes, S., Blom, A. W., Welton, N. J., Hollingworth, W., López-López, J. A., Beswick, A. D., Burston, A., Rolfson, O., Garellick, G., & Marques, E. M. R. (2019). Choice of Prosthetic Implant Combinations in Total Hip Replacement: Cost-Effectiveness Analysis Using UK and Swedish Hip Joint Registries Data. *Value in Health*, *22*(3), 303–312. https://doi.org/10.1016/j.jval.2018.08.013

Fessler, H., & Fricker, D. C. (1989). Friction in Femoral Prosthesis and Photoelastic Model Cone Taper Joints. *Proceedings of the Institution of Mechanical Engineers, Part H: Journal of Engineering in Medicine*, *203*(1), 1–14. https://doi.org/10.1243/PIME_PROC_1989_203_003_01

Feyzi, M., Fallahnezhad, K., Taylor, M., & Hashemi, R. (2021a). A review on the finite element simulation of fretting wear and corrosion in the taper junction of hip replacement implants. *Computers in Biology and Medicine*, *130*, 104196. https://doi.org/10.1016/j.compbiomed.2020.104196

Feyzi, M., Fallahnezhad, K., Taylor, M., & Hashemi, R. (2021b). The mechanics of head-neck taper junctions: What do we know from finite element analysis? *Journal of the Mechanical Behavior of Biomedical Materials*, *116*, 104338. https://doi.org/10.1016/j.jmbbm.2021.104338

Fillingham, Y. A., della Valle, C. J., Bohl, D. D., Kelly, M. P., Hall, D. J., Pourzal, R., & Jacobs, J. J. (2017). Serum Metal Levels for Diagnosis of Adverse Local Tissue Reactions Secondary to Corrosion in Metal-on-Polyethylene Total Hip Arthroplasty. *The Journal of Arthroplasty*, *32*(9), S272–S277. https://doi.org/10.1016/j.arth.2017.04.016

Fischer, A., Beckmann, C., Heermant, S., Wittrock, A., Telouk, P., Debus, J., & Wimmer, M. A. (2023). Topography rules the ultra-mild wear regime under boundary lubricated gross-slip fretting corrosion. *Wear*, 204716. https://doi.org/10.1016/j.wear.2023.204716

Fitz, D., Klemt, C., Chen, W., Xiong, L., Yeo, I., & Kwon, Y.-M. (2020). Head-Neck Taper Corrosion in Metal-on-Polyethylene Total Hip Arthroplasty: Risk Factors, Clinical Evaluation, and Treatment of Adverse Local Tissue Reactions. *Journal of the American Academy of Orthopaedic Surgeons*, *28*(22), 907–913. https://doi.org/10.5435/JAAOS-D-20-00475

Friedebold, G. (1976). *Advances in artificial hip and knee joint technology*. Springer Berlin Heidelberg.

Gibon, E., Amanatullah, D. F., Loi, F., Pajarinen, J., Nabeshima, A., Yao, Z., Hamadouche, M., & Goodman, S. B. (2017). The biological response to orthopaedic implants for joint replacement: Part I: Metals. *Journal of Biomedical Materials Research Part B: Applied Biomaterials*, *105*(7), 2162–2173. https://doi.org/10.1002/jbm.b.33734

Gilbert, J. L. (2012). Mechanically Assisted Corrosion of Metallic Biomaterials. In *Materials for Medical Devices* (pp. 79–89). ASM International. https://doi.org/10.31399/asm.hb.v23.a0005653

Gilbert, J. L., Mali, S. A., & Sivan, S. (2015). Corrosion of Modular Tapers in Total Joint Replacements: A Critical Assessment of Design, Materials, Surface Structure, Mechanics, Electrochemistry, and Biology. In *Modularity and Tapers in Total Joint Replacement Devices* (pp. 192–223). ASTM International. https://doi.org/10.1520/STP159120140135

Gilbert, J. L., Mehta, M., & Pinder, B. (2009). Fretting crevice corrosion of stainless steel stem-CoCr femoral head connections: Comparisons of materials, initial moisture, and offset length. *Journal of Biomedical Materials Research Part B: Applied Biomaterials*, *88B*(1), 162–173. https://doi.org/10.1002/jbm.b.31164

Gilbert, J. L., Sivan, S., Liu, Y., Kocagöz, S. B., Arnholt, C. M., & Kurtz, S. M. (2015). Direct in vivo inflammatory cell-induced corrosion of CoCrMo alloy orthopedic implant surfaces. *Journal of Biomedical Materials Research Part A*, *103*(1), 211–223. https://doi.org/10.1002/jbm.a.35165

Godoy, M., Gustafson, J. A., Hertzler, J. S., Bischoff, J. E., Pourzal, R., & Lundberg, H. J. (2022). Model validation for estimating taper microgroove deformation during total hip arthroplasty head-neck assembly. *Journal of Biomechanics*, *140*, 111172. https://doi.org/10.1016/j.jbiomech.2022.111172

Goldberg, J. R., & Gilbert, J. L. (2003). In vitro corrosion testing of modular hip tapers. *Journal of Biomedical Materials Research*, *64B*(2), 78–93. https://doi.org/10.1002/jbm.b.10526

Goldberg, J. R., Gilbert, J. L., Jacobs, J. J., Bauer, T. W., Paprosky, W., & Leurgans, S. (2002). A Multicenter Retrieval Study of the Taper Interfaces of Modular Hip Prostheses. *Clinical Orthopaedics and Related Research*, *401*, 149–161. https://doi.org/10.1097/00003086-200208000-00018

Green, A. P. (1955). Friction between unlubricated metals: a theoretical analysis of the junction model. *Proceedings of the Royal Society of London. Series A. Mathematical and Physical Sciences*, *228*(1173), 191–204. https://doi.org/10.1098/rspa.1955.0043

Gustafson, J. A., Mell, S. P., Levine, B. R., Pourzal, R., & Lundberg, H. J. (2022). Interaction of surface topography and taper mismatch on head-stem modular junction contact mechanics during assembly in modern total hip replacement. *Journal of Orthopaedic Research*. https://doi.org/10.1002/jor.25357

Gustafson, J. A., Pourzal, R., Levine, B. R., Jacobs, J. J., & Lundberg, H. J. (2020a). Modelling changes in modular taper micromechanics due to surgeon assembly technique in total hip arthroplasty. *The Bone & Joint Journal*, *102-B*(7_Supple_B), 33–40. https://doi.org/10.1302/0301-620X.102B7.BJJ-2019-1678.R1

Gustafson, J. A., Pourzal, R., Levine, B. R., Jacobs, J. J., & Lundberg, H. J. (2020b). Modelling changes in modular taper micromechanics due to surgeon assembly

technique in total hip arthroplasty. *The Bone & Joint Journal*, *102-B*(7_Supple_B), 33–40. https://doi.org/10.1302/0301-620X.102B7.BJJ-2019-1678.R1

Hall, D. J., Pourzal, R., Lundberg, H. J., Mathew, M. T., Jacobs, J. J., & Urban, R. M. (2018). Mechanical, chemical and biological damage modes within head-neck tapers of CoCrMo and Ti6Al4V contemporary hip replacements. *Journal of Biomedical Materials Research Part B: Applied Biomaterials*, *106*(5), 1672–1685. https://doi.org/10.1002/jbm.b.33972

Hanawa, T., Hiromoto, S., & Asami, K. (2001). Characterization of the surface oxide film of a Co–Cr–Mo alloy after being located in quasi-biological environments using XPS. *Applied Surface Science*, *183*(1–2), 68–75. https://doi.org/10.1016/S0169-4332(01)00551-7

Haschke, H., Konow, T., Huber, G., & Morlock, M. M. (2019). Influence of flexural rigidity on micromotion at the head-stem taper interface of modular hip prostheses. *Medical Engineering & Physics*, *68*, 1–10. https://doi.org/10.1016/j.medengphy.2019.03.020

Hernigou, P., Queinnec, S., & Flouzat Lachaniette, C. H. (2013). One hundred and fifty years of history of the Morse taper: from Stephen A. Morse in 1864 to complications related to modularity in hip arthroplasty. *International Orthopaedics*, *37*(10), 2081–2088. https://doi.org/10.1007/s00264-013-1927-0

Higgs, G. B., MacDonald, D. W., Gilbert, J. L., Rimnac, C. M., Kurtz, S. M., Chen, A. F., Klein, G. R., Hamlin, B. R., Lee, G.-C., Mont, M. A., Cates, H. E., Malkani, A. L., & Kraay, M. J. (2016). Does Taper Size Have an Effect on Taper Damage in Retrieved Metal-on-Polyethylene Total Hip Devices? *The Journal of Arthroplasty*, *31*(9), 277–281. https://doi.org/10.1016/j.arth.2016.06.053

Hothi, H. S., Eskelinen, A. P., Berber, R., Lainiala, O. S., Moilanen, T. P. S., Skinner, J. A., & Hart, A. J. (2017). Factors Associated with Trunnionosis in the Metal-on-Metal Pinnacle Hip. *The Journal of Arthroplasty*, *32*(1), 286–290. https://doi.org/10.1016/j.arth.2016.06.038

Hothi, H. S., Whittaker, R. K., Meswania, J. M., Blunn, G. W., Skinner, J. A., & Hart, A. J. (2015). Influence of stem type on material loss at the metal-on-metal pinnacle taper junction. *Proceedings of the Institution of Mechanical Engineers. Part H, Journal of Engineering in Medicine*, *229*(1), 91–97. https://doi.org/10.1177/0954411914567931

Hu, J., Song, H., Sandfeld, S., Liu, X., & Wei, Y. (2021). Multiscale study of the dynamic friction coefficient due to asperity plowing. *Friction*, *9*(4), 822–839. https://doi.org/10.1007/s40544-020-0438-4

Hussenbocus, S., Kosuge, D., Solomon, L. B., Howie, D. W., & Oskouei, R. H. (2015). Head-Neck Taper Corrosion in Hip Arthroplasty. *BioMed Research International*, *2015*, 1–9. https://doi.org/10.1155/2015/758123

ISO 1947. (1973). *System of cone tolerances for conical workpieces from C = 1:3 to 1:500 and lengths from 6 to 630 mm*.

Jacobs, T. D. B., Junge, T., & Pastewka, L. (2017). Quantitative characterization of surface topography using spectral analysis. *Surface Topography: Metrology and Properties*, *5*(1), 013001. https://doi.org/10.1088/2051-672X/aa51f8

Jaekel, D. J., Ong, K. L., Lau, E. C., Watson, H. N., & Kurtz, S. M. (2014). Epidemiology of Total Hip and Knee Arthroplasty Infection. In *Periprosthetic Joint Infection of*

the Hip and Knee (pp. 1–14). Springer New York. https://doi.org/10.1007/978-1-4614-7928-4_1

Jauch-Matt, S. Y., Miles, A. W., & Gill, H. S. (2017). Effect of trunnion roughness and length on the modular taper junction strength under typical intraoperative assembly forces. *Medical Engineering & Physics*, *39*, 94–101. https://doi.org/10.1016/j.medengphy.2016.11.001

Kao, Y.-Y. J., Koch, C. N., Wright, T. M., & Padgett, D. E. (2016). Flexural Rigidity, Taper Angle, and Contact Length Affect Fretting of the Femoral Stem Trunnion in Total Hip Arthroplasty. *The Journal of Arthroplasty*, *31*(9), 254–258. https://doi.org/10.1016/j.arth.2016.02.079

Kaur, Ghadirinejad, & Oskouei. (2019). An Overview on the Tribological Performance of Titanium Alloys with Surface Modifications for Biomedical Applications. *Lubricants*, *7*(8), 65. https://doi.org/10.3390/lubricants7080065

Kocagöz, S. B., Underwood, R. J., Sivan, S., Gilbert, J. L., MacDonald, D. W., Day, J. S., & Kurtz, S. M. (2013). Does taper angle clearance influence fretting and corrosion damage at the head–stem interface? A matched cohort retrieval study. *Seminars in Arthroplasty*, *24*(4), 246–254. https://doi.org/10.1053/j.sart.2014.01.002

Krishnan, H., Krishnan, S. P., Blunn, G., Skinner, J. A., & Hart, A. J. (2013). Modular neck femoral stems. *The Bone & Joint Journal*, *95-B*(8), 1011–1021. https://doi.org/10.1302/0301-620X.95B8.31525

Krolczyk, G. M., Maruda, R. W., Nieslony, P., & Wieczorowski, M. (2016). Surface morphology analysis of Duplex Stainless Steel (DSS) in Clean Production using the Power Spectral Density. *Measurement*, *94*, 464–470. https://doi.org/10.1016/j.measurement.2016.08.023

Krull, A., Morlock, M. M., & Bishop, N. E. (2018). Factors influencing taper failure of modular revision hip stems. *Medical Engineering & Physics*, *54*, 65–73. https://doi.org/10.1016/j.medengphy.2018.02.001

Langton, D. J., Sidaginamale, R., Lord, J. K., Nargol, A. V. F., & Joyce, T. J. (2012). Taper junction failure in large-diameter metal-on-metal bearings. *Bone & Joint Research*, *1*(4), 56–63. https://doi.org/10.1302/2046-3758.14.2000047

Lavernia, C. J., Iacobelli, D. A., Villa, J. M., Jones, K., Gonzalez, J. L., & Jones, W. K. (2015). Trunnion–Head Stresses in THA: Are Big Heads Trouble? *The Journal of Arthroplasty*, *30*(6), 1085–1088. https://doi.org/10.1016/j.arth.2015.01.021

Learmonth, I. D., Young, C., & Rorabeck, C. (2007). The operation of the century: total hip replacement. *The Lancet*, *370*(9597), 1508–1519. https://doi.org/10.1016/S0140-6736(07)60457-7

Lecerf, G., Fessy, M. H., Philippot, R., Massin, P., Giraud, F., Flecher, X., Girard, J., Mertl, P., Marchetti, E., & Stindel, E. (2009). Femoral offset: Anatomical concept, definition, assessment, implications for preoperative templating and hip arthroplasty. *Orthopaedics & Traumatology: Surgery & Research*, *95*(3), 210–219. https://doi.org/10.1016/j.otsr.2009.03.010

Li, B., Li, P., Zhou, R., Feng, X.-Q., & Zhou, K. (2022). Contact mechanics in tribological and contact damage-related problems: A review. *Tribology International*, *171*, 107534. https://doi.org/10.1016/j.triboint.2022.107534

Liao, Y., Hoffman, E., Wimmer, M., Fischer, A., Jacobs, J., & Marks, L. (2013). CoCrMo metal-on-metal hip replacements. *Phys. Chem. Chem. Phys.*, *15*(3), 746–756. https://doi.org/10.1039/C2CP42968C

Liu, Y., Mace, A., Lee, H., Camargo, M., & Gilbert, J. L. (2022). Single asperity sub-nano to nanoscale wear and tribocorrosion of wrought CoCrMo and additively manufactured CoCrMoW alloys. *Tribology International*, *174*, 107770. https://doi.org/10.1016/j.triboint.2022.107770

Liu, Y., Zhu, D., Pierre, D., & Gilbert, J. L. (2019). Fretting initiated crevice corrosion of 316LVM stainless steel in physiological phosphate buffered saline: Potential and cycles to initiation. *Acta Biomaterialia*. https://doi.org/10.1016/j.actbio.2019.07.051

Lundberg, H. J., Ha, N. Q., Hall, D. J., Urban, R. M., Levine, B. R., & Pourzal, R. (2015). Contact Mechanics and Plastic Deformation at the Local Surface Topography Level After Assembly of Modular Head-Neck Junctions in Modern Total Hip Replacement Devices. In *Modularity and Tapers in Total Joint Replacement Devices* (pp. 59–82). ASTM International. https://doi.org/10.1520/STP159120140148

Lützner, J., Günther, K.-P., Postler, A., & Morlock, M. (2020). Metal Ion Release after Hip and Knee Arthroplasty – Causes, Biological Effects and Diagnostics. *Zeitschrift Für Orthopädie Und Unfallchirurgie*, *158*(04), 369–382. https://doi.org/10.1055/a-0929-8121

MacLeod, A. R., Sullivan, N. P. T., Whitehouse, M. R., & Gill, H. S. (2016). Large-diameter total hip arthroplasty modular heads require greater assembly forces for initial stability. *Bone & Joint Research*, *5*(8), 338–346. https://doi.org/10.1302/2046-3758.58.BJR-2016-0044.R1

Mai, P. T., Bormann, T., Müller, U., Kretzer, J. P., & Gibmeier, J. (2022). Effect of surface topography and residual stress on the taper connection stability in total hip arthroplasty. *Journal of the Mechanical Behavior of Biomedical Materials*, *128*, 105119. https://doi.org/10.1016/j.jmbbm.2022.105119

Mali, S. A. (2016). Mechanically assisted crevice corrosion in metallic biomaterials: a review. *Materials Technology*, *31*(12), 732–739. https://doi.org/10.1080/10667857.2016.1223909

Mali, S. A., & Gilbert, J. L. (2015). Correlating Fretting Corrosion and Micromotions in Modular Tapers: Test Method Development and Assessment. In *Modularity and Tapers in Total Joint Replacement Devices* (pp. 259–282). ASTM International. https://doi.org/10.1520/STP159120140136

Malyshev, V. N. (2014). Tribological aspects in friction stir welding and processing. In *Advances in Friction-Stir Welding and Processing* (pp. 329–386). Elsevier. https://doi.org/10.1533/9780857094551.329

Matharu, G. S., Pandit, H. G., Murray, D. W., & Judge, A. (2016). Adverse reactions to metal debris occur with all types of hip replacement not just metal-on-metal hips: a retrospective observational study of 3340 revisions for adverse reactions to metal debris from the National Joint Registry for England, Wales, Northern Ireland and the Isle of Man. *BMC Musculoskeletal Disorders*, *17*(1), 495. https://doi.org/10.1186/s12891-016-1329-8

McGrory, B. J., & McKenney, B. R. (2016). Revision for taper corrosion at the head-neck junction: pearls and pitfalls. *Current Reviews in Musculoskeletal Medicine*, *9*(1), 97–102. https://doi.org/10.1007/s12178-016-9325-z

McTighe, T., Brazil, D., Keppler, L., Keggi, J., & McPherson, E. (2015a). Metallic Modular Taper Junctions in Total Hip Arthroplasty. *Reconstructive Review*, *5*(2). https://doi.org/10.15438/rr.5.2.108

McTighe, T., Brazil, D., Keppler, L., Keggi, J., & McPherson, E. (2015b). Metallic Modular Taper Junctions in Total Hip Arthroplasty. *Reconstructive Review*, *5*(2). https://doi.org/10.15438/rr.5.2.108

Messellek, A. C., Ould Ouali, M., & Amrouche, A. (2020). Adaptive finite element simulation of fretting wear and fatigue in a taper junction of modular hip prosthesis. *Journal of the Mechanical Behavior of Biomedical Materials*, *111*, 103993. https://doi.org/10.1016/j.jmbbm.2020.103993

Mistry, J. B., Chughtai, M., Elmallah, R. K., Diedrich, A., Le, S., Thomas, M., & Mont, M. A. (2016). Trunnionosis in total hip arthroplasty: a review. *Journal of Orthopaedics and Traumatology*, *17*(1), 1–6. https://doi.org/10.1007/s10195-016-0391-1

Morlock, M. M., Hube, R., Wassilew, G., Prange, F., Huber, G., & Perka, C. (2020). Taper corrosion: a complication of total hip arthroplasty. *EFORT Open Reviews*, *5*(11), 776–784. https://doi.org/10.1302/2058-5241.5.200013

Morlock, M. M., Huber, G., & Bishop, N. (2014). Large-Diameter Total Hip Replacement Bearings. In *Tribology in Total Hip and Knee Arthroplasty* (pp. 3–14). Springer Berlin Heidelberg. https://doi.org/10.1007/978-3-642-45266-6_1

Mroczkowski, M. L., Hertzler, J. S., Humphrey, S. M., Johnson, T., & Blanchard, C. R. (2006). Effect of impact assembly on the fretting corrosion of modular hip tapers. *Journal of Orthopaedic Research*, *24*(2), 271–279. https://doi.org/10.1002/jor.20048

Mueller, U., Bormann, T., Schroeder, S., & Kretzer, J. P. (2021). Taper junctions in modular hip joint replacements: What affects their stability? *Journal of the Mechanical Behavior of Biomedical Materials*, *116*, 104258. https://doi.org/10.1016/j.jmbbm.2020.104258

Mueller, U., Braun, S., Schroeder, S., Sonntag, R., & Kretzer, J. P. (2017). Same Same but Different? 12/14 Stem and Head Tapers in Total Hip Arthroplasty. *The Journal of Arthroplasty*, *32*(10), 3191–3199. https://doi.org/10.1016/j.arth.2017.04.027

Mulvihill, D. M., Kartal, M. E., Nowell, D., & Hills, D. A. (2011). An elastic–plastic asperity interaction model for sliding friction. *Tribology International*, *44*(12), 1679–1694. https://doi.org/10.1016/j.triboint.2011.06.018

Munir, S., Walter, W. L., & Walsh, W. R. (2015). Variations in the trunnion surface topography between different commercially available hip replacement stems. *Journal of Orthopaedic Research*, *33*(1), 98–105. https://doi.org/10.1002/jor.22741

Nassif, N. A., Nawabi, D. H., Stoner, K., Elpers, M., Wright, T., & Padgett, D. E. (2014). Taper Design Affects Failure of Large-head Metal-on-metal Total Hip Replacements. *Clinical Orthopaedics and Related Research®*, *472*(2), 564–571. https://doi.org/10.1007/s11999-013-3115-3

NJR. (2022). *National Joint Registry, 19th Annual Report*.

Norman, T. L., Denen, J. E., Land, A. J., Kienitz, D. M., & Fehring, T. A. (2019). Taper-Trunnion Interface Stress Varies Significantly With Head Size and Activity. *The Journal of Arthroplasty*, *34*(1), 157–162. https://doi.org/10.1016/j.arth.2018.09.004

Oberg, E., Jones, F. D., Horton, H. L., & Ryffel, H. H. (2012). *Machinery's Handbook* (29th ed.). Industrial Press, Inc.

Oladokun, A., Hall, R. M., Neville, A., & Bryant, M. G. (2019). The evolution of subsurface micro-structure and tribo-chemical processes in cocrmo-ti6al4v fretting-corrosion contacts: What lies at and below the surface? *Wear*, *440–441*, 203095. https://doi.org/10.1016/j.wear.2019.203095

Ouellette, E. S., Mali, S. A., Kim, J., Grostefon, J., & Gilbert, J. L. (2019). Design, Material, and Seating Load Effects on In Vitro Fretting Corrosion Performance of Modular Head-Neck Tapers. *The Journal of Arthroplasty*, *34*(5), 991–1002. https://doi.org/10.1016/j.arth.2019.01.043

Panagiotidou, A., Cobb, T., Meswania, J., Skinner, J., Hart, A., Haddad, F., & Blunn, G. (2017). Effect of impact assembly on the interface deformation and fretting corrosion of modular hip tapers: An in vitro study. *Journal of Orthopaedic Research*. https://doi.org/10.1002/jor.23601

Panagiotidou, A., Meswania, J., Hua, J., Muirhead-Allwood, S., Hart, A., & Blunn, G. (2013). Enhanced wear and corrosion in modular tapers in total hip replacement is associated with the contact area and surface topography. *Journal of Orthopaedic Research*, *31*(12), 2032–2039. https://doi.org/10.1002/jor.22461

Pastides, P. S. (2013). Trunnionosis: A pain in the neck. *World Journal of Orthopedics*, *4*(4), 161. https://doi.org/10.5312/wjo.v4.i4.161

Patil, D. B., & Eriten, M. (2014). Effects of Interfacial Strength and Roughness on the Static Friction Coefficient. *Tribology Letters*, *56*(2), 355–374. https://doi.org/10.1007/s11249-014-0414-0

Pennock, A. T., Schmidt, A. H., & Bourgeault, C. A. (2002). Morse-type tapers: factors that may influence taper strength during total hip arthroplasty. *The Journal of Arthroplasty*, *17*(6), 773–778. http://www.ncbi.nlm.nih.gov/pubmed/12216033

Pivec, R., Meneghini, R. M., Hozack, W. J., Westrich, G. H., & Mont, M. A. (2014). Modular Taper Junction Corrosion and Failure: How to Approach a Recalled Total Hip Arthroplasty Implant. *The Journal of Arthroplasty*, *29*(1), 1–6. https://doi.org/10.1016/j.arth.2013.08.026

Plummer, D. R., Berger, R. A., Paprosky, W. G., Sporer, S. M., Jacobs, J. J., & della Valle, C. J. (2016). Diagnosis and Management of Adverse Local Tissue Reactions Secondary to Corrosion at the Head-Neck Junction in Patients with Metal on Polyethylene Bearings. *The Journal of Arthroplasty*, *31*(1), 264–268. https://doi.org/10.1016/j.arth.2015.07.039

Podulka, P. (2022). Selection of Methods of Surface Texture Characterisation for Reduction of the Frequency-Based Errors in the Measurement and Data Analysis Processes. *Sensors*, *22*(3), 791. https://doi.org/10.3390/s22030791

Porter, D. A., Urban, R. M., Jacobs, J. J., Gilbert, J. L., Rodriguez, J. A., & Cooper, H. J. (2014a). Modern Trunnions Are More Flexible: A Mechanical Analysis of THA

Taper Designs. *Clinical Orthopaedics and Related Research®*, *472*(12), 3963–3970. https://doi.org/10.1007/s11999-014-3965-3

Porter, D. A., Urban, R. M., Jacobs, J. J., Gilbert, J. L., Rodriguez, J. A., & Cooper, H. J. (2014b). Modern Trunnions Are More Flexible: A Mechanical Analysis of THA Taper Designs. *Clinical Orthopaedics and Related Research®*, *472*(12), 3963–3970. https://doi.org/10.1007/s11999-014-3965-3

Pourzal, R., Hall, D. J., Ha, N. Q., Urban, R. M., Levine, B. R., Jacobs, J. J., & Lundberg, H. J. (2016). Does Surface Topography Play a Role in Taper Damage in Head-neck Modular Junctions? *Clinical Orthopaedics and Related Research®*, *474*(10), 2232–2242. https://doi.org/10.1007/s11999-016-4933-x

Pourzal, R., Lundberg, H. J., Hall, D. J., & Jacobs, J. J. (2018). What Factors Drive Taper Corrosion? *The Journal of Arthroplasty*, *33*(9), 2707–2711. https://doi.org/10.1016/j.arth.2018.03.055

Racasan, R., Bills, P., Blunt, L., Hart, A., & Skinner, J. (2015a). Method for Characterization of Material Loss from Modular Head-Stem Taper Surfaces of Hip Replacement Devices. In *Modularity and Tapers in Total Joint Replacement Devices* (pp. 132–146). ASTM International. https://doi.org/10.1520/STP159120140139

Racasan, R., Bills, P., Blunt, L., Hart, A., & Skinner, J. (2015b). Method for Characterization of Material Loss from Modular Head-Stem Taper Surfaces of Hip Replacement Devices. In *Modularity and Tapers in Total Joint Replacement Devices* (pp. 132–146). ASTM International. https://doi.org/10.1520/STP159120140139

Raji, H. Y., & Shelton, J. C. (2019). Prediction of taper performance using quasi static FE models: The influence of loading, taper clearance and trunnion length. *Journal of Biomedical Materials Research. Part B, Applied Biomaterials*, *107*(1), 138–148. https://doi.org/10.1002/jbm.b.34104

Raju, S., Chinnakkannu, K., Puttaswamy, M. K., & Phillips, M. J. (2017). Trunnion Corrosion in Metal-on-Polyethylene Total Hip Arthroplasty. *Journal of the American Academy of Orthopaedic Surgeons*, *25*(2), 133–139. https://doi.org/10.5435/JAAOS-D-16-00352

Rehmer, A., Bishop, N. E., & Morlock, M. M. (2012). Influence of assembly procedure and material combination on the strength of the taper connection at the head–neck junction of modular hip endoprostheses. *Clinical Biomechanics*, *27*(1), 77–83. https://doi.org/10.1016/j.clinbiomech.2011.08.002

Rogers, B. A., Garbedian, S., Kuchinad, R. A., Backstein, D., Safir, O., & Gross, A. E. (2012). Total Hip Arthroplasty for Adult Hip Dysplasia. *Journal of Bone and Joint Surgery*, *94*(19), 1809–1821. https://doi.org/10.2106/JBJS.K.00779

Royhman, D., Patel, M., Runa, M. J., Jacobs, J. J., Hallab, N. J., Wimmer, M. A., & Mathew, M. T. (2015). Fretting-corrosion in hip implant modular junctions: New experimental set-up and initial outcome. *Tribology International*, *91*, 235–245. https://doi.org/10.1016/j.triboint.2015.04.032

Royhman, D., Pourzal, R., Hall, D., Lundberg, H. J., Wimmer, M. A., Jacobs, J., Hallab, N. J., & Mathew, M. T. (2021). Fretting-corrosion in hip taper modular junctions: The influence of topography and pH levels – An in-vitro study.

Journal of the Mechanical Behavior of Biomedical Materials, *118*, 104443. https://doi.org/10.1016/j.jmbbm.2021.104443

Smith, A. M., & Scott, S. H. (1996). Subjective scaling of smooth surface friction. *Journal of Neurophysiology*, *75*(5), 1957–1962. https://doi.org/10.1152/jn.1996.75.5.1957

Stockhausen, K. E., Riedel, C., Belinski, A. V., Rothe, D., Gehrke, T., Klebig, F., Gebauer, M., Amling, M., Citak, M., & Busse, B. (2021). Variability in stem taper surface topography affects the degree of corrosion and fretting in total hip arthroplasty. *Scientific Reports*, *11*(1), 9348. https://doi.org/10.1038/s41598-021-88234-3

Swaminathan, V., & Gilbert, J. L. (2012). Fretting corrosion of CoCrMo and Ti6Al4V interfaces. *Biomaterials*, *33*(22), 5487–5503. https://doi.org/10.1016/j.biomaterials.2012.04.015

Tan, S. C., Teeter, M. G., del Balso, C., Howard, J. L., & Lanting, B. A. (2015). Effect of Taper Design on Trunnionosis in Metal on Polyethylene Total Hip Arthroplasty. *The Journal of Arthroplasty*, *30*(7), 1269–1272. https://doi.org/10.1016/j.arth.2015.02.031

Toh, S. M. S., Ashkanfar, A., English, R., Rothwell, G., Langton, D. J., & Joyce, T. J. (2023). How does bicycling affect the longevity of Total Hip Arthroplasty? A finite element wear analysis. *Journal of the Mechanical Behavior of Biomedical Materials*, *139*, 105673. https://doi.org/10.1016/j.jmbbm.2023.105673

Triantafyllopoulos, G. K., Elpers, M. E., Burket, J. C., Esposito, C. I., Padgett, D. E., & Wright, T. M. (2016). Otto Aufranc Award: Large Heads Do Not Increase Damage at the Head-neck Taper of Metal-on-polyethylene Total Hip Arthroplasties. *Clinical Orthopaedics & Related Research*, *474*(2), 330–338. https://doi.org/10.1007/s11999-015-4468-6

Tsikandylakis, G., Mohaddes, M., Cnudde, P., Eskelinen, A., Kärrholm, J., & Rolfson, O. (2018). Head size in primary total hip arthroplasty. *EFORT Open Reviews*, *3*(5), 225–231. https://doi.org/10.1302/2058-5241.3.170061

Wade, A., Beadling, A. R., Neville, A., de Villiers, D., Cullum, C. J., Collins, S., & Bryant, M. G. (2020). Geometric Variations of Modular Head-Stem Taper Junctions of Total Hip Replacements. *Medical Engineering & Physics*, *83*, 34–47. https://doi.org/10.1016/j.medengphy.2020.07.017

Wade, A., Beadling, A. R., Neville, A., De Villiers, D., Cullum, C. J., Collins, S., & Bryant, M. G. (2020). Geometric Variations of Modular Head-Stem Taper Junctions of Total Hip Replacements. *Medical Engineering & Physics*, *83*, 34–47. https://doi.org/10.1016/j.medengphy.2020.07.017

Walton, K., Petrucci, M., Racasan, R., Blunt, L., Hart, A., & Bills, P. (2019). Focus variation measurement and advanced analysis of volumetric loss at the femoral head taper interface of retrieved modular replacement hips in replica. *Journal of Physics: Conference Series*, *1183*, 012004. https://doi.org/10.1088/1742-6596/1183/1/012004

Weiser, M. C., & Lavernia, C. J. (2017). Trunnionosis in Total Hip Arthroplasty. *Journal of Bone and Joint Surgery*, *99*(17), 1489–1501. https://doi.org/10.2106/JBJS.17.00345

Werner, P. H., Ettema, H. B., Witt, F., Morlock, M. M., & Verheyen, C. C. P. M. (2015). Basic Principles and Uniform Terminology for the Head-Neck Junction

in Hip Replacement. *HIP International*, *25*(2), 115–119. https://doi.org/10.5301/hipint.5000204

Whitehouse, M. R., Endo, M., Zachara, S., Nielsen, T. O., Greidanus, N. v., Masri, B. A., Garbuz, D. S., & Duncan, C. P. (2015). Adverse local tissue reactions in metal-on-polyethylene total hip arthroplasty due to trunnion corrosion. *The Bone & Joint Journal*, *97-B*(8), 1024–1030. https://doi.org/10.1302/0301-620X.97B8.34682

Whittaker, R. K., Hothi, H. S., Eskelinen, A., Blunn, G. W., Skinner, J. A., & Hart, A. J. (2017). Variation in taper surface roughness for a single design effects the wear rate in total hip arthroplasty. *Journal of Orthopaedic Research*, *35*(8), 1784–1792. https://doi.org/10.1002/jor.23456

Wight, C. M., Lanting, B., & Schemitsch, E. H. (2017). Evidence Based Recommendations for Reducing Head-Neck Taper Connection Fretting Corrosion in Hip Replacement Prostheses. *HIP International*, *27*(6), 523–531. https://doi.org/10.5301/hipint.5000545

Wiklund, I., & Romanus, B. (1991). A comparison of quality of life before and after arthroplasty in patients who had arthrosis of the hip joint. *The Journal of Bone and Joint Surgery. American Volume*, *73*(5), 765–769. http://www.ncbi.nlm.nih.gov/pubmed/2045402

Witt, F., Gührs, J., Morlock, M. M., & Bishop, N. E. (2015). Quantification of the Contact Area at the Head-Stem Taper Interface of Modular Hip Prostheses. *PLOS ONE*, *10*(8), e0135517. https://doi.org/10.1371/journal.pone.0135517

Yavari, M. R., & Hasbullah, M. (2017). Effect of surface roughness and taper angle on junction strength of modular biomedical implant. *International Journal of Mechanical and Mechatronics Engineering*, *16*(2), 42–47.

Zhang, T., Harrison, N. M., McDonnell, P. F., McHugh, P. E., & Leen, S. B. (2013). A finite element methodology for wear–fatigue analysis for modular hip implants. *Tribology International*, *65*, 113–127. https://doi.org/10.1016/j.triboint.2013.02.016

Appendices

A1. Post-processing and visualisation scripts

Script function: Post process Abaqus ODB files, creates text files with COORD (Coordinate) node data.

Language: Python

```python
#Import packages#########################################
from odbAccess import *
from abaqusConstants import *
from sys import argv, exit
import os
import pickle
import numpy

if __name__ == '__main__':

    path=''
    odbName = ''
    surface='TRUNNIONSURFACE' #'BORESURFACE'
    odbName=odbName+'.odb'
    WalkingStepFramesLen=[0,9]#
    VariableToObserve=['COORD']


    if (os.path.exists(path+odbName)):

        odb = openOdb(path+odbName)

        odbRAss=odb.rootAssembly
        print(odb.steps.values()[0].name)
        print(odbName)
        print(surface)

        frame=0
        while frame<len(WalkingStepFramesLen):
            vvv=0

            while vvv<len(VariableToObserve):
                txtName=odbName+'-'+VariableToObserve[vvv]+'-f%d'%WalkingStepFramesLen[frame]
                NoSteps=len(odb.steps.keys())
                StepList=['' for x in range(NoSteps)]
                i=0
                for stepName in odb.steps.keys():
                    StepList[i]=odb.steps.values()[i]
                    i+=1

                CPRESSValues=
StepList[0].frames[WalkingStepFramesLen[frame]].fieldOutputs[VariableToObserve[vvv]]#step list 1
for 0.15, 3 for >0.15
```

223

```
        odbRAss=odb.rootAssembly.nodeSets[surface]
        CPRESSValues = CPRESSValues.getSubset(region=odbRAss)

        print CPRESSValues.values[0].nodeLabel
        print CPRESSValues.values[0].data[0]

        txtfile=open(txtName+'_'+surface+'.txt','w')
        txtfile.write('NodeLabel, DefXCoordinate, DefYCoordinate, DefZCoordinate\n')
        print txtName
        v=0
        while v<len(CPRESSValues.values):
            DeformedCrds=CPRESSValues.values[v].data#.dot(RotX)
            DeformedCrds=DeformedCrds.tolist()
            txtfile.write('%d, %.6f,
%.6f\n'%(CPRESSValues.values[v].nodeLabel,DeformedCrds[0],DeformedCrds[1]))


            v+=1
        txtfile.close()
        vvv+=1
      frame+=1

    odb.close()
  else:
    print 'Odb name does not exist'
```

Script function: Post processing Abaqus ODB files, creates text files with CPRESS and CAREA (Contact pressure and contact area) node data.

Language: Python

```python
#Import packages#########################################
from odbAccess import *
from abaqusConstants import *
from sys import argv, exit
import os
import pickle
import numpy

if __name__ == '__main__':

    path='Z:/Documents/Doctorado Reynol/OUTPUT/ODB/'
    odbName = ''
    odbName=odbName+'.odb'
    WalkingStepFramesLen=[4,6,9]
    VariableToObserve=['CPRESS']

    if (os.path.exists(path+odbName)):

        odb = openOdb(path+odbName)
        odbRAss=odb.rootAssembly
        print(odb.steps.values()[0].name)

        frame=0
        while frame<len(WalkingStepFramesLen):
            vvv=0

            while vvv<len(VariableToObserve):
                txtName=odbName+'-'+VariableToObserve[vvv]+'-f%d'%WalkingStepFramesLen[frame]
                NoSteps=len(odb.steps.keys())
                StepList=['' for x in range(NoSteps)]
                i=0
                for stepName in odb.steps.keys():
                    StepList[i]=odb.steps.values()[i]
                    i+=1

                CPRESSValues=
StepList[0].frames[WalkingStepFramesLen[frame]].fieldOutputs[VariableToObserve[vvv]].values#step list 1 for 0.15, 3 for >0.15#
                NoCPRESSValues = len(CPRESSValues)

                print txtName


                odbRAss=odb.rootAssembly.nodeSets['TRUNNIONSURFACE']

                dummyrootAssembly=list(odbRAss.nodes[0])
                print len(dummyrootAssembly)
                txtfile=open(txtName+'_'+'TrunnionSurface'+'.txt','w')
                txtfile.write('NodeLabel, XCoordinate, YCoordinate, ZCoordinate, Variable\n')

                v=0
```

```
        while v<NoCPRESSValues:
            NoNodeSurface=len(dummyrootAssembly)
            s=0
            while s<NoNodeSurface:
                if CPRESSValues[v].nodeLabel==dummyrootAssembly[s].label:
                    NodeCrds=dummyrootAssembly[s].coordinates#.dot(RotX)
                    NodeCoordsRot=NodeCrds.tolist()
                    txtfile.write('%d, %.3f, %.3f, %.3f,
%.5f\n'%(dummyrootAssembly[s].label,NodeCoordsRot[0],NodeCoordsRot[1],NodeCoordsRot[2],CP
RESSValues[v].data))
                    del dummyrootAssembly[s]
                    break
                s+=1
            v+=1
        txtfile.close()
        vvv+=1
    frame+=1

    odb.close()
else:
    print 'Odb name does not exist'
```

Script function: Processes node data in text files, it links nodes in the trunnion surface with the closest bore surface nodes.

Language: MATLAB

```
clc
clear
%Start variables
variables=["COORD"];
odbName='';
linS = {'-','--','--o','--.','--s','--d','--*','--+'};
variablesSize=size(variables);
variablesSize=variablesSize(1,2);


tt=1;
%ModelVariables
AngleMismatch="0";
CoeficientOfFriction="";
AssemblyForce="";
centre={0,0,0};




%Bore and Trunnion initial position
Step0PositionCoordsTxt='Job-'+AngleMismatch+CoeficientOfFriction+AssemblyForce+'Activity.odb-
COORD-f0_TrunnionSurface';
Step0PositionCoordsTxt=strcat(Step0PositionCoordsTxt,'.txt');
Step0PositionCoordsTxt=strcat(odbName,'.odb-COORD-f0_TrunnionSurface_preLoad','.txt');
Step0PositionCoordsOdb=strcat(path,Step0PositionCoordsTxt);
Step0PositionCoords=readtable(Step0PositionCoordsOdb);
Step0PositionCoords.DefZCoordinate=round( Step0PositionCoords.DefZCoordinate,2);

Step0PositionCoordsTxtBore='Job'+AngleMismatch+CoeficientOfFriction+AssemblyForce+'Activity.o
db-COORD-f0_BoreSurface';
Step0PositionCoordsTxtBore=strcat(Step0PositionCoordsTxtBore,'.txt');
Step0PositionCoordsTxtBore=strcat(odbName,'.odb-COORD-f0_BoreSurface_preLoad','.txt');
Step0PositionCoordsBoreOdb=strcat(path,Step0PositionCoordsTxtBore);
Step0PositionBoreCoords=readtable(Step0PositionCoordsBoreOdb);
Step0PositionBoreCoords.DefZCoordinate=round( Step0PositionBoreCoords.DefZCoordinate,2);
%Select the distal surface of the trunnion and bore
noZUniqueValuesTrunnion=sort(unique(Step0PositionCoords.DefZCoordinate));
noZUniqueValuesTrunnion_dummy=noZUniqueValuesTrunnion;
MinZUniqueValuesTrunnion=min(unique(Step0PositionCoords.DefZCoordinate));




noZUniqueValuesBore=sort(unique(Step0PositionBoreCoords.DefZCoordinate));

DummyZCoordArray = unique(Step0PositionBoreCoords.DefZCoordinate);
[val, indx] = min(abs(MinZUniqueValuesTrunnion-DummyZCoordArray));

MinZUniqueValuesBore=DummyZCoordArray(indx);
```

```
Step0PositionCoords=Step0PositionCoords((Step0PositionCoords.DefZCoordinate==MinZUniqueValu
esTrunnion),:);
Step0PositionBoreCoords=Step0PositionBoreCoords((Step0PositionBoreCoords.DefZCoordinate==Mi
nZUniqueValuesBore),:);

Trunnion_Xcentre=(max(Step0PositionCoords.DefXCoordinate)+min(Step0PositionCoords.DefXCoor
dinate))/2;
Trunnion_Ycentre=(max(Step0PositionCoords.DefYCoordinate)+min(Step0PositionCoords.DefYCoor
dinate))/2;

a_TrunnionRadius = abs(max(Step0PositionCoords.DefXCoordinate)-Trunnion_Xcentre)
b_TrunnionRadius = abs(max(Step0PositionCoords.DefYCoordinate)-Trunnion_Ycentre)

noZUniqueValuesTrunnion=size(unique(Step0PositionCoords.NodeLabel));
noZUniqueValuesBore=size(unique(Step0PositionBoreCoords.NodeLabel));

centreTrunnionX=Trunnion_Xcentre;
centreTrunnionY=Trunnion_Ycentre;
centreCoords={centreTrunnionX,centreTrunnionY,min(min(Step0PositionBoreCoords.DefZCoordinat
e))};

%Link trunnion surface to bore surface nodes
linkID=1;

TableID=cell2table(cell(0,3),'VariableNames',{'linkID','TrunnionNodeLabel','BoreNodeLabel'});


for trunnionSurf2Link=1:noZUniqueValuesTrunnion
    minDistance=1000;
    for boreSurf2Link=1:noZUniqueValuesBore
        TrunnionX=table2cell(Step0PositionCoords(trunnionSurf2Link,'DefXCoordinate'));
        TrunnionY=table2cell(Step0PositionCoords(trunnionSurf2Link,'DefYCoordinate'));
        TrunnionZ=table2cell(Step0PositionCoords(trunnionSurf2Link,'DefZCoordinate'));

        BoreX=table2cell(Step0PositionBoreCoords(boreSurf2Link,'DefXCoordinate'));
        BoreY=table2cell(Step0PositionBoreCoords(boreSurf2Link,'DefYCoordinate'));
        BoreZ=table2cell(Step0PositionBoreCoords(boreSurf2Link,'DefZCoordinate'));

        currentDistance=sqrt(((TrunnionX{1}-BoreX{1})^2)+((TrunnionY{1}-BoreY{1})^2)+((TrunnionZ{1}-
BoreZ{1})^2));
        if minDistance>currentDistance
            minDistance=currentDistance;
            TrunnionNodeLabel=table2cell(Step0PositionCoords(trunnionSurf2Link,'NodeLabel'));
            BoreNodeLabel=table2cell(Step0PositionBoreCoords(boreSurf2Link,'NodeLabel'));
        end
    end
    T1=table(linkID, TrunnionNodeLabel{1},
BoreNodeLabel{1},'VariableNames',{'linkID','TrunnionNodeLabel','BoreNodeLabel'});
    Step0PositionCoords.linkID(Step0PositionCoords.NodeLabel==TrunnionNodeLabel{1} ) = linkID;
    Step0PositionBoreCoords.linkID(Step0PositionBoreCoords.NodeLabel==BoreNodeLabel{1} ) =
linkID;
    TableID=[TableID;T1];
    linkID=linkID+1;
end
Step0PositionBoreCoords=Step0PositionBoreCoords((Step0PositionBoreCoords.linkID>0),:);
```

228

Script function: Processes node data in text files, calculates accumulated micromotions over activity phase using data of linked nodes.

Language: MATLAB

```matlab
path2='';
segment=[{'0','3'};{'3','6'};{'6','10'};{'10','13'};{'13','18'};{'18','20'}];%Walking 1-6

ppc=1;
step=[segment(ppc,1),segment(ppc,2)];

scaleLoad=0.01;
scaleMotion=200;
%figure('visible','off');

WlakingGte=ppc+1;
if step{2}=="0"; WlakingGte=2;
elseif step{2}=="1"; WlakingGte=2;
elseif step{2}=="3"; WlakingGte=3;
elseif step{2}=="6"; WlakingGte=4;
elseif step{2}=="10"; WlakingGte=5;
elseif step{2}=="12"; WlakingGte=6;
elseif step{2}=="16"; WlakingGte=7;
elseif step{2}=="20"; WlakingGte=8;
end
stepSize=size(step);
stepSize=stepSize(1,2);

TrunnionAngle=0;
if AngleMismatch=="0"
   TrunnionAngle=5.6/2;
elseif AngleMismatch=="0d06"
   TrunnionAngle=5.54/2;
elseif AngleMismatch=="0d18"
   TrunnionAngle=5.47/2; %Good angle
elseif AngleMismatch=="N0d06"
   TrunnionAngle=5.66/2;
elseif AngleMismatch=="N0d13"
   TrunnionAngle=5.73/2;
end


%Trunnion Diff
StepNPositionCoordsTxt=strcat(odbName,'.odb-COORD-f',step(1,1),'_TrunnionSurface.txt');
StepNPositionCoordsOdb=strcat(path,StepNPositionCoordsTxt);
StepNPositionCoordsOdb = StepNPositionCoordsOdb{1};
StepNPositionCoords=readtable(StepNPositionCoordsOdb);
StepMPositionCoordsTxt=strcat(odbName,'.odb-COORD-f',step(1,2),'_TrunnionSurface','.txt');
StepMPositionCoordsOdb=strcat(path,StepMPositionCoordsTxt);
StepMPositionCoordsOdb = StepMPositionCoordsOdb{1};
StepMPositionCoords=readtable(StepMPositionCoordsOdb);

StepNPositionCoords=sortrows(StepNPositionCoords,'NodeLabel','descend');
StepMPositionCoords=sortrows(StepMPositionCoords,'NodeLabel','descend');
```

```
diffCoords=innerjoin(StepNPositionCoords, StepMPositionCoords,'LeftKeys',1,'RightKeys',1);
diffCoords.DifferenceX=diffCoords.DefXCoordinate_StepNPositionCoords -
diffCoords.DefXCoordinate_StepMPositionCoords;
diffCoords.DifferenceY=diffCoords.DefYCoordinate_StepNPositionCoords -
diffCoords.DefYCoordinate_StepMPositionCoords;
diffCoords.DifferenceZ=diffCoords.DefZCoordinate_StepNPositionCoords -
diffCoords.DefZCoordinate_StepMPositionCoords;

diffCoords=innerjoin(diffCoords, Step0PositionCoords,'LeftKeys',1,'RightKeys',1);

%Bore diff
StepNPositionCoordsBoreTxt=strcat(odbName,'.odb-COORD-f',step(1,1),'_BoreSurface','.txt');
StepNPositionCoordsBoreOdb=strcat(path,StepNPositionCoordsBoreTxt);
StepNPositionCoordsBoreOdb = StepNPositionCoordsBoreOdb{1};
StepNPositionBoreCoords=readtable(StepNPositionCoordsBoreOdb);
StepMPositionCoordsBoreTxt=strcat(odbName,'.odb-COORD-f',step(1,2),'_BoreSurface','.txt');
StepMPositionCoordsBoreOdb=strcat(path,StepMPositionCoordsBoreTxt);
StepMPositionCoordsBoreOdb = StepMPositionCoordsBoreOdb{1};
StepMPositionBoreCoords=readtable(StepMPositionCoordsBoreOdb);

StepNPositionBoreCoords=sortrows(StepNPositionBoreCoords,'NodeLabel','descend');
StepMPositionBoreCoords=sortrows(StepMPositionBoreCoords,'NodeLabel','descend');

diffBoreCoords=innerjoin(StepNPositionBoreCoords,
StepMPositionBoreCoords,'LeftKeys',1,'RightKeys',1);
diffBoreCoords.DifferenceX=diffBoreCoords.DefXCoordinate_StepNPositionBoreCoords -
diffBoreCoords.DefXCoordinate_StepMPositionBoreCoords;
diffBoreCoords.DifferenceY=diffBoreCoords.DefYCoordinate_StepNPositionBoreCoords -
diffBoreCoords.DefYCoordinate_StepMPositionBoreCoords;
diffBoreCoords.DifferenceZ=diffBoreCoords.DefZCoordinate_StepNPositionBoreCoords -
diffBoreCoords.DefZCoordinate_StepMPositionBoreCoords;

diffBoreCoords=innerjoin(diffBoreCoords, Step0PositionBoreCoords,'LeftKeys',1,'RightKeys',1);

diffRelativeCoords=innerjoin(diffCoords, diffBoreCoords,'LeftKeys',14,'RightKeys',14);
diffRelativeCoords.RelativeDifferenceX=diffRelativeCoords.DifferenceX_diffBoreCoords -
diffRelativeCoords.DifferenceX_diffCoords;
diffRelativeCoords.RelativeDifferenceY=diffRelativeCoords.DifferenceY_diffBoreCoords -
diffRelativeCoords.DifferenceY_diffCoords;
diffRelativeCoords.RelativeDifferenceZ=diffRelativeCoords.DifferenceZ_diffBoreCoords -
diffRelativeCoords.DifferenceZ_diffCoords;

diffRelativeCoords=innerjoin(diffRelativeCoords, Step0PositionCoords,'LeftKeys',1,'RightKeys',1);


%Rotation X
diffRelativeCoords.RelativeDifferenceXRot=(diffRelativeCoords.RelativeDifferenceX*1)+ ...
                    (diffRelativeCoords.RelativeDifferenceY*0)+ ...
                    (diffRelativeCoords.RelativeDifferenceZ*0);
diffRelativeCoords.RelativeDifferenceYRot=(diffRelativeCoords.RelativeDifferenceX*0)+ ...

(diffRelativeCoords.RelativeDifferenceY.*cosd(TrunnionAngle*cosd(atan2d(diffRelativeCoords.DefYC
oordinate-centreCoords{2},diffRelativeCoords.DefXCoordinate-centreCoords{1}))))+ ...
```

```
(diffRelativeCoords.RelativeDifferenceZ.*sind(TrunnionAngle*cosd(atan2d(diffRelativeCoords.DefYC
oordinate-centreCoords{2},diffRelativeCoords.DefXCoordinate-centreCoords{1}))));
diffRelativeCoords.RelativeDifferenceZRot=(diffRelativeCoords.RelativeDifferenceX*0)+ ...
                (diffRelativeCoords.RelativeDifferenceY.*-
sind(TrunnionAngle*cosd(atan2d(diffRelativeCoords.DefYCoordinate-
centreCoords{2},diffRelativeCoords.DefXCoordinate-centreCoords{1}))))+ ...

(diffRelativeCoords.RelativeDifferenceZ.*cosd(TrunnionAngle*cosd(atan2d(diffRelativeCoords.DefYC
oordinate-centreCoords{2},diffRelativeCoords.DefXCoordinate-centreCoords{1}))));
%
% %Rotation Y
diffRelativeCoords.RelativeDifferenceXRot1=(diffRelativeCoords.RelativeDifferenceXRot.*cosd(Trunn
ionAngle*sind(atan2d(diffRelativeCoords.DefYCoordinate-
centreCoords{2},diffRelativeCoords.DefXCoordinate-centreCoords{1}))))+ ...
                (diffRelativeCoords.RelativeDifferenceYRot*0)+ ...
                (diffRelativeCoords.RelativeDifferenceZRot.*-
sind(TrunnionAngle*sind(atan2d(diffRelativeCoords.DefYCoordinate-
centreCoords{2},diffRelativeCoords.DefXCoordinate-centreCoords{1}))));
diffRelativeCoords.RelativeDifferenceYRot1=(diffRelativeCoords.RelativeDifferenceXRot*0)+ ...
                (diffRelativeCoords.RelativeDifferenceYRot*1)+ ...
                (diffRelativeCoords.RelativeDifferenceZRot*0);
diffRelativeCoords.RelativeDifferenceZRot1=(diffRelativeCoords.RelativeDifferenceXRot.*sind(Trunni
onAngle*sind(atan2d(diffRelativeCoords.DefYCoordinate-
centreCoords{2},diffRelativeCoords.DefXCoordinate-centreCoords{1}))))+ ...
                (diffRelativeCoords.RelativeDifferenceYRot*0)+ ...

(diffRelativeCoords.RelativeDifferenceZRot.*cosd(TrunnionAngle*sind(atan2d(diffRelativeCoords.De
fYCoordinate-centreCoords{2},diffRelativeCoords.DefXCoordinate-centreCoords{1}))));
%Rotation Z
Step0PositionCoords=sortrows(Step0PositionCoords,'NodeLabel','descend');
diffRelativeCoords=sortrows(diffRelativeCoords,'NodeLabel_diffCoords','descend');

diffRelativeCoords.RelativeDifferenceXRot2=(diffRelativeCoords.RelativeDifferenceXRot1.*cosd(atan
2d(diffRelativeCoords.DefYCoordinate-centreCoords{2},diffRelativeCoords.DefXCoordinate-
centreCoords{1})))+ ...

(diffRelativeCoords.RelativeDifferenceYRot1.*sind(atan2d(diffRelativeCoords.DefYCoordinate-
centreCoords{2},diffRelativeCoords.DefXCoordinate-centreCoords{1})))+ ...
                (diffRelativeCoords.RelativeDifferenceZRot1*0);
diffRelativeCoords.RelativeDifferenceYRot2=(diffRelativeCoords.RelativeDifferenceXRot1.*-
sind(atan2d(diffRelativeCoords.DefYCoordinate-centreCoords{2},diffRelativeCoords.DefXCoordinate-
centreCoords{1})))+ ...

(diffRelativeCoords.RelativeDifferenceYRot1.*cosd(atan2d(diffRelativeCoords.DefYCoordinate-
centreCoords{2},diffRelativeCoords.DefXCoordinate-centreCoords{1})))+ ...
                (diffRelativeCoords.RelativeDifferenceZRot1*0);
diffRelativeCoords.RelativeDifferenceZRot2=(diffRelativeCoords.RelativeDifferenceXRot1*0)+ ...
                (diffRelativeCoords.RelativeDifferenceYRot1*0)+ ...
                (diffRelativeCoords.RelativeDifferenceZRot1*1);
%Rotate on Z to adjust normal to ellipse surface
diffRelativeCoords.nx=(((diffRelativeCoords.DefXCoordinate)*2)-
Trunnion_Xcentre)*(b_TrunnionRadius/a_TrunnionRadius);
diffRelativeCoords.ny=(((diffRelativeCoords.DefYCoordinate)*2)-
Trunnion_Ycentre)*(a_TrunnionRadius/b_TrunnionRadius);
```

```matlab
diffRelativeCoords.nx=diffRelativeCoords.nx-(diffRelativeCoords.DefXCoordinate);
diffRelativeCoords.ny=diffRelativeCoords.ny-(diffRelativeCoords.DefYCoordinate);

diffRelativeCoords.RelativeDifferenceXRot3=(diffRelativeCoords.RelativeDifferenceXRot2.*cosd(atan
2d(diffRelativeCoords.ny,diffRelativeCoords.nx)-atan2d((diffRelativeCoords.DefYCoordinate-
centreCoords{2}),(diffRelativeCoords.DefXCoordinate-centreCoords{1}))))+ ...

(diffRelativeCoords.RelativeDifferenceYRot2.*sind(atan2d(diffRelativeCoords.ny,diffRelativeCoords.
nx)-atan2d((diffRelativeCoords.DefYCoordinate-
centreCoords{2}),(diffRelativeCoords.DefXCoordinate-centreCoords{1}))))+ ...
                        (diffRelativeCoords.RelativeDifferenceZRot2*0);
diffRelativeCoords.RelativeDifferenceYRot3=(diffRelativeCoords.RelativeDifferenceXRot2.*-
sind(atan2d(diffRelativeCoords.ny,diffRelativeCoords.nx)-
atan2d((diffRelativeCoords.DefYCoordinate-centreCoords{2}),(diffRelativeCoords.DefXCoordinate-
centreCoords{1}))))+ ...

(diffRelativeCoords.RelativeDifferenceYRot2.*cosd(atan2d(diffRelativeCoords.ny,diffRelativeCoords.
nx)-atan2d((diffRelativeCoords.DefYCoordinate-
centreCoords{2}),(diffRelativeCoords.DefXCoordinate-centreCoords{1}))))+ ...
                        (diffRelativeCoords.RelativeDifferenceZRot2*0);
diffRelativeCoords.RelativeDifferenceZRot3=(diffRelativeCoords.RelativeDifferenceXRot2*0)+ ...
                        (diffRelativeCoords.RelativeDifferenceYRot2*0)+ ...
                        (diffRelativeCoords.RelativeDifferenceZRot2*1);

hold on
RelativeMotions=quiver3(diffRelativeCoords.DefXCoordinate,diffRelativeCoords.DefYCoordinate,diff
RelativeCoords.DefZCoordinate,...
diffRelativeCoords.RelativeDifferenceX*scaleMotion,diffRelativeCoords.RelativeDifferenceY*scaleM
otion,diffRelativeCoords.RelativeDifferenceZ*scaleMotion,'AutoScale','off');


diffRelativeCoords.TotalRealtiveMotionMagnitude =
sqrt((diffRelativeCoords.RelativeDifferenceXRot2.^2)+(diffRelativeCoords.RelativeDifferenceYRot2.^
2)+(diffRelativeCoords.RelativeDifferenceZRot2.^2));




maxTrunnionNormalDisplacement = max(diffRelativeCoords.RelativeDifferenceXRot3)*1000
maxTrunnionTangntialDisplacement = max(diffRelativeCoords.RelativeDifferenceYRot3)*1000
maxTrunnionPistoningDisplacement = max(diffRelativeCoords.RelativeDifferenceZRot3)*1000
MaxTotalRealtiveMotionMagnitude=max(diffRelativeCoords.TotalRealtiveMotionMagnitude)*1000
AverageTotalRelativeMotionMagnitude=mean(diffRelativeCoords.TotalRealtiveMotionMagnitude);

atesto=diffRelativeCoords(diffRelativeCoords.TotalRealtiveMotionMagnitude==max(diffRelativeCoor
ds.TotalRealtiveMotionMagnitude),:);

RelativeMotions=quiver3(atesto.DefXCoordinate,atesto.DefYCoordinate,atesto.DefZCoordinate,...
atesto.RelativeDifferenceX*scaleMotion,atesto.RelativeDifferenceY*scaleMotion,atesto.RelativeDiff
erenceZ*scaleMotion,'r','AutoScale','off');

imgOdbName=strcat(path2,odbName,'TotalRelative_Motion',step(1,1),'to',step(1,2),'.png');
imgOdbName=imgOdbName{1};
saveas(RelativeMotions,imgOdbName);
```

```
 figure(1)

MaxNormalDisplacemenDirectionX=diffRelativeCoords.DefXCoordinate(diffRelativeCoords.RelativeD
ifferenceXRot2==maxTrunnionNormalDisplacement);
MaxNormalDisplacemenDirectionY=diffRelativeCoords.DefYCoordinate(diffRelativeCoords.RelativeD
ifferenceXRot2==maxTrunnionNormalDisplacement);

MaxNormalDisplacemenDirection=atan2d(MaxNormalDisplacemenDirectionY-
centreCoords{2},MaxNormalDisplacemenDirectionX-centreCoords{1});
TestX=(diffRelativeCoords.RelativeDifferenceXRot3.*cosd(-
atan2d(diffRelativeCoords.DefYCoordinate-centreCoords{2},diffRelativeCoords.DefXCoordinate-
centreCoords{1})))+ ...
                (diffRelativeCoords.RelativeDifferenceYRot3.*sind(-
atan2d(diffRelativeCoords.DefYCoordinate-centreCoords{2},diffRelativeCoords.DefXCoordinate-
centreCoords{1}))*0)+ ...
                (diffRelativeCoords.RelativeDifferenceZRot3*0);
TestY=(diffRelativeCoords.RelativeDifferenceXRot3.*-sind(-
atan2d(diffRelativeCoords.DefYCoordinate-centreCoords{2},diffRelativeCoords.DefXCoordinate-
centreCoords{1})))+ ...
                (diffRelativeCoords.RelativeDifferenceYRot3.*cosd(-
atan2d(diffRelativeCoords.DefYCoordinate-centreCoords{2},diffRelativeCoords.DefXCoordinate-
centreCoords{1}))*0)+ ...
                (diffRelativeCoords.RelativeDifferenceZRot3*0);
TestZ=(diffRelativeCoords.RelativeDifferenceX*0)+ ...
                (diffRelativeCoords.RelativeDifferenceY*0)+ ...
                (diffRelativeCoords.RelativeDifferenceZ*0);
hold on

NormalMotion=quiver3(diffRelativeCoords.DefXCoordinate,diffRelativeCoords.DefYCoordinate,diffR
elativeCoords.DefZCoordinate, ...
    TestX*scaleMotion,TestY*scaleMotion,TestZ*scaleMotion,'AutoScale','off');
imgOdbName=strcat(path2,odbName,'Normal_RelativeMotion',step(1,1),'to',step(1,2),'.png');
imgOdbName=imgOdbName{1};
saveas(NormalMotion,imgOdbName);
hold on
```

Script function: Creates images to visualise accumulated micromotions of nodes in contact.

Language: MATLAB

```
clf
caxis_upperLimit=45;
sizeDot=5;
pepe=2;
mango=atan2d(dummy_TrunnionContact.DefYCoordinate,dummy_TrunnionContact.DefXCoordinate);
mango=round(mango,pepe);
upperlimitss=45;
ballsize=10;


x_contour = mango.*(-1);
y_contour = dummy_TrunnionContact.DefZCoordinate;
v_contour = dummy_TrunnionContact.Resultant*1000;%Z Data

pointss=1000;

xx = linspace(min(x_contour),max(x_contour),pointss);
zz = linspace(min(y_contour),max(y_contour),pointss);
[xq_contour,yq_contour] = meshgrid(xx,zz);         % create 2d mesh
vq_contour = griddata(x_contour,y_contour,v_contour,xq_contour,yq_contour,'natural');

alpshh=alphaShape(x_contour,y_contour,ballsize);
alpshh2=inShape(alpshh,xq_contour,yq_contour);
vq_contour(~alpshh2) = NaN;

figure(2)
contourplot_fig=contourf(xq_contour, yq_contour, vq_contour,100,'LineColor','none');
xlim([-180 180])
ylim([min(y_contour) max(y_contour)])
xticks(-180:90:180)
caxis([0,upperlimitss])
shading flat

imgOdbName=strcat(path2,odbName,"TotalRelative_Motion_allSegments_contour.png");
imgOdbName=imgOdbName{1};
saveas(gcf,imgOdbName);


v_contour = dummy_TrunnionContact.Tangential*1000;%Z Data
vq_contour = griddata(x_contour,y_contour,v_contour,xq_contour,yq_contour,'natural');

alpshh=alphaShape(x_contour,y_contour,ballsize);
alpshh2=inShape(alpshh,xq_contour,yq_contour);
vq_contour(~alpshh2) = NaN;

figure(3)
contourplot_fig=contourf(xq_contour, yq_contour, vq_contour,100,'LineColor','none');
```

```
xlim([-180 180])
ylim([min(y_contour) max(y_contour)])
xticks(-180:90:180)
caxis([0,upperlimitss])
shading flat

imgOdbName=strcat(path2,odbName,"TangentialRelative_Motion_allSegments_contour.png");
imgOdbName=imgOdbName{1};
saveas(gcf,imgOdbName);

v_contour = dummy_TrunnionContact.Pistoning*1000;%Z Data
vq_contour = griddata(x_contour,y_contour,v_contour,xq_contour,yq_contour,'natural');

alpshh=alphaShape(x_contour,y_contour,ballsize);
alpshh2=inShape(alpshh,xq_contour,yq_contour);
vq_contour(~alpshh2) = NaN;

figure(9)
contourplot_fig=contourf(xq_contour, yq_contour, vq_contour,100,'LineColor','none');
xlim([-180 180])
ylim([min(y_contour) max(y_contour)])
xticks(-180:90:180)
caxis([0,upperlimitss])
shading flat

imgOdbName=strcat(path2,odbName,"PistoningRelative_Motion_allSegments_contour.png");
imgOdbName=imgOdbName{1};
saveas(gcf,imgOdbName);

v_contour = dummy_TrunnionContact.Normal*1000;%Z Data

vq_contour = griddata(x_contour,y_contour,v_contour,xq_contour,yq_contour,'natural');

alpshh=alphaShape(x_contour,y_contour,ballsize);
alpshh2=inShape(alpshh,xq_contour,yq_contour);
vq_contour(~alpshh2) = NaN;

figure(10)
contourf(xq_contour, yq_contour, vq_contour,100,'LineColor','none')
xlim([-180 180])
ylim([min(y_contour) max(y_contour)])
xticks(-180:90:180)
caxis([0,upperlimitss])
shading flat

imgOdbName=strcat(path2,odbName,"NormalRelative_Motion_allSegments_contour.png");
imgOdbName=imgOdbName{1};
saveas(gcf,imgOdbName);
```

Script function: Creates polar plots to visualise node data.

Language: MATLAB

```matlab
clc
clear
clf

AngleMismatch="0";
CoeficientOfFriction="";
AssemblyForce="";
scale=1000;

%Start variables
variables=["COPEN"];
step=["0","3","6","10","13","18","20"];

stanceImg="";
stanceInfo="";
stancePercentage="";


linS = {'-','--','--o','--p','--s','--d','--*','--+'};
variablesSize=size(variables);
variablesSize=variablesSize(1,2);
stepSize=size(step);
stepSize=stepSize(1,2);
figMatsize=zeros(stepSize,variablesSize);
MaxGapOpening={};
plotColour=rand(1,3);

for steps=1:stepSize
  for vars=1:variablesSize
fig=figure('visible','off','Position', [10 10 900 600]);

path=' ';
PlotTittle='Angle mismatch: 0.18';
odbName="Job-Model-0d18Mismatch-Oval-0d1mm";
subject = "Round Taper";

odbTXT=odbName+'.odb-'+variables(1,vars)+'-f'+step(1,steps)+'_TrunnionSurface';
odbTXT_preLoad=odbName+'.odb-'+variables(1,vars)+'-f0_TrunnionSurface_preLoad';

imgOdbName=odbTXT;

disp('Frame: '+step(1,steps));

intVal=0;
transformedSurface={};
zMatrix={};

s=0;
```

```matlab
%Script starts
odbTXT=strcat(odbTXT,'.txt');
odbFile=strcat(path,odbTXT);

odbTXT_preLoad=strcat(odbTXT_preLoad,'.txt');
odbFile_preLoad=strcat(path,odbTXT);

if exist(odbFile,'file')
   taperSurface=readtable(odbFile);
   taperSurface_preLoad=readtable(odbFile);

   noZUniqueValues_preLoad=sort(unique(taperSurface_preLoad.ZCoordinate));
   noZUniqueValues_preLoad=unique(unique(taperSurface_preLoad.ZCoordinate));
   noZUniqueValues_preLoad=min(unique(taperSurface_preLoad.ZCoordinate));


taperSurface_preLoad=taperSurface_preLoad((taperSurface_preLoad.ZCoordinate==noZUniqueValu
es_preLoad),:);


trunnionCentre_X=(max(taperSurface_preLoad.XCoordinate)+min(taperSurface_preLoad.XCoordinat
e))/2;

trunnionCentre_Y=(max(taperSurface_preLoad.YCoordinate)+min(taperSurface_preLoad.YCoordinat
e))/2;

   taperSurface_preLoad.XCoordinate=taperSurface_preLoad.XCoordinate-trunnionCentre_X;
   taperSurface_preLoad.YCoordinate=taperSurface_preLoad.YCoordinate-trunnionCentre_Y;


taperSurface_preLoad.rad_distance=sqrt((taperSurface_preLoad.XCoordinate.^2)+(taperSurface_pr
eLoad.YCoordinate.^2));

taperSurface_preLoad.rad_angle=((atan2(taperSurface_preLoad.YCoordinate,taperSurface_preLoad.
XCoordinate))*(-1));

   tableJoin = join(taperSurface_preLoad,taperSurface,'LeftKeys',1,'RightKeys',1);

   tableJoin.gap=(tableJoin.Variable_taperSurface.*scale);

   tableJoin = sortrows(tableJoin,'rad_angle','ascend');

   theta=table2array(tableJoin(:,7:7));
   theta=theta';

   rho=table2array(tableJoin(:,12:12));
   rho=rho';

   rho_circumference=table2array(tableJoin(:,6:6));
   rho_circumference=rho_circumference';

   path2='';
```

```matlab
    polarplot(theta,rho,'LineWidth',6)
    %tabla=find(rho<=0)
    [Gap_max, index_max] = max(rho);
    max(rho)
    Gap_max_circum=theta(index_max);
    [Gap_min, index_min] = min(rho);
    Gap_min_circum=theta(index_min);
    hold on
    ax = gca;
    ax.FontSize = 24;
    %ax.ThetaTickLabel = [];

    hold on

    rlim([0,80]);
    lgd = legend('Taper separation','Location','NorthOutside','Box','off');
    text(deg2rad(90),25,'Supero-
lateral','HorizontalAlignment','center','VerticalAlignment','bottom','FontSize',24)
    text(deg2rad(270),20,'Infero-
medial','HorizontalAlignment','center','VerticalAlignment','bottom','FontSize',24)
    %lgd.Position=[0.41 -0.41 1 1];
    %axes('pos',[.65 .64 .5 .3])
    %imshow('Z:\Pictures\'+stanceImg, 'InitialMagnification',0.1)

    frame=getframe(fig);
    frame=frame2im(frame);

else
    disp(strcat(odbTXT,' file does not exist.'))
end

    filename=path2+odbName+'_COPEN.gif';
    filename_frame=path2+odbName+'_Step'+step{steps}+'_COPEN.png';

    [A,map] = rgb2ind(frame,256);
    imwrite(A,map,filename_frame);

    if steps == 1
        imwrite(A,map,filename,'gif','LoopCount',Inf,'DelayTime',1);
    else
        imwrite(A,map,filename,'gif','WriteMode','append','DelayTime',1);
    end

  end
end
```

Script function: Methods to create 2D geometries from surface measured data.

Language: Python

```python
# -*- coding: mbcs -*-
# Do not delete the following import lines
from abaqus import *
from abaqusConstants import *
import __main__

def CreateTrunnion():
    import section
    import regionToolset
    import displayGroupMdbToolset as dgm
    import part
    import material
    import assembly
    import step
    import interaction
    import load
    import mesh
    import optimization
    import job
    import sketch
    import visualization
    import xyPlot
    import displayGroupOdbToolset as dgo
    import connectorBehavior
    import numpy as np

    surface='Trunnion_taperAngle-5.679_threadNo-128_Amp-14um_Surface'
    NamePart='Trunnion_5p679_128_14um'

    path='G:/Surfaces Profiles/Trunnion/Ideal/'+surface+'.txt'


    #From MATLAB file get MinYY

    a=0.35
    b=0.35


    #Create sketch
    s1 = mdb.models['Model-1'].ConstrainedSketch(name='__profile__', sheetSize=100.0)
    g, v, d, c = s1.geometry, s1.vertices, s1.dimensions, s1.constraints
    s1.sketchOptions.setValues(viewStyle=AXISYM)
    s1.setPrimaryObject(option=STANDALONE)
    s1.ConstructionLine(point1=(0.0, -100.0), point2=(0.0, 100.0))
    s1.FixedConstraint(entity=g[2])

    #Drawing start
    points_surface=[]
    #Draw surface trunnion
    with open(path, 'r') as f:
        for line in f:
            x=line.rstrip().split(" ")
```

```python
            x=[float(x[0]),float(x[1])]
            points_surface.append(x)


##    points_surface=[[float(ele) for ele in sub] for sub in points_surface]

##    points_surface=[[sub[0],sub[1]] for sub in points_surface]

    points_surface=[tuple(sub) for sub in points_surface]
    points_surface=tuple(points_surface)
    s1.Spline(points=points_surface)
##    s1.Line(point1=(points_surface[0]), point2=(points_surface[len(points_surface)-1]))


    x_startingPoint=points_surface[0][0]
    z_startingPoint=points_surface[0][1]

    x_endingPoint=points_surface[len(points_surface)-1][0]
    z_endingPoint=points_surface[len(points_surface)-1][1]
##    #Draw top chamfer
    s1.Line(point1=(x_startingPoint, z_startingPoint), point2=(x_startingPoint-a, z_startingPoint+b))
##
##    #Draw top taper
    s1.Line(point1=(x_startingPoint-a, z_startingPoint+b), point2=(0, z_startingPoint+b))
##
##    #Draw centre taper
    s1.Line(point1=(0, z_startingPoint+b), point2=(0, z_endingPoint-b))
##
##    #Draw bottom taper
    s1.Line(point1=(0, z_endingPoint-b), point2=(x_endingPoint-a, z_endingPoint-b))
##
##    #Draw bottom chamfer
    s1.Line(point1=(x_endingPoint-a, z_endingPoint-b), point2=(x_endingPoint, z_endingPoint))

    #Create part from Sketch
    p = mdb.models['Model-1'].Part(name=NamePart, dimensionality=AXISYMMETRIC,
type=DEFORMABLE_BODY)
    p = mdb.models['Model-1'].parts[NamePart]
    p.BaseShell(sketch=s1)
    s1.unsetPrimaryObject()
    p = mdb.models['Model-1'].parts[NamePart]
    session.viewports['Viewport: 1'].setValues(displayedObject=p)
####    del mdb.models['Model-1'].sketches['__profile__']
def CreateFemoralHead():
    import section
    import regionToolset
    import displayGroupMdbToolset as dgm
    import part
    import material
    import assembly
    import step
    import interaction
    import load
    import mesh
    import optimization
    import job
    import sketch
```

```python
import visualization
import xyPlot
import displayGroupOdbToolset as dgo
import connectorBehavior
surface='Bore_taperAngle-5.76_threadNo-0_Amp-2um_Surface'
NamePart='Bore_5p76_0_2um'

path='G:/Surfaces Profiles/Bore/'+surface+'.txt'

#From MATLAB file get MinYY
minYY=6.30126

a=0.35
b=0.35

taperAngle=3


#Create sketch
s1 = mdb.models['Model-1'].ConstrainedSketch(name='Sketch taper', sheetSize=100.0)
g, v, d, c = s1.geometry, s1.vertices, s1.dimensions, s1.constraints
s1.sketchOptions.setValues(viewStyle=AXISYM)
s1.setPrimaryObject(option=STANDALONE)
s1.ConstructionLine(point1=(0.0, -100.0), point2=(0.0, 100.0))
s1.FixedConstraint(entity=g[2])

#Drawing start
#Draw top of the trunnion
s1.CircleByCenterPerimeter(center=(0.0, 10.0), point1=(15.0, 30.0))
s1.ObliqueDimension(vertex1=v[0], vertex2=v[1], textPoint=(15.4477615356445,
    16.7405052185059), value=18.0)


#Draw trunnion surface
x_offSet=minYY
z_offSet=0

with open(path) as f:
    points_surface = [line.rstrip().split(" ") for line in f]

points_surface=[[float(ele) for ele in sub] for sub in points_surface]

points_surface=[tuple(sub) for sub in points_surface]
points_surface=tuple(points_surface)

previousCoord=(x_offSet,30-z_offSet)

##  s1.Spline(points=points_surface)
  s1.Line(point1=(points_surface[0]), point2=(points_surface[len(points_surface)-1]))

  x_startPoint=points_surface[0][0]
  z_startPoint=points_surface[0][1]

  x_endPoint=points_surface[len(points_surface)-1][0]
  z_endPoint=points_surface[len(points_surface)-1][1]

  #Draw bottom of the taper
```

```
    s1.Line(point1=(x_endPoint, z_endPoint), point2=(x_endPoint+a, z_endPoint-b))
    s1.Line(point1=(x_endPoint+a, z_endPoint-b), point2=(x_endPoint+a+20, z_endPoint-b))
    s1.autoTrimCurve(curve1=g[len(g)+1], point1=(x_endPoint+a+20-0.01, z_endPoint-b))

    #Draw top of the taper
    s1.Line(point1=(x_startPoint,z_startPoint), point2=(0, z_startPoint))
    s1.Line(point1=(0, z_startPoint), point2=(0, 45))
    s1.autoTrimCurve(curve1=g[len(g)+2], point1=(0, 44.5))
    s1.autoTrimCurve(curve1=g[3], point1=(-20.0130023956299, 20.1609764099121))
    s1.autoTrimCurve(curve1=g[12], point1=(2.20605754852295, -10.183872222900391))

    #Create part from Sketch
    p = mdb.models['Model-1'].Part(name=NamePart, dimensionality=AXISYMMETRIC,
type=DEFORMABLE_BODY)
    p = mdb.models['Model-1'].parts[NamePart]
    p.BaseShell(sketch=s1)
    s1.unsetPrimaryObject()
    p = mdb.models['Model-1'].parts[NamePart]
    session.viewports['Viewport: 1'].setValues(displayedObject=p)




def CreateMaterials():
    import section
    import regionToolset
    import displayGroupMdbToolset as dgm
    import part
    import material
    import assembly
    import step
    import interaction
    import load
    import mesh
    import optimization
    import job
    import sketch
    import visualization
    import xyPlot
    import displayGroupOdbToolset as dgo
    import connectorBehavior
    session.viewports['Viewport: 1'].partDisplay.setValues(sectionAssignments=ON,
        engineeringFeatures=ON)
    session.viewports['Viewport: 1'].partDisplay.geometryOptions.setValues(
        referenceRepresentation=OFF)
    mdb.models['Model-1'].Material(name='Titanium')
    mdb.models['Model-1'].materials['Titanium'].Elastic(table=((109000.0, 0.33), ))
    mdb.models['Model-1'].materials['Titanium'].Plastic(table=((941.0, 0.0), (
        1200.0, 0.14)))
    mdb.models['Model-1'].Material(name='Cobalt')
    mdb.models['Model-1'].materials['Cobalt'].Elastic(table=((213000.0, 0.33), ))
    mdb.models['Model-1'].materials['Cobalt'].Plastic(table=((1026.0, 0.0), (
        1350.0, 0.13)))
```

A2. Publications

Papers

- Diaz-Lopez, R. A., Wen, P. H., & Shelton, J. C. (2022). Influence of taper design and loading on taper micromotion. *Journal of the Mechanical Behavior of Biomedical Materials*, *128*, 105106. https://doi.org/10.1016/j.jmbbm.2022.105106
- Diaz-Lopez, R. A., Wen, P. H., & Shelton, J. C. (2023). Influence of Taper surface topographies on contact deformation and stresses. *Journal of the Mechanical Behavior of Biomedical Materials* **(Under review)**

Conference

- International Society for Technology in Arthroplasty (*ISTA*) · Influence of Taper Design and Loading on Taper Micromotion (2020).